

QUANTUM TURBULENCE IN A PLANAR BOSE–EINSTEIN CONDENSATE

SHAUN PHILLIP JOHNSTONE
BScAdv(Hons)

SUPERVISED BY:
Prof. Kristian Helmerson
Dr. Lincoln Turner
Dr. Tapio Simula



A thesis submitted for the degree of
Doctor of Philosophy
at the School of Physics and Astronomy,
Monash University, Australia

December 2018

COPYRIGHT NOTICE

Quantum Turbulence in a Planar Bose–Einstein Condensate

© Shaun Phillip Johnstone, 2018

I certify that I have made all reasonable efforts to secure copyright permissions for third-party content included in this thesis and have not knowingly added copyright content to my work without the owner's permission.

ABSTRACT

Hydrodynamic turbulence remains one of the great unsolved problems of classical physics. The chaotic, swirling dynamics of fluids are governed by non-linear equations of motion, making direct predictions near impossible. However, some statistical properties of turbulence are seemingly universal. Quantum fluids, such as atomic Bose–Einstein condensates (BECs), can also feature turbulent flows. The quantum nature of these systems results in a simplification of their dynamics when compared with their classical counterpart: vortices are only allowed to take quantised units of circulation. Despite this difference, in three dimensions, these quantum fluids have been shown to exhibit the same universal dynamics as a classical fluid (on scales large compared with the inter-vortex spacing), such as the power-law scaling of the kinetic energy spectrum.

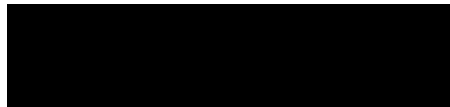
In two-dimensional (2D) flows, turbulence can produce counter-intuitive results. As noted by Lars Onsager, chaotic flows tend to develop order. Smaller vortices preferentially group with others of the same sign of circulation, developing large-scale features. Onsager pointed out that by analysing the kinetic energy of these flows, and the entropy associated with the vortex configurations, a ‘vortex temperature’ can be assigned. Surprisingly, for such vortices in a bound system, this *absolute* temperature can take on *negative* values!

If a BEC is confined such that its flow is essentially 2D, the quantised vortices become point-like objects, with either clockwise or counter-clockwise circulation. A recently developed experimental technique has allowed the simultaneous measurement of both the sign of circulation, and location of each vortex in these systems. With this information, the full incompressible velocity field of the BEC can be calculated, allowing the kinetic energy spectrum to be measured directly from experimental data. Statistical measures of the vortex distribution, such as the degree of clustering of like-signed vortices, can be made, which in turn allows the assignment of a vortex temperature.

This thesis presents the results of experiments on the distribution of vortices in a highly oblate, uniform BEC of ^{87}Rb , along with a description of the apparatus used. Vortices were generated by stirring with obstacles at various length scales, resulting in distributions spanning from positive to negative temperatures. A dynamic increase in the degree of vortex clustering was observed in some cases, corresponding to heating of the vortices. These results are in agreement with Onsager’s description of 2D turbulence, and add to the small, but growing, body of experimental works investigating the dynamics of these chaotic vortex configurations.

DECLARATION

This thesis contains no material that has been accepted for the award of any other degree or diploma at any university or equivalent institution and that, to the best of my knowledge and belief, this thesis contains no material previously published or written by another person, except where due reference is made in the text of the thesis.



Shaun Phillip Johnstone
17 December 2018

ACKNOWLEDGMENTS

There have been many people who have provided me with help and support through the various stages of my candidature. I would especially like to thank my primary supervisor, Kris, for his ongoing support and endless positivity. Kris, you've given me plenty of freedom to grow as a scientist in the lab, while always being there provide direction and advice.

Initially, building the lab and associated infrastructure was a huge team effort. Luckily I was part of an enthusiastic cohort of new students, spread between Kris's dual species BEC lab and Lincoln and Russ's spinor BEC lab. The coordination between the two labs in this initial building stage helped to speed up the process, as we shared the overheads of selecting parts, working out how to integrate them into our systems, and debugging. In particular, thank you Phil for sharing the brunt of the countless hours spent aligning lasers and optimising the apparatus with me, as well as your work building up the software suite that runs everything. Chris (Bilbo), thanks for being there as a repository of Python knowledge, and your work on the control system. Brad must also be thanked for getting the ball rolling in the lab with the design and construction of the vacuum system. The spinor lab students, Alex, Martijn and Lisa, your comradery and the friendly race to see which lab could make a BEC first (we did!) was much appreciated.

Thanks to my co-supervisor Lincoln, along with Russ (who acted as an additional unofficial mentor), for their roles in developing my lab skills and teaching me so much. Brett, Nino and everyone in the Monash workshops helped to make building a complex scientific apparatus a reality. Their expertise allowed many components to be developed in-house, and repairs to be made without sending parts overseas.

Mikhail came on board as a postdoc in our lab just as the apparatus was beginning to take shape—thank you for bringing your experience to the lab, I'm sure it would have taken us even longer to get it all working if it weren't for you. Seb, thank you for your work generating holograms—I have also enjoyed helping you build the new apparatus, having the chance to do things differently the second time around.

Tapio became increasingly involved in my work once I began generating vortices in the lab, eventually becoming my co-supervisor. It was great to see you get so excited seeing experimental results in the lab, and your knowledge of quantum turbulence has been invaluable. Thanks must also go to Andrew for your theoretical support in analysing and interpreting the results of my experiments.

I am also grateful for the support I have received from the School of Physics and Astronomy. Thanks to postgraduate coordinators, David and Alexis (who continued to act in this role for me when Kris took over as coordinator), and particularly our wonderful student services officer, Jean, for keeping us all organised. Michael, your continual questions about when we'd have results kept us from slacking off. Rob Seefeld, thank you so much for your hard work coordinating the move to New Horizons, making sure issues with the lab space get fixed and dealing with all the contractors for us. The postgraduate students in the school have added a wonderful social aspect to the PhD experience—thanks to everyone who I've shared a beer with on a Friday evening.

Beyond Monash, it's been a pleasure to be involved in the cold atoms and optics community in Australia, New Zealand and beyond. In particular, I'd like to thank Rob Scholten for always being happy to loan us lasers or promptly solve any issues with MOGLABS products. Thanks to Nick Robins for answering many questions and sending us spare parts during an unplanned vacuum repair. To Tyler, Matt and the team at UQ, thank you for your cooperation in working toward having our complimentary results published together, our many discussions have strengthened both manuscripts.

I have been lucky enough to attend many of the annual KOALA student conferences around Australia and New Zealand, and made many friends along the way. These conferences also prompted us to start the Monash student chapter of the OSA (thanks in particular to Chris W), and eventuated in us hosting IONS KOALA 2016. Thanks to everyone on the conference committee, our invited speakers, sponsors and most importantly, the attendees, for making it such a great conference! Organising an event of this scale and managing a committee spread across two institutions was a challenging but valuable experience.

The OSA also gave me the opportunity to visit the USA to attend their Frontiers in Optics conference—an experience made all the more enjoyable by the company of travel mates Rory and Bianca. It has also given me the opportunity to try to get the next generation of scientists excited about optics with our many school outreach visits. Recently FLEET and JMSS have provided additional outreach opportunities, which I look forward to continuing to participate in.

Thank you to my family—Mum, Dad, Grace and Mark—for your support over the last few years. Melissa, thank you for your love and putting up with me as a seemingly never ending student!

CONTENTS

1	INTRODUCTION AND BACKGROUND	1
1.1	Classical Turbulence	2
1.1.1	Statistical properties of turbulence	4
1.1.2	Turbulence in two dimensions	6
1.2	Bose–Einstein condensation and superfluidity	15
1.2.1	A brief introduction to Bose–Einstein condensates	15
1.2.2	Making BECs	16
1.2.3	Superfluidity and quantum hydrodynamics	18
1.2.4	Excitations	18
1.2.5	Quantum vortices	19
1.2.6	The kinetic energy spectrum	24
1.2.7	Creating and observing vortices	25
1.3	Quantum turbulence	31
1.3.1	Statistical properties of quantum turbulence	31
1.3.2	2D quantum turbulence	34
1.4	More on negative absolute temperature systems	47
1.4.1	Ramsey’s description of negative absolute temperatures	47
1.4.2	Do negative absolute temperature states really exist?	48
2	BUILDING A BEC APPARATUS	51
2.1	Contributions to the KRb lab	51
2.2	The vacuum system	53
2.2.1	The atomic sources	54
2.2.2	The UHV chamber	55
2.2.3	Repairs to the vacuum system	55
2.3	Lasers	58
2.4	Electromagnets	62
2.5	Control of the experiment	63
2.5.1	Hardware	63
2.5.2	Software	64
2.5.3	Hardware timed serial commands	66
2.6	Laser cooling and trapping	67
2.6.1	Cold atomic sources	69
2.6.2	The dual species central MOT and magnetic trap	70
2.6.3	Microwave-induced evaporation	74
2.7	Optical dipole traps	75
2.7.1	Dipole trap alignment	75
2.7.2	Loading the dipole trap	77
2.7.3	Dipole trap configurations	77

2.8	Imaging	82
2.8.1	Side imaging in the central chamber	84
2.8.2	High resolution imaging in the square cell	84
2.8.3	Side imaging in the square cell	87
2.8.4	High resolution imaging in the central chamber	87
2.8.5	Fringe suppression	89
3	CREATING A UNIFORM OBLATE BEC	93
3.1	Axial confinement	93
3.1.1	Red-detuned light sheets	93
3.1.2	Blue-detuned Hermite–Gaussian mode	94
3.1.3	Tilting 2D traps	97
3.2	Radial confinement	100
3.2.1	Harmonic confinement	100
3.2.2	Holographic blue-detuned potentials	100
3.2.3	Digital micromirror device potentials	102
3.3	Generating vortices	104
3.3.1	Moving the BEC through an obstacle	105
3.3.2	Moving an obstacle through the BEC	105
4	2D QUANTUM TURBULENCE IN A UNIFORM BEC	109
4.1	Generating grid turbulence	109
4.2	Imaging the vortex distribution	110
4.2.1	Processing the Bragg images	113
4.3	Analysing the vortex distribution	119
4.3.1	Incompressible kinetic energy	121
4.3.2	Vortex cluster detection	122
4.3.3	Thermometry	123
4.3.4	Vortex decay process	126
4.4	Discussion	132
5	CONCLUSIONS	135
5.1	Summary	135
5.2	Outlook	136
	BIBLIOGRAPHY	139

LIST OF FIGURES

Figure 1.1	A sketch of turbulent flow by Leonardo da Vinci	3
Figure 1.2	Flow past a cylinder	5
Figure 1.3	The energy spectrum of classical turbulence	6
Figure 1.4	Point vortex density of states	9
Figure 1.5	Energy spectra in two dimensional turbulence	10
Figure 1.6	Turbulent dynamics on Jupiter	13
Figure 1.7	Energy cascades in electrolyte solutions	14
Figure 1.8	Dual cascade in a soap film	14
Figure 1.9	The onset of Bose–Einstein condensation	17
Figure 1.10	A vortex lattice in a BEC	21
Figure 1.11	Decay of a Jones–Roberts soliton	23
Figure 1.12	Bragg resonance condition around a vortex	30
Figure 1.13	Differential Bragg signal of turbulent vortices	30
Figure 1.14	A quantum von Kármán vortex street	32
Figure 1.15	Vortex clustering in harmonic and uniform traps	39
Figure 1.16	Turbulent vortices in a toroidal BEC	44
Figure 1.17	A vortex street in BEC	45
Figure 2.1	The vacuum chamber	54
Figure 2.2	Magnetic trap lifetime measurements	56
Figure 2.3	The failed vacuum window	57
Figure 2.4	Rubidium laser frequencies	59
Figure 2.5	Potassium laser frequencies	59
Figure 2.6	Schematic of the laser table	60
Figure 2.7	Overview of the lab control hardware	65
Figure 2.8	An overview of the labscript suite workflow	66
Figure 2.9	The dual species MOT layout	71
Figure 2.10	The dual species MOT load sequence	73
Figure 2.11	Alignment of optical dipole traps	76
Figure 2.12	The final stages of evaporation to our first BEC	78
Figure 2.13	Attempt to observe six wave mixing	79
Figure 2.14	Layout of the transport dipole trap	80
Figure 2.15	Layout of the crossed dipole trap	83
Figure 2.16	Side imaging systems	85
Figure 2.17	High resolution imaging in the square cell	86
Figure 2.18	Central chamber top imaging	89
Figure 2.19	Eigenbasis image processing	91
Figure 3.1	Fringes in the red-detuned light sheet	94
Figure 3.2	Recording transmission holograms	95
Figure 3.3	Hermite–Gaussian mode hologram optics	96
Figure 3.4	The Hermite–Gaussian mode trap	97
Figure 3.5	Photograph of the rotating lens	98

Figure 3.6	Axicon mode profile	102
Figure 3.7	Digital micromirror device potentials	104
Figure 3.8	A vortex lattice in the harmonic 2D trap	106
Figure 3.9	Grid obstacles passing through a BEC	108
Figure 4.1	DMD trap layout	111
Figure 4.2	Detection of vortex locations	115
Figure 4.3	Example vortex configurations	118
Figure 4.4	Determining the vortex sign configuration	119
Figure 4.5	Vortices at positive and negative temperatures	120
Figure 4.6	Energy spectra for varying grid spacings	122
Figure 4.7	Thermometry curves	125
Figure 4.8	Uncertainty in temperature measurements	125
Figure 4.9	Temperature assignment	127
Figure 4.10	4.2 μm grid dynamical evolution	128
Figure 4.11	6.0 μm grid dynamical evolution	129
Figure 4.12	7.9 μm grid dynamical evolution	129
Figure 4.13	9.7 μm grid dynamical evolution	130
Figure 4.14	11.5 μm grid dynamical evolution	130
Figure 4.15	Vortex number decay	131

LEGEND TO OPTICAL LAYOUT FIGURES

 780nm/767nm laser	 Half Waveplate	 Plano-convex lens	 Acousto-Optic Modulator (AOM), resonant at f MHz
 532nm laser	 Quarter Waveplate	 Bi-convex lens	 Fibre Couple
 1064nm laser	 Polariser	 Plano-concave lens	 Balanced Photodiode
 Broadband mirror	 Polarising Beam Splitter Cube	 Bi-concave lens	 Beam Dump
 Long-pass dichroic mirror	 Non-Polarising Beam Splitter Cube	 Achromat lens	 Aperture
 Short-pass dichroic mirror	 Flipper mirror	 Gaussian Telescope Magnification M	 Alkali Vapour Cell

ABBREVIATIONS

2D	two-dimensional
2DQT	2D quantum turbulence
3D	three-dimensional
AOM	acousto-optic modulator
BEC	Bose–Einstein condensate

BKT	Berezinskii–Kosterlitz–Thouless
DDS	direct digital synthesizer
DMD	digital micromirror device
EBC	Einstein–Bose condensate
ECDL	external cavity diode laser
EMCCD	electron multiplying charge-coupled device
GPE	Gross–Pitaevskii equation
HDF	hierarchical data format
HG	Hermite–Gaussian
LG	Laguerre–Gaussian
MC	Monte Carlo
MOT	magneto-optical trap
NAT	negative absolute temperature
NI	NATIONAL INSTRUMENTS
NTPP	nonthermal fixed point
OD	optical density
PGC	polarisation gradient cooling
PIV	particle image velocimetry
QT	quantum turbulence
rf	radio frequency
ROI	region of interest
s.e.m.	standard error of the mean
SLM	spatial light modulator
TA	tapered amplifier
TF	Thomas–Fermi
UHV	ultra-high vacuum

INTRODUCTION AND BACKGROUND

Atomic Bose–Einstein condensates (BECs) are macroscopic quantum systems, typically consisting of a cloud of alkali atoms cooled to below a few hundred nanokelvin [1–3]. In a scalar BEC (with no spin degree of freedom) the quantum properties of the cloud result in the quantisation of circulation, meaning that vortices are well defined, localised objects with known circulation. This is in stark contrast to a classical fluid, in which circulation can take any value, making it hard to pinpoint the location and strength of vortices. This thesis describes experiments observing the behaviour of vortices in a turbulent BEC, confined in a highly oblate geometry, such that the vortex dynamics are two-dimensional (2D). In this *planar* system, the BEC is essentially pancake shaped, with an in-plane profile that is uniform away from the boundary.

Turbulence is a phenomenon, which is ubiquitous in nature, characterised by the chaotic flow of a fluid. In three-dimensional (3D) flows, a cascade process carries energy from the largest length scales to the smallest, causing large flow patterns due to stirring to break down to smaller and smaller features. Turbulence can be seen as a hindrance, for example, restricting the flow of water through a pipe [4] or increasing drag on an object passing through air or a fluid [5]. However, it can also be beneficial, such as in mixing processes, where it can improve efficiency of industrial chemical mixing [6], or the combining of gases in an internal combustion engine [7]. Elements of the statistical description of turbulence can also be used to describe other dynamical systems, such as the inflation of the early universe [8], the dynamics of quark-gluon plasmas [9] and even financial markets [10].

In flows restricted to 2D, the dynamics of turbulence are remarkably different to the 3D case. A distinct feature of 2D flows is the common appearance of large-scale flow features, which can form due to the turbulent dynamics. In contrast to the energy cascade of 3D turbulence, an inverse energy cascade can transport energy from small to large scales. Such 2D flows can even be seen in 3D systems that are highly oblate, such that motion is predominantly in-plane. Natural examples of this can be seen in ocean currents [11, 12] and atmospheric dynamics on both Earth [13] and Jupiter [14–16], where large-scale features such as the Great Red Spot are prominent.

Vortices are believed to play an important role in turbulent dynamics, however their role is hard to probe in a classical fluid as they are not well defined objects. In superfluids, however, the quantisation of vortices results in flows characterised entirely by the position and

circulation of these particle-like defects. It is hoped that by studying the role of interactions of these quantum vortices in the superfluid case, new insights may be translated across to the classical problem. However, while the flow properties of a superfluid may appear to be a simplification, experimentally obtaining this information can be challenging.

In classical fluids, particle image velocimetry (PIV) can be used to obtain information about the flow field with high spatial and temporal resolution [17, 18]. The positions of particles, such as polystyrene microspheres, are tracked from frame to frame as they follow the motion of the fluid. To apply similar techniques to a superfluid, the particles must be small enough to resolve the relevant length scales, and cold so as to not heat the system. In liquid helium, frozen hydrogen particles have been used to determine the location of vortex cores [19], and liquid neon has been used for PIV [20]. No such technique has been applied to BECs, however, as the flow is quantised, by knowing the circulation and position of every vortex in a system the velocity field can be calculated. Though this full vortex tomography is not yet experimentally feasible for a turbulent 3D BECs, it has recently been achieved in 2D [21]. The experiments in this thesis take advantage of this recently demonstrated experimental technique, using velocity selective Bragg spectroscopy to measure the sign of every vortex in a planar BEC.

These introductory sections aim to provide enough background information to allow the experimental results to be interpreted. I will provide references in side notes like this where the reader can find much more detailed coverage of each topic.

This Chapter will begin by introducing the problem of classical turbulence in §1.1, which motivates the study of the quantum analogue. Then, to move to the quantum world, §1.2 will discuss the key features of BECs, and the quantised vortices that arise in them. We will return to turbulence in §1.3, this time in the context of these quantised vortices in a BEC. The vortex configurations generated in 2D turbulence can be described as having a *negative absolute temperature* (NAT). In §1.4 we will compare these configurations with other systems that have been described using NATs, and discuss the ongoing controversy over whether this is a useful way of describing physical systems.

In Chapter 2, the apparatus built during my candidature will be described, while discussing the experimental procedure for producing a BEC. Chapter 3 will then focus on the techniques used to form an oblate BEC, and generating vortices in this geometry. I will then report on our measurements of 2D quantum turbulence (2DQT) in this system in Chapter 4, where the clustering of vortices was observed. I will conclude with a summary and some remarks about possible follow-up experiments in Chapter 5.

1.1 CLASSICAL TURBULENCE

Despite its ubiquity throughout nature, turbulence is not particularly well defined. It can, however, be characterised by chaotic fluid flow,



FIGURE 1.1: A SKETCH OF TURBULENT FLOW BY LEONARDO DA VINCI.

This sketch, circa 1500, depicts the flow of water into a pool. In the accompanying notes, da Vinci noted the role of vortices in the chaotic component of the fluid motion, which perturbs the underlying current [22]. Reproduced with permission from detail of RCIN 912660 Verso: *Studies of flowing water, with notes* [23]. Royal Collection Trust / © Her Majesty Queen Elizabeth II 2018.

with a proliferation of vortices, across large ranges of length scales. An early example of an appreciation of the complexity of turbulence is the depiction of water flowing into a pool by Leonardo da Vinci (Fig. 1.1). He described how the vortices appear to move randomly due to the flow produced by other vortices, with the larger scale flows advecting the smaller vortices [22]. Despite having been studied for centuries, turbulence has been labelled as one of the last great unsolved problems of classical physics, as there is no way to infer the properties of turbulent flow from first principles.

As with most fluid dynamics problems, a theoretical description of classical turbulence generally begins with the Navier–Stokes equation for an incompressible Newtonian fluid,

$$\rho \frac{\partial \mathbf{v}}{\partial t} = -\rho(\mathbf{v} \cdot \nabla)\mathbf{v} - \nabla p + \rho\nu\nabla^2\mathbf{v} + \mathbf{f}, \quad (1.1)$$

which describes the velocity field $\mathbf{v}(\mathbf{r}, t)$ of a fluid of density ρ , pressure $p(\mathbf{r}, t)$ and kinematic viscosity ν , with external forcing $\mathbf{f}(\mathbf{r}, t)$. This is essentially Newton’s second law for the velocity of a parcel of fluid. Most fluids can be approximated as incompressible, in which case $\nabla \cdot \mathbf{v} = 0$.

Vortices play an important role in turbulence, though they are not particularly well defined objects in classical fluids. A vortex is characterised as a tube about which a fluid circulates. As vortices can change strength or merge it is hard to track them individually. We can, however, define the net vorticity of a fluid as $\boldsymbol{\omega} = \nabla \times \mathbf{v}$. The line integral of the velocity field around a contour \mathcal{C} gives the circula-

A detailed introduction to classical turbulence can be found in books by Davidson [24] and Frisch [25].

In the discussion of classical turbulence, I will use the terms vortex and eddy interchangeably, indicating swirling fluid motion.

tion, which is equal to the integral of the vorticity over the enclosed area \mathcal{A} ,

$$\Gamma = \oint_{\mathcal{C}} \mathbf{v} \cdot d\mathbf{l} = \int_{\mathcal{A}} \boldsymbol{\omega} \cdot d\mathbf{A}. \quad (1.2)$$

While (1.1) describes the full properties of fluid flow, the non-linearity makes it impossible to find analytic solutions in most cases. Even the most minute changes to a problem's initial conditions are amplified, changing the resulting flow. Numerical solutions are also difficult to compute for turbulent systems, due to the wide range of length and time scales involved in such a problem. Therein lies the 'unsolved' nature of turbulence.

1.1.1 Statistical properties of turbulence

Despite the highly dynamic, chaotic nature of turbulence, in most scenarios the time-averaged properties of flows are actually predictable. This has led to the development of statistical descriptions of turbulence, which have become very powerful tools for both describing and predicting the properties of these systems.

1.1.1.1 The Reynolds number

While it is generally difficult to compute properties of a fluid directly from (1.1), for a system with characteristic length scale L and velocity scale u , one can compute a *Reynolds number* [26, 27],

$$\text{Re} = \frac{Lu}{\nu}, \quad (1.3)$$

which can be used to predict the nature of the flow. This can be thought of as the ratio of inertial and viscous forces. At low Reynolds number, the viscous forces dominate, smoothing out perturbations in the flow, whereas at high Reynolds number, the inertial forces amplify them.

A classic example of the effect of the Reynolds number on the nature of a flow is the case of flow past a cylinder, depicted in Fig. 1.2. For small Re , the flow remains laminar, passing around the obstacle smoothly with little visible wake. As Re increases, vortex structures begin to form in the wake, and eventually pairs of vortices are shed in a *von Kármán vortex street*. At even higher Re , turbulence begins to emerge, as the predictable flow breaks down into a chaotic tangle of vortices. Though the Reynolds number can be thought of as a proxy for the degree of turbulence, there is no clear critical transition point characterising the onset of turbulence.

1.1.1.2 Energy cascades

In Fig. 1.1, eddies are shown spanning many length scales, from the system size, down to small specks. This common feature of turbulent

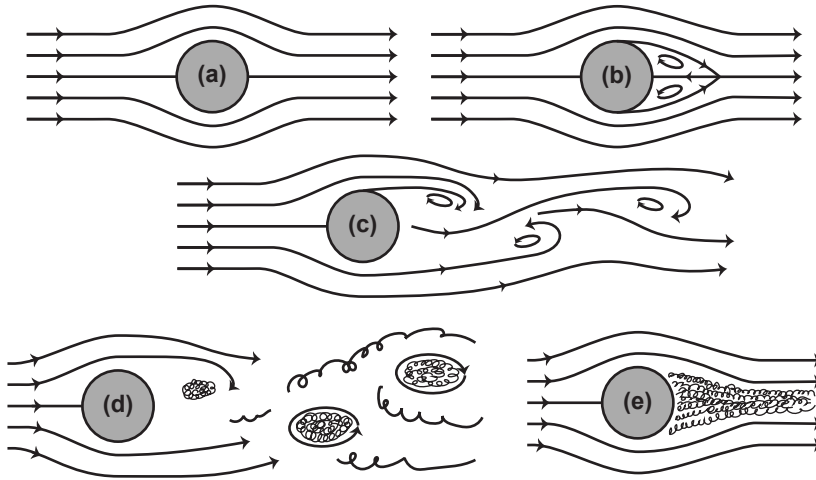


FIGURE 1.2: FLOW PAST A CYLINDER.

The wake of a cylindrical obstacle is dependent on the Reynolds number. **(a)** At $Re < 1$ the flow is laminar. The streamlines bend around the obstacle, then return to a uniform flow downstream. **(b)** As Re increases ($10 \lesssim Re \lesssim 30$) the downstream symmetry is broken by a pair of vortices, formed directly behind the cylinder. **(c)** For $40 \lesssim Re \lesssim 200$ the vortices begin to break away one by one, forming an alternating chain of vorticity, known as the von Kármán vortex street. **(d)** Beyond $Re \approx 400$ the vortices begin to break down into turbulent pockets of net circulation, still periodically shedding behind the obstacle. **(e)** Eventually for $Re \gtrsim 10^4$ the wake becomes fully turbulent. To the edges of the wake, however, the flow appears almost laminar again.

fluids arises due to the local transfer of energy across length scales. Motion is transferred to the fluid at some large scale, such as that of the container or a paddle. This forms large-scale eddies, which, due to inertial instabilities, break down into smaller eddies. These break down into even smaller scale features, and so on, a process known as the Richardson cascade [28]. The cascade continues, until a scale at which the *local* Reynolds number—that is, Re calculated based on the scale and velocity of fluid in a particular vortex—approaches unity, at which point the viscous term begins to dominate the flow. As Richardson put it, “*big whirls have little whirls that feed on their velocity, and little whirls have lesser whirls and so on to viscosity*” [28].

In 1941, Kolmogorov [34] quantified the nature of this cascade process, finding a universal scaling law. He proposed that below some length scale, l , known as the *integral scale*, turbulence becomes isotropic, with no information remaining about the large scale stirring motion. Furthermore, above the *Kolmogorov scale*, $\eta \sim (\nu^3/\epsilon)^{1/4}$, where viscosity begins to dominate, the cascade depends only on the dissipation rate ϵ of the fluid. This range, $\eta < |r| < l$, is known as the *inertial range*. Remarkably, Kolmogorov showed that the energy spectrum in this range has a universal form,

$$E(k) = C\epsilon^{2/3}k^{-5/3}, \quad (1.4)$$

Though this result is generally attributed to Kolmogorov, it is also attributed to his student, Obukhov [29], and was later independently derived by both Onsager [30] and Weizsäcker [31], and built upon by Heisenberg [32, 33].

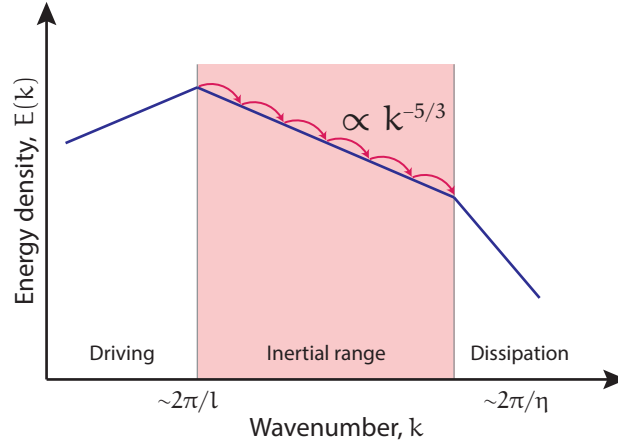


FIGURE 1.3: THE ENERGY SPECTRUM OF CLASSICAL TURBULENCE.

When viewed on a log-log scale, the energy spectrum has three distinct regions: driving occurs in the integral range (or energy containing range), with eddies created on the largest scales of the flow; the energy cascade occurs (indicated by arrows) over the inertial range, with the spectrum featuring a $k^{-5/3}$ slope; and dissipation occurs on the Kolmogorov scale, where viscosity damps out remaining energy.

the so called five thirds rule, where $k = |2\pi/r|$ is the wavenumber, and C is a universal dimensionless constant.

A representation of the energy spectrum is given in Fig. 1.3, showing the various length scales involved. For the inertial range to exist, the Reynolds number must satisfy $Re^{3/8} \gg 1$. There have been experimental confirmations of the $k^{-5/3}$ rule in many types of flow, and the value of $C \approx 1.5$ is consistent across many experiments [24, 25].

1.1.2 Turbulence in two dimensions

In $2D$ the statistical properties of turbulence change dramatically. In fact, even in $3D$ fluids, if there is little flow in one direction, such as in a highly oblate geometry, the dynamics follow that of a $2D$ system. Such systems are seen throughout nature, such as in the large scale flows of the atmosphere and oceans.

If we take the curl of (1.1) we get an equation for the vorticity of a fluid:

$$\frac{\partial \boldsymbol{\omega}}{\partial t} = (\boldsymbol{\omega} \cdot \nabla) \mathbf{v} - (\mathbf{v} \cdot \nabla) \boldsymbol{\omega} + \nu \nabla^2 \boldsymbol{\omega} + \frac{1}{\rho} \nabla \times \mathbf{f}. \quad (1.5)$$

The first term on the right hand side relates to the stretching of vortices in $3D$. In $2D$, this term must vanish, a fact that fundamentally alters the properties of the flow. In the limit of an inviscid $2D$ fluid, not only is energy conserved, but also *enstrophy*, $\Omega = \int \boldsymbol{\omega}^2 d\mathbf{r}$. When viscosity is present, neither energy or enstrophy are conserved, however, both are bounded, such that they can only decrease in the absence of forcing.

1.1.2.1 The point vortex approximation

Before discussing the statistical properties of 2D turbulence, I will introduce the *point vortex model*. This model will be of importance for both classical and quantum turbulence in 2D. It was first noted by Helmholtz [35] and Kirchhoff [36] that vortices in 2D fluids can be approximated as singular points about which a flow field exists. The flow field of the system is then given by the sum of the contributing vortices,

$$\omega(\mathbf{r}) = \sum_i \Gamma_i \delta(\mathbf{r} - \mathbf{r}_i), \quad (1.6)$$

where the i^{th} vortex is located at \mathbf{r}_i with circulation Γ_i .

The dynamics of these point vortices are governed by the equations

$$\Gamma_i \frac{dx_i}{dt} = \frac{\partial H}{\partial y_i}, \quad \Gamma_i \frac{dy_i}{dt} = -\frac{\partial H}{\partial x_i}, \quad (1.7)$$

which resemble Hamilton's equations in one dimension, with the fluid's kinetic energy given by a Hamiltonian H . For an unbounded system, the energy of each vortex is infinite, however the dynamics are given by the pair-wise interaction of vortices, given by

$$H = -\frac{1}{4\pi} \sum_{i < j} \Gamma_i \Gamma_j \ln \left(\frac{|\mathbf{r}_i - \mathbf{r}_j|}{R} \right), \quad (1.8)$$

where R is an arbitrary reference scale (an additive constant is not relevant to the vortex dynamics).

The more general case of a fluid in a multiply connected region was considered by Lin [37, 38]. Here, (1.8) must be replaced with a Kirchhoff–Routh function, derived from a Green's function. This is equivalent to including fictitious *image vortices* beyond the boundary. For the case of a uniform circular system of radius R , the boundary conditions are satisfied by introducing one image vortex for each real vortex, with the same magnitude, but opposite sign, located outside the boundary. For a vortex at position \mathbf{r}_v , an image will be located at $\mathbf{r}_{\text{img}} = R^2 \mathbf{r}_v / |\mathbf{r}_v|^2$.

Of course, a classical fluid can support arbitrary continuous values of Γ , and the vortices are not always point-like. As pointed out by Onsager [39], the model is, however, ideally suited to a superfluid, where the quantised vortices have fixed circulation, and are indeed almost point-like. We shall return to this point in §1.2.5.2.

The point vortex model is also applicable to systems beyond fluid dynamics, such as guiding-centre plasmas [40] and self-gravitating systems [41]. Guiding-centre plasmas are systems containing filaments of charge, aligned parallel to a magnetic field. It was experiments in such systems in the 1970's that sparked much of the research utilising the point vortex model. As the equations of motion are identical

(within a scale transformation), these results have direct applicability to the original fluid dynamics context.

1.1.2.2 Statistical mechanics of point vortices

Eyink and Sreenivasan [42] have reviewed Onsager's contribution to the field of turbulence, including unpublished notes and letters to colleagues.

A statistical theory of turbulence in 2D was presented by Onsager in 1949 in his seminal paper titled *Statistical Hydrodynamics* [39], in which he discussed the common observation of large-scale vortices in unsteady flows. Onsager noted that “the formation of large, isolated vortices is an extremely common, yet spectacular phenomenon in unsteady flow. Its ubiquity suggests an explanation on statistical grounds.”

For a system of N vortices confined to a finite area A , the spatial coordinates of the vortices are canonical conjugates. This means that the configuration-space is also the phase-space, and is finite, with A^N available states. The kinetic energy of the system [given by the generalised form of (1.8)] can take values from ∞ (corresponding to vortices of the same sign on top of each other) to $-\infty$ (corresponding to vortices of opposite sign on top of each other). The number of vortex configurations leading to a given energy E is known as the density of states, $w(E)$. Since the phase-space is finite, the integral of the density of states,

$$\int_{-\infty}^{\infty} w(E) dE = A^N, \quad (1.9)$$

implies that at the maximum energy states, $w(E)$ must go to zero. This means that $w(E)$ must have a maximum at some intermediate, finite energy.

Onsager pointed out that the usual definition of temperature,

$$\frac{1}{T} = \frac{\partial S}{\partial E}, \quad (1.10)$$

where $S(E) = k_B \log [w(E)]$ is the Boltzmann entropy (and k_B is Boltzmann's constant), can be applied to assign a *vortex temperature*. Furthermore, as S has a maximum value at some finite energy, there exists a regime in which entropy will *decrease* as more energy is added to the system. This corresponds to (1.10) taking a *negative* value, which is described, counter-intuitively, as a *negative absolute temperature* (NAT) state. These NATs are, in fact, hotter than positive temperatures. It is most intuitive to consider the inverse temperature, $\beta = 1/k_B T$, which spans from $\beta \rightarrow \infty$ as $T \rightarrow 0$, through $\beta = \pm 0$ at the maximum entropy state (where $T \rightarrow \pm\infty$) to $\beta \rightarrow -\infty$ as $T \rightarrow -0$. Physically, this means that beyond this maximum entropy state, the system of vortices will regain order, as like-sign vortices gather together. The relation between $w(E)$, β and the vortex configuration is shown in Fig. 1.4.

At positive temperatures, vortices of opposite sign approach each other, as this minimises their net energy, whereas at NATs the opposite

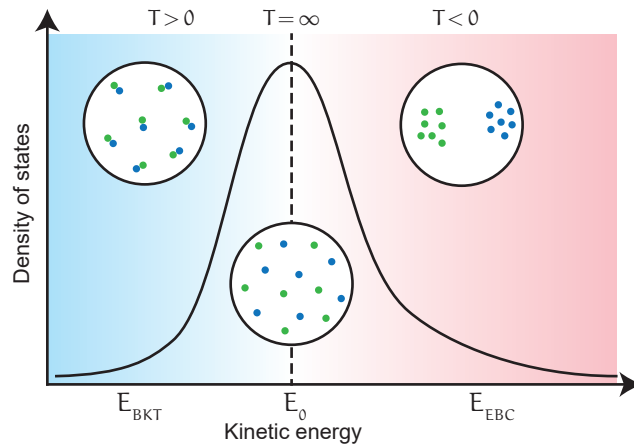


FIGURE 1.4: POINT VORTEX DENSITY OF STATES.

A depiction of the typical form of the density of states, $w(E)$, for point vortices in a finite domain. At low energies, $w(E)$ increases as a function of energy, and so the system has a positive temperature. In this region, the vortex configuration consists of many vortex–antivortex pairs. Beyond a critical point E_0 , $w(E)$ begins to decrease as the system energy is increased, so the system can be described with a NAT. The configuration becomes more ordered as higher energy clusters of like-sign vortices are formed. Insets show typical vortex configurations (blue and green dots represent vortices of opposite signs) near the BKT transition, near infinite temperature and near the EBC transition (these transitions will be discussed in §1.1.2.4).

occurs. Onsager suggested that the strongest vortices of each sign would arrange themselves together to ‘use up excess energy at the least possible cost in terms of degrees of freedom.’ This then leaves these large scale clusters as the dominant features of the flow, with smaller vortices free to roam at random between them.

It should be noted that the vortex ‘temperature’ is not necessarily that of the thermodynamic limit. Due to the long-range nature of vortex interactions, the temperature depends on the size and geometry of the system [43]. It can be shown, however, that as the system size goes to infinity (with vortex density and energy per vortex held constant) a thermodynamic limit does exist, with only positive temperatures supported [44]. This is not surprising, given that the argument for the existence of NATs was due to the finite phase-space. I will discuss systems that support NAT states in a more general context in §1.4.

1.1.2.3 Energy cascades in 2D

Given the success of Kolmogorov’s description of the energy spectrum of 3D turbulence, it is natural to look for similar universal scaling laws for the 2D case. However, the presence of a conservation law for enstrophy (in the inviscid limit) complicated the matter, with Lee showing that it implies that the direct energy cascade is not possible in 2D [45]. Fjørtoft showed that energy must instead evolve toward large length scales, while enstrophy moves to small scales [46].

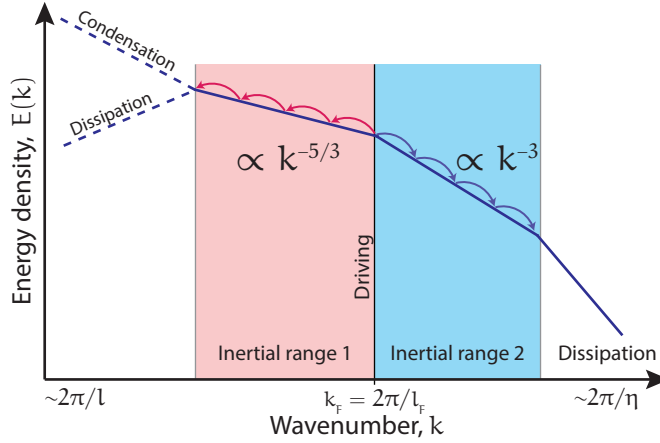


FIGURE 1.5: ENERGY SPECTRA IN TWO DIMENSIONAL TURBULENCE.

In driven 2D turbulence, the dual cascades of energy and enstrophy lead to two inertial ranges, with characteristic scaling. At scales larger than the driving (lower k), the inverse energy cascade (indicated by red arrows) leads to $k^{-5/3}$ scaling, whereas at smaller length scales (higher k), a direct enstrophy cascade (indicated by blue arrows) gives rise to k^{-3} scaling. At the lowest wavenumbers, on the scale of the system size, the energy can either decay, in the presence of large-scale damping, or build up, causing spectral condensation. In the absence of a driving force, only the second inertial range remains, with the enstrophy cascade persisting with k^{-3} scaling.

Kraichnan showed that this corresponds to a *dual cascade* of both energy and enstrophy [47], depicted in Fig. 1.5. If a 2D fluid is driven at an intermediate length scale l_F , energy will undergo an *inverse* cascade to longer scales (lower wavenumber), while enstrophy will undergo a *direct* cascade to smaller scales (high wavenumber). Though the energy cascade has the opposite direction to that of the 3D case, the scaling is the same, with $E(k) \propto k^{-5/3}$ for an inertial range from the driving scale to scales on the order of the system size. At the largest scales, one of two things can occur. If there is a large-scale damping effect, such as friction between the fluid and the 2D confinement, this can cause dissipation on the system size scale. In the absence of such damping, however, energy can build up in the lowest modes, leading to *spectral condensation*. We will discuss this in more detail, and the relation to Onsager's picture of large-scale clusters in §1.1.2.4. It is worth noting that the emergence of spectral condensation is not necessarily evidence of an inverse energy cascade. A relative increase in long-range energy may also arise if there is preferential removal of energy at short scales.

The enstrophy cascade, on the other hand, occurs over a second inertial range, from the driving scale down to the Kolmogorov scale, and results in the energy spectrum taking the form $E(k) \propto k^{-3}$ in this region. The enstrophy spectrum in this second inertial range takes the form $\Omega(k) \propto k^{-1}$. Batchelor independently derived the existence of this enstrophy cascade, though in the case of decaying turbulence [48].

In the case where there is no driving, the inverse energy cascade does not occur. The enstrophy cascade, however, persists, with the energy spectrum following the same k^{-3} scaling.

1.1.2.4 Vortex phase transitions in 2D

At each extreme of the vortex temperature range, there are phase transitions in the vortex configuration. For point vortices, at positive temperatures (where vortices like to approach those of opposite sign) there is a ‘pair collapse’ transition, where every vortex pairs up with one of the opposite sign, forming bound molecule-like states [49]. For ideal point vortices this occurs at inverse temperatures above the critical temperature,

$$\beta_{\text{PC}} = \frac{4\pi}{\rho\Gamma^2}, \quad (1.11)$$

corresponding to a discontinuity in the mean energy per vortex. However, if the vortex core size is finite, this transition is no longer sharp, with the energy varying smoothly with temperature.

The BKT transition [50–52] of the XY model of spins on a 2D lattice corresponds to the unbinding of vortex pairs in a superfluid. This causes a proliferation of vortices above a critical temperature [53], corresponding to the inverse temperature

$$\beta_{\text{BKT}} = \frac{8\pi}{\rho\Gamma^2}. \quad (1.12)$$

This causes a breakdown of the long-range coherence of the system, resulting in a sudden loss of superfluidity. It was shown by Viectelli [54] that applying a finite vortex core size to the point vortex model leads to the pair collapse transition temperature (1.11) moving to coincide with the BKT transition (1.12).

For NATs, there is a phase transition associated with the clustering of like-sign vortices. This effect is known by several names, including the *supervortex* transition, *supercondensation*, or the *Einstein–Bose condensate* (EBC) transition [49]. Prior to this phase transition, so-called *Onsager vortices* form, corresponding to large-scale groupings of like-sign vortices. It has been suggested by Xu et al. [55] that there is a *clustering transition* associated with the symmetry breaking that occurs when vortices separate into two distinct clusters. Once all vortices in the system are clustered, they begin to condense, until the vortices occupy the minimum possible phase-space area. The transition temperature associated with this condensation is dependent on the number of vortices in the system,

$$\beta_{\text{EBC}} = -\frac{16\pi}{N_v\rho\Gamma^2}. \quad (1.13)$$

Valani et al. [56] showed that this condensation process bears similarity to the condensation of a one-dimensional Bose gas. They showed

We’ll discuss superfluids in detail in the next section. For now, these systems can be considered as being equivalent to a point vortex model with finite vortex core size.

that a condensate fraction can be defined based on the number of vortices in the largest cluster, and the average spacing of the vortices. This condensate fraction begins to grow as the vortex temperature passes the critical temperature (1.13), analogous to the growth of a BEC fraction of bosons below a critical temperature (see §1.2.2).

1.1.2.5 Experiments in 2D turbulence

There have been studies of 2D turbulence in both natural and lab-based systems. On Earth, inverse energy cascades have been observed in both the oceans [11, 12] and the atmosphere [13]. The atmosphere of Jupiter is one of the most turbulent features in the Solar System, with Reynolds numbers on the order of 10^{13} . The atmosphere contains many large-scale features, such as the prominent striped jets, and the Great Red Spot, shown in Fig. 1.6a [14]. An analysis of images taken by the *Cassini* spacecraft revealed that these jets appear to be driven by an inverse energy cascade at the largest scales, while at smaller scales the dynamics are more reminiscent of 3D turbulence [15]. Recently, the *Juno* spacecraft has captured images of lattices of cyclones at each pole [16], shown here in Fig. 1.6b, reminiscent of NAT clustered states. The formation and dynamics of these clusters are not yet understood, though they are reminiscent of ‘vortex crystals’ seen in a magnetised electron column (a type of guiding-centre plasma) [57], which are thought to arise when several strong vortices are surrounded by a background of smaller vortices that have maximised their entropy [58, 59]. The presence of these clusters, combined with new information about the depth of the atmosphere [60, 61] and further data from *Juno* as it completes its mission, will no doubt fuel much ongoing research into Jupiter’s atmospheric dynamics.

The reviews by Kellay and Goldburg [63], Clercx and van Heijst [64] and Kellay [65] provide a more detailed overview of these classical 2D turbulence experiments.

In a laboratory setting, 2D turbulence has been studied in systems including guiding-centre plasmas, magnetofluids and soap films. Magnetofluids consist of a shallow bath containing an electrically conductive fluid, such as mercury or an electrolyte. A combination of electric currents and magnetic fields can be used to stir the fluid by the Lorentz force. This allows stirring patterns to be engineered by the arrangement of magnets or electrodes under the fluid. There have, however, been questions as to the degree to which these systems are truly 2D [64, 66–68]. Motion in the third dimension can be suppressed by using a strong magnetic field in the shallow direction, and driving the motion with electric currents [69], or by using a stratified electrolyte, in which thin layers of solutions of different densities are used [70]. Stratified layers do, however, have the added complication of shear forces and other interactions between the layers, which can introduce 3D motion [66, 70].

Soap films provide a more idealised 2D fluid, where a soapy water solution is used to form a film across a frame. Early experiments were performed by dragging combs through these films and observing the

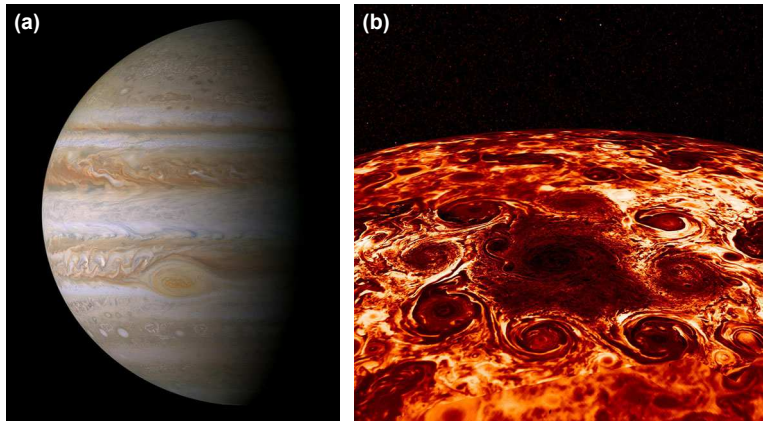


FIGURE 1.6: TURBULENT DYNAMICS ON JUPITER.

(a) Jupiter, as seen in detail by Cassini on its way to Saturn (NASA image PIA04866, courtesy NASA/JPL/Space Science Institute). The presence of large-scale structures, such as the banded jets and the Great Red Spot suggest that $2D$ dynamics are involved. We have observed the largest features of Jupiter's atmosphere from Earth for centuries, but recent close encounters with spacecraft have provided stunning new resolution of the finer scales. **(b)** The most recent mission, Juno, discovered a double-square lattice of cyclones at the north pole (NASA image PIA22335, courtesy NASA/JPL-Caltech/SwRI/ASI/INAF/JIRAM). A similar pentagon pattern was also seen at the south pole. These structures had not been expected, and are not yet understood, highlighting the need for ongoing research in $2D$ turbulence. Images from the NASA/JPL [Planetary Photojournal](#) [62].

wake [71]. This technique was further refined by allowing the film to flow along the frame, using a water jet to pull the film, which was replenished from a bath [72], or allowing the film to fall under gravity, using a pump to replenish the soap solution at the top [73]. In these geometries, the film can pass through a comb with a higher Reynolds number, with the resulting turbulent state decaying downstream. The thickness of a soap film does vary, particularly around strong vortices and boundaries, and the finite thickness may compromise the ideal $2D$ nature of the flow [63, 74–77].

In the first soap film experiments by Couder, decaying turbulence was observed after a sweep of a comb [71]. Vortices were seen to merge, with the typical eddy size increasing over time. Later studies using flowing films were able to observe an enstrophy cascade [73, 78, 79], with measurements of the kinetic energy spectrum consistent with k^{-3} scaling.

Though both cascades should be present in driven turbulence, they can be suppressed by choosing a driving scale that is too large to 'leave room' for the energy cascade, or too small to allow an enstrophy cascade to be observed. Due to the finite length scales available, most driven experiments have focussed on observing only one of the two cascades. The inverse energy cascade, and corresponding $k^{-5/3}$ scaling of the energy spectrum, was first observed by Sommeria in mer-

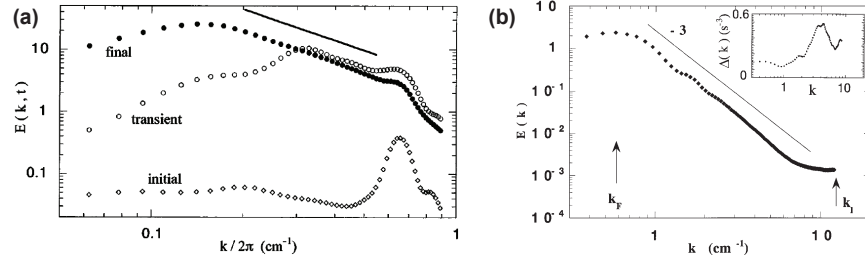


FIGURE 1.7: ENERGY CASCADES IN ELECTROLYTE SOLUTIONS.

The inverse energy cascade, and direct enstrophy cascade, can be seen independently if the driving scale is chosen such that only one inertial range can exist. **(a)** The inverse energy cascade can be seen to form dynamically. Initially, energy can be seen at the driving scale. Energy cascades to lower wavenumbers, and once a steady state has been achieved the $k^{-5/3}$ spectrum develops. The solid line is a guide to the eye with $k^{-5/3}$ scaling. Reprinted figure with permission from Paret and Tabeling, *Physical Review Letters* **79**, 4162 (1997) [80]. © 1997 American Physical Society. **(b)** The enstrophy cascade can be seen when driven at a larger scale (k_F), characterised by k^{-3} scaling (solid line). In this case, the driving scale, k_F is too close to the system scale for the energy cascade to form. Reprinted figure with permission from Paret, Jullien and Tabeling, *Physical Review Letters* **83**, 3418 (1999) [81]. © 1999 American Physical Society.

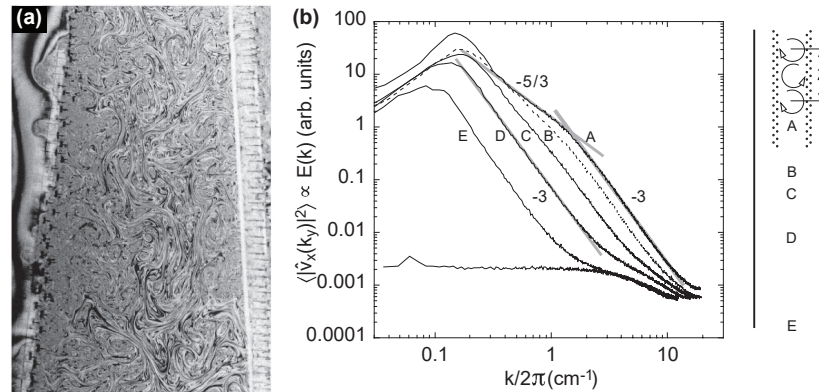


FIGURE 1.8: DUAL CASCADE IN A SOAP FILM.

A simultaneous dual cascade was seen for the first time in a soap film. **(a)** Combs were placed along the edges of the soap film channel to provide continuous forcing. In this photograph, the combs are slightly tilted in an inverted 'V' shape, with a separation of 5 cm at the bottom. **(b)** Energy spectra taken at various points along the channel (guide to the right) for a pair of parallel combs spaced 2.5 cm apart in an 8 cm wide channel. Within the combs, where there is forcing, spectrum A shows both $k^{-5/3}$ and k^{-3} scaling ranges. Beyond the forcing region the $k^{-5/3}$ inertial range vanishes and the k^{-3} scaling extends into these lower k scales. This shows evidence for both a dual cascade in forced turbulence, and an enstrophy cascade for decaying turbulence. Reprinted figures with permission from Rutgers, *Physical Review Letters* **81**, 2244 (1998) [82]. © 1998 American Physical Society.

cury [69], and subsequently by Paret and Tabeling [80, 83] in an electrolyte solution. In the latter case, the energy spectrum was seen to begin with a peak at the driving scale, then smooth out to the characteristic inverse energy cascade as the system reached a steady state, shown in Fig. 1.7a. The enstrophy cascade was seen by Paret et al. [81] in the same electrolyte apparatus, driven at larger scales, showing a k^{-3} scaling range of the energy spectrum, as seen in Fig. 1.7b. The first experiment to show the presence of a dual cascade was in a soap film by Rutgers [82]. Here, a soap film flowed past a comb of cylindrical obstacles on its boundary, rather than a single comb at the top of the frame, which injected energy as the film flowed past over a finite range, illustrated in Fig. 1.8. The energy spectrum shows the two distinct power laws as expected.

1.2 BOSE-EINSTEIN CONDENSATION AND SUPERFLUIDITY

Now that turbulence has been introduced in a classical fluid, I will discuss the *quantum fluid* in which we can next consider turbulence. Bose-Einstein condensation was first theorised by Albert Einstein in 1925 [84], based on the work of Satyendra Nath Bose [85], predicting a phase transition in a gas of non-interacting atoms. Until the discovery of superfluidity in liquid helium in 1938 [86, 87], it was assumed that this BEC phase transition—in which particles condense in a ground state—was not possible in real systems of interacting particles. It was London who first suggested the connection between superfluidity and BEC [88], which was built upon to develop a consistent theoretical framework [89–93]. It was not until 1995 that BEC was realised in dilute atomic gases [94–96], the system in which the experiments described in this thesis are based. In this section I will discuss the key features of BECs that make them an ideal system to use in quantum turbulence (QT) experiments.

1.2.1 A brief introduction to Bose-Einstein condensates

While atomic BECs typically consist of a collection of 10^4 to 10^6 particles, they can be described by a single macroscopic wavefunction, $\Psi(\mathbf{r}, t)$, with the particle density given by $n = |\Psi(\mathbf{r}, t)|^2$ and total atom number $N = \int |\Psi(\mathbf{r}, t)|^2 d\mathbf{r}$. In the mean field approximation—which applies to the majority of experiments to date—the evolution of $\Psi(\mathbf{r}, t)$ is governed by the Gross-Pitaevskii equation (GPE) [97, 98],

$$i\hbar \frac{\partial}{\partial t} \Psi(\mathbf{r}, t) = \left[-\frac{\hbar^2}{2m} \nabla^2 + V_{\text{trap}}(\mathbf{r}, t) + g |\Psi(\mathbf{r}, t)|^2 \right] \Psi(\mathbf{r}, t), \quad (1.14)$$

where m is the particle mass, V_{trap} is a trapping potential (usually a combination of magnetic and optical forces, such as those discussed in later chapters), and $g = 4\pi\hbar^2 a/m$ is an interaction term, set by the

The detailed theory of BEC is well documented (see, e.g., [1–3]). I will not be covering the microscopic details of the condensation mechanism here, as it is not needed to interpret the experiments in this thesis.

s-wave scattering length a . Historically, most BEC experiments have been performed in trapping potentials that can be approximated as harmonic oscillators of the form $V(\mathbf{r}) = \sum_i \frac{1}{2} m \omega_i^2 x_i^2$, with characteristic frequencies ω_i along the trap axes $x_i = x, y, z$.

The energy functional of (1.14) is

$$E(\psi) = \int \left(\frac{\hbar^2}{2m} |\nabla\psi|^2 + V_{\text{trap}} |\psi|^2 + \frac{g}{2} |\psi|^4 \right) d\mathbf{r}. \quad (1.15)$$

This can be broken down into the three terms, which correspond to the kinetic, potential and interaction energies, respectively. When the kinetic energy term is small compared with the interaction energy, as is the case for large atom number condensates, we can use the Thomas–Fermi (TF) approximation to obtain the ground state solution to the GPE (1.14)

$$|\Psi(\mathbf{r}, t)|^2 = \frac{\mu - V(\mathbf{r})}{g} = n(\mathbf{r}), \quad (1.16)$$

where μ is the chemical potential, $\mu \equiv \partial E / \partial N$. For the harmonic potential, this gives

$$n(\mathbf{r}) = n_0 \left(1 - \sum_i \frac{x_i^2}{R_i^2} \right) > 0, \quad (1.17)$$

where $n_0 = \mu/g$ is the peak density, and R_i are the TF radii, given by $\frac{1}{2} m \omega_i^2 R_i^2 = \mu$. Another key length scale in a BEC is the healing length

$$\xi = \sqrt{\frac{\hbar^2}{2mgn}}, \quad (1.18)$$

corresponding to the shortest length over which the density can go to zero. This is of particular interest in the scale of vortices in a BEC, as will be discussed in §1.2.5.

1.2.2 Making BECs

To form a BEC, one must increase the *phase space density*, $\text{PSD} = n\lambda_{\text{dB}}^3$, of a collection of atoms such that they cross the condensation transition. Here λ_{dB} is the thermal de Broglie wavelength of an atom of mass m at temperature T , given by

$$\lambda_{\text{dB}} = \sqrt{\frac{2\pi\hbar^2}{mk_B T}}. \quad (1.19)$$

The intuitive picture of the onset of BEC is that as a gas is cooled, λ_{dB} increases. Once λ_{dB} becomes comparable to the inter-atomic spacing, the atomic wavefunctions begin to overlap, eventually merging into

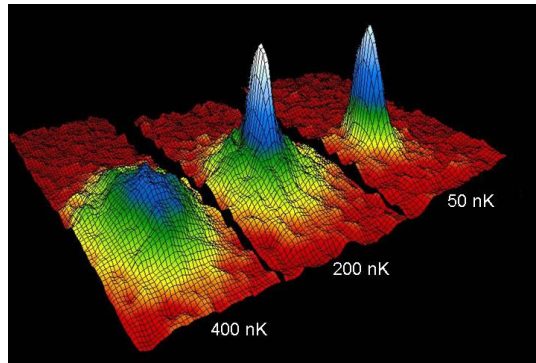


FIGURE 1.9: THE ONSET OF BOSE–EINSTEIN CONDENSATION.

Three-dimensional false colour representations of atomic density distributions, taken from optical density images. From left to right, the atoms have been cooled to progressively lower temperatures. In the first frame, at around 400 nK, the cloud is thermal, with a Gaussian distribution. Beyond the critical temperature, a peak, indicating the condensation of atoms in a low momentum state, begins to grow, until almost all atoms become condensed in the last frame. Figure reproduced from the Cornell Group (JILA, NIST, and the Department of Physics, University of Colorado at Boulder) [99].

the single quantum wavefunction of a BEC. This occurs as the atoms condense into the lowest energy state of the confining potential below a critical temperature T_c , corresponding to $\text{PSD} = \zeta(3/2) \approx 2.61$, where ζ is the Riemann zeta function.

In a harmonic potential, the number of condensed atoms, N_c , is approximately

$$\frac{N_c}{N} = 1 - \left(\frac{T}{T_c} \right)^3. \quad (1.20)$$

The presence of both condensed and thermal atoms gives rise to a bimodal distribution of atoms in momentum space. Releasing a gas of cold atoms from their confining potential allows them to fly away with their instantaneous momentum. For sufficiently long time-of-flight, this is effectively a Fourier transform, converting momentum space into position space. For a BEC near T_c , this leads to images such as the iconic Fig. 1.9, with the low-momentum condensed atoms remaining spatially localised, and the thermal background gas expanding isotropically at a faster rate.

Chapter 2 will outline the details of the laboratory equipment required to take room temperature atoms down to the nanokelvin-scale transition temperature. Briefly, it involves *laser cooling*, where the momentum of light is used to slow atoms, and *evaporative cooling*, where the hottest atoms are selectively removed from the gas, reducing the overall average temperature.

1.2.3 Superfluidity and quantum hydrodynamics

Superfluidity was first observed in liquid helium, and is characterised by frictionless flow below a critical velocity, v_c . This phenomenon is understood to arise due to the macroscopic phase coherence of interactions between Bose–Einstein condensed particles. There are, however, subtleties in the link between BEC and superfluidity, as not all BECs are superfluids, and vice versa. Dilute atomic BECs, however, do exhibit superfluidity, which will be shown in §1.2.4. To explore the properties of flow in a superfluid, we will first derive the superfluid velocity, then use this to write the GPE (1.14) in the so-called hydrodynamic form.

The complex superfluid wavefunction, Ψ , can be written in terms of scalar fields for the amplitude, \sqrt{n} , and phase, ϕ , using the Madelung transform,

$$\Psi(\mathbf{r}, t) = \sqrt{n(\mathbf{r}, t)} e^{i\phi(\mathbf{r}, t)}. \quad (1.21)$$

Substituting this into the probability current,

$$\mathbf{j}(\mathbf{r}, t) = \frac{i\hbar}{2m} (\Psi\nabla\Psi^* - \Psi^*\nabla\Psi), \quad (1.22)$$

gives $\mathbf{j} = n\mathbf{v}_s$, where

$$\mathbf{v}_s(\mathbf{r}, t) = \frac{\hbar}{m} \nabla\phi(\mathbf{r}, t) \quad (1.23)$$

is the superfluid velocity.

Substituting (1.21) into the GPE (1.14), results in two coupled equations; the real part gives the Euler equation,

$$m \frac{\partial \mathbf{v}_s}{\partial t} = -\nabla \left[\frac{1}{2} m \mathbf{v}_s^2 + V_{\text{trap}} + gn - \frac{\hbar^2}{2m\sqrt{n}} \nabla^2 \sqrt{n} \right], \quad (1.24)$$

while the imaginary part gives the continuity equation,

$$\frac{\partial n}{\partial t} + \nabla \cdot (n\mathbf{v}_s) = 0. \quad (1.25)$$

Note that these equations closely resemble those of a classical incompressible fluid (1.1), with an additional *quantum pressure* term [the last term in (1.24)], no kinematic viscosity, and the constraint irrotational flow.

1.2.4 Excitations

Excitations of a BEC above the ground state can be considered as quasiparticles, with energy given by the Bogoliubov dispersion law [91],

$$\epsilon(\mathbf{p}) = \left[\frac{gn}{m} p^2 + \left(\frac{p^2}{2m} \right)^2 \right]^{1/2} \quad (1.26)$$

(for a uniform system). For quasiparticles with small momentum $p \ll mc$, (1.26) reduces to a phonon-like relation, $\epsilon(p) = cp$, where $c = \sqrt{gn/m} = \sqrt{\mu/m}$ is the *speed of sound*. These long-wavelength excitations are commonly referred to as sound waves.

In §1.2.3 we mentioned that superfluids are characterised by frictionless flow below a critical velocity v_c . To expand on this point, Landau's criteria for superfluidity [90] gives this critical velocity as corresponding to the fluid's excitation spectrum, by

$$v_c = \min \left(\frac{\epsilon(p)}{p} \right). \quad (1.27)$$

In the limit $p \rightarrow 0$, (1.26) gives that $v_c = c$. Given that c must be finite and non-zero if there are interactions ($g \neq 0$), it holds that atomic BECs must be superfluids.

The Bogoliubov excitations transition from phonon-like to particle-like when $p \approx mc$, which corresponds to $p = \hbar/\xi$. In §1.2.5 we will see that as well as Bogoliubov excitations, superfluids support topological excitations, vortices, which will play an important role in the study of QT.

1.2.5 Quantum vortices

As discussed in §1.1, vortices can be defined as lines about which the fluid flow circulates. In a classical fluid these vortices can have any magnitude, and can occur on any length scale. In a superfluid (and quantum wavefunctions in general), however, vortices are remarkably different, due to a quantisation condition arising from the underlying wavefunction.

The quantisation of circulation in quantum wavefunctions arises from the condition that their phase must be single-valued and continuous. This was first predicted by Dirac in 1931 [100] in his description of magnetic monopoles. It was Onsager [39], in a footnote, no less, who first suggested that vortices in a superfluid would be quantised, an idea that was later developed further by Feynman in 1955 [101]. Flux quantisation in superconductors was described by Fritz London [102, 103], and Abrikosov subsequently derived the presence of vortices in 1957 [104], likening his findings to those of Onsager and Feynman. Quantised vortices in optical fields were discussed by Nye & Berry in 1974 [105]. The mathematical equivalence of optical and superfluid vortices is highlighted by the fact that optical vortices can be used to engineer vortices in BECs, by imprinting their phase onto the condensate [106]. Optical vortices also have applications in atom trapping, as will be discussed in §3.2.2.

Here I will focus on the presence of vortices in superfluids. We have already seen that the superfluid velocity is the gradient of the wave-

function phase (1.23). Using this, the circulation, Γ , about a closed contour, \mathcal{C} , must satisfy

$$\Gamma = \oint_{\mathcal{C}} \mathbf{v}_s \cdot d\mathbf{l} = \frac{\hbar}{m} \oint_{\mathcal{C}} \nabla\phi \cdot d\mathbf{l} = \frac{\hbar}{m} 2\pi s = \kappa s, \quad (1.28)$$

for integer *vortex charge* (or *winding number*) s and *quantum of circulation* $\kappa = \hbar/m$. This implies that any circulation in the fluid must be quantised in units of κ , with the phase accumulating in multiples of 2π .

These quantum vortices are *topological defects* in the fluid, as the phase circulations cannot be removed by local perturbations. The fluid density must go to zero at a point at the centre of a vortex, to prevent the wavefunction from becoming multi-valued. Rearranging (1.28), for a circular contour centred on a vortex, gives that the velocity field due to a vortex is

$$\mathbf{v}_s(\mathbf{r}) = \frac{\hbar}{m} \frac{s}{r} \hat{\theta}, \quad (1.29)$$

where $\hat{\theta}$ is the unit vector pointing tangentially to the contour.

The current density is prevented from diverging at the centre of the vortex since the density drops to zero. For a singly charged ($s = \pm 1$) vortex, the core structure can be approximated [107] as

$$f(r) = \frac{r}{\sqrt{r^2 + \Lambda^{-2}\xi^2}}, \quad (1.30)$$

where $\Lambda = 0.82475\dots$ is the density gradient near the centre of the core. Since the core size is on the scale of the healing length (1.18), it depends on the local condensate density. In §1.2.7.2 we will see that this allows the imaging of vortex cores in time-of-flight, as they rapidly grow in size as the density of the expanding condensate drops.

It can be shown that it is energetically unfavourable for vortices to maintain a charge $|s| > 1$, instead they tend to break into s single charged vortices. This has been shown theoretically [108, 109], as well as observed in experiments [110]. The ground state of a BEC with total circulation N is a triangular lattice of N vortices with $|s| = 1$ [111], as demonstrated in Fig. 1.10. In some circumstances multi-quantum vortices can be stabilised [108, 112, 113], however, for the remainder of this thesis, we will assume that all vortices have $|s| = 1$. Furthermore, we will often refer to vortices with $s = -1$ as *antivortices*, when we need to distinguish these from *vortices* with $s = 1$. There are also a range of more exotic generalised vortex structures possible in systems with a spin degree of freedom, such as fractional quantum vortices, which are beyond the scope of the scalar condensates considered in this thesis.

1.2.5.1 Vortices in highly oblate condensates

So far I have only discussed BECs in traps which are considered $3\mathcal{D}$, that is, the harmonic oscillator length in each dimension, $l_x = \sqrt{\hbar/m\omega_x}$

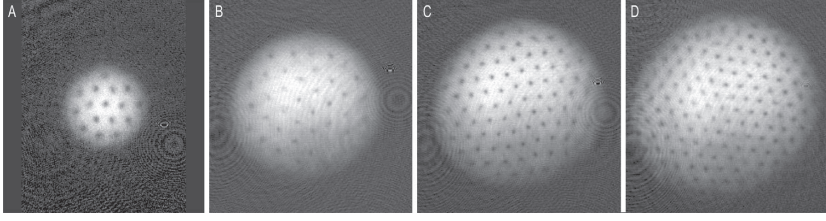


FIGURE 1.10: A VORTEX LATTICE IN A BEC.

Images from the first experiment reporting the observation of a vortex lattice. A sodium BEC was rotated using a pair of blue detuned (repulsive) lasers, rotating about opposite sides of the trap. This generated many vortices of the same sign, which distributed themselves evenly across the cloud, such that the total velocity field approximates that of rigid body rotation. The number of vortices in each image are approximately (A) 16, (B) 32, (C) 80 and (D) 130. Figure from Abo-Shaeer et al., *Science* **292**, 476 (2001) [111]. Reprinted with permission from AAAS.

is large compared with the healing length. If one dimension (we will use z and call it the *axial direction*) is confined tightly, with $\omega_z \gg \omega_\perp$ ($\omega_\perp \equiv \omega_x = \omega_y$), the dynamics of the system are essentially 2D. Vortices will preferentially align in the axial direction, as it is energetically favourable to reduce their total length. If $l_z \sim \xi$, so that the axial dimension is comparable to the vortex core size, wave excitations along vortex lines (Kelvin modes) and vortex reconnection events will be suppressed. For harmonic traps, Rooney et al. [114] showed that these are even suppressed for thicker condensates provided the trap aspect ratio satisfies $\omega_\perp/\omega_z \gtrsim 8$. In these thicker BECs sound waves, such as those generated during vortex–antivortex annihilation events (discussed in the following section), may still excite low order Kelvin waves, which tilt the vortex causing it to appear as a spinning ellipse. Examples of this can be seen, e.g., in the supplementary movie of Simula et al. [115]. Provided that the inter-vortex spacing is larger than this tilting (i.e., on the order of the BEC thickness), these vortex excitations will not impact the dynamics, as the far-field vortex flow will remain the same.

1.2.5.2 Vortex dynamics

Vortices in a uniform BEC will move with the background superfluid velocity [116] (in an inhomogeneous BEC the motion depends on gradients in both the density and phase [117]). Thus, in an otherwise stationary system, the vortex dynamics are governed by the flow field generated by the vortices themselves. In an infinite 3D system containing N_v vortices, the velocity field at any point \mathbf{r} is well approximated by the Biot–Savart law,

$$\mathbf{v}_s(\mathbf{r}) = \frac{\kappa}{4\pi} \sum_j^{N_v} \int_{\mathcal{L}_j} \frac{(\mathbf{r}' - \mathbf{r}) \times d\mathbf{r}'}{|\mathbf{r}' - \mathbf{r}|^3}, \quad (1.31)$$

where the integral is along positions \mathbf{r}' along each vortex line \mathcal{L}_j corresponding to the j^{th} vortex.

If the vortices are all parallel, as is the case in a highly oblate (or 2D) BEC, (1.31) reduces to the sum of the velocity field, (1.29), of each vortex:

$$\mathbf{v}_s(\mathbf{r}) = \frac{\kappa}{4\pi} \sum_j^{N_v} s_j \hat{\mathbf{z}} \times \frac{\mathbf{r} - \mathbf{r}_j}{|\mathbf{r} - \mathbf{r}_j|^2}, \quad (1.32)$$

where the j^{th} vortex is located at \mathbf{r}_j , and has charge s_j .

Note that this is the point vortex model, as introduced in the context of classical fluids in §1.1.2.1, with the circulation of each vortex set to the quantum of circulation, $\Gamma = \kappa s$. Unlike the classical case, quantum vortices in a 2D system can be well approximated as the discrete points used in the model, provided that the mean inter-vortex spacing l_v satisfies $l_v \gg \xi$. Recalling from §1.1.2.1, for a finite system, boundary effects must be taken into consideration, with the superfluid velocity reducing to zero at the boundary.

In a uniform, circular system of radius R , the point vortex Hamiltonian takes the form [54, 115, 118–120]

$$\begin{aligned} H_0 &= H_v + H_i + H_s \\ &= -\frac{\rho_s \kappa^2}{4\pi} \sum_{i < j} s_i s_j \log \left(\frac{|\mathbf{r}_i - \mathbf{r}_j|^2}{R^2} \right) \\ &\quad + \frac{\rho_s \kappa^2}{4\pi} \sum_{i < j} s_i s_j \log \left(1 - 2 \frac{\mathbf{r}_i \cdot \mathbf{r}_j}{R^2} + \frac{|\mathbf{r}_i|^2 |\mathbf{r}_j|^2}{R^4} \right) \\ &\quad + \frac{\rho_s \kappa^2}{4\pi} \sum_i s_i^2 \log \left(1 - \frac{|\mathbf{r}_i|^2}{R^2} \right), \end{aligned} \quad (1.33)$$

where ρ_s is the superfluid density. The first term, H_v , is due to the interaction between pairs of vortices. For vortices of the same sign, this interaction is repulsive, and for opposite sign vortices it is attractive. The second term, H_i , is due to the interaction of vortices with the image of every other vortex (recall that in such a system every vortex has an image of opposite sign, at $\mathbf{r}_{\text{img}} = R^2 \mathbf{r}_v / |\mathbf{r}_v|^2$). The third term, H_s , is due to the interaction of vortices with their own image.

1.2.5.3 Vortex loss mechanisms

While we assume that the dynamics of QT is dominated by vortices, there are still interactions between the vortices and phonons. When looking at only the vortex dynamics, these interactions tend to appear as damping in the system, as the energy of the vortices is converted to sound.

Accelerating vortices will radiate sound waves, just as an accelerating charged particle will radiate electromagnetic radiation [121]. This

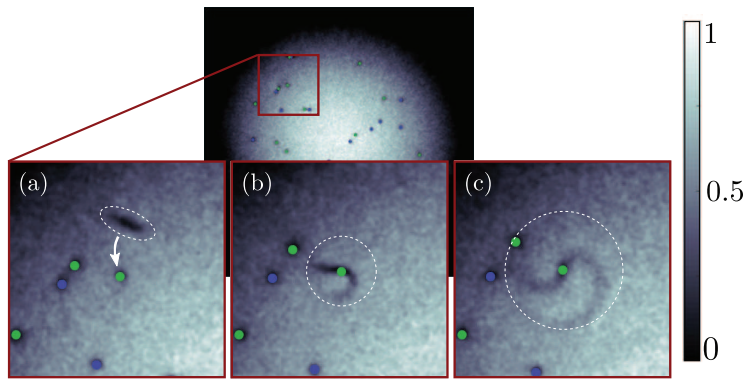


FIGURE 1.11: DECAY OF A JONES–ROBERTS SOLITON.

A numerical GPE simulation shows the decay of a Jones–Roberts soliton (highlighted by dashed white region), interacting with a single vortex (indicated by arrow in (a)). Here the grey-scale represents the normalised atomic density and the location of vortices (antivortices) are highlighted by blue (green) dots. As the collision occurs in (b) sound waves are generated, which dissipate quickly, as seen in (c). Reprinted figure with permission from Groszek et al., *Physical Review A* **93**, 043614 (2016) [129]. © 2016 American Physical Society.

occurs whenever vortices come close to each other or a boundary (i. e. their image vortex). The effect of this, however, is usually small, as the emission is proportional to the vortex configuration’s quadrupole mode [121]. Vortices can also gain energy by absorbing phonons [122], and sound-mediated interactions between vortices may be experimentally observable [123].

Sound can also be emitted by vortex line reconnection events in $3D$, or vortex–antivortex annihilations in $2D$. Reconnections occur when two vortex lines cross and break apart, swapping line ends. This causes the vortices to recoil, inducing Kelvin waves in the vortex lines, as well as radiating phonons [124, 125]. In $2D$ these events cannot occur, however, vortices of the opposite sign can come together and annihilate, releasing sound. Prior to annihilation, the pair will generally form a bound state known as a Jones–Roberts soliton [126, 127]. Interactions between this soliton and another vortex or soliton can cause it to decay (shown in Fig. 1.11), or break apart into a pair of vortices again. As a third vortex, or second soliton is required to catalyse this annihilation process, the decay is a three- or four-body scattering process. These annihilation events can also occur at the system boundary, where the vortex can interact with its image. Vortex–antivortex pairs can also be spontaneously generated by strong sound fields, or in $3D$, vortex rings can form [128].

A further source of energy loss is through thermal dissipation. The thermal component of a BEC (or normal component of liquid helium) is always present at finite temperatures, though BECs can be made at very high purity. This thermal component is a thermal bath into which energy can be lost, acting as friction on the vortices [130].

1.2.6 The kinetic energy spectrum

In the discussion of classical turbulence, it was clear that the kinetic energy spectrum of the fluid played an important role in characterising the flow, and so it makes sense to consider the equivalent spectrum of a superfluid. Here we will only consider the case of a (quasi) 2D BEC. In §1.2.1 we saw that the total kinetic energy of a BEC is given by $E_k = \int \frac{\hbar^2}{2m} |\nabla\psi|^2 d\mathbf{r} = \frac{1}{2} m \int |\mathbf{v}_s|^2 d\mathbf{r}$. As the density is not uniform, we now write this as $E_k = \frac{1}{2} \int |\mathbf{w}|^2 d\mathbf{r}$, where $\mathbf{w} = \sqrt{\rho_s} \mathbf{v}_s$ is the density-weighted velocity field. This can be decomposed into three parts,

$$\begin{aligned} E_k &= E_k^i + E_k^c + E_q \\ &= \frac{1}{2} \int |\mathbf{w}^i|^2 d\mathbf{r} \\ &\quad + \frac{1}{2} \int |\mathbf{w}^c|^2 d\mathbf{r} \\ &\quad + \frac{\hbar^2}{2m} \int \frac{\nabla^2 \sqrt{n}}{\sqrt{n}} d\mathbf{r}, \end{aligned} \tag{1.34}$$

corresponding to the incompressible kinetic energy E_k^i , the compressible kinetic energy E_k^c and the quantum pressure E_q . The incompressible part corresponds to the parts of the superfluid velocity field that satisfy $\nabla \cdot \mathbf{v}_s^i = 0$, which is due to vortices. The compressible term corresponds to sound, which satisfies $\nabla \times \mathbf{v}_s^c = 0$.

Taking the Fourier transform of the density-weighted velocity field, we can obtain the incompressible and compressible kinetic energy spectra as

$$E^i(k) = \frac{1}{2} \int k |\mathcal{F}(\mathbf{w}^i)|^2 d\theta, \quad E^c(k) = \frac{1}{2} \int k |\mathcal{F}(\mathbf{w}^c)|^2 d\theta. \tag{1.35}$$

It is the incompressible kinetic energy spectrum that we will be interested in when dealing with vortex dynamics. While the compressible part of the energy plays a role in the vortex dynamics, as discussed in §1.2.5.3, it is small compared with the incompressible part. This can be seen by the agreement between numerical results using the point vortex model (which has no compressible energy) and both experiments and the GPE (which does include compressible energy) when modelling vortex dynamics (see, e. g., [115, 130–133]).

The incompressible energy spectrum can be calculated for a system on N_v vortices, each with sign s_i at location \mathbf{r}_i , by [107]

$$E^i(k) = \frac{\rho_0 \kappa^2 \xi}{2\pi} F_\Lambda(k\xi) \left[N_v + \sum_{i \neq j} s_i s_j J_0(k|\mathbf{r}_i - \mathbf{r}_j|) \right], \tag{1.36}$$

where J_0 is the Bessel function of the first kind, and $F_\Lambda(k\xi)$ is a function that incorporates the shape of the vortex core, (1.30). The asymptotes of $F_\Lambda(k\xi)$ are

$$F_\Lambda(k\xi) = \frac{1}{k\xi} \quad k\xi \ll 1 \quad (1.37a)$$

and

$$F_\Lambda(k\xi) = \frac{\Lambda^2}{(k\xi)^3} \quad k\xi \gg 1. \quad (1.37b)$$

In these limits, the incompressible energy spectrum behaves as

$$E(k) \propto k^{-1} \quad k\xi \ll 1 \quad (1.38a)$$

and

$$E(k) \propto k^{-3} \quad k\xi \gg 1, \quad (1.38b)$$

which correspond to the far field behaviour of a vortex and the effect of the vortex core shape respectively.

1.2.7 *Creating and observing vortices*

While I have now given the theoretical context to move on to talking about the turbulent dynamics of the quantised vortices of a superfluid, first let us take a moment to consider the experimental details of actually creating and observing these interesting features. Quantised vortices have been observed in a wide range of systems, including light [134, 135] (even at the single photon level [136]), electrons [137–139], neutrons [140], exciton–polariton condensates [141], superfluid helium [142] and magnetic flux vortices in superconductors [143]. Some of the helium experiments will be mentioned in the context of turbulence in §1.3, but for now I will focus on vortex experiments in atomic BECs. The first quantum vortex in a BEC was created in 1999 by a phase imprinting technique [144]. In this experiment, a laser was rotated around a BEC, bringing parts of it into resonance with a microwave transition, coupling atoms to a different internal state. This coupling was engineered such that the BEC formed in the second state contained a single phase winding, forming a vortex, with the core filled by the original component.

Since then, there have been many techniques used to form vortices, including phase imprinting, rotating condensates, stirring and stochastic processes. A comprehensive list of experiments investigating vortices in BECs from 1999 to 2010 has been compiled by Brian Anderson [145], who also maintains an up-to-date version online [146]. I will focus on the experiments most relevant to this thesis, relating to the generation of vortices by dragging a barrier through the condensate, as well as techniques used for the imaging of vortices.

1.2.7.1 *Stirring vortices*

The primary vortex creation method used in the experiments in this thesis involves forcing superfluid flow past an obstacle. This method is analogous to familiar counterparts in classical fluids—you may have noticed vortices forming as you pulled a canoe paddle through water, or stirred a spoon through your coffee cup. In a BEC, our ‘spoon’ is formed by a repulsive (far blue detuned) laser beam. Above a critical velocity, related to the speed of sound in the superfluid, pairs of vortices of opposite sign will be shed from either side of the potential barrier.

Vortices are nucleated when the superfluid velocity locally exceeds the speed of sound. For a large ($R \gg \xi$) circular obstacle with an impenetrable potential barrier, this occurs when the barrier moves through the condensate at half the speed of sound [147]. However, as the condensate density must reduce to zero at the potential barrier, the local speed of sound is reduced, further decreasing the critical velocity to approximately $0.37 c$ [148–152]. Geometry arguments can be used to show that for elliptical shaped barriers, the critical velocity is lower than that of a symmetric barrier, as the velocity of the local flow at the vertices must increase relative to the barrier speed [153].

Experimentally, repulsive lasers were first stirred through BECs to show the presence of a critical velocity [154, 155], and subsequently the nucleation of vortices was observed [156]. In an oblate condensate geometry, pairs of vortices of opposite sign were seen to be shed, forming *vortex dipoles* [157]. The critical velocity for shedding from a stiff, round barrier has been measured to be $0.4 c$, in good agreement with theoretical predictions [158].

As the condensate density must go to zero at the centre of a vortex, it is energetically favourable for them to be *pinned* to regions of low density. Pinning was first demonstrated in the context of a vortex lattice pinned to an optical lattice [159]. Persistent flow in toroidal condensates [160] can be thought of as the pinning of a multiquantum vortex by the central density hole. More recently, the pinning and manipulation of individual vortices has been demonstrated [161, 162]. Here, a pair of tightly focussed pinning potentials were swept through an oblate BEC together, then separated, resulting in a single vortex pinned to each beam, each with opposite sign. By utilising multiple pinning beams, it would be possible to generate deterministic arrangements of multiple vortices on demand.

1.2.7.2 *Imaging vortices*

As with most properties of BECs, the usual method of obtaining information about vortices in a condensate is through taking an image. A more detailed discussion of imaging BECs in general will be given in §2.8, but for now it suffices to say that most common imaging

techniques use light at a wavelength near the atomic resonance to form an image of either the shadow cast on a probe beam (absorption imaging), or the light scattered by the atoms (e.g., fluorescence imaging or phase contrast imaging). Vortices can be seen as ‘holes’ in the density distribution of the condensate when they are aligned with the imaging axis. Resolving vortices *in situ* is technically challenging, as the vortex cores are typically on the same length scale as the wavelength of light.

In the first vortex experiments, the cores were filled with atoms in a different state, which caused the core to expand to a resolvable size [144]. The most widely used vortex imaging technique is to allow the condensate to expand in time-of-flight—as the condensate density drops, the local healing length increases, and hence the vortex cores grow [163]. In highly oblate trap configurations, the tightly confined direction will expand rapidly upon release, with the vortex cores increasing to a resolvable size before the radial size of the BEC has changed significantly.

While time-of-flight imaging reveals the location of vortices, it does not provide any information about their dynamics, and is naturally destructive. In highly repeatable experiments, sequential runs with different imaging times can reveal the vortex dynamics [144, 157, 164], though this is impossible for the random, turbulent configurations studied in this thesis.

To study the dynamics of vortices within a single experiment, a small fraction of atoms can be released from the trapping potential, by outcoupling to an untrapped state [165]. This allows the majority of the condensate to continue evolving before subsequent images are taken. However, due to the very low density of atoms in each outcoupled portion, the imaged vortex cores are much larger than in a typical time-of-flight image, which may limit the number of vortices that can be uniquely identified. The density of the remaining condensate is also reduced at a much faster rate than the usual background loss rates, potentially impacting the vortex dynamics and limiting the duration of experiments. Additionally, for large numbers of randomly configured vortices, a high frame rate would be required in order to track the position of each vortex from one frame to the next to recover the dynamics. Overcoming these limitations would require a careful choice of atomic states (so that there is an easy way to outcouple atoms from the trap), expansion times, camera hardware, and trapping and imaging geometries.

As in the first vortex experiment, *in situ* imaging of vortex cores is possible through the expansion of the cores by a ‘filler’ component of a second atomic state [144, 164]. Techniques such as off-resonant imaging can then be used to probe these larger cores with minimal destruction of the BEC, allowing multiple images to be taken. Unfortunately, this technique is of limited use, as the presence of the filler

state alters the dynamics. Another technique, which may prove useful, would be the imaging of the filler atoms rather than the vortices themselves, as has been demonstrated for hydrogen particles in liquid helium [19]. If a different atomic species were trapped in the vortex cores, then they could be imaged in fluorescence at a wavelength far from the resonance of the host BEC. A smaller number of filler atoms may be able to be used, with the location of the fluorescing points indicating the location of vortices. This may have less of an impact on the vortex dynamics. Some preliminary simulations of this *tracer particle* technique are presented in Chris Billington’s thesis [166].

More recently, dark-field imaging has been used to resolve the position of vortex cores *in situ* without any expansion [167]. As this technique can be used with a large probe beam detuning, multiple images can be taken before the condensate is destroyed. Higher resolution imaging optics have now allowed the *in situ* imaging of vortex cores with bright-field techniques, as well as Faraday imaging [168]. Sequences of up to four images of a single condensate have been demonstrated with each of these minimally destructive imaging configurations, though the group has had issues implementing the technique in highly oblate geometries, which they attribute to a higher atomic density [168].

1.2.7.3 Vortex sign detection

While the techniques discussed so far allow the position of vortices to be observed, they do not provide any direct information about the sign of the circulation of the vortices. Observation of the dynamics of vortices using the partial transfer method, or successive *in situ* images of the same condensate could be used to determine the signs of vortices, though this would become increasingly complex to calculate for more than a few vortices (unless they are all the same sign, such as in a vortex lattice). This has led to the development of techniques to determine the sign of vortices, directly.

The first method used was the observation of fork patterns in the interference fringes between two BECs [156, 169]. This technique dates back to early vortex experiments, and was used to confirm that there was a phase winding around a vortex core. The interference patterns observed are analogous to the fringes formed by light fields containing optical vortices [170]. The phase winding of the vortex causes a discontinuity in the otherwise linear interference fringes formed between two condensates with slightly different velocities. This has been demonstrated with both a uniform reference condensate [156] and by using a recombined copy of the same condensate [169]. In the first case, the vortex sign can be determined based on the orientation of the fork relative to the difference in velocity of the two condensates—the side of the vortex where the flow would, in a sense, increase the relative velocity between the condensates will have an

extra fringe compared with the side flowing counter to the velocity difference. In the latter case, the interference pattern is more complex, featuring a double fork for each vortex. While the presence of a phase winding is striking, this technique is not suitable for measuring more than a few vortices, as this would require extremely fine fringe spacings, and correspondingly high resolution imaging, to be able to resolve fringes around the closely spaced cores.

Powis et al. [171] proposed that it would be possible to induce a gyroscope-like Kelvin mode in all vortices in a quasi-2D condensate by tilting it. This would lead to the precession of tilted vortices and antivortices in opposite directions about the condensate plane, which, under the right conditions, would look like spinning ellipses when imaged in plane. If imaged at an appropriate time (e.g., after $1/8$ of a precession period), the orientation of the elliptical vortex images would allow their signs to be determined. While this technique has not been used in the context of detecting the sign of arbitrary vortex distributions, similar tilting techniques have previously been used to study the motion of a single vortex [172] and collective oscillations in a vortex lattice [173]. Though this technique was not ultimately used in the experiments in this thesis, we did spend time developing a technique for tilting our optical trap, which I will briefly discuss in §3.1.3.

The technique used in the experiments in this thesis uses Bragg spectroscopy [174, 175] to detect the sign of vortices. Spatially resolved Bragg spectroscopy was originally proposed in the context of detecting the presence of vortices [176], and first implemented on a rotating BEC to probe the velocity field of a vortex lattice [177, 178]. For atoms at rest, (first order) Bragg scattering occurs when a pair of counter-propagating lasers have a frequency difference $\delta_0 = 2\hbar k^2/m$, where $k = 2\pi/\lambda$ is the wavenumber of the laser. At this frequency difference, an atom can absorb a photon from the higher frequency beam, gaining a momentum kick in the direction of that beam's propagation, then emit a photon by stimulated emission into the lower frequency beam, gaining a second momentum kick in the same direction as the first. The frequency difference between the beams is equal to the resulting kinetic energy gained by the atom, such that both energy and momentum are conserved in the process.

The flow around a vortex results in a Doppler shift δ_d of the local Bragg resonant frequency, as shown in Fig. 1.12. Depending on the detuning of a pair of Bragg laser beams, atoms will be preferentially scattered from one side of each vortex, dependent on its circulation. If two sets of Bragg beams are generated by counter-propagating beams with both frequencies, atoms are scattered in one of two directions, depending on the local direction of the flow. Recently, Seo et al. [21] used this technique to detect the sign of vortices in random distributions. A differential signal was generated from the scattered distribu-

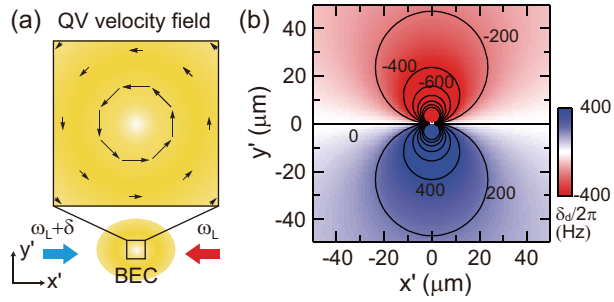


FIGURE 1.12: BRAGG RESONANCE CONDITION AROUND A VORTEX.

(a) The flow field around a single quantum vortex (QV) in a BEC. A pair of counterpropagating Bragg laser beams with frequency difference $\delta = \delta_0 + \delta_d$ are shown along the x' axis. (b) The spatial resonance condition for δ_d around the vortex core due to its flow field. Figure reproduced from Seo et al. [21] under the [Creative Commons Attribution 4.0 International License](#) [179].

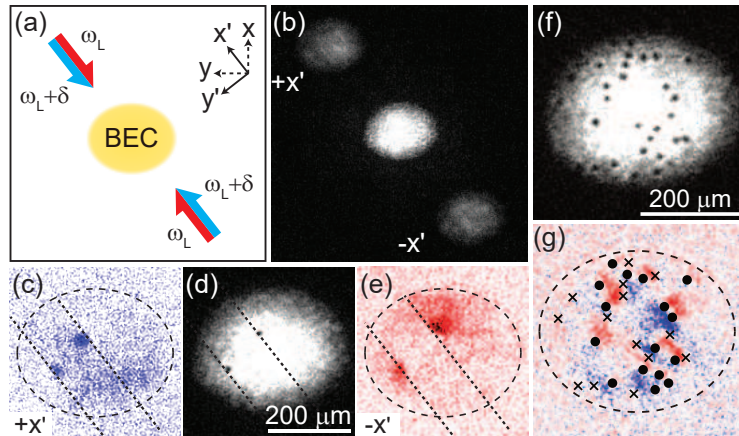


FIGURE 1.13: DIFFERENTIAL BRAGG SIGNAL OF TURBULENT VORTICES.

(a) In the experiments of Seo et al., counterpropagating lasers containing two frequencies, separated by $\delta = \delta_0 + \delta_d$ were aligned along the x' axis. (b) Close to $\delta = \delta_0$ atoms are scattered from a stationary BEC in $\pm x'$. (c–e) For a BEC containing a vortex dipole, at $\delta_d = 2\pi \times (-1.1)$ kHz atoms are scattered in the direction of their initial velocity. The upper (lower) vortex has positive (negative) circulation. The dashed line indicates the BEC edge, and dotted lines are parallel to the Bragg lasers. (f) The unscattered part of a turbulent BEC, taken immediately after stirring the condensate. (g) The differential Bragg signal corresponding to (f). The signal, $S_B = n_+ - n_-$, is generated from the density distributions n_{\pm} of atoms scattered in the $\pm x'$ direction (blue [red] sections are positive [negative]). The position of each vortex identified in (f) is marked in (g), with the sign determined based on inspecting S_B . Positive (negative) vortices are marked as circles (crosses). Figure adapted from Seo et al. [21] under the [Creative Commons Attribution 4.0 International License](#) [179].

tions in each direction, as shown in Fig. 1.13. This allowed the sign of each vortex to be identified by locally inspecting the sign of the gradient of the differential signal transverse to the scattering direction. In §4.2, this technique will be further developed, using the point vortex model (1.32) to unambiguously determine the vortex signs.

1.3 QUANTUM TURBULENCE

Now that we have seen that superfluids support quantised vortices, which are well defined excitations of the system, it is natural to consider their dynamics in configurations reminiscent of turbulence. This so-called *quantum turbulence* (QT), was first described in detail by Feynman [101], though, as mentioned in §1.1.2.2, Onsager had also remarked in a footnote the applicability of his model for 2D systems to superfluids [39]. Feynman realised that despite the lack of viscosity, there are mechanisms for the dissipation of energy from a quantum vortex tangle. He suggested that vortex reconnections may play a role, whereby large vortex rings can be broken into smaller and smaller rings, reminiscent of the energy cascade of classical turbulence. The first experiment associated with such a vortex tangle was by Vinen [189, 190], who showed that the mutual friction of a heat current through superfluid ^4He could be explained by Feynman's description of turbulence [190, 191], though it was not until several decades later that QT itself was studied in detail.

While the ultimate focus of this thesis is 2DQT, it is useful to discuss the 3D case too. There is more literature on this topic, as it is the regime accessible by liquid helium systems, in which most experiments have been performed. Seeing how the 3D case compares with classical 3D turbulence also provides motivation and justification for studying the 2D case, in search of similar comparisons.

1.3.1 Statistical properties of quantum turbulence

We have already seen in §1.2.3 that superfluids can be described by equations closely resembling those of a classical fluid. Just as in the classical case, the non-linear nature of these equations, coupled with the large range of length scales relevant to a turbulent flow, make it natural look for statistical properties of the flow.

1.3.1.1 A superfluid Reynolds number

In §1.1.1.1 we introduced the Reynolds number, Re (1.3), which can be used to characterise a flow and predict the onset of turbulence. Since Re is inversely proportional to viscosity, which for a superfluid is zero, the classical Reynolds number is seemingly not useful here. For superfluid helium systems, where the mutual friction between

There have been several detailed reviews of quantum turbulence by Tsubota et al. [180–182]. Other good resources include a volume of Progress in Low Temperature Physics dedicated to the subject [183], as well as a special feature in the Proceedings of the National Academy of Science [184–188].

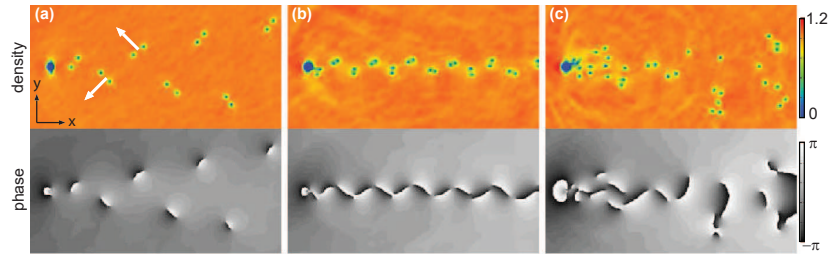


FIGURE 1.14: A QUANTUM VON KÁRMÁNN VORTEX STREET.

Numerical results show vortices shed in the wake of a cylindrical object (largest low-density region to the left of each panel) moving through a BEC at different velocities. The top panels show the density distributions and the bottom panels show the phase profile. **(a)** An obstacle with size $d = 0.04\zeta$ moving at velocity $\tilde{v} = 2.4$ produces vortex dipole pairs. The dipoles arrange themselves in a ‘V’ formation, moving in alternating directions, as marked by the arrows. **(b)** An obstacle with $d = 0.05\zeta$ moving at $\tilde{v} = 2.6$ produces alternating pairs of same-sign vortices, reminiscent of the classical von Kármán vortex street. **(c)** An obstacle with $d = 0.05\zeta$ moving at $\tilde{v} = 3.0$ has a more disordered wake, reminiscent of the onset of turbulence. Here $\zeta = \sqrt{2 \times 10^3} \xi$ and $\tilde{v} = v(10^3 \text{ m/gn})^{1/2}/(2\pi)$. Figure adapted from Sasaki et al. [200] under the [Creative Commons Attribution 3.0 International License](#) [202].

the superfluid and normal components plays a significant role, a dimensionless parameter q , relating to this mutual friction, has been shown to play a similar role to Re [192, 193].

Onsager postulated that the quantum of circulation may play a similar role to viscosity in a superfluid, as they have the same units [194]. This naturally leads to a definition of the superfluid Reynolds number as $\text{Re}_s = uLm/h$ [192, 193, 195], where again u is the characteristic superfluid velocity and L is the characteristic length scale of the system. Using this definition, turbulent flows have been observed with $\text{Re}_s \gg 1$ [196–199], however measurements have not been made in the low Re_s regime in the transition to QT.

Recall that in §1.1.1.1, a prototypical example of the effect of the Reynolds number was the nature of flow past a cylinder. In superfluids, early work, discussed in §1.2.7.1, studied the process of generating vortices via shedding from a repulsive obstacle. More recently, Sasaki et al. [200] showed that at higher flow rates, a quantum analogue of the von Kármán vortex street should occur, as depicted in Fig. 1.14. Stagg et al. [153] extended this theory work to elliptical and 3D obstacles. This periodic vortex shedding was recently experimentally achieved by Kwon et al. [201].

Reeves et al. [203] used the wake of a cylinder as motivation to refine the definition of a superfluid Reynolds number. They found that using

$$\text{Re}_s = \frac{(u - v_c)Lm}{\hbar}, \quad (1.39)$$

gives universal scaling of the shedding frequency of vortices for varying obstacle size or velocity, as in the classical definition. The use of \hbar rather than h in this definition scales the quantity such that the onset of turbulence occurs at $\text{Re}_s \approx 1$.

1.3.1.2 Energy cascades

Another natural comparison to make between quantum and classical turbulence is the transport of energy. In §1.1.1.2 we discussed how in 3D turbulence, energy flows from large scales to small scales in the Richardson cascade, with the energy spectrum following Kolmogorov's five thirds law. I have already mentioned Feynman's description of vortex rings breaking down to smaller and smaller rings as they undergo reconnections, which provides a mechanism by which a cascade may occur. A requirement for the Richardson cascade is, of course, dissipation at the smallest length scales, to remove the energy that has been transported here. It has been proposed that Kelvin waves form the mechanism for this, with high frequency excitations radiating phonons [204, 205].

Surprisingly, given the stark differences between classical fluids and superfluids, experiments in superfluid ^4He showed the same $\kappa^{-5/3}$ spectral scaling as Kolmogorov's classical prediction [206–209]. However, it turns out that the superfluid case is more subtle, with multiple possible turbulent regimes. The filament-like nature of quantised vortices introduces a new length-scale to the system, the total length of vortices per unit volume, L , and correspondingly, the mean inter-vortex spacing $l = L^{-1/2}$. On scales much larger than l , the flow field approximates that of a classical fluid, and the quantum nature of the vortices is inconsequential. Large scale structures are present, in the form of bundles of polarised vortex lines. In this case, the cascade process is much the same as for a classical fluid, and is termed quasiclassical turbulence. Here the vortex length decays as $L \propto t^{-3/2}$. Below l , however, the quantum nature of the vortex lines dominate the dynamics, and the turbulent cascade is facilitated by Feynman's reconnections, as well as Kelvin excitations of vortex lines. When the force driving turbulence occurs on these small scales, the resulting state is known as ultraquantum turbulence. In this case, the vortex length decays as $L \propto t^{-1}$. There is currently no agreement as to how the energy spectrum should scale in this ultraquantum range [181, 188, 210–212], and to date, no experimental measurements of the spectrum have been made. It is also unclear what happens in the intermediate regime, where the transition from quasiclassical to ultraquantum turbulence occurs [181, 188].

Atomic BECs provide different conditions to those of superfluid helium. In helium, the system size is that of the storage dewar, which can be tens of centimetres, and the vortex thickness is on the order of Ångström, providing eight or nine decades of scale. Typical BECs,

however, are up to $100\ \mu\text{m}$, with vortex core sizes around $1\ \mu\text{m}$, resulting in only two decades of length scale. It is for this reason that much of the focus of 3DQT has been in helium systems. BECs do, however, offer superior tunability to helium systems. Interactions between atoms are adjustable via Feshbach resonances [213–218], and individual vortices can be created, manipulated and resolved in images (§1.2.7). There have been numerical studies of 3DQT in the context of BECs, which show that the Kolmogorov power-law scaling persists in the semiclassical inertial range of these systems too [219–222]. Experimentally, Henn et al. [223] were able to produce a vortex tangle in a ^{87}Rb BEC, which inhibited the usual aspect ratio inversion in time-of-flight. More recently, Navon et al. observed a turbulent cascade in a uniform 3D BEC [224] and have subsequently measured the flux of a cascade while continuously driving the BEC [225]. In these cases, the cascade process resembled that of turbulence dominated by waves, rather than vortices.

1.3.2 2D quantum turbulence

In 2D , vortices in a superfluid become point-like objects. As in the classical case (§1.1.2), this dramatically alters the turbulent behaviour of a superfluid when flow is confined to a plane. Just as a classical fluid need not be truly 2D to achieve strikingly different behaviour compared with 3D turbulence, the superfluid itself need not be strictly 2D . As discussed in §1.2.5.1, vortices will align themselves with the shortest path through the BEC to minimise their energy, and provided that high-order Kelvin modes are not excited, these parallel vortices will behave identically to zero-length point vortices in 2D . This regime is not easily accessible by liquid helium, as the Ångström-scale cores mean that the fluid must be in an extremely thin film to suppress Kelvin modes. At this scale, impurities and roughness of the substrate on which the film is deposited provide vortex pinning sites, which may alter the turbulent dynamics. BECs on the other hand can be readily trapped in oblate geometries, which restrict the flow to 2D .

1.3.2.1 Cascades in 2D quantum turbulence

It is not immediately obvious whether the dual energy cascade of classical 2D turbulence should exist in the superfluid case. Numasato et al. [226, 227] suggested that as compressibility and vortex–antivortex annihilations provide dissipation mechanisms on small length scales, a *direct* energy cascade may be possible, as in the 3D case. On the other hand, Reeves et al. [228] argued that the clustering of same-sign vortices would suppress dipole annihilation events, removing the possibility of a direct cascade. While energy spectra have been measured in many numerical studies [115, 226–238], the scaling appears to depend on the particular configuration, and there has not yet been an

unambiguous demonstration of a dual cascade. Kobayakov et al. [233] even saw $k^{-5/3}$ scaling in a simulation of decaying turbulence, which goes against the classical theory.

The presence of the long-range k^{-1} and short-range k^{-3} energy scaling, due to the vortex core (§1.2.6, [107]) leads to an intermediate range which can appear to briefly follow a $k^{-5/3}$ curve. Zamora-Zmaora et al. [239] even showed that $k^{-5/3}$ scaling appears for configurations of only two vortices, which can not be considered turbulent! In typical experimentally realisable BEC geometries, there may not be a large enough range of scales to allow an energy cascade to exist across a large enough range for it to be unambiguously measured. Reeves et al. [231] simulated a much larger condensate, and were able to see $k^{-5/3}$ scaling across a larger range, as well as an increase in energy at the longest scales over time, leading them to conclude that there was in fact an inverse energy cascade present.

Experimentally, it is much easier to study decaying turbulence, as continuously driving a condensate will typically generate large amounts of sound, and heat the system. Based on classical turbulence, the inverse energy cascade should not be present in this case. On small scales, the enstrophy cascade is obscured by the vortex core scaling, so observation of the spectral scaling must occur on scales $k < 1/\xi$. Reeves et al. [238] examined decaying turbulence, beginning with an extremely large number of vortices to first make the enstrophy cascade prominent, then scaled back the number to see if it could be observed for experimentally realisable numbers. They found that to observe k^{-3} scaling beyond the vortex core size, an experiment would require around 500 vortices in a large trap with $R_{\perp} \approx 800 \xi$. These numbers are quite high compared with current experiments, which can typically achieve on the order of 100 vortices in traps with $R_{\perp} \approx 200 \xi$.

1.3.2.2 Detection of vortex clustering

Due to the difficulty in obtaining clear signatures of cascades from the energy spectrum, it appears as though other metrics must be used to characterise the dynamics in experimentally realisable configurations. A characteristic of 2D turbulence is the build up of energy at low wavenumbers, which has been observed in the energy spectrum of several numerical studies [115, 231, 234, 235].

As the inverse energy cascade is associated with the clustering of like-sign vortices, White et al. [240] used statistical measures of the vortex distribution to determine the degree of clustering. Other nearest-neighbour correlation functions have been used [231, 234, 241], which typically take the form of

$$C_n = \frac{1}{nN_v} \sum_{i=1}^{N_v} \sum_j^n c_{ij}, \quad (1.40)$$

where $c_{ij} = 1 (-1)$ if the circulation of the j^{th} nearest neighbour of the i^{th} vortex has the same (opposite) sign, comparing up to the n^{th} nearest vortices. The simplest of these is the nearest-neighbour correlation function, C_1 . For a configuration dominated by dipoles, the sign of C_1 is negative, while cluster dominated configurations give positive values, with C_1 vanishing for more disordered configurations between these two extremes. Higher order correlation functions give similar responses to C_1 in the presence of clusters, due to the grouping of large numbers of like-sign vortices. In dipole-dominated configurations, however, while there are strong first-order anticorrelations, the second-nearest neighbour is essentially random, depending on the relative orientation of the dipoles, leading to a lower magnitude signal. This makes higher order correlation functions useful for the detection of vortex clustering, however C_1 is more useful for quantitatively comparing vortex systems across the full range of possible configurations.

To further quantify the degree of clustering, Reeves et al. [231] introduced a vortex classification algorithm, which uniquely assigns each vortex as belonging to a cluster of same-sign vortices, a dipole pair consisting of a vortex and an antivortex, or as a free vortex. The prescription for this classification is a recursive algorithm, where first, opposite sign vortices that are mutual nearest neighbours are identified as dipole pairs, and ignored in subsequent iterations. Same-sign vortices that are closer to each other than either is to an opposite sign vortex are then determined to be in a cluster. These two steps are repeated until no new classifications are found, at which point any remaining vortices are said to be free. The initial removal of the dipole pairs in this algorithm ensures that the presence of a single vortex of the opposite sign does not discount an otherwise strong cluster of same sign vortices, acknowledging that the short-range field produced by dipole pairs is less dominant than that of clusters.

Valani et al. [56] proposed an alternative algorithm for classification, which uniquely classifies the vortices in a single pass, rather than in an iterative process. In this algorithm, first, the nearest vortex of opposite sign is identified for each vortex. Any vortices closer than the nearest opposite sign vortex (which must therefore be of the same sign as the vortex under consideration) are labelled as cluster candidates for that vortex, or, if there are none, the nearest opposite vortex is labelled as a dipole pair candidate. Once these candidates have been identified, the labels are compared. If two vortices are dipole pair candidates for each other, and neither are cluster candidates for other vortices, they are classified as a dipole pair (this means that the pair must be mutual nearest-neighbours). If two vortices have each other as cluster candidates, then they are classified as belonging to the same cluster. Any remaining vortices are again classified as free vortices.

Groszek et al. [242] found that the vortex temperature (§1.1.2.2) can be determined based solely on this vortex classification. Monte Carlo simulations were run to determine the equilibrium vortex distributions at fixed vortex temperatures. They found that as the inverse temperature goes from positive to negative values, the clustered fraction of the classified vortices increases monotonically, while the fraction of dipole pairs decreases monotonically. This is consistent with the picture that positive temperatures are dipole dominated, while NATs are cluster dominated. As these populations evolve monotonically, they can be used to read off the temperature of the vortex configuration. While these so-called thermometry curves depend on the number of vortices, the general shape remains the same, and small changes in vortex number do not alter them significantly. This thermometry technique was used to analyse the data in the experiments described in Chapter 4, where I will go into the details of how we assigned temperatures.

Other measures of the clustering process that have been used include the radius and net circulation of the largest classified clusters in a system [56, 231, 234], and statistics of the resulting velocity fields [236, 243]. A dipole moment of the vortices of sign s_i at position \mathbf{r}_i can be calculated as

$$d = \left| \sum_i s_i \kappa \mathbf{r}_i \right|, \quad (1.41)$$

which should be largest in the presence of two distinct clusters of opposite sign [115, 129]. An increase in the average kinetic energy per vortex [244], or per number of vortices squared [115, 129] has also been used as an indicator of the clustering process.

Reeves et al. [243] found that in the presence of strong clusters, the spectral build up results in a peak in the energy spectrum at a scale corresponding to the size of the largest cluster. At scales larger than this, the energy spectrum was seen to scale as k^3 , steeper than the $E(k) \propto k$ scaling expected for a system with no net vorticity [107]. It was suggested that this scaling occurs due to the stagnation of flow at points between the clusters. Salman and Maestrini [244] demonstrated that these signatures should be measurable in the time-of-flight distribution of atoms released from their trap, which corresponds to the Fourier transform of the number density distribution, or the momentum distribution.

1.3.2.3 Numerical studies of vortex cluster formation

While Reeves et al. [231] saw an increase in vortex clustering, and build up of energy at low k , Billam et al. [234] were able to observe the formation of large-scale clusters, which they called Onsager–Kraichnan condensation. In these simulations, a high energy, low en-

tropy initial condition was used in periodic boundary conditions, and was seen to evolve to the equilibrium clustered state.

Simula et al. [115] examined the decay of turbulence in a uniform oblate trap from a random initial condition, and found that both the dipole moment and kinetic energy per number of vortices squared increased over time. By eye, the distribution of vortices and antivortices could be seen to separate from a random initial condition to a distinct pair of clusters. It was noted that vortex–antivortex annihilations dominated the vortex dynamics, events which remove only a small fraction of the incompressible kinetic energy—dipole pairs have a low energy associated with them, since they effectively cancel each other’s velocity field. These annihilation events increase the average energy per vortex, while the total number of vortices decreases, so the process was described as *evaporative heating*, in contrast to the process of evaporative cooling, where the hottest particles are lost, leaving the average energy per remaining particle lower.

While these clustering results are seemingly inconsistent with past studies, such as those of Numasato et al. [226, 227], where no clustering was seen, the geometry of the BEC was different. Groszek et al. [129] found that as the trapping potential is varied from harmonic to higher order polynomials, approaching a uniform square potential, the clustering process becomes stronger. While there are some signs of clustering in harmonic traps, it occurs on much slower time scales when compared with traps that are essentially uniform, as seen in Fig. 1.15. These simulations showed that the evaporative heating mechanism is dominated by three- and four-body vortex interactions. As noted in §1.2.5.3, annihilation events can require a catalyst, in the form of a third vortex, or another bound dipole pair. I will discuss the vortex decay process in more detail in the following section, as it is the subject of ongoing research.

There are several key differences in the dynamics of vortices in a harmonically trapped BEC compared with a uniform BEC. In a harmonic trap, the edges are soft, and the atomic density gradient attracts vortices to the edges, allowing individual vortices to be lost. In a uniform potential with hard walls, vortices interact with the boundary via their image vortex. This can result in bound pairs of vortices and their images running around the boundary, and annihilations catalysed by image vortices. The density gradient in a harmonic trap also alters the maximum energy state of the vortices, with the highest energy clusters located much closer together than in the uniform case. This reduces the difference in measurements such as the dipole moment or kinetic energy between the clustered state and a random initial condition, making it much harder to identify the vortex heating process.

While it is now clear that evaporative heating can drive a vortex distribution to clustered states, it is unlikely that this will allow

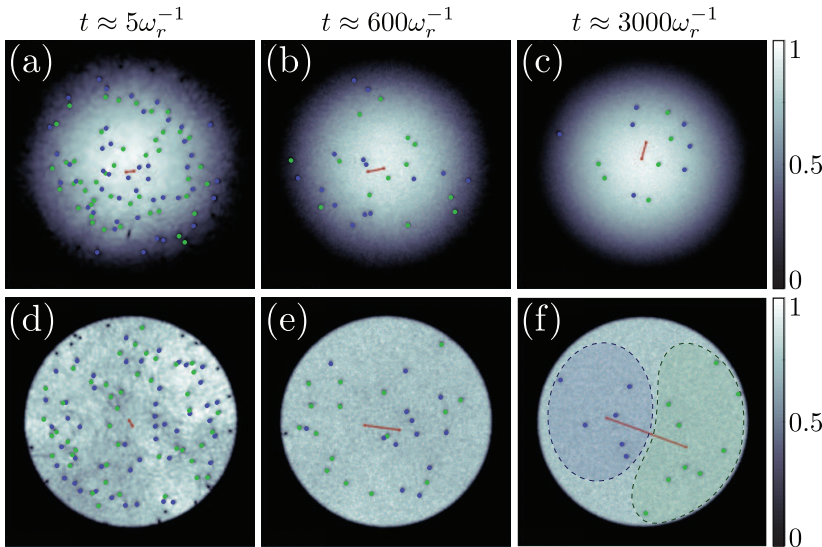


FIGURE 1.15: VORTEX CLUSTERING IN HARMONIC AND UNIFORM TRAPS. Numerical GPE results of turbulent dynamics in a 2D BEC. The grey-scale represents the normalised atomic density and the location of vortices (antivortices) are highlighted by blue (green) dots. (a–c) show the time evolution in a harmonic trap. No strong clustering occurs, though the distribution appears to become more ordered. (d–f) show the equivalent evolution in a trap with an order 100 polynomial radial profile, which is essentially uniform. In this case, the vortices and antivortices separate into two distinct clusters. The red lines represent the vortex dipole moment d . While d grows in magnitude in both traps, the increase is much more pronounced in the uniform trap. Reprinted figure with permission from Groszek et al., *Physical Review A* **93**, 043614 (2016) [129]. © 2016 American Physical Society.

the EBC transition to be reached. The separation of clusters (denoted as the clustering transition by Yu et al. [55]) suppresses the vortex–antivortex annihilation rate, effectively stalling the heating. Valani et al. [56] suggest that the most convenient experiment to observe the crossing of the EBC transition would instead be in a system with vortices of only one sign. Beginning with an initial multi-quantum vortex with high winding number, the system would decay into individual $|s| = 1$ vortices in an EBC state, which would eventually become disordered, cooling below the EBC transition temperature. This would be observed as a sudden increase in the spatial extent of the vortex distribution.

1.3.2.4 Vortex decay in 2DQT

The decay process of vortices in a turbulent system is the subject of ongoing discussion in the literature. There are variations in the observed decay rates, which may be largely due to differences in trapping geometries and finite temperature effects between the different simulations.

Schole et al. [241] found that for a homogeneous system (with periodic boundary conditions), the early time dynamics, when the vortex density is high, are dominated by vortex–antivortex annihilations, which follow a two-body loss rate, $dN_v/dt = -\Gamma_2 N_v^2$, where Γ_2 is a decay constant. At later times they observed a change in the dynamics, which they associated with the lower vortex density resulting in fewer tightly bound vortex pairs, meaning that each vortex tends to interact with a larger number of vortices. They found that a four-body rate of $dN_v/dt = -\Gamma_4 N_v^4$ matches their data well. These two rates correspond to the vortex population decaying as $N_v(t) \propto t^{-\alpha}$, with $\alpha = 1$ for the two-body decay, and $\alpha = 1/3$ for the four-body decay. In general, $\alpha = -1/(1 - k)$ for a $k > 1$ body process. In their simulations, they noted that the early time decay was sensitive to the initial conditions, with measured values of $1 \lesssim \alpha \lesssim 2$, while the later dynamics were more consistent, with $0.3 \lesssim \alpha \lesssim 0.4$, in agreement with the four-body process.

An experiment by Kwon et al. [245] measured the vortex loss rate in a harmonic trap, proposing that their data could be described by a one- and two-body loss process, $dN_v/dt = -\Gamma_1 N_v - \Gamma_2 N_v^2$. This was motivated by the possibility of individual vortices drifting out of the condensate, and vortex–antivortex annihilations. Stagg et al. [246] ran simulations based on this experiment, which produced results consistent with these loss processes.

Groszek et al. [129] found that in zero temperature simulations of a harmonic trap the process appeared to be dominated by three- and four-body interactions. A general loss rate equation of the form

$$\frac{dN_v}{dt} = \sum_k -\Gamma_k N_v^k \quad (1.42)$$

was proposed, where Γ_k are the decay constants associated with interactions between k vortices, and typically $1 \leq k \leq 4$. When damping was introduced, the one- and two-body terms dominated the dynamics instead, consistent with the previously discussed results, indicating that damping plays an important role.

Cidrim et al. [247] found that in their simulation of polarised turbulence (i.e. configurations with unequal numbers of vortices and antivortices), the $k \in [1, 2]$ form of (1.42) resulted in a negative first order decay constant. While the naive interpretation of this would be vortex formation, this was ruled out, and instead the single vortex loss process was studied in more detail. As the vortices are subject to the velocity field of every other vortex in the system, it was suggested that the drift process would not be a simple single-body process. Instead, the velocity field due to the nearest same-sign vortex (which will act to push the vortex away) was considered. This adds an additional factor of $N_v^{1/2}$ to the process, resulting in a rate of $dN_v/dt = -\Gamma_1 N_v^{3/2}$. Due to the polarisation of the system, they

also argued that vortex–antivortex annihilation would be less common, scaling as $\propto N_v^+ N_v^-$, where N_v^\pm are the number of positive and negative vortices, rather than $\propto N_v^2$. This resulted in a modified loss rate of the form

$$\frac{dN_v}{dt} = -\Gamma_1 N_v^{3/2} - \Gamma_2 N_v^4. \quad (1.43)$$

Similarly, Karl and Gasenzer [248] found that a factor of $N_v^{1/2}$ was necessary to account for the background vortex velocity field. In this case, they found that in the presence of vortex clustering, losses were predominantly due to interactions between dipole pairs travelling between the clusters, and individual vortices on the edge of a cluster. In these interactions, one vortex would catalyse the collapse of the pair into a Jones–Roberts soliton, which would then decay due to interactions with fluctuations in the BEC. When the background velocity field was taken into consideration, this three-body process was modelled as $dN_v/dt = -\Gamma_3 N_v^{7/2}$.

To further investigate the nature of dipole pair annihilation, Baggaley and Barenghi [249] studied a uniform system with periodic boundary conditions, to eliminate losses due to drift. They assumed a rate equation of the form

$$\frac{dN_v}{dt} = -\Gamma N_v^k, \quad (1.44)$$

and sought to find the value of the exponent k in the case of no dissipation, weak dissipation and strong dissipation. In the case of no dissipation, the number decayed as $N_v \propto t^{-0.3}$, close to the $t^{-1/3}$ scaling expected when $k = 4$. In the presence of dissipation, however, the decay process began at a rate consistent with $N_v \propto t^{-1/2}$, associated with $k = 3$, then transitioned to a faster t^{-1} decay, associated with $k = 2$. The transient $k = 3$ behaviour was interpreted as being due to a higher vortex density at early times, meaning that dipole pairs are more likely to encounter other vortices. At later times when the vortex density is lower, dissipation becomes the dominant loss mechanism, bringing pairs of vortices and antivortices closer together.

While it seems clear that the vortex decay process is, in general, due to a combination of drift and dipole annihilation events, the number of vortices participating in the dipole annihilations appears to depend on the configuration of vortices, and the level of damping in the system. It is unclear, however, whether the background velocity field of other vortices is important for collisions of all orders. In a four-body process, taking this background into account using a power of $k = 9/2$ would result in scaling of $t^{-(2/7 \approx 0.29)}$, which agrees well with the scaling seen in the case of no dissipation by Baggaley and Barenghi [249]. In their dissipative cases, the background field does not appear to be required, with the data matching the integer scaling

laws well. In his thesis [250], Andrew Groszek notes that when the results in Ref. [129] are re-analysed with the additional factor of $N_v^{1/2}$ a good fit to the data is still achieved. Given that these high vortex number simulations cannot easily determine the precise nature of the decay process, it is unlikely that the $N_v^{1/2}$ factor will be noticed in experiments with lower vortex numbers.

Groszek et al. [242] also investigated the evolution of classified vortex populations (in a system with no damping), proposing that the total number of vortices classified as being either part of a cluster, a dipole pair or as a free vortex, follow power-law functions of the total vortex number, $N_c \propto N_v^\alpha$, $N_d \propto N_v^\gamma$ and $N_f \propto N_v^\delta$ respectively. The measured values, $\alpha = 0.79$, $\gamma = 1.21$ and $\delta = 1.18$ were considered indicative of rational values $\alpha = 4/5$ and $\gamma = \delta = 6/5$, though no physical interpretation of these laws was suggested. As these power-laws are effectively re-scaled decay rates (as N_v is constantly decaying), they show that the number of clustered vortices decays at a slower rate than the number of vortices in dipole pairs and free vortices, which is consistent with the notion that losses are due to vortex–antivortex annihilations. This further suggests that three-body losses may be more likely to occur between dipole pairs and a free vortex than dipoles and a vortex that is part of a cluster. The net result is that despite the decay in all three populations, the fraction of vortices in clusters tends to increase throughout the process.

1.3.2.5 *Nonthermal fixed points*

The evolution of vortices in \mathcal{N} DQT has also been analysed in the context of nonthermal fixed points (NTFPs) [241, 248, 251, 252]. In this picture, the vortices are seen to evolve toward a stationary point, such as a pair of vortex clusters, which does not correspond to the thermal ground state of the system. Near these NTFPs there is a critical slowing of the dynamics, and correlation functions of the system exhibit universal scaling. This universal scaling suggests that examining \mathcal{N} DQT may provide experimental insight into other dynamical systems, such as biological systems [253, 254], early universe inflation [8], and quark-gluon plasma dynamics [9].

Nowak et al. [251, 252] interpreted the momentum occupation spectrum $n(k)$ in terms of NTFPs, finding universal k^{-4} scaling at large length scales, in agreement with analytic field theory results. In the work of Schole et al. [241], discussed in §1.3.2.4, the change in scaling of the vortex decay process was interpreted as a critical slowing of the process as the system approached a NTFP. The slowing occurred as the occupation spectrum developed the k^{-4} scaling associated with the fixed point. In this work, the vortex configuration was close to the BKT transition, dominated by bound vortex–antivortex pairs. The NTFP was described as the non-equilibrium unbinding of several of these pairs.

Karl and Gasenzer [248] showed that different fixed points can be approached depending on the initial conditions. While the dynamics near a *NTFP* are universal, without memory of the initial state, there can be more than one *NTFP*, with the initial state determining which will be approached. For an initial condition consisting of a lattice of vortex clusters, a fixed point was seen to exhibit universal scaling of the occupation spectrum, with an anomalously high scaling exponent. In the case of a random initial condition, the scaling is close to Gaussian, corresponding to the scaling expected due to the velocity field of the vortices.

They found that the evolution of the characteristic inter-vortex spacing scale l_v depends on which fixed point the system is close to. Near the anomalous *NTFP*, the distance scales as $l_v \propto t^{1/5}$, whereas near the Gaussian fixed point the scaling is $l_v \propto t^{1/2}$. In all cases, the system was seen to eventually evolve toward the Gaussian fixed point scaling. This was interpreted as critical slowing of the dynamics near the anomalous fixed point, before the system moved toward the equilibrium Gaussian fixed point. The scaling of the vortex spacings was shown to be consistent with vortex decay as a three-body process involving the background velocity field for the anomalous fixed point, and two-body loss for the Gaussian fixed point.

1.3.2.6 Experiments in 2D quantum turbulence

The *BKT* transition has been demonstrated in both superfluid ^4He [255] and a 2D atomic gas [256] (note that in this case the trapping was sufficiently 2D that a *BEC* cannot form, in contrast to the quasi-2D *BEC* systems that will be discussed next). These experiments concentrated on the physics of the phase transition itself, and focussed on the coherence of the system and breakdown of superfluidity across the transition, rather than relating the phenomenon to turbulence. While experiments in helium are able to observe the breakdown of superfluidity, it was only in the atomic gas that the microscopic details of the vortex pair unbinding was able to be seen. I will not go into the details of these *BKT* experiments, and instead focus on those explicitly examining 2DQT.

In addition to our lab at Monash, there are currently three other experimental groups actively researching 2DQT: Brian Anderson's group at the University of Arizona, Yong-il Shin's group at Seoul National University and Tyler Neely's group at the University of Queensland. To date only a few experiments have directly addressed 2DQT in a scalar *BEC*. Many experiments on few-vortex systems, however, have also contributed to our understanding of turbulence by examining the creation and dynamics of the vortices themselves. Wilson et al. [257] (from the Arizona group) also published a compilation of ways that they have kicked, poked, spun and wobbled their *BEC* to induce large

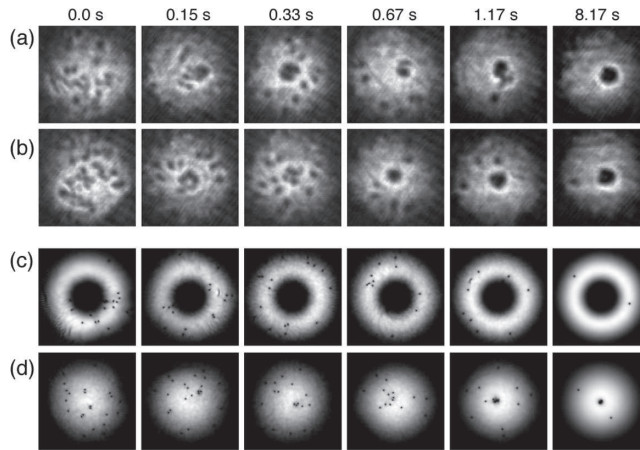


FIGURE 1.16: TURBULENT VORTICES IN A TOROIDAL BEC.

Data is shown from the first experimental investigation of $2DQT$. (a–b) Optical density images showing vortices at sequentially longer hold times after stirring. The optical plug creating the toroidal geometry has been removed prior to time-of-flight expansion, however, at later times the distribution maintains a large central hole, indicative of a persistent current. Numerical simulations of the experiment are shown (c) *in situ* with the central plug present, and (d) after ramping off the plugging potential for the corresponding data in (c). Reprinted figure with permission from Neely et al., *Physical Review Letters* **111**, 235301 (2013) [258]. © 2013 American Physical Society.

numbers of randomly distributed vortices to generate a turbulent state.

The first experiment to study $2DQT$ in detail was by Neely et al. [258] in Arizona. In this experiment, a ring-shaped trapping potential was formed by passing a repulsive Gaussian laser beam through the centre of an oblate trap, formed by a combination of magnetic field gradients and a focussed light sheet. By moving the magnetic field gradient, which forms the radial confinement, relative to the central laser beam, a disordered distribution of vortices were shed from the central barrier. The vortices were allowed to evolve in the annular trap, before the central barrier was slowly removed and an image of the vortex distribution was taken, shown here in Fig. 1.16. Vortices became pinned to the central obstacle during the experiment. As the vortices decayed, a persistent current formed in the trap, which was observed as a density depletion persisting in the centre of the trap once the obstacle had been removed. They were able to distinguish that the formation of the persistent current was due to the vortex dynamics, and not angular momentum injected in the stirring process.

However, as standard absorption imaging was used, only the vortex positions were known, not their signs. This meant that any further analysis required comparison to numerical simulations of the experiment parameters. These simulations showed that the incompressible energy spectrum developed a $k^{-5/3}$ scaling during the stirring process, which slowly decayed as the persistent current formed post-stir.

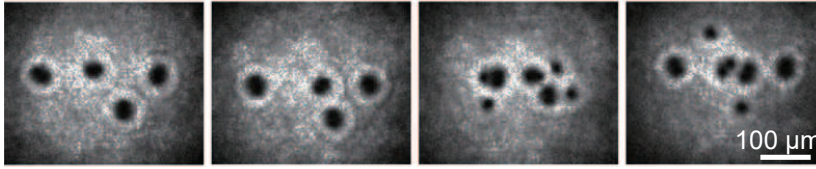


FIGURE 1.17: A VORTEX STREET IN BEC.

Vortices are seen in a zig-zag pattern after an obstacle has been dragged through a BEC of sodium atoms. Each image was produced with identical parameters, with an obstacle diameter of $D \approx 29\xi$, depth $V_0 \approx 1.8\mu$ and velocity $v = 1.39 \text{ mm s}^{-1} \approx 1.25v_c$. In some cases, individual vortices are seen (smaller black holes), though in many cases clusters of two vortices of the same sign form, merging into a single larger feature in time-of-flight imaging. Reprinted figure with permission from Kwon et al. *Physical Review Letters* **117**, 245301 (2016) [201]. © 2016 American Physical Society.

Clustering of same-sign vortices was also seen in the simulations. While this experiment saw results consistent with the transport of energy from small scales to large scales, in the form of vortex clustering, and ultimately the formation of a persistent current, it lacked the ability to directly infer this from the experimental data, as the signs of vortices imaged throughout the process was unknown. It is also likely that the pinning of vortices to the central obstacle played a role in the vortex dynamics.

Kwon et al. [245] in Seoul investigated the vortex number statistics of decaying turbulence, as discussed in §1.3.2.4. Around 60 vortices were injected into a harmonic trap by sweeping a repulsive stirring beam through the centre of the trap. Many crescent-shaped vortex–antivortex pairs were seen in their data, indicating that pair annihilations played a significant role in the dynamics. The vortex loss rate was seen to match (1.42) with $k \in [1, 2]$, indicating that the loss was due to single-body losses (presumably at the boundary) and two-body losses associated with annihilation events. The behaviour of the decay rates was investigated as a function of temperature and chemical potential. As the condensate temperature was increased, both decay rates grew, though the two-body rate appeared to increase quadratically, while this one-body rate grew linearly.

As mentioned in §1.3.1.1, the Seoul group has also generated a von Kármán vortex street [201]. By varying the speed of an obstacle through their BEC, they were able to observe periodic shedding of vortices, which seemingly injected transient clusters of like-sign vortices, seen in Fig. 1.17. As this was performed in a harmonic trap the classic zig-zag structure of many such clusters eventually became deformed as the vortices began to orbit within the finite area.

The first experiment to achieve full velocity information in 2DQT was by Seo et al. [21], who implemented the Bragg spectroscopy technique discussed in §1.2.7.3. This experiment was performed in the same harmonic trap as the previous work in Seoul, and looked at the

decay process again, this time focussing on the vortex configuration since the signs were known. It was seen that the distribution was dominated by vortex–antivortex pairs, which persisted throughout 12 s of evolution time. They attribute the pairing to dissipation, due to the considerable thermal fraction ($T/T_c \approx 0.5$ in this case), as well as the harmonic potential. An incompressible kinetic energy spectrum was generated using (1.36), marking the first such calculation based on experimental measurements. This spectrum showed the usual k^{-1} and k^{-3} asymptotes, but there was no convincing inertial range between these.

Most recently, in Queensland, Gauthier et al. [259] observed the formation of large-scale vortex clusters by sweeping pairs of ‘paddles’ through an oblate BEC with a hard-walled elliptical in-plane profile. While no vortex sign detection was implemented, the sign of vortices in each of the two clusters of vortices formed could be inferred based on the geometry of the sweep. These clusters were seen to persist with almost no decay over 10 s, indicating that they must be highly pure, with vortices and antivortices isolated from each other inhibiting the annihilation process. For comparison, a similar number of vortices were injected using a grid of obstacles to form a more random distribution, in which case the vortex number decayed to 40 % in the same time. While these clusters were not energetic enough to be EBC states, they represent a NTFP where the time scaling has been almost completely frozen.

The decay of the clusters was investigated as a function of BEC temperature, as well as trap size. As the trap was made bigger, residual harmonic trapping from the light sheet (providing the tight confinement) became non-negligible, which tends to push the pair of clusters closer to each other, facilitating annihilation events. Similarly, as the condensate fraction was reduced with increasing BEC temperature, the added dissipation caused the clusters to relax to larger (lower energy) configurations, which began to overlap and allow vortex–antivortex annihilations. While this experiment essentially began at the ‘end point’ of the expected dynamic evolution of 2DQT, it shows an ideal example of a NAT state, and confirms the role of trap geometry and dissipation in the stability of these states.

The experiments in Queensland were performed and analysed during the same time period as our experiments, which will be described in Chapter 4. Briefly, our experiment used the sign detection technique of Seo et al. [21] in a trap similar to Gauthier et al. [259], and observed the dynamic evolution of vortices to clustered states. Our clusters, however, were much smaller, typically consisting of multiple clusters of only a few vortices, though still had NATs. In Chapter 5 I will discuss some possible follow-up experiments that are now experimentally feasible, that will expand the current knowledge of 2DQT.

1.4 MORE ON NEGATIVE ABSOLUTE TEMPERATURE SYSTEMS

The arguments made by Onsager, discussed in §1.1.2.2, have also been made to assign NATs to other systems with a finite phase-space. Purcell and Pound [260] used a non-adiabatic magnetic field reversal to initialise a system of nuclear spins in a highly ordered, high energy state. This state evolved to a higher entropy while losing energy, and was thus described as a NAT state.

Braun et al. [261] realised a NAT state in the motional degrees of freedom of atoms in an optical lattice. Here, a Feshbach resonance was used to tune the inter-atom interactions from positive to negative values, effectively changing the sign of their Hamiltonian. In this system, for repulsive (attractive) interactions, only positive (negative) temperatures are accessible, as the interaction energy only has a lower (upper) bound.

Both of these NAT systems differ from the point vortex case, as they are essentially a change of state for single particles. A positive temperature distribution is taken, and the sign of a parameter is non-adiabatically swapped, causing the system to suddenly swap to a NAT state. For point vortices, however, energy is injected into the system in a continuous manner and it is the interactions of the constituent particles (vortices) that results in a NAT configuration.

Recently Gartside et al. [262] demonstrated an artificial spin ice in a NAT state. These are systems of nanomagnets arranged in geometrically frustrated arrays, which arrange themselves to minimise the net magnetic charge at each vertex of the array. Due to the finite number of nanomagnets, the total number of microstates (spin configurations) is bounded, and hence NATs are allowed. By using a new direct spin writing technique, injecting topological defects in magnetic nanowires, arbitrary configurations of artificial spin ices were able to be made, including monopole chains, which are high-energy, low-entropy states with NATs.

As NATs can result in negative pressures, they have been considered as a potential source of inflation in cosmology [263]. Saha et al. [264] recently suggest that ‘dark energy’ may not be required if the cosmic fluid is an ideal gas with a varying NAT.

1.4.1 Ramsey’s description of negative absolute temperatures

Following the experiment of Purcell and Pound, Ramsey [265] discussed the properties of systems capable of NATs in general (though with a focus on spin systems). He claimed that in terms of thermodynamics, NATs can occur when entropy is not a monotonic function of energy, such that (1.10) takes a negative value. He pointed out that NATs are hotter than positive temperatures, admitting that the term seems poorly named, lamenting that the existing definitions of

temperature, combined with the mathematical description, resulted in this confusing scenario, where the derivation makes sense, but the physical description is counter-intuitive.

Ramsey stated that for a system to support NATs, its elements must be in thermodynamic equilibrium with each other, the system must have an upper energy bound, and the system must be sufficiently isolated from other systems that do not meet these criteria. Practically speaking, this means that the time taken for the system to equilibrate must be short compared with the time taken for energy to be lost to or gained from an outside system. He asserted that usual statistical mechanics approaches are not limited to unbound systems, and so can readily be applied to bound systems supporting NATs.

1.4.2 *Do negative absolute temperature states really exist?*

Due to the counter-intuitive nature of NATs, there has been ongoing debate as to whether they are a meaningful way to describe these systems. In the case of Onsager's description of negative temperature vortices, Berdichevsky et al. [266] considered the presence of NATs to be a paradox, and showed that this can be 'resolved' by using a different definition of entropy. Instead of the Boltzmann entropy, $S_B(E) = k_B \log [w(E)]$, they advocate for the use of the Gibbs entropy, $S_G(E) = k_B \log [\Omega(E)]$, where $\Omega(E)$ is the number of microstates with energy less than E , the integrated density of states. In the limit of large, classical systems, the two are almost identical, but for finite sized systems they differ. When the density of states is not monotonic, the Gibbs entropy remains monotonic, resulting in only positive temperatures.

This suggestion sparked a chain of comment papers, with Montgomery arguing that there was no paradox to be solved in the first place [267]. It was argued that the negative temperature description is useful for understanding the different dynamics of the vortices in the two regimes. This was seen as being more important than redefining quantities such that these particular finite systems mimic the thermodynamics of macroscopic systems. In response to these comments, Berdichevsky et al. [268] argued that thermodynamics of finite systems should only be valid for ergodic systems that are chaotic. They argue that this rules out a thermodynamic description of the high energy clustered vortex states. Rather than viewing these high energy states as a result of a NAT, they view them as loss of ergodicity of the system.

O'Neil and Campbell [269] argued against these ergodicity claims, suggesting that the clustering of vortices is not inconsistent with the system being ergodic. They argued that there is a physical consequence of NATs: at positive temperatures vortices of opposite sign attract, and vortices of the same sign repel, whereas at negative tem-

peratures vortices of the same sign statistically attract. Berdichevsky et al. [270] responded to this comment, suggesting that further research was needed regarding the ergodicity of high energy vortex systems. They maintained that while negative temperatures make sense in some physical systems (presumably referring to the experiments with nuclear spins), the appearance in the vortex system is paradoxical, as the average direction of rotation of vortices should change as the temperature transitions from positive to negative.

Following the atomic lattice experiment there has been a renewed theoretical interest in NATs. In particular, another debate of Boltzmann vs. Gibbs entropy has been ongoing, in the context of both this experiment and the earlier nuclear spin experiments.

Romero-Rochín [271] claimed that NATs are not physical, as states beyond infinite positive temperature are not stable, and hence not in equilibrium, a requirement of a thermodynamic description. This argument was based on the fact that if a system with NAT were brought into thermal contact with any system which did not support NATs, the system would rethermalise to a positive temperature, no matter how small the positive temperature system is. This argument ignores the criteria for NATs set out by Ramsey [265], namely that the system must be isolated from systems that do not support NATs. The description as a NAT state was only ever meant for isolated systems with an upper energy bound.

Dunkel and Hilbert [272] wrote that “*consistent thermodynamics forbids negative absolute temperatures.*” They state that it is invalid to use NATs, because the entropy definition used to obtain such states is inconsistent both mathematically and thermodynamically. They claim that the Gibbs entropy produces sensible predictions for thermodynamic observables where the Boltzmann entropy does not.

Vilar and Rubi [274] rebutted the claim that the Gibbs entropy is superior. They showed that it results in lost information for bound systems, as S_G levels off beyond the maximum of the density of states. Furthermore, they showed that using the Gibbs entropy results in inconsistent temperatures for finite systems, with the measured value scaling exponentially with system size. Frenkel and Warren [275] also argued against the use of the Gibbs entropy. They showed that it leads to situations where two bodies in thermal equilibrium had different temperatures, which does not agree with the principles of thermodynamics.

Hilbert et al. [276] retaliated, claiming that temperature-based heat-flow arguments cannot be used to judge the two entropy formalisms. Instead, they argued that they should be evaluated based on the laws of thermodynamics. They found that only the Gibbs entropy can simultaneously satisfy the zeroth, first and second laws of thermodynamics for a broad range of systems. Campisi [277] used the second law of thermodynamics and the ideal gas law to build an expression for

Poulter reviewed these counter arguments to the Gibbs entropy in a pedagogical article “In defense of negative temperature” [273].

the entropy, finding that this was satisfied by the Gibbs entropy. This work also showed that the Boltzmann entropy can predict unphysical phase transitions in the magnetisation of spin systems.

There have many publications since, comparing aspects of thermodynamics with each entropy definition (e. g., [278–283]). These have shown that the Boltzmann entropy is in fact valid to use, and that negative temperatures are a valid extension to thermodynamics. Abraham and Penrose [284] recently reviewed the arguments for each entropy, concluding that NATs make theoretical sense, and should be used in the descriptions of the experiments.

BUILDING A BEC APPARATUS

Although the results presented in later chapters use single species ^{87}Rb BECs, the apparatus used was designed to trap and cool both ^{87}Rb and ^{41}K . At the beginning of my PhD, in February 2011, the lab consisted of little more than optical tables, a few commercial lasers, and drawers full of optics and vacuum components which were yet to be assembled. Now, in a laboratory a few hundred meters north east of the original space, those optical tables are home to the dual-species ‘KRb’ apparatus. This Chapter will outline the construction and general operation of this apparatus.

The construction of the KRb lab was a team effort, so first I will begin with a brief overview of the contributions of everyone involved. The KRb apparatus was also built in parallel with a second BEC laboratory at Monash, the ‘spinor’ lab, headed by Lincoln Turner and Russell Anderson, and so much of the hardware and software in our lab was developed alongside theirs.

I will then outline the main hardware components in our lab, namely the vacuum system, lasers and magnetic coils. The control hardware and software will be discussed, before an explanation of how it all goes together to make the experiment work. The experiment sequence will be outlined in approximately the order in which the stages happen during a typical run of the machine, though with some asides where multiple configurations have been used for some stages.

2.1 CONTRIBUTIONS TO THE KRb LAB

The vacuum chamber was bolted together, pumped down and baked in 2011 by Brad and Chris, while Phil & I began setting up the lasers required for cooling, trapping and probing the ultracold atoms. Beyond this, the majority of the work in the lab has been a team effort by Phil & I, with some input from Mikhail, and, of course, guidance from our supervisor, Kris. The key people who made contributions, and a brief summary of their main contribution to the KRb apparatus are as follows:

PHILIP (PHIL) STARKEY: Phil started his PhD with me in 2011 and is currently writing his thesis [285]. Phil’s main contributions were:

- Building the laser systems for trapping, cooling and probing ^{87}Rb and ^{41}K (in conjunction with me),

We moved the entire lab from the original physics space in the old ground floor annex of building 27 (the foundations of which are now beneath the Green Chemical Futures building) to the (at the time not quite completed) New Horizons building in 2013.

- Putting together a lot of the electronics in the lab, including radio frequency (rf) sources and fail-safe interlocks,
- Writing the control system, the labscript suite (in conjunction with Chris, with contributions from Martijn, Russ & myself)—I am a co-author on a publication describing this work [286],
- Constructing and aligning the optics for the magneto-optical traps (MOTs), and developing and optimising the experiment sequence (in conjunction with me, with later assistance from Mikhail).

CHRISTOPHER (CHRIS) BILLINGTON: Chris started his PhD with me in 2011, and recently submitted his thesis [166]. Chris ended up having a mostly theory based project but made contributions to the lab, including:

- Helping Brad bolt the vacuum system together, then leading the bakeout of the system,
- Writing the control system, the labscript suite (in conjunction with Phil, with contributions from Martijn, Russ & myself).

DR. MIKHAIL EGOROV: Mikhail worked in our lab as a post-doctoral researcher from December 2011 to April 2014. Mikhail's main contributions were:

- Assisting Phil & I with the construction and alignment of the optics for the MOTs, and developing and optimising the experiment sequence,
- Installation of the first iteration of our optical dipole trap (in conjunction with me),
- Assisting me with work on the transport of atoms to the square science chamber.

BRADLEY (BRAD) MURNANE: Brad was a student in our lab from 2010–2012, who was subsequently employed as a technician the mechanical workshop. Brad's main contributions were:

- Designing and constructing the vacuum chamber,
- Winding the anti-Helmholtz electromagnet coils.

SEBASTIEN (SEB) TEMPONE-WILTSHIRE: Seb started his PhD in our lab in 2015. Seb's main contribution to the KRb machine was developing methods for generating static holographic elements, copying a pattern from a spatial light modulator (SLM) to a polymer film (an idea initiated by me)—I am a co-author on a publication describing this work [287]. Though not related to this thesis, Seb is currently building the next generation 'KRb2' machine, taking into account the advice of Phil & I based on our

experiences with the KRb machine. I also assisted Seb in the development of an experiment in which he generated optical knots using an SLM, which, on average, contained only a single photon at a time. I am a co-author on the paper resulting from this experiment [288].

DR. MARTIJN JASPERSE Martijn was a PhD student in the spinor lab from 2010–2015. Several of Martijn’s contributions to the spinor lab, which are described in his thesis [289], were also used in our lab, in particular:

- BIAS, the imaging system component of the labscript suite,
- The microwave offset laser lock, which I duplicated with minor modifications.

DR. ALEXANDER (ALEX) WOOD: Alex was a PhD student in the spinor lab from 2011–2015. Several of Alex’s contributions to the spinor lab, which are described in his thesis [290], were also used in our lab. In particular, I developed our microwave modulation equipment in conjunction with Alex. Alex and I also worked together on the implementation of optical dipole traps, purchasing identical lasers and using a similar optical layout. I also made use of a MATHEMATICA notebook developed by Alex and Russ for calculating dipole trap parameters.

Of course my experimental supervisors, Prof. Kristian (Kris) Helmerston and Dr. Lincoln Turner, along with Dr. Russell (Russ) Anderson, also contributed to the development of the lab with plenty of guidance and advice.

2.2 THE VACUUM SYSTEM

As BECs are extremely fragile, they must be prepared in an ultra-high vacuum (UHV) chamber—collisions with only a few room temperature atoms would be enough to heat and destroy the condensate. Our apparatus is designed to cool both ^{87}Rb and ^{41}K , and so is inherently more complicated than most single species designs, which have become quite compact and simple over the last two decades since the first condensates were made. Our vacuum system, depicted in Fig. 2.1, was designed and constructed by Brad. The vacuum system consists of two *source* regions, one containing around 5 g of elemental rubidium and the other around 5 g of elemental potassium, and a central UHV chamber, off which there are two high quality glass *science chambers*.

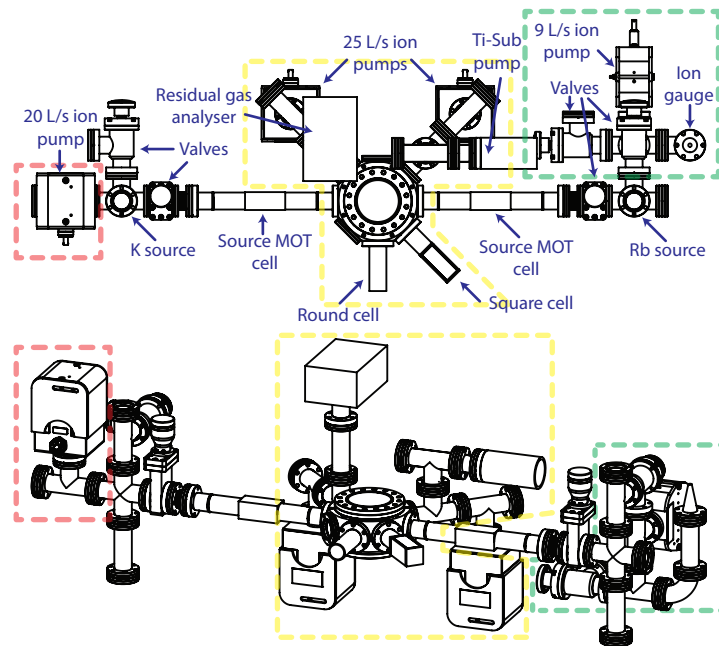


FIGURE 2.1: THE VACUUM CHAMBER.

The vacuum chamber has a central ultra high vacuum section (yellow), with two source sections, potassium on the left and rubidium on the right. The top panel shows a birds eye view of the chamber, with labels to the main components described in the text. The red section indicates the additions made when the potassium source developed a leak, while the green section was added when the rubidium source was limiting the central chamber pressure. The lower panel shows a side view of the chamber to help visualise the 3D layout.

2.2.1 The atomic sources

The source sections are almost identical. Each contains an ampoule of the relevant element in the bottom of a 2.75" CF vacuum tube. This section of tubing has nichrome wire wrapped around its exterior to form a resistive heater, used to increase the background alkali vapour pressure in the section. The ampoules were placed in the tube during construction, along with a small block of steel, which was held at the top of the tube by a strong magnet on the outside of the tube during bakeout. Once the vacuum system was pumped down and baked, the magnet was removed, allowing the block to fall and smash the ampoule open. In practice, this required dragging the block up and down with the magnet several times before the glass gave way.

Each oven section is then connected, via a gate valve, to a glass tube in which a MOT is loaded from the background vapour. The details of these MOTs will be outlined in §2.6.1. There is also an angle valve from each oven section, to which a turbo pump was connected during the initial pump down and bakeout of the system.

2.2.2 *The UHV chamber*

Each source section is attached to opposing sides of a KIMBALL spherical octagon chamber, via a differential pumping tube built into a custom copper gasket. This central chamber of the system is pumped by two GAMMA 25 L s^{-1} ion pumps, along with a titanium sublimation pump, as shown in Fig. 2.1. The two larger faces of the central KIMBALL chamber, on the top and bottom, have large diameter windows, which are recessed such that there is only $\approx 25 \text{ mm}$ between the internal glass surfaces. This allows us to mount electromagnets, antennas and lenses as close to the atoms as possible, without having them in vacuum.

Two glass science chambers are attached to the ‘front’ side of the central chamber. One science chamber is cylindrical, which was intended to be used by Brad for experiments with physically rotating optical lattices, but has never been utilised, other than as a window for the central chamber. The other is a rectangular chamber, with 4 mm thick BOROFLOAT glass walls, where we had planned to conduct experiments requiring good optical access and high resolution imaging. As I will discuss in §2.7.3.2, this did not go as well as planned, and we ended up running most experiments in the central chamber, despite the reduced optical access.

2.2.3 *Repairs to the vacuum system*

In an ideal world, the vacuum system should never need to be brought back to atmospheric pressure or modified after the initial bakeout. Unfortunately, ours has had to have two major repairs during its life.

During construction, the copper-seal valve on the rubidium end was found to be leaky, and replaced with one with a VITON rubber seal. Shortly after obtaining our first magnetically trapped atoms in 2012, we noticed that the magnetic trap lifetime in our UHV chamber was much shorter than expected. Using a residual gas analyser built in to the UHV section of the chamber, we found that the level of hydrogen in the chamber was much higher than expected, but lowered when the gate valve to the rubidium source was closed. Since the VITON valve had been kept below 150°C during bakeout to prevent damaging the seal, it was our primary suspect as the source of the excess hydrogen. An additional section of vacuum chamber was bolted on after this valve, consisting of a small 9 L s^{-1} ion pump and a new copper sealed angle valve (see green section of Fig. 2.1). We also added an ion gauge, as the main chamber did not have any, though we suspect that this short circuited to the vacuum chamber, as it has never worked. We believe that readings from the ion pumps in both the UHV and rubidium source have been accurate enough to monitor the vacuum pressure, with the UHV pump controller readings

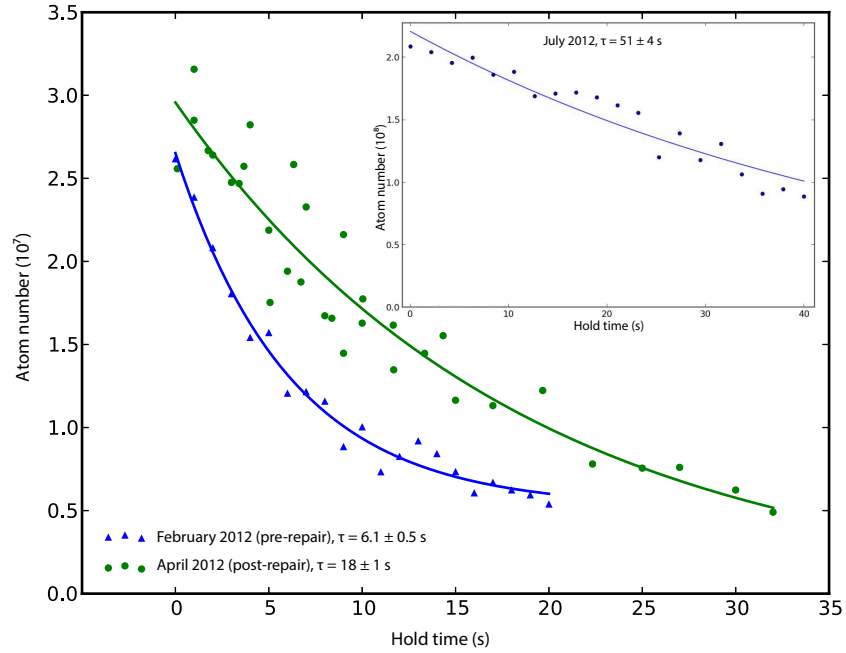


FIGURE 2.2: MAGNETIC TRAP LIFETIME MEASUREMENTS.

Our first magnetic traps showed poor lifetimes of only 6 s (blue), pointing to an issue with our vacuum. After adding an ion pump to the rubidium source section, the lifetime was improved to 18 s (green), which improved further to 51 s (inset) after a few months.

‘bottoming out’ on their lowest possible reading of 1.00×10^{-11} Torr. The new section was re-pumped and baked without losing vacuum in the UHV section. After opening the old VITON valve to join the new section the lifetime measurement in magnetic trap improved, shown in Fig. 2.2, as did the vacuum pressure readings on the ion pumps.

The potassium end of the system did not have a pump added to it at the time, as we had no issues with excess hydrogen originating from here, presumably since the all-metal angle valve on this end was baked well. However, at 11:55 pm on the 11th of July 2016, there was a sudden increase in pressure registered by the ion pumps in the UHV section. This was caused by the failure of the window on the end of the potassium oven. As can just be made out in Fig. 2.3, the glass around the rim of the window appears to have shattered. We do not know what caused this, however we suspect that the potassium could have weakened either the glass or the glass-to-metal seal. After unsuccessfully attempting to patch up the window with TORR SEAL (which we happened to have on hand; a less viscous vacuum sealant may have been more suitable here), we made the decision to break vacuum and replace the window.

The gate valve between the oven section and the MOT chamber was closed, however this valve does not seal well (most likely again due to a VITON seal, which could have been damaged during bakeout), and nitrogen was used to back-fill the chamber from the angle valve,



FIGURE 2.3: THE FAILED VACUUM WINDOW.

The reflection of my finger (holding my phone while taking the photo) conveniently points towards the upper edge of the window where the glass appears to be crystalline. It is most likely that the reason the TORR SEAL did not work was due to air trapped within this shattered glass, as well as the proximity to the vacuum bolts, which prevented us from fully sealing the edge of the window.

taking the whole chamber to a slightly positive pressure. We decided to add a spare 20 L s^{-1} ion pump that we had, to assist with pumping the source end (see red section of Fig. 2.1), as we would not be able to properly bake the repaired section due to the potassium present. Unfortunately, the pump controller stopped working after a few weeks, however by then the vacuum pressure had more or less recovered, and did not seem to be severely impacted by leaving this extra pump turned off. Over a year later, the vacuum pressure seems to be worse than prior to the incident, but good enough, with a magnetic trap lifetime of 24 seconds (comparable with the lifetime measured immediately after the rubidium oven repair), shorter than our best recorded lifetime of 51 seconds (Fig. 2.2).

While writing this thesis, another leak opened up in the system, this time in a window on the rubidium source end. The window on top of the rubidium oven section appeared to have a similar crack to the failed potassium window, though it appeared smaller, and the central chamber vacuum pressure did not get as high (in fact, it was only by chance that I noticed it, a week or so later, when checking on something else in the lab, as it had not reached a high enough level to set off our alert system). This time I had some VACSEAL on hand, which is less viscous than TORR SEAL, and as the window was mounted flat I was able to pour it into the groove between the window and the flange. This seems to have stopped the leak, however the

pressure reading on the ion pumps is still high (around 1×10^{-9} Torr in the UHV chamber). This does not seem to be a correct reading (the ion pumps possibly formed ‘filaments’ during the ordeal causing an increased pumping current), as when the apparatus was turned back on the lifetime was consistent with previous measurements. The atom number took a few weeks to recover, since the rubidium source oven had been off for several months. During this warm up period the magnetic trap lifetime was seen to decrease from around 50 s to 20 s, consistent with the best lifetime measurement in Fig. 2.2 and the lifetime seen more recently after the potassium window repair. A possible interpretation of these observations is that the background-limited lifetime is on the order of 50 s, with the reduction to a trap lifetime of 20 s caused by another effect. This further reduction is most likely due to a higher background pressure in the central chamber when the rubidium source is at its optimal operational pressure.

2.3 LASERS

In order to trap and cool ^{87}Rb and ^{41}K atoms, we use lasers tuned close to resonance with the D2 transition in each atomic species. For each species we need cooling (red detuned from $|F = 2\rangle \rightarrow |F' = 3\rangle$) and repumping ($|F = 1\rangle \rightarrow |F' = 2\rangle$) beams for both the source and central MOTs, an optical pumping beam ($|F = 2\rangle \rightarrow |F' = 2\rangle$) and an imaging beam ($|F = 2\rangle \rightarrow |F' = 3\rangle$), as well as a push beam for transferring atoms from the source MOT to the central MOT (close to $|F = 2\rangle \rightarrow |F' = 3\rangle$). Here the $|F\rangle$ states are $^2S_{1/2}$ ground states and $|F'\rangle$ states are $^2P_{3/2}$ excited states of the D2 line. A summary of the laser frequencies used for ^{87}Rb are shown in Fig. 2.4, and for ^{41}K in Fig. 2.5.

The laser light was originally sourced from a pair of lasers from SACHER LASERTECHNIK, each consisting of a Littman–Metcalf external cavity diode laser (ECDL) and a tapered amplifier (TA). An additional home made Littrow configuration ECDL was used for the rubidium repump transition. Over the years the diodes in each of the Littman–Metcalf lasers burnt out, and we found it more convenient to replace the lasers with home made Littrow ECDLs rather than have the original lasers repaired, as this would have been expensive, and they proved hard to re-align ourselves. The SACHER TA on the rubidium laser was replaced with a more powerful, fibre coupled TA from THORLABS (TPA780P20) and the SACHER unit was added to the repump laser. The SACHER TAs are now mounted on heat sinks, with 3D printed covers so that they take up less room than their original cases, and seem to be more thermally stable.

The optical layout of the laser table is shown in Fig. 2.6, and mostly consists of sets of AOMs in front of optical fibres, which take the light to the optical table on which the vacuum chamber sits. The AOMs al-

The Littrow ECDLs used for ^{87}Rb were made by students in Prof. Robert Scholten’s labs at the University of Melbourne, who kindly gave them to us on a long term loan. The Littrow ECDL used for ^{41}K was built by Phil during an undergraduate project, originally for the spinor lab.

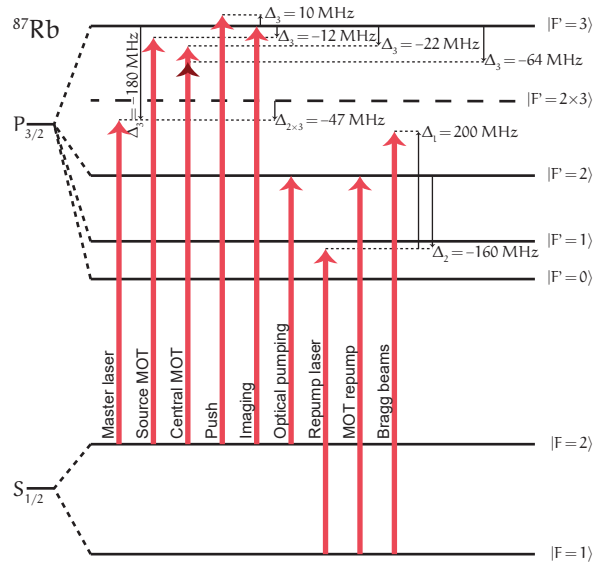


FIGURE 2.4: RUBIDIUM LASER FREQUENCIES.

Typical detunings of the laser beams used for ^{87}Rb are shown, relative to the D2 transitions (not to scale). The central MOT beams are further detuned for PGC, indicated by darker arrow head. The push and imaging beams are generated by the same AOM and split on the vacuum table (see Fig. 2.6). The MOT repump light is generated by separate AOMs for the source and central MOTs for independent control. The Bragg beam will be discussed in Chapter 4.

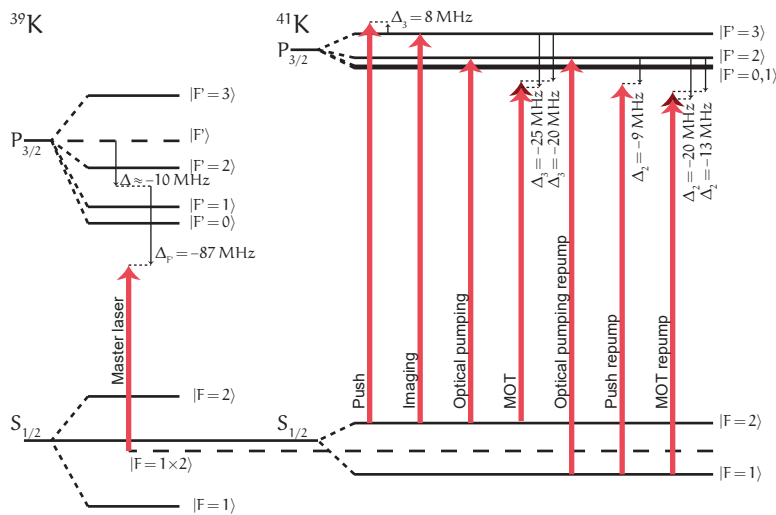


FIGURE 2.5: POTASSIUM LASER FREQUENCIES.

Typical detunings of the laser beams used for ^{41}K are shown, relative to the D2 transition (not to scale). The laser is locked relative to a crossover between the ground states of ^{39}K . The same beam is used for optical pumping and imaging (as with their repump counterparts), and the same AOM also generates the push beam, which is split off on the vacuum table. The darker arrow heads on the MOT frequencies indicate the values used during a compressed MOT stage (see Fig. 2.10).

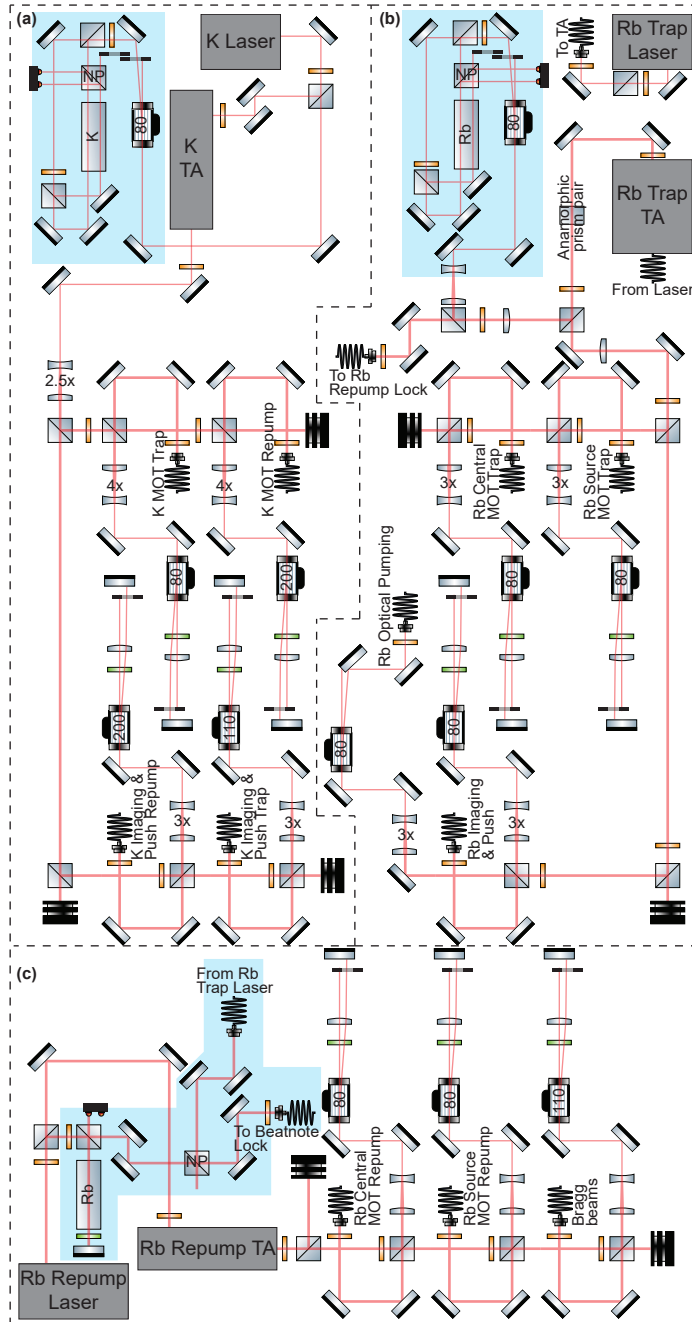


FIGURE 2.6: SCHEMATIC OF THE LASER TABLE.

The laser table is divided into three regions, corresponding to optical elements after each of three lasers: **(a)** the potassium laser, **(b)** the rubidium master laser and **(c)** the rubidium repump laser. Each laser, before being amplified by a TA, has a small amount of light picked off for locking (blue shaded regions, note in **(b)** the locking occurs post-amplification). The amplified beam is then split between a series of AOMs to generate the frequencies required during the experiment, before being coupled into an optical fibre to take the light to the apparatus on the vacuum table. Figure adapted with permission from the thesis of Philip Starkey [285].

low the frequency of the light to be shifted, as well as providing fast shuttering. The majority of the AOMs are in a cat-eye double-pass configuration, which has the advantage of allowing the frequency to be tuned over a wide range without the output beam changing direction, hence maintaining its coupling into the fibre. This is especially important for the central MOT light, which has its frequency ramped over a wide range during the polarisation gradient cooling (PGC) stage of the experiment.

The rubidium and potassium master lasers are locked to atomic transitions using the built in locking circuits of the MOGLABS diode control box (DLC-202 revision 7). We use current modulation on the laser diodes to build up the error signal to lock to. For potassium, we lock to the crossover between the two ground states of ^{39}K , since this is the most prominent feature in the saturated absorption spectrum. We offset the lock point by 87 MHz by passing the light through a single passed AOM before it reaches the potassium vapour cell. There is also an anomalous 10 MHz shift, which is most likely due to the shape and offset of the locking error signal. For the rubidium master laser, we lock to the $|F = 2\rangle \rightarrow |F' = 2\rangle \times |F' = 3\rangle$ crossover signal, again, offset by an AOM, this time by 47 MHz. These lock points were chosen to make the transitions we needed to address accessible by the AOMs we had available, which have resonances centred at 80 MHz, 110 MHz or 200 MHz (see Figs. 2.4 and 2.5).

The rubidium repump laser is locked by referencing it to the master laser, using a beat-note signal. We use a fast photodiode (HAMAMATSU G4176) and microwave amplifiers to collect the microwave-frequency signal, and feed it into a phase-locked loop circuit. The design of this locking scheme is almost identical to that implemented by Martijn for the spinor lab [289]. In our lock, we couple light from both lasers into a fibre, which enters the rack-mount box holding the electronics via a fibre port mounted to the back panel. The photodiode is then held inside the box on a small x-y translation stage, attached to the fibre mount via a miniature cage-rod system. This reduces the amplification requirements, since the signal does not have to pass through such a long, lossy microwave cable. It also makes it easy to re-align the beat-note by fibre-coupling, rather than having to check that the two beams are perfectly overlapped and looking at the beat-note on a spectrum analyser. The repump laser is locked 6.59 GHz off the master laser's lock point, which is 160 MHz red detuned from the repump transition, allowing easy access via a double-passed 80 MHz AOM.

We also use lasers for trapping the atoms via the dipole force, which will be detailed in §2.7, as well as Chapter 3.

2.4 ELECTROMAGNETS

Besides lasers, the other main tool used to interact with the atoms is magnetic fields. We use a range of magnetic field gradients for imparting forces on atoms, e.g., for trapping (§2.6.2) or levitating (§3.1.2), and uniform bias fields for producing quantisation axes, e.g., for absorption imaging (§2.8). The majority of these fields are produced by four pairs of electromagnet coils around the central vacuum chamber (one quadrupole pair and a pair of bias coils in each dimension), as well as the source MOT coils.

Our quadrupole trapping coils, which are used in both a MOT and pure magnetic trap stage, are a pair of coils wired in anti-Helmholtz configuration. These are wound using copper tubing with a square profile. The profile allows the winding density to be high, while the hollow core is used to run cooling water through the coils. These coils sit within the recessed viewports on the top and bottom of the central chamber. Each has a diameter of approximately 120 mm, with an internal bore of 60 mm, and consists of 30 turns of wire. In anti-Helmholtz configuration, they produce approximately $0.8 \text{ G cm}^{-1} \text{ A}^{-1}$. The rubidium source MOT uses a pair of anti-Helmholtz coils, consisting of 46 turns of the same hollow wire (though we do not actually water cool these), with a diameter of 150 mm and internal bore of 60 mm. The potassium source MOT coils have been replaced by four rectangular coils consisting of 20 turns of thinner wire each, to form a 2D MOT, discussed in §2.6.1.

We have a set of coils close to Helmholtz configuration sitting between the quadrupole coils, with similar radial dimensions, consisting of 56 turns of 2 mm square profile wire. These coils provide roughly homogeneous magnetic fields in the vertical (z) direction of 7.9 G A^{-1} . For the horizontal (x, y) directions, we use coils made from computer ribbon cables. This was due to the ‘long’ x axis not having coils pre-installed while the vacuum system was being built. While we could have wound coils *in situ*, it seemed easier at the time to use ribbon cables. I wired the cables into connectors such that current would flow to consecutive cores, forming a 50 turn coil, which can be wrapped around the vacuum chamber and clipped together. These were also used for the side imaging (y) axis, though here it would have been easy to fit a more traditional rigid coil.

The ribbon cable coils have quite a high resistance, due to the large number of turns of quite fine wire, meaning that we can only run $\approx 1.5 \text{ A}$ through them, at about 20 V. Due to the flexible nature of the coils, they must be secured well (by cable ties) to the vacuum chamber mounts to prevent them from moving, which would change the magnetic field profiles produced. While rudimentary, the coils do their job, and I have been able to use them to fine-tune the position of the quadrupole field zero for use in our flat traps (§3.2.1).

The apparatus also contains a large pair of racetrack-shaped coils, which run almost the full length of the vacuum system, from the ^{41}K source MOT to the ^{87}Rb source MOT. These were planned to be used for a magnetic transport scheme devised by Brad, which, as briefly mentioned in §2.6.2 was never successful. These coils contain 280 turns of wire, with a resistance of $2\ \Omega$ and inductance of 25 mH, making it hard to switch them quickly.

2.5 CONTROL OF THE EXPERIMENT

So far, I have described the vacuum system, the lasers, and the magnetic coils, which are the primary pieces of equipment required to trap and cool atoms. Before running through the details of how the experimental sequence proceeds, it is worth mentioning the hardware and software used to control these. We require precise timing and control of a variety of laser beams, magnetic fields and rf fields during each run of the experiment. This is achieved via a mix of commercial and in-house hardware, all controlled by our own custom software suite.

2.5.1 Hardware

Most of our control hardware is one of three types of output devices: *digital outputs*, which can switch between *off* and *on* states (typically being 0 V and either 3.3 V [LVTTTL] or 5 V [TTL] respectively), *analogue voltage outputs*, which can be varied, and *radio frequency (rf) outputs*, which can have their frequency, amplitude and phase set. The rf sources are used for both driving AOMs, as well as rf coils to address the atoms directly, the analogue outputs are mostly used for setting the current in magnetic coils (via home-made current control circuits) and the digital lines are used for switching the state of laser shutters, rf switches on AOMs and triggering other devices.

We use two NATIONAL INSTRUMENTS (NI) boards (PCI-6733 and PCIe-6363) for analogue and digital outputs. The PCIe-6363 also has *analogue inputs* which can be used to monitor signals, such as the current through magnetic coils or photodiode signals. Three SPIN-CORE PULSEBLASTER DDS-300-AWG boards are used for further digital outputs along with rf outputs. Four NOVATECH DDS9ms are used for further rf sources, each having two channels that can be loaded with a table of data to step through during an experiment and two static channels that we can only control the on/off status of via an rf switch. We also utilise two RFBLASTERS, devices developed by Vladimir Negnevitski in the spinor lab, which each provide two dynamic rf channels. A LIGHTCRAFTER digital micromirror device (DMD) is used to shape laser beams to form trapping potentials, which will be dis-

cussed in §3.2.3. This device displays sequences of binary images on an array of mirrors.

In order to keep each of the devices in the lab synchronised during a run of the experiment, we use one of the PULSEBLASTER boards as a *master pseudoclock*, from which all other devices in the lab are referenced. This is achieved using its digital outputs to either trigger devices to start their own internal clock (for the other PULSEBLASTERS and the RFBLASTERS) or step them through their instructions (in the case of the NI and NOVATECH boards), though sometimes these triggers come via an intermediate PULSEBLASTER or NI device. The pseudoclock only sends triggers to devices when they need to update, rather than providing a constant rate clock, limiting the number of superfluous instructions that need to be programmed into each device. Every device used during the experiment is pre-loaded with a set of instructions, then stepped through by hardware, not relying on the timing of the host computer. All clocking devices are referenced to a 10 MHz signal produced by a GPS disciplined atomic clock (QUARTZLOCK E8010). Figure 2.7 shows an overview of how the different devices in the lab are wired and interact with each other.

2.5.2 Software

To program the instructions for each experiment into the hardware, as well as analyse data, we wrote an extensive software suite, mostly in python. The majority of the software was developed by Phil and Chris, though I was heavily involved in the planning and testing stages, and implemented interfaces for several devices in our lab. An overview of the software, known as ‘the labscrip suite’, has been published [286], and the source code is freely available online [291, 292]. The software is now in use in many institutions around the world, and is developing an active community of contributors who are constantly improving the code and implementing new features.

To control hardware during a run of the experiment (which we sometimes refer to as a *shot*), the user writes a simple python script in which each device is represented by an object, with relevant methods to control its state, such as `DDS.setfreq(time, frequency)`. This script can contain variables, which are modified via a graphical interface, `runmanager`. The script is compiled into hardware instructions specific to each device, which are saved in a single hierarchical data format (HDF) file, and queued up in the control program, BLACS, to run. Communication for each device in BLACS is sand-boxed in its own process, to protect against hardware issues freezing the whole program. At the start of an experiment, the hardware instructions are read from the HDF file and programmed into the devices. A start command is sent to the master clock, which then triggers subsequent devices (see §2.5.1). At the end of an experiment, any analogue inputs

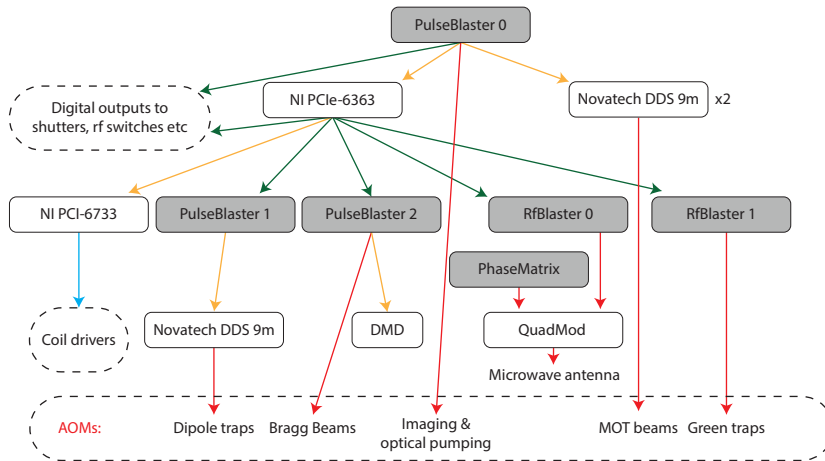


FIGURE 2.7: OVERVIEW OF THE LAB CONTROL HARDWARE.

We use a PULSEBLASTER DDS-300-AWG as our *master pseudoclock* (PULSEBLASTER 0), which is triggered by software to begin the experiment sequence. The master pseudoclock then sends hardware triggers and clock lines to other devices in the lab, including *secondary clock* devices. This ensures that every device remains perfectly synchronised throughout each run of the experiment. Here, devices shaded in grey are referenced to a 10 MHz signal from an atomic clock, and keep track of time themselves (clock devices), while white devices are sent triggers each time their output needs updating. Green lines indicate digital triggers (either signalling for a secondary clock to start, or switching the state of a piece of hardware such as an rf switch on an AOM or a shutter). Yellow lines indicate clock lines. These are simply digital lines that tell connected devices to update their output. Note that the NI PCIe-6363 feeds the clock line from the master pseudoclock to the NI PCIe-6733. Red lines are rf outputs, which are usually amplified before being fed to an AOM or antenna. The blue line indicates analogue outputs, which are used to set the current through each electromagnet. Dashed boxes indicate groups of output devices.

acquired are saved to the same HDF file, as are the images from the camera (via the camera control program, BIAS). The file is then sent on to the analysis program, lyse, where python scripts are run in sequence over both individual runs of the experiment and sequences of multiple runs. Analysis results are also saved to the original file containing the hardware instructions, such that this file contains a comprehensive record of the experiment. This workflow is summarised in Fig. 2.8.

One key feature of BLACS, which I implemented, is *smart programming* of the NOVATECH boards, which was subsequently implemented on other devices in varying forms. These NOVATECH devices are programmed over an RS232 serial connection, with one command sent for each instruction in their table of data to be stepped through. This can be a slow process, taking up to three minutes to program a full table of 32768 time points. Since large sections of the experiment do not change from shot to shot once they have been optimised, we

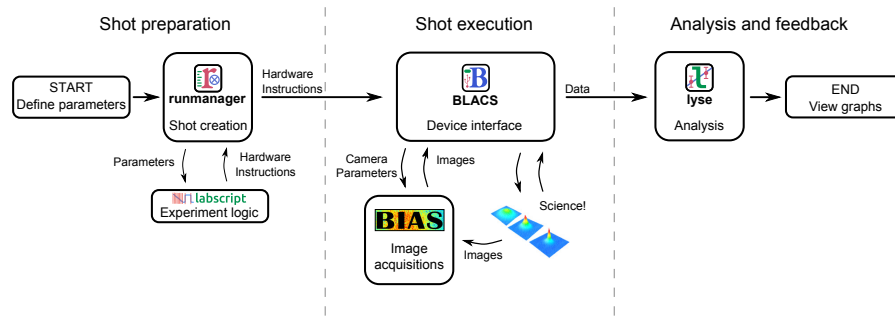


FIGURE 2.8: AN OVERVIEW OF THE LABSCRIPT SUITE WORKFLOW.

Each experiment shot comprises three stages: preparation, execution, and analysis. Arrows indicate how the HDF file for an experiment shot passes between software components of the labscript suite. Only the shot execution stage is coupled to hardware timing, allowing new shots to be created and queued while others are running. Similarly, analysis can be performed on executed shots at any time. Reprinted from Starkey et al. *Review of Scientific Instruments* **84**, 085111 (2013) [286], with the permission of AIP Publishing.

only re-program the points in the table that have changed since the last time the device was programmed. This is possible, since each instruction is programmed to a specific memory address corresponding to its position in the table. It does not matter what order these addresses are programmed in, the table is always stepped through the memory addresses sequentially. This cuts the programming time for most experiments in our lab from minutes down to seconds, with full programming only required after hardware restarts.

I was also responsible for implementing the code to program our LIGHTCRAFTER DMD with a table of images. This built on an incomplete code base that Phil had previously begun writing for a static SLM device. I wrote two interfaces for controlling ZABER motorised translation stages too, one which directly programmed stages via their RS232 serial connection, which could only set a fixed location for each run of the experiment (as there was no way of hardware triggering the programming of these stages) and one to allow hardware timed moves of a pair of translation stages, briefly described in the following subsection.

2.5.3 Hardware timed serial commands

One of the main principles of the labscript suite is that the timing of every event during a shot is determined by the master clock. For some devices, this is simply not possible, if, for example, they can only be controlled by sending them a command over a serial connection, with no memory buffer or triggering mechanism. For most devices, we deliberately ensured that we purchased hardware which could be pre-loaded with instructions, and triggered with a TTL signal.

Some devices, such as the NOVATECH boards, had further capabilities (programming the second two outputs) which we chose to leave as ‘static’ values throughout the experiment. In one particular case, however, we required a work around, to allow pseudo-hardware timing of an otherwise static serial device.

We have several ZABER motorised linear translation stages, which we inherited from an old lab in the school. In order to set up a retracting mirror and objective lens, described in §2.8.4, we needed to synchronise the movement of a pair of translation stages mid-experiment. Rather than purchase new stages, I came up with a scheme to achieve this with what we had. The two stages were connected (via a USB to serial converter) to a RASPBERRY PI microcomputer, which ran a simple python program. This looked for a signal on one of the RASPBERRY PI digital input pins to know when to move the stages, using the following basic logic:

- The program was set to experiment mode by a message from BLACS over the network, sending the desired position of the stage holding the imaging objective lens.
- It then waits for a signal on one of the RASPBERRY PI digital inputs to go high, indicating the time in the experiment when the stages should move.
- On this signal, the stage holding a mirror above the vacuum chamber window is retracted.
- Once a command to the mirror stage has confirmed that it is in the retracted position, the second stage, with the objective lens, is lowered into the recessed window, previously blocked by the mirror, to the requested focus position.
- The program then waits for the digital input signal to go low again, indicating that the experiment is over, retracting the lens before restoring the mirror position.

In this configuration, the stages can be moved during the experiment with reasonable temporal precision (there is presumably some jitter on the timing due to processor cycles in both the RASPBERRY PI and the ZABER stages’ internal controllers). This is sufficient for our application, as the stages can be moved at times when their positions are not relevant to the experiment, such that they are ready for when they are needed later.

2.6 LASER COOLING AND TRAPPING

Now that I have discussed the main hardware and software in the lab, I will describe how we use this to initially trap and cool atoms as they begin their journey from hot thermal sources to BEC. In nearly every

I will only briefly cover the theory of laser cooling and trapping here. For a far more detailed explanation, please refer to books by Metcalf [293] or Foot [294].

cold atom apparatus, including this one, this begins with a magneto-optical trap (MOT).

The 3D MOT uses a combination of optical and magnetic fields, consisting of three orthogonal pairs of counterpropagating, circularly polarised laser beams, overlapped with a quadrupole magnetic field gradient. The laser beams are red-detuned from the zero-field resonance condition, such that photons will preferentially be absorbed by atoms moving towards a counterpropagating laser beam (due to the Doppler effect), or at a spatial position where the field gradient Zeeman shifts the atom onto resonance with the laser beam of appropriate circular polarisation. In these conditions, the absorbed photon transfers its momentum onto the atom, and the corresponding spontaneous emission gives the atom a second momentum kick, in a random direction. After many of these scattering events, the net result is to remove kinetic energy (due to Doppler shifted absorptions), and push atoms towards the quadrupole centre (due to Zeeman shifted absorptions). Thus the MOT produces a spatially localised, cold cloud of atoms.

Temperatures in a MOT are typically limited by the linewidth of the atomic transition being driven. Once the atoms are cooler than the so-called *Doppler limit*, the absorption is no longer velocity selective, as the finite transition linewidth allows photons from all directions to be absorbed. To get colder, we use polarisation gradient cooling (PGC), which takes advantage of polarisation dependent light shifts of the atomic energy levels. Here, the magnetic field gradient is switched off, and the laser beams are detuned further from resonance. The configuration of counterpropagating circularly polarised beams causes polarisation gradients, which produce spatially dependant light shifts. This leads to a process known as *Sisyphus cooling*, where atoms give up kinetic energy as they move up a potential hill formed by the spatially dependant light shifts. The atoms then scatter a photon, optically pumping them to a lower energy state, where they begin the process of climbing the hill again. This process is still limited to $\approx 50 \mu\text{K}$, well above $\approx 100 \text{ nK}$ BEC transition temperatures. Additionally, the atomic number density achieved is much lower than that required for condensation (§1.2.2).

To cool beyond this limit, and increase the density, we transfer the atoms to a purely magnetic trap. We use the same quadrupole configuration as in the MOT stage, with a higher field gradient. If the atoms are spin polarised in a low-field seeking state, then they will experience a restoring force toward the magnetic field zero at the centre of the trap. By increasing the magnetic field gradient, the oscillation frequency of atoms in the trap increases, as does the collision rate. This allows fast rethermalisation of the cloud, which is important for the next stage of cooling. In this next stage, evaporative cooling is performed by selectively removing the highest energy atoms, resulting in

a net reduction of energy, and hence lower temperature. This process is typically performed by coupling atoms at a given energy, set by the spatially varying Zeeman splitting, to an anti-trapped (high field seeking) state by an rf field. The resonance of the rf can be tuned over time to be closer to the field zero, to continually address the hottest atoms in the tail of the Gaussian thermal distribution.

The remainder of this section will describe the configurations and sequences used in our apparatus to take atoms from the ampoules sitting in each source section of the vacuum chamber, through to a magnetic trap containing both ^{87}Rb and ^{41}K , and the subsequent evaporative cooling process.

2.6.1 Cold atomic sources

Each atomic source is heated to around its melting point, resulting in a partial pressure in the source chambers of around 10^{-6} Torr. A MOT is loaded from this background vapour in the glass tube between the oven and the UHV section for each species. The original design was to then magnetically transfer atoms from these MOTs into a centrally located double species MOT in the UHV section, using a large pair of racetrack-shaped coils in quadrupole configuration. It became apparent that this would be rather complicated to get working, in part due to the high inductance of the coils, as well as the alignment requirements. This also required magnetic trapping of the atoms in the source chamber, which, due to the thermal background source, would have very short lifetimes.

Rather than pursuing this, a simpler solution (taken by many other groups) was used, which was to push atoms out of the source MOTs with a near resonance laser beam. To transfer atoms out of the ^{87}Rb source MOT, we use a pulsed pushing beam, around 10 MHz blue detuned from resonance. We sequentially turn off the MOT light, then turn on the push light for 1 ms. We then turn the MOT light back on and allow it to reload for 12 ms before repeating (see inset of Fig. 2.10). Although the ^{87}Rb source MOT is in a 3D configuration, the ^{41}K source MOT is in a 2D configuration due to trouble optimising the alignment of a 3D MOT.

This 2D MOT configuration involved replacing the quadrupole coils with four racetrack shaped coils, and using two pairs of counter propagating beams, orthogonal to the axis of the cell [295]. The result is a line of laser cooled atoms, free to move along the axis. We find that the central ^{41}K 3D MOT loads significantly faster when this source is turned on than it would from background atoms, and faster still if a push beam is used along the axis. We typically use a continuous push beam, consisting mostly of light ≈ 10 MHz red detuned from the repump resonance, with a small amount of light ≈ 8 MHz blue detuned from the cooling transition resonance.

The potassium source MOT was initially aligned using ^{39}K , since it has a much higher natural abundance than ^{41}K , so the fluorescence signal was stronger. This required swapping the configuration of the laser lock and MOT AOMs while the alignment was done. Four independent beams were used, rather than two retro-reflected beams since the cell is slightly curved and seemingly birefringent, deforming the beam by the time it has made a single pass through the cell. Likewise, the rubidium source consists of six independent beams. The position of the 2D MOT relative to the differential pumping tube in the vacuum chamber can be adjusted by tuning the balance between the currents in opposing coils. We found that to form a MOT centred well on the chamber, the coils had to be quite miss-matched, most likely due to the coils not being perfectly centred around the cell, but possibly also due to stray magnetic fields from the nearby ion pumps.

2.6.2 *The dual species central MOT and magnetic trap*

The central MOT can trap both rubidium and potassium simultaneously. Both wavelengths are overlapped before being split into the six beams that form the MOT, shown in Fig. 2.9. Since the frequency spacing between excited states on the D2 transition of ^{41}K is the same order of magnitude as the natural linewidth of the transitions, we detune our MOT beams below the entire excited state manifold (see Fig. 2.5). Since we are driving many transitions, rather than just the closed cycling transition, the depumping rate to the $|F = 1\rangle$ ground state is much higher. To compensate for this we must use a significant amount of repump light (around a 2:3 ratio of repump to cooling), effectively using both transitions for laser cooling. This means that we must use the correct polarisation in both cooling and repumping beams, whereas in the rubidium MOT the repump light does not play a role in the cooling process, so its polarisation is not important.

To achieve this, we combine the potassium cooling and repump MOT beams on a non-polarising beam splitter, and send one output to the source MOT and one to the central MOT. One major disadvantage of this arrangement is that we do not have independent control over the intensity or frequency of the light for the two MOTs. An alternative method of combining the beams could be to use two double passed AOMs in series, with the first generating the correct frequency for the cooling transition, and the second shifting this by the 254 MHz ground state hyperfine splitting to generate the repump light, while allowing the zero-order to pass through for cooling light. Other groups combine their beams on non-polarising beam splitters, then pass the beam through a TA, meaning that the output of the second port of the beam splitter does not have a significant amount of wasted light, though this can lead to wave mixing effects in the TA,

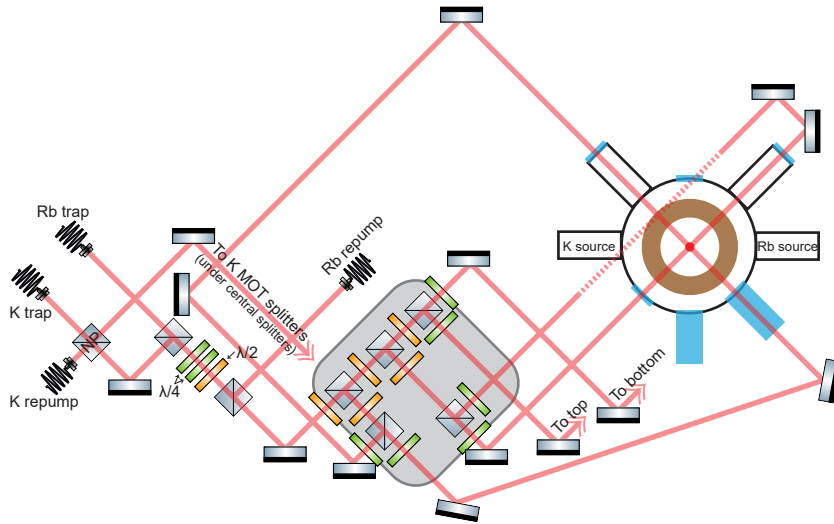


FIGURE 2.9: THE DUAL SPECIES MOT LAYOUT.

Trapping and repump light for potassium are combined on a non-polarising beam splitter, before being combined with rubidium trap light of opposite (linear) polarisation on a polarising beam splitter. A dichroic waveplate is formed by a series of two multi-order $\lambda/4$ (green) and one multi-order $\lambda/2$ (yellow) waveplates, which rotates the polarisation of the potassium light to match the rubidium light. Some rubidium repump light is added on a polarising beam splitter, which also acts to clean up the polarisation of the light which has passed through the dichroic waveplate. The combined light then passes through a series of polarising beam splitters to form six independent MOT beams, with zero-order $\lambda/2$ waveplates to control each splitting ratio. Note that many mirrors, as well as the telescopes in each of the six beams, have been omitted for clarity, and the drawing is not to scale.

creating extra frequencies, reducing the total power available, and in some cases, accidentally driving atomic transitions in the ^{87}Rb [296].

The potassium light is then combined with the rubidium cooling light on a polarising beam splitter. We rotate the polarisation of the potassium light to match the rubidium polarisation by using a homemade ‘magic’ waveplate. This device consists of two THORLABS multi-order quarter waveplates and one multi-order half waveplate, all designed for 780 nm. With their fast axes aligned, the combined waveplates have a minimal effect on the polarisation of the 780 nm rubidium light, while are approximately a half waveplate at 767 nm for potassium. The rubidium repump light is then combined on a second polarising beam splitter, which also acts to clean up the polarisation of the other beams following the waveplates.

The combined MOT beams enter an array of polarising beam splitter cubes, where zero-order half waveplates are used to control the split of power between each of the six beams generated, affecting the potassium and rubidium beams almost equally. Zero-order quarter waveplates are used to form circularly polarised light before each beam is expanded and enters the vacuum chamber. To align the MOT

well, we ensure that each beam comes back through the beam expander of the opposing beam, and opposing beams are well overlapped all the way back to the beam splitters. The balance between powers in counterpropagating beams were adjusted to maximise the number of rubidium atoms remaining after a PGC stage, during which the magnetic field is switched off and the MOT beams are detuned further from resonance. The potassium beams were then overlapped with the rubidium beams by coupling one of the rubidium MOT beams into a fibre, then using mirrors at the output of the potassium fibres, coupling each potassium beam into the same fibre. Once a potassium MOT was seen in the central chamber, it was fine tuned by making small adjustments to the potassium beam position before the combination with rubidium light, to overlap the MOT with the rubidium MOT and maximise the fluorescence seen on the camera.

Despite being much better than multi-order waveplates, the zero-order half waveplates used still have slight differences in their behaviour at 767 nm compared with 780 nm. The polarising beam splitter cubes may also behave slightly differently for the two wavelengths. Due to this, the potassium MOT is not as well optimised as the rubidium MOT, and achieves lower atom numbers. This could be improved by using dichroic waveplates, designed to independently control the two wavelengths. Typically, we can load in excess of 4×10^8 ^{87}Rb atoms (the images are too saturated to get reliable atom number estimates in the MOT) in 8 seconds, or $\approx 10^5$ ^{41}K atoms in 20 seconds. The MOT alignment described here was in place for several years after first setting up the apparatus, however, more recently, we have swapped to a retro-reflected configuration, the motivation for which will be discussed in §2.8.4. This involved replacing the MOT beams that enter from the top, and the two side windows closest to the rubidium source with retro-reflecting mirrors and a quarter waveplate to maintain the correct polarisation for the reflected beam.

We find that having the MOTs for both species on at the same time results in lower atom numbers, particularly for potassium. We suspect that this may be due to light assisted collisions between the two species. We tried two different approaches to overcoming this problem. First, we used an additional laser beam to push the rubidium MOT slightly away from the potassium MOT. We opted to use our optical pumping beam for this—the imaging beam may have worked better, but it is controlled by the same AOM as the push beam, so would have required rearranging the optical set-up on the laser table to allow independent control. The potassium atom number increased with increasing ‘displacement beam’ power, while the rubidium atom number only started decreasing when the power was high enough to start destroying the MOT.

An alternative scheme, which seems to result in better loading of both species, was to load the MOTs sequentially, following a method

the $|2, 2\rangle$ state before ramping up the magnetic field gradient to trap both species.

The $|2, 2\rangle$ state is used for magnetic trapping both species as there are no spin-changing collisions allowed between ^{87}Rb & ^{41}K atoms in these states [299]. Additionally, the Paschen–Back effect limits the ability to trap ^{41}K in the $|1, -1\rangle$ state [300].

2.6.3 Microwave-induced evaporation

Once the atoms are loaded into the magnetic trap, the field gradient is increased to around 100 G cm^{-1} , and evaporative cooling is performed on the rubidium. When loading both species, we choose to force the evaporation of only the rubidium atoms, since it has a much higher initial atom number than potassium, and rely on inter-species collisions to provide sympathetic cooling of the potassium. Since ^{87}Rb and ^{41}K have the same Zeeman structure, we use the 6.8 GHz hyperfine transition between the ground states of rubidium to avoid transitions in potassium [299].

A half-wave dipole antenna was made using copper from the core of a coaxial cable, and trimmed to a length that reduced the back reflections measured via a microwave circulator at 6.8 GHz. Microwaves were generated by a PhaseMatrix FSW-0010 synthesiser, running at 7.034 GHz, modulated by single sideband quadrature amplitude modulation, allowing the microwave frequency to be tuned around the 6.834 GHz resonance of ^{87}Rb . This is achieved using a POLYPHASE MICROWAVE am4080n quadrature modulator, driven by two channels of an RFBLEASTER direct digital synthesizer (DDS). Our microwave modulation set-up was developed in conjunction with the spinor lab, and so is almost identical to that described in Alex’s thesis [290].

We linearly sweep the microwave frequency from 53 MHz detuning from the ^{87}Rb resonance to 40 MHz detuning in 1.3 s, then to 16 MHz detuning in a further 2.66 s. For a pure rubidium sample this takes the atom number and temperature from approximately 4×10^8 atoms at $150\text{ }\mu\text{K}$ to 8×10^7 atoms at $70\text{ }\mu\text{K}$. For dual species loads, we have found it hard to optimise, with the ^{41}K number appearing to decrease during the process. We attribute this to imperfect optical pumping of ^{87}Rb , and a low initial ^{41}K atom number. If the ^{87}Rb polarisation is 99% pure, but we have three orders of magnitude less ^{41}K to begin with, then for every ^{41}K atom there will be ten ^{87}Rb atoms in a state with which it can undergo spin exchange collisions. This is where my involvement with ^{41}K ended—Phil attempted to load ^{41}K through to a pure dipole trap, sacrificing all ^{87}Rb during a faster evaporative cooling stage, to generate cold samples containing only ^{41}K , however never managed to achieve more than a few thousand atoms, making it hard to perform any experiments on them. We have not yet produced ^{41}K BECs, or trapped cold ^{41}K atoms alongside ^{87}Rb BECs (an

original goal of the apparatus was to use cold atoms of one species to interact with a BEC of the other, while being manipulated by lasers at wavelengths only seen by one species).

2.7 OPTICAL DIPOLE TRAPS

Evaporating to temperatures approaching tens of microkelvin in a quadrupole magnetic trap becomes impossible due to Majorana spin flip losses [301–303]. To overcome this limitation, we use a red detuned far off resonant optical dipole trap [304], offset from the magnetic field zero following a similar technique to Lin et al. [305] to form a *hybrid* magnetic and optical trap.

Over the years we have had several different configurations of dipole traps. Each of these had common features, such as the way in which we aligned the optics and the sequence for initially loading atoms into them. Here I will describe these common aspects first, before briefly commenting on the various configurations used.

2.7.1 Dipole trap alignment

To pre-align a dipole trap onto the magnetically trapped atoms, we first use an iris to aperture down the MOT beam that it propagates along, while watching the MOT on a camera. We move the iris such that the MOT remains in approximately the same position in the central chamber. This results in the smallest possible beam which passes near the centre of the MOT. We then overlap the dipole beam on top of this apertured beam on both sides of the vacuum chamber (i.e., entrance and exit of the beam). Removing the aperture, and leaving the dipole beam on at full power, we run experiments through to the end of PGC, and image the atoms after a short drop time. Provided that our pre-alignment is close enough, atoms can usually be seen localised in the beam, revealing its position. It can then be adjusted to coincide with the centre of the magnetic trap based on the images. We then swap to looking at atoms that have been evaporatively cooled in the magnetic trap to get closer to the final desired position, just below the magnetic field zero.

The final alignment is achieved by manually adjusting the beam position in one direction at a time, while plotting the atom number against the position of fits to the cloud after a short time of flight. The position is optimised by iterating between the horizontal and vertical directions. Firstly scanning over the horizontal direction, a maximum in atom number is usually seen when the beam is aligned with the vertical axis of the magnetic trap, provided that beam is not at the vertical position of the field zero. Scanning over the vertical direction then results in a double-peaked distribution of atom number as a function of dipole trap position. This is due to the loss of atoms when

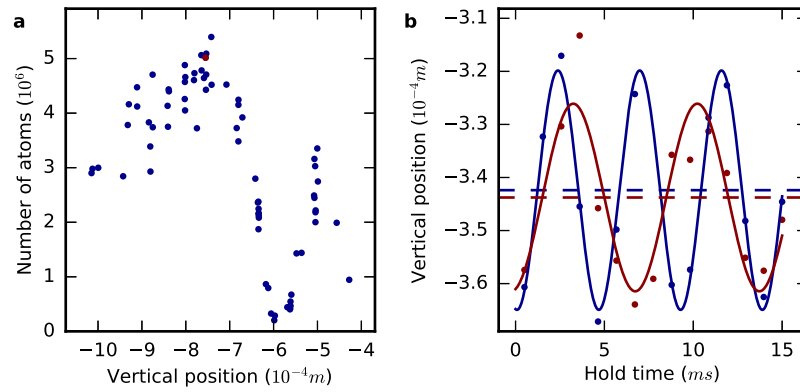


FIGURE 2.11: ALIGNMENT OF OPTICAL DIPOLE TRAPS.

(a) Initially the vertical alignment of each beam is adjusted to maximise the atom number. This is achieved by plotting the atom number against the vertical position of the cloud, both extracted from a Gaussian fit to the OD image. The final position (red point) is chosen to have a position as close to that with the maximum atom number obtained in the scan, which is typically around one beam waist below the magnetic field zero (where a sudden loss of atoms occurs, around $-6 \times 10^{-4}m$ here). (b) The crossing of two dipole traps (red and blue) is checked by measuring the centre of sloshing motion (dashed line) in each beam individually. As the beam is snapped to a higher amplitude to minimise gravitational sag, the initial motion of the atoms is upwards, before oscillations develop at the new trapping frequency. Differential drives on the final mirror mounts of each beam can be used to fine-tune the positions to minimise the difference. Note that vertical positions in each figure are relative to an arbitrary region of interest (ROI) chosen around the images in each case.

the dipole trap is too close to the magnetic field zero, increasing the rate of spin flip loss as it pulls more atoms to the zero region. The trap is then placed at the local maximum corresponding to a position below the field zero. Typical data from this process are shown in Fig. 2.11a.

In crossed beam configurations, a technique was developed to fine tune the overlap of the beams. Once the crossing was sufficient to localise atoms without a magnetic field gradient, the power in the beams are reduced, evaporatively cooling the atoms. *In situ* side images can then be used to guide adjustments to the beam positions to maintain the symmetry of the trap. The final touches are achieved by then turning off one beam, while switching the remaining beam to full power. By varying a hold time after this, and looking at *in situ* side images, oscillations in the vertical position of the trapped atoms are revealed. Assuming that the beam power is high enough to minimise gravitational sag, the centre point of these oscillations reveals the height of the dipole beam. This ‘sloshing’ measurement is then repeated for each beam, and fine adjustments are made until the heights are as close as possible. Typical data from this process are shown in Fig. 2.11b.

2.7.2 Loading the dipole trap

The load of atoms into a hybrid trap is achieved by lowering the magnetic field gradient of the quadrupole trap at the end of the microwave evaporation ramp. The gradient is lowered over 1.7 s to a vertical component of around 15 G cm^{-1} , where it just holds ^{87}Rb atoms in $|2, 2\rangle$ against gravity. The microwave field is ramped from the end point of the microwave evaporation stage (16 MHz detuned) to a detuning of 6 MHz over the first half of the field decompression, then remains at this final value until the field gradient has stopped ramping. During this process the atoms are cooled further, resulting in around 2×10^7 atoms at $15 \mu\text{K}$ in the hybrid magnetic and optical trap.

If there are stray magnetic fields present, the quadrupole field zero will move as the field gradient is ramped down, making the transfer less efficient (and sometimes even dragging the field zero through the atoms in the dipole trap). To minimise the movement of the zero, we scanned the current through bias fields in three orthogonal directions (one at a time, while the other two directions are held at the latest 'best' value), while observing the resulting atomic cloud position for a range of field gradients. The field that resulted in the least movement of the trap was chosen for each axis. For the horizontal and vertical directions in the side imaging plane, this could be achieved using only the quadrupole trap, without the dipole beam, so long as we avoided field gradients low enough that the cloud began to sag under gravity. For the third dimension, along the side imaging axis, we took advantage of the dipole beam being at 45° to the camera. By loading the hybrid trap, we were able to see the effect of the atoms being pushed along the dipole beam by the magnetic trap moving in an otherwise undetectable direction. The dipole trap was also used to refine the horizontal direction in the plane of the camera, to enable lower field gradients to be reached without the atom position sagging, since this is where the measurement is most sensitive.

2.7.3 Dipole trap configurations

As previously mentioned, we have used several different configurations of dipole beams. Here I will outline the main configurations used and the reasons for (and against) using each.

2.7.3.1 Original single beam hybrid trap

Our first BEC was formed in a single beam hybrid trap, using an IPG YLR-10-1064-LP 10 W, 1064 nm fibre laser, which was passed through an AOM for amplitude control, then focused to a waist of around $35 \mu\text{m}$. This beam entered the vacuum system through the window opposite the square science chamber, overlapped with the MOT beam

Note that this first BEC was formed using a slightly different procedure leading up to the dipole trap than described in the previous sections. Instead of optical pumping to the $|2, 2\rangle$ state before magnetic trapping, we simply turned off the repump light at the end of the PGC stage, to allow the majority of atoms to be depumped to the $|1, -1\rangle$ ground state. We then used rf evaporation, via an antenna formed by a single turn of copper wire with a diameter of around 4 cm placed on the top window of the central chamber.

using a short pass dichroic mirror. We forced evaporative cooling in this hybrid trap by exponentially ramping down the laser power. This produced samples with around 10^5 ^{87}Rb atoms in the $|1, -1\rangle$ ground state at 200 nK, with around 15% of atoms condensed, an example of which is shown in Fig. 2.12. After switching to the $|2, 2\rangle$ state, and making further optimisations, we were able to create almost pure condensates of 10^5 atoms in this trap.

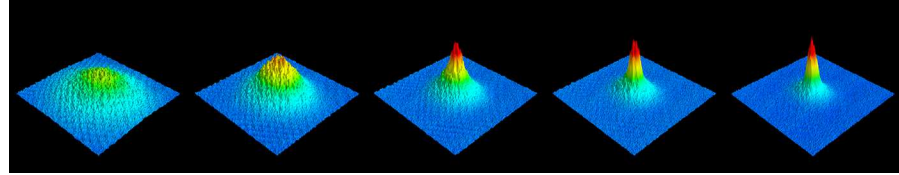


FIGURE 2.12: THE FINAL STAGES OF EVAPORATION TO OUR FIRST BEC.

The dipole power is lowered to successively lower values for a series of experiments (left to right), resulting in a BEC with about 15% of the 1×10^5 remaining atoms condensing.

We performed some preliminary experiments with this $|2, 2\rangle$ BEC, looking at wave mixing. There was an idea that we could extend on previous work on four wave mixing of BECs [306] to see higher order mixing, in particular six wave mixing. I installed three Bragg beams, one coming from each source end through the differential pumping tubes, and one through the bottom window of the central chamber. Some preliminary experiments were then performed by Phil, Mikhail, Chris & I, but we did not see the signature of six wave mixing that we'd expected (see Fig. 2.13). The experiments were put on hold while Chris ran further simulations, and in the mean time, we were keen to move on to make dual species BECs in the science chamber for other experiments we had planned. Chris found that the results we'd seen were in fact consistent with his GPE simulations, which he interpreted as an off-resonant four wave mixing process, arising due to fluctuations in the coupling between momentum states. We are unsure exactly why we do not see the six wave process, which was predicted by earlier calculations. It is possible that these calculations were too idealised, and did not take into consideration density variations, and that low levels of noise cause the off-resonant mixing to dominate over the six wave process.

At the time we had not yet fully developed a plan for getting the atoms to the science chambers, where we planned to carry out experiments, a distance on the order of 30 cm from the central magnetic trap. We were also awaiting the arrival of a more powerful, narrower linewidth laser from KEOPSY, to use for dipole traps, but wanted to make a BEC to ensure that our vacuum was sufficient. One early plan was to use this single beam trap to form a BEC (or cool atoms very close to BEC), then load the atoms into a travelling optical lattice formed by the new laser, in a similar fashion to Schmid et al. [307].

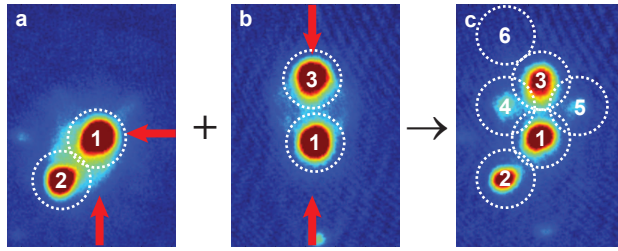


FIGURE 2.13: ATTEMPT TO OBSERVE SIX WAVE MIXING.

We attempted to observe a six wave mixing process by applying two sequential Bragg pulses to a stationary BEC, with lasers pulsed on the axes represented by arrows in (a) and (b). Here the time-of-flight distribution shows the momentum states produced by each pulse. (c) When both pulses are used, wave mixing occurs, producing states 4 and 5, but not the predicted state 6.

Once the KEOPSYS laser arrived, we developed a new plan involving only a single beam which could be loaded in the central chamber, then have its focus moved to drag atoms to the science chamber, and so this IPG trap was dismantled.

2.7.3.2 Transport of atoms to the square science chamber

We formed a new dipole trap—the ‘transport beam’—using the KEOPSYS CYFL-MEGA-20-LP-1064-AM0-ST0-0M1-B208-C4 1064 nm fibre laser. Approximately 12 W was split from the output of the laser using a polarising beam splitter, and passed through an AOM for amplitude control of the beam. The diffracted order was then passed through a lens system based on Leonard et al. [308], with a single OPTOTUNE EL-10-30-NIR-LD focus tunable lens. When current is passed through an internal coil in the OPTOTUNE device, the gel lens is deformed, changing its focal length.

The beam was overlapped with a MOT beam on a short-pass dichroic mirror, entering the vacuum system through the end of the square science chamber, as shown in Fig. 2.14. The system was configured such that when no current was applied, the beam focussed just behind the magnetic trap, with a waist of 60 μm . This allowed a small current to be applied to fine tune the focus of the beam onto the magnetic trap for loading atoms. Applying higher currents caused the focus to shift towards the square cell, while maintaining a constant waist. The alignment of this system was critical to ensure that the focus of the dipole trap moved smoothly along the propagation path of the beam, without forming aberrations or moving off axis. The OPTOTUNE lens was mounted such that light passed through it vertically, to minimise any astigmatism caused by the lens material sagging under gravity.

It is worth noting that prior to the publication of the work of Leonard et al. [308] we had been independently attempting to use the OPTOTUNE lens for the transport of our atoms. Our original at-

This is approximately the point in this apparatus building story where we had to pack up the lab to move to New Horizons. We had made BEC in the first single beam trap, and replaced it with the first iteration of a beam going through the tunable lens. We had even seen very short (to the edge of the camera field of view and back) movements of the atoms in this transport beam. Due to initial teething problems in the new lab space, it was almost a year before we had the machine up and running to this stage again.

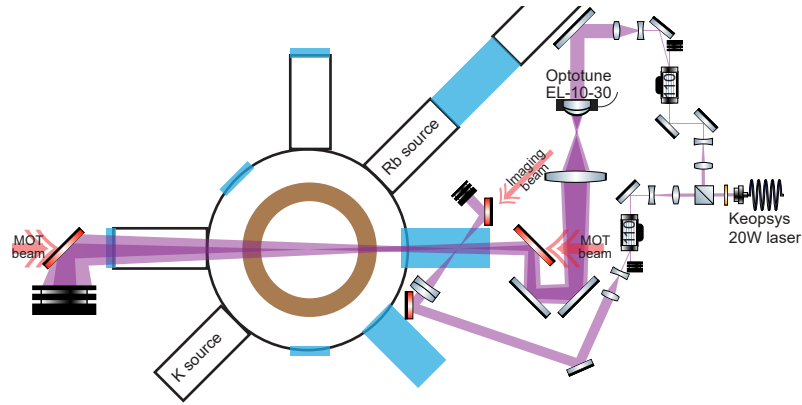


FIGURE 2.14: LAYOUT OF THE TRANSPORT DIPOLE TRAP.

The optical layout of the transport beam is shown, along with the square cell crossed dipole trap. When current is run through the OPTOTUNE lens, the focus shifts from the central chamber to the centre of the square cell. The cross beam comes in from close to the round cell, on the same axis as the square cell side imaging (see Fig. 2.16). Note that several mirrors have been omitted, with the AOMs and lens systems at different heights to the vacuum chamber. The OPTOTUNE lens is mounted such that the beam comes up through it, so that the lens does not sag asymmetrically.

tempts involved configurations that tightened the spot size of the focus throughout the transport, which seemed to result in issues with increased atomic densities heating the atoms. The shorter focal length after the initial load of atoms into the dipole beam from the magnetic trap may however help to keep the atoms localised closer to the focus of the beam, improving the transfer to a crossed beam trap in the science chamber. We adopted the configuration of Leonard et al. due to its simplicity.

To load this transport beam, we first used the usual hybrid load technique in §2.7.2, before completely turning off the magnetic confinement. After magnetic trap is completely extinguished it was hard to determine the atom number, since the cloud spreads out along the dipole beam further than the field of view of our camera. This made it hard to estimate the transport efficiency. We then transported the atoms by ramping the current through the OPTOTUNE lens using a smooth sinusoidal function, over two seconds.

When initially attempting to transport the atoms, we came across a complication. We used return trips, where the atoms were moved a short distance, then returned to their initial position, to test the transport process. Performing sequentially longer return trips from the central chamber, we found a sharp drop off in the surviving atom number at a certain distance, much shorter than the end of the square cell. The position appears to correspond to the flange connecting the science chamber to the central chamber. We believe the problem has to do with magnetic fields, with one possible source being the bolts attaching the flange, which were measured with a gauss meter to be

highly magnetised (presumably due to their proximity to the quadrupole coils). Another possible explanation is that the glass-to-metal seal could contain a material that acts as a mu-metal, creating a region of almost zero magnetic field, leading to Majorana losses.

We found that transporting the atoms in lower m_F states was more efficient, which further supports the idea that the issue was due to magnetic fields. An adiabatic rapid passage microwave sweep [301, 309–312] was used to transfer ^{87}Rb from $|2, 2\rangle$ to $|1, 1\rangle$. While further transfers could be performed to place the atoms in $|2, 0\rangle$ or $|1, 0\rangle$, where the atoms would be completely insensitive to stray field gradients, this was found to be unnecessary, as the small loss of each transfer seemed to be comparable to the gain made in efficiency passing the flange.

2.7.3.3 Square cell crossed dipole trap

The transport beam had only weak trapping in the axial direction, so atoms were spread out far beyond the field of view of the square cell imaging systems (discussed in §2.8). Once the atoms were in the science chamber, a cross dipole beam was turned on to localise them. The remaining power split off from the output of the KEOPSYS laser was passed through a second AOM to produce this beam. To maintain optical access through the side of the square cell, this beam was placed at approximately 45° to the transport beam axis, coming from close to the round cell, as shown in Fig. 2.14. This beam required some careful measurements, and a lot of patience to align (plenty of power in the beam helped too!), as there is no MOT in the square cell to use for pre-alignment.

A third dipole beam was also used, with an elliptical profile, which we had planned on using for 2D confinement experiments. The use of this 2D beam appeared to help to get more atoms into the crossing region, and aided the evaporation. Attempts were also made to add a quadrupole magnetic trap to assist in the radial confinement, which was also used for some of the first attempts to create a 2D trap, discussed in Chapter 3.

When the atoms were evaporated by lowering the intensity of the dipole beams, less than 10^4 atoms were left in the BECs that we were able to form. The shot-to-shot stability was poor in the square cell, and the position of the transport beam would drift throughout the day, presumably due to the OPTOTUNE lens warming up. While the lens issues may have been overcome by upgrading to a newer model with a built-in temperature sensor and a calibrated controller, we felt that the low atom number, in part due to the anomalous magnetic issues during transport, was a major bottleneck to getting higher atom numbers in the condensates, and so it was decided that we would attempt to run our experiments in the central chamber instead.

2.7.3.4 A crossed dipole trap in the central chamber

The primary reason to use the science chamber was the good optical quality of its walls for imaging. We had a custom objective lens made, which was designed to correct for the square cell's glass to achieve a resolution below $1\ \mu\text{m}$. In the central chamber, it is near impossible to achieve this resolution, as the closest windows to the atoms, the top and bottom windows on the central octagon chamber, are around $6\ \text{mm}$ thick. The windows are recessed though, so sit only $12.5\ \text{mm}$ from the atoms. With these parameters, our objective lens should still be able to resolve down to around $2\ \mu\text{m}$. We also have a commercial long working distance objective, which when bench tested through similar glass to the windows could resolve lines on a USAF 1951 target down to $2\ \mu\text{m}$. We decided that this would be sufficient for imaging vortices after short expansion times, and so we abandoned the square cell and swapped to a configuration based entirely in the central chamber.

We also ran into trouble with this crossed dipole trap, only months after the potassium source leak (§2.2.3), when our KEOPSYS laser died. Luckily, once again, Prof. Robert Scholten from the University of Melbourne saved the day, loaning us an identical laser while ours was repaired.

The transport dipole beam was removed, and replaced with a crossed dipole trap with static lenses, shown in Fig. 2.15. Each beam has a waist of around $70\ \mu\text{m}$, and differ in frequency by $200\ \text{MHz}$ to prevent forming a standing wave interference pattern, by using opposite orders of the AOMs used for amplitude control. The dipole beams were aligned independently, following the procedure as described in §2.7.1, before the cross was optimised using the sloshing technique.

In this trap, we are able to create ^{87}Rb BECs with around 2×10^5 atoms. To achieve this, we ramp the power in both beams together, exponentially decreasing the power provided to the AOMs over $3\ \text{s}$, with a time constant of $0.8\ \text{s}$. During the first $0.5\ \text{s}$ of this ramp, we also reduce the remaining magnetic quadrupole field to zero. This is the final configuration which was used as a starting point for the creation of uniform BECs discussed in Chapter 3.

2.8 IMAGING

The primary method for probing BECs, and cold atoms in general, is to take an image of their spatial distribution. The most common method for this is absorption imaging, whereby resonant light passes through the atoms, and their shadow is imaged onto a camera. Other common methods include fluorescence imaging, where the light scattered off the atoms is collected, and phase contrast methods, where the phase shift of off-resonant light passing through the atoms is measured. As we had several configurations of dipole traps in differing locations in the vacuum system, we also had several imaging systems, though all used the basic absorption imaging technique. Here I will briefly discuss the principles of absorption imaging, before discussing the specific configurations used.

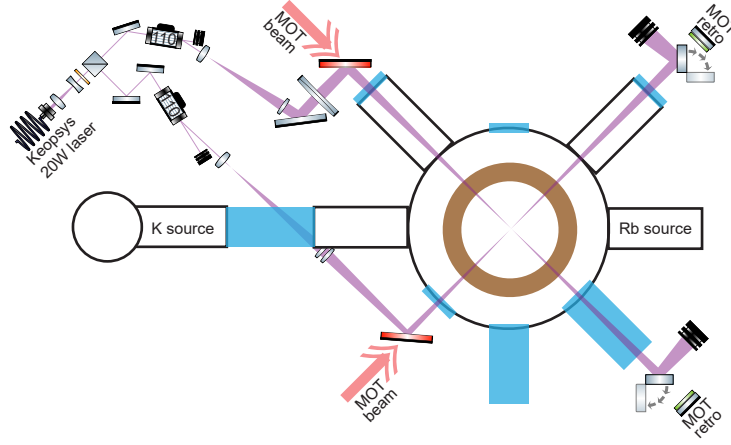


FIGURE 2.15: LAYOUT OF THE CROSSED DIPOLE TRAP.

The optical layout of the crossed dipole trap in the central chamber is shown. Note that several mirrors have been omitted, with the laser output and AOMs on the table, and beams passing under the potassium source section before rising up to the vacuum chamber height. The retro-reflectors for the MOT used with this trap configuration are also shown. Flipper mirrors redirect the dipole beams into dumps before they are turned on, after the MOT has loaded.

When resonant light at a low intensity, I_0 , passes through a cloud of atoms, it is absorbed according to Beer's law,

$$I(x, y) = I_0 e^{-OD(x, y)}, \quad (2.1)$$

where the optical density is $OD(x, y) = \int n(\mathbf{r})\sigma_0 dz$ for a given atomic distribution $n(\mathbf{r})$ and optical scattering cross-section σ_0 . We can measure the atomic cloud's OD as

$$OD(x, y) = \ln \left(\frac{I_r - I_d}{I_a - I_d} \right), \quad (2.2)$$

where I_a is the (spatially resolved) intensity of the probe after it has passed through the atoms, I_r is the intensity of a reference image, taken with no atoms present, and I_d is a *dark frame* taken with the probe beam turned off, to account for any stray light, electronic noise, or other offsets. The total atom number, N , can then be calculated from the OD by

$$N = \frac{1}{\sigma_0} \int OD(x, y) dx dy. \quad (2.3)$$

In practice, the optical transition in the atoms becomes saturated due to the linewidth of the transition, limiting the rate at which photons can be absorbed and re-emitted. This causes the measured OD to appear lower, as proportionally more photons make it through the atoms unabsorbed. We can correct for this by using a generalised Beer's law,

$$\frac{dI'}{dz} = -n(\mathbf{r})\sigma_0 \frac{I'}{1 + I'}, \quad (2.4)$$

where $I' = I/I_s$, for the transition's saturation intensity I_s . This leads to correction to (2.2) to give the saturation corrected OD as

$$\text{OD}(x, y) = \ln \left(\frac{I_r - I_d}{I_a - I_d} \right) + \frac{I_r - I_a}{I_s}. \quad (2.5)$$

To measure I_s in terms of the light level recorded by the camera, we substitute (2.5) into (2.3), using a discrete sum over the pixels of the camera, which gives

$$\frac{1}{\sigma_0} \sum_{x,y} I_r \left(1 - e^{-\text{OD}_0(x,y)} \right) = I_s \left(N - \frac{1}{\sigma_0} \sum_{x,y} \text{OD}_0(x,y) \right), \quad (2.6)$$

where $\text{OD}_0(x, y)$ is the uncorrected OD given by (2.2). By running experiments where the total number of atoms is assumed to be constant, but with varying imaging probe power, a graph of $\sum_{x,y} I_r (1 - e^{-\text{OD}_0}) = \sum_{x,y} (I_r - I_a)$ against $\sum_{x,y} \text{OD}_0$ can be generated, which has gradient of $-I_s$.

Typically, before using absorption imaging, the atoms are released from their trap, and allowed to expand freely. The in trap distribution is often too optically dense to image directly, and, depending on the optics used, is often at the limits of the imaging resolution, making it hard to extract useful information such as the number of atoms. For long time of flight, the spatial distribution becomes that of the momentum distribution, as atoms in motion will continue at a constant momentum when there is no potential to confine them.

2.8.1 Side imaging in the central chamber

The longest standing of our imaging systems is the central chamber side camera, which has been virtually unchanged since we made our first central chamber MOT. This is our main diagnostic tool, as it can measure atom distributions at each stage from a MOT to a BEC. The system, shown in Fig. 2.16, is a simple two lens configuration, with an $f = 150$ mm achromat against the 'back' window of the central chamber (opposite the round cell), focussed on the atoms in the central chamber, followed by an $f = 100$ mm achromat, which refocuses the image onto a PHOTONFOCUS MV1-D1312(I) CMOS camera. Each pixel on this camera corresponds to approximately $5.9 \mu\text{m}$ in the images formed. With this imaging system, we can measure atoms dropped for close to 30 ms (dependent on the vertical alignment of the camera).

2.8.2 High resolution imaging in the square cell

The primary reason for moving atoms to the square cell was to enable high resolution imaging. We had a custom objective lens made

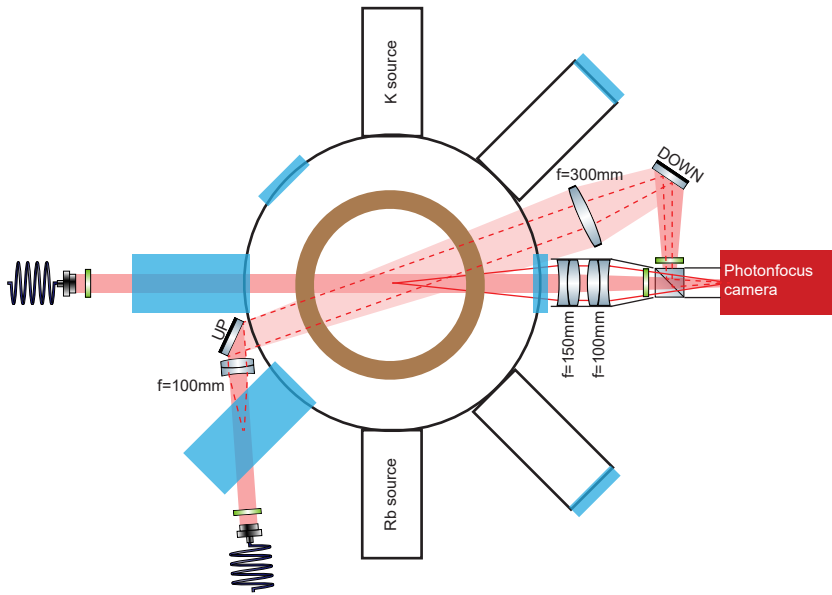


FIGURE 2.16: SIDE IMAGING SYSTEMS.

Side imaging in the square cell used the same camera as for central chamber side imaging, with the two able to be used interchangeably without alterations to the optics. The shaded areas show the approximate path of the probe light, solid red rays show the imaging of a point in the central chamber, and dashed red rays show the imaging of a point in the square cell. Note that the mirrors labelled UP and DOWN in the square cell beam path are actually pairs of mirrors forming periscopes, passing the beam over the central section of the vacuum chamber. A dipole trap was also focussed into the square cell through the same lens as used for imaging (see Fig. 2.14), injected on top of the imaging axis by a short-pass dichroic mirror in the vertical section immediately prior to the lens (not shown here). The polarisation of the two imaging beams is converted to linear by a $\lambda/4$ waveplate just before they reach a polarising beam splitter to ensure that the full probe power reaches the camera. At one point in time, optical pumping light was also sent into the central chamber via this beam splitter (not shown here).

by SPECIAL OPTICS, designed to image with both 780 nm and 767 nm light through the 4 mm BOROFLOAT glass of the cell. The lens was designed to be pressed up against the outside of the cell, with a working distance of around 150 mm inside the cell. The numerical aperture is 0.53, giving a diffraction limited spot size of $d = \lambda/2NA = 740$ nm for $\lambda = 780$ nm.

We used this objective lens with an ANDOR IXON electron multiplying charge-coupled device (EMCCD) camera, with 512×512 pixels, each of which is $16 \mu\text{m} \times 16 \mu\text{m}$. To achieve the best resolving power, each diffraction limited spot should be spread over a few pixels, which in our case would require just over $50\times$ total magnification. Given the objective's effective focal length of 31 mm, using a single refocusing lens would require a very long optical path. Instead, we opted for a multi-stage system, with a virtual image formed by a pair of $f = 250$ mm achromats, which was then re-imaged by a mi-

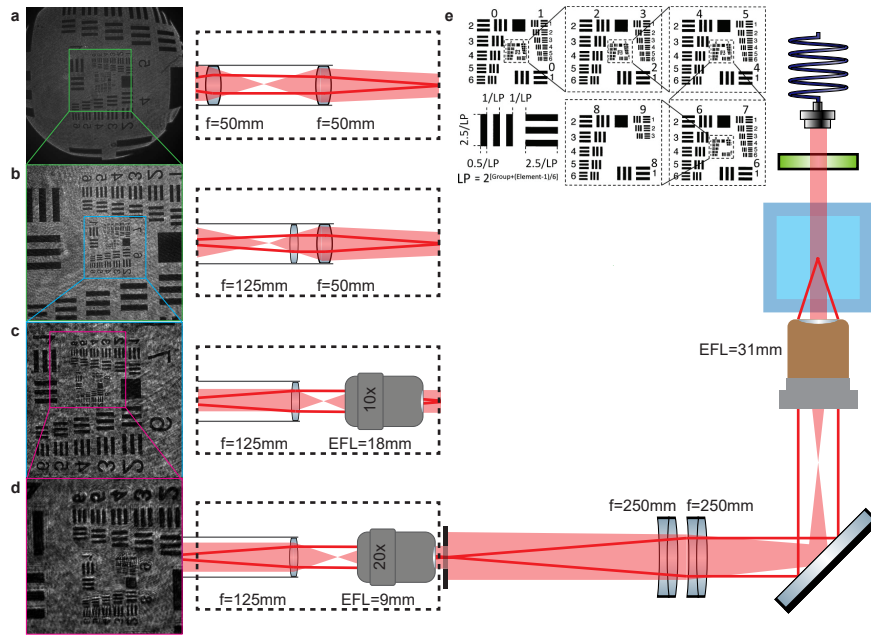


FIGURE 2.17: HIGH RESOLUTION IMAGING IN THE SQUARE CELL.

The custom objective is corrected for imaging through the 4 mm BOROFLOAT walls of the square cell. Dark red lines show an indication of the approximate image ray path, while light red shaded areas are an indication of the probe beam path. (e) shows the layout of a USAF 1951 resolution target, which was used for bench testing the imaging system in the four configurations shown in (a–d). Configuration (a) was used for initial alignment of the imaging system and the dipole beams, while (b) was used for most other work. In the test image for (d) the lines of group 9 element 2 ($0.87 \mu\text{m}$ width) are just distinguishable, limited by fringing on the illuminating beam.

crosscope objective, followed by an $f = 125 \text{ mm}$ lens focussed on the camera. The optical layout is shown in Fig. 2.17.

By swapping the secondary objective lens, we could change the system magnification. Using a $20\times$ objective lens in the system results in an overall magnification of $53.7\times$, which limits the field of view to only $150 \mu\text{m}$, but provides the best possible resolution (Fig. 2.17d). Swapping to a $10\times$ objective increases the field of view by a factor of 2 while maintaining reasonable resolution (Fig. 2.17c). In order to get the traps in the square cell set up, however, we required an even larger field of view, which was achieved by replacing both the objective and the camera lens with a pair of $f = 50 \text{ mm}$ lenses (Fig. 2.17a). For most day-to-day work, I used an $f = 50 \text{ mm}$ lens in place of the objective (Fig. 2.17b), with the $f = 125 \text{ mm}$ camera lens, which provides around twice the field of view of the $10\times$ objective.

When we first transported atoms to the square cell, one of the biggest challenges was to measure them at the end of their journey. To achieve this, we pre-aligned this imaging system as best as we could (with the $f = 50 \text{ mm}$ lenses), using a probe beam propagating from the centre of the glass cell through to the camera. We then used

fluorescence imaging, using the MOT beams as our probe, with a high EMCCD gain, to look for signs of scattered photons as we varied the final focus position of the transport beam. Once we saw a very weak signal, we were able to then adjust the position of the objective in the direction perpendicular to the transport beam, again maximising the fluorescence signal, before adjusting the focus by altering the height of the objective lens. After iterating through all three dimensions we were able to see a stripe of atoms corresponding to the dipole trap, and switch to absorption imaging.

2.8.3 *Side imaging in the square cell*

Imaging from the side is much easier for time of flight measurements, required for diagnostics such as atom number and temperature measurements, so once we had atoms localised in a crossed dipole trap in the square cell, we needed a way of seeing them from the side. As we had a limited amount of space around the square cell, we decided to use the same lens as the crossing dipole beam for the imaging lens. We inserted a dichroic mirror, and then directed the imaged probe beam up over the vacuum chamber to the other side, where the central chamber side imaging camera is located (see Fig. 2.16). A polarising beam splitter was added to the side camera, with a $\lambda/4$ waveplate converting the circular polarised probe beam into the appropriate linear polarisation to reflect onto the camera. At the time, we also moved the optical pumping beam to be projected into the central chamber via the side imaging lenses, injected using this same beam splitter. Due to the angles of mirrors, the images produced were rotated by close to 45° .

2.8.4 *High resolution imaging in the central chamber*

When the decision was made to attempt our experiments in the central chamber rather than the square cell, a new challenge had to be overcome to allow high resolution imaging of vortices. The microscope lens needs to be up against one of the recessed central chamber windows, as close to the atoms as possible, however, the MOT beams need to go through these windows too. We attempted to use the objective lens in a telescope configuration to pass a MOT beam through into the chamber, however the diameter of the beam coming out was severely limited by the objective, with aberrations appearing if it was bigger than around 5 mm diameter.

While we may have been able to get away with a defocused beam coming from an objective for a rubidium MOT, we still wanted to be able to trap both rubidium and potassium, which proved difficult, since the light for each species would have to have exactly the same divergence to balance each MOT. Instead, as discussed in §2.6.2, we

switched to a retro-reflecting MOT configuration. To achieve this, we placed a retro-reflector for the top MOT beam on a motorised translation stage, and the objective lens on a second stage, as mentioned in §2.5.3. During the MOT loading stage, the objective is held in the retracted position, with the retro-reflecting mirror inserted above the window. During evaporation in the magnetic trap, the mirror is retracted and the objective is inserted, in time for imaging the cooled atoms. We also re-built the side MOT beams in a retro-reflecting configuration, with beams entering the same windows as the crossed dipole trap, with the dipole beams dumped by flipper mirrors to avoid attenuating the returning MOT beam.

The imaging system is shown in Fig. 2.18, and has a field of view of around 0.5 mm. We use the same ANDOR IXON electron multiplied camera as previously used in the square cell. Instead of using the custom objective lens, we use a TECH-SPECIALITIES, INC. M Plan APO 20x metallurgical near-infrared objective, as it has a shorter effective focal length, for similar resolving power through the thicker glass. This lens has a numerical aperture of 0.35, working distance of 20.2 mm, and is corrected for 3 mm glass. We are not sure of the exact thickness of the top vacuum window, however believe that it is on the order of 6 mm, limiting the resolution of this lens to around 2 μm , compared with the diffraction limit of 1.1 μm .

To initially align the objective, since we cannot use the MOT (as the up-down beam is unavailable when the lens is inserted), I instead ran a sequence where the source MOT was being pushed into the central chamber, where the side MOT beams and the quadrupole coils were on. This resulted in a strong fluorescence signal, which got brighter as the objective lens got closer to the centre of the quadrupole field. After this pre-alignment, evaporatively cooled atoms in magnetic traps were used, looking at brightness of the *in situ* fluorescence signal (the whole fluorescence distribution was still much bigger than the field of view). I evaporated magnetically trapped atoms much further than the usual parameters (microwaves to 2 MHz off resonance), which produced a smaller cloud of atoms to align to and focus on. Since the objective lens is mounted to a motorised translation stage, the focus adjustment could be automated.

To insert the imaging probe beam on top of the bottom MOT beam, a motorised flipper mirror is mounted above the final MOT mirror. We could have used the MOT beam as the probe, however it was easier to use a separate probe, particularly due to the fringes on the beam, which I will discuss in §2.8.5. This flipper mirror was also used to insert a blue detuned beam for generating vortices, overlapped with the probe beam on a non-polarising beam splitter, discussed in §3.3.1. Absorption imaging of BECs in the crossed dipole trap, and subsequently vortices, were used to fine-tune the focus.

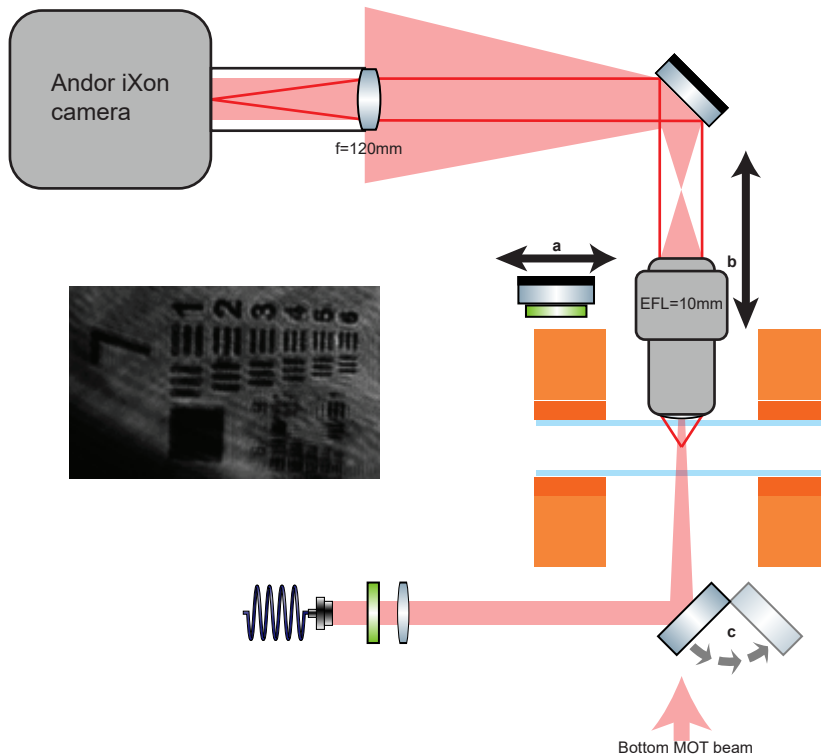


FIGURE 2.18: CENTRAL CHAMBER TOP IMAGING.

To image through the top window of the central chamber, first, the top MOT retro-reflector and $\lambda/4$ waveplate (a) are moved out of the way, and the objective lens (b) is lowered into the bore of the electromagnet coils (orange). A flipper mirror (c) allows the imaging probe beam (light red) to be inserted through the bottom window along the MOT beam path. An indication of the image ray path is shown in darker red. The inset shows group 7 of a USAF 1951 resolution target taken during initial bench testing, which is resolved down to element 6 ($2.19\ \mu\text{m}$ line thickness).

2.8.5 Fringe suppression

Our high resolution imaging systems suffer from fringes in the probe beam, which move on millisecond time-scales, such that the reference image does not match the atoms image well. We suspect that these arise due to reflections between the surfaces of the vacuum windows, which in the central chamber, are only $\approx 25\ \text{mm}$ apart (this also happened in the square cell, which has close, parallel walls). As the laser beam path changes slightly (possibly due to small air currents or vibrations), the phase of these fringes changes.

Our first approach to suppress these fringes in absorption images was to use the *frame transfer* capability of the iXON camera to achieve extremely fast back-to-back images. The EMCCD chip is actually twice the reported size, with half masked. Two frames can be taken with very short inter-frame times, by moving the first image to the masked section, then reading it out during the second exposure. To implement this, we set the probe beam pulse for the atoms frame to coin-

cide with the very end of the first exposure, and the reference pulse at the very start of the second exposure.

The reference image should not have any atoms in it, however, with the short (170 μs) inter-frame times, there is no time for the atoms to go anywhere. We found that the probe beam was heating the atoms significantly, and possibly pushing them upwards, out of focus, with the atoms remaining in the second frame having a wider distribution. By shifting the imaging beam frequency by -20 MHz, the signal from these atoms was insignificant, and could be used as a reference (the fringes did not visibly move when changing the probe frequency over this range). The downside to this mode of imaging, is that the exposure time for each frame must be 30 ms, matching the time taken to read out of the previous frame. This means that any stray light hitting the camera prior to imaging (such as trapping light for time of flight times less than the exposure time) will spoil the image.

As most of our imaging of vortices requires expansion times less than this (see §4.2), we had to take a different approach. Instead of attempting to stabilise the fringes for a pair of atom and reference images, we implemented a technique which computes an ideal reference frame from a collection of frames taken in the past [313, 314]. Frames from prior experiments are used to form an *eigenbasis* of reference image components. For each experiment, we then project a masked copy of the atom frame onto the masked eigenbasis, to compute a reference image that best matches the atoms image outside the masked area (where the atoms are). The unmasked version of this computed frame is then used as the reference frame for that experiment. This results in the suppression of fringe features caused by the movement of the fringe pattern, as seen in Fig. 2.19, though we still find that images where the ‘raw’ OD image has few fringes seem to have the best images of vortices.

Finally, it was found that adjusting the size and collimation of the probe beam helped to reduce the number and spatial frequency of fringes. Focussing the beam onto the atoms, with a waist just larger than the spread of the atoms, almost completely removes all fringes, however, also restricts the field of view. In order to perform Bragg experiments, we found that setting the beam to focus past the atoms, so that in the imaging plane the beam covered approximately three trap diameters (to allow the separation of Bragg scattered components), reduced the fringing enough that the eigenbasis fringe removal was almost always sufficient.

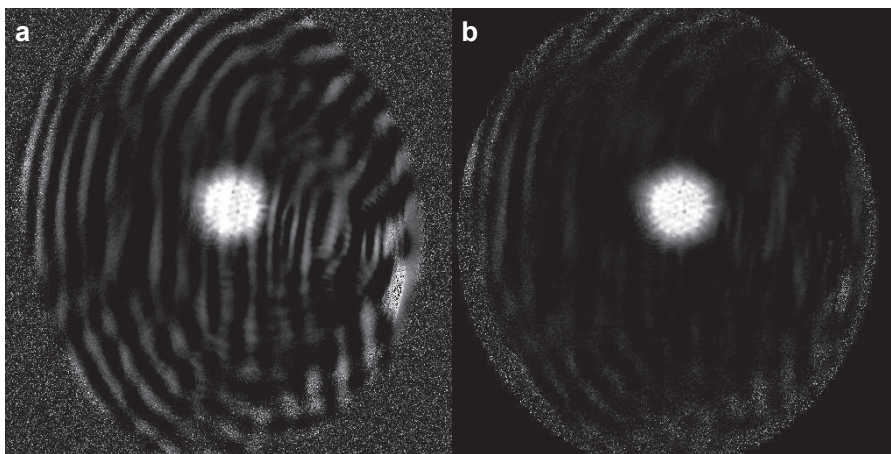


FIGURE 2.19: EIGENBASIS IMAGE PROCESSING.

A comparison of optical density images **(a)** using a regular reference frame and **(b)** using a reference frame computed to best match the absorption image. Note that the area outside the aperture of the imaging system has been masked in **(b)**, as there is no light hitting the camera here.

CREATING A UNIFORM OBLATE BEC

In the previous Chapter, I described the KRb apparatus, and the procedure for making and imaging a BEC of ^{87}Rb atoms. So far, I have only mentioned trapping configurations that produce 3D BECs, however, as mentioned in Chapter 1, we are particularly interested in studying vortices in condensates where the dynamics can be considered 2D. In this Chapter I will discuss the ways in which we trapped the BECs produced in this apparatus in oblate geometries, with either harmonic or uniform radial profiles. I will then cover the various methods we used to create vortices in these oblate condensates.

3.1 AXIAL CONFINEMENT

First I will discuss the configurations used to confine the atoms in the *tight* or *axial* dimension, effectively squashing the BEC into a pancake shape. It should be noted that our experiments use an oblate geometry, but are not strictly 2D (as discussed in §1.2.5.1, the vortices will still behave as 2D point vortices provided the BEC is highly oblate). The BEC is still technically 3D in the sense that there is still more than one energy mode in the tight direction. The most common method for confining atoms to a 2D sheet is with an optical dipole trap, shaping the beam to the desired geometry. This can be achieved in several ways, using either attractive (red-detuned) or repulsive (blue-detuned) traps.

3.1.1 Red-detuned light sheets

The simplest method is to focus an attractive dipole trap through a cylindrical lens, forming a light sheet in which the atoms can be confined [315]. Provided that the beam waist in the wide direction is large compared with the BEC size, as is the Rayleigh range through the tight focus, a light sheet can be superimposed on an existing 3D trap, such as a magnetic trap, to provide additional confinement in one direction.

This was the initial method used in our apparatus, though we ran into issues with the beam profile. We observed a striped pattern in the distribution of thermal atoms loaded into the sheet, an example of which is shown in Fig. 3.1. The position of these stripes appeared to move when the position of the beam was adjusted horizontally, leading us to believe that the pattern was due to intensity variations in the laser beam itself. We suspect that they must have originated

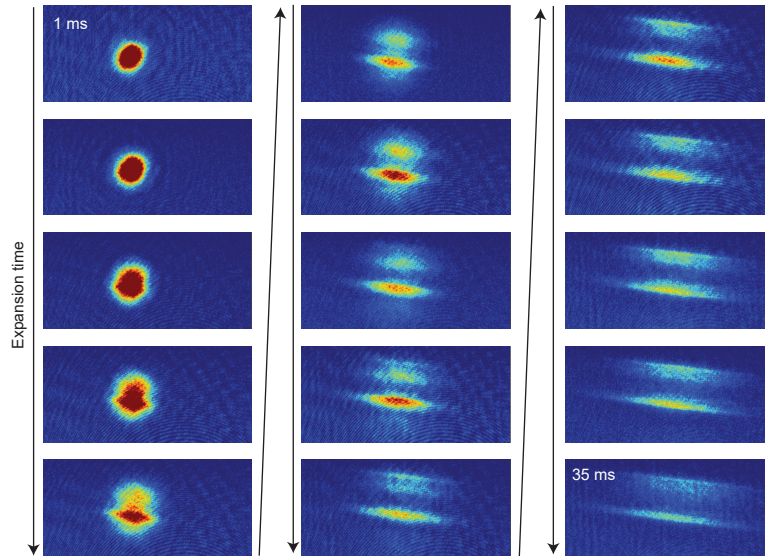


FIGURE 3.1: FRINGES IN THE RED-DETUNED LIGHT SHEET.

Expansion of atoms into a red-detuned light sheet. Initially, the atoms are held in a trap formed by superimposing the light sheet with the crossed dipole trap in the square science chamber. After the crossed dipole trap is extinguished, the atoms are free to expand. Here, each image from top-left through to bottom-right is taken after a successively longer expansion time. Localisation of the atoms is seen, which is attributed to interference fringes in the light sheet. The light sheet is propagating in the same direction as the observed fringing.

from multiple reflections in the glass window of the vacuum chamber, which does not have an anti-reflection coating for the 1064 nm wavelength of the trap. We saw this in both the square cell, as well as the central chamber. In the central chamber case we were inserting the trap through the round cell, which has similar optical properties to the square cell glass, so perhaps we would have had better luck using a different window.

3.1.2 Blue-detuned Hermite–Gaussian mode

To overcome this issue, we switched to a blue-detuned trapping configuration, using a Hermite–Gaussian (HG) mode to confine the atoms between two light sheets [316]. We used an SLM to produce a $HG_{0,1}$ mode (a Gaussian with a single horizontal nodal line), which was recorded onto a piece of BAYFOL HX photopolymer. This process is the same as that for creating a hologram using an object and a reference beam, except that in this case the object beam is generated by the SLM rather than by reflecting off a physical object. We have published our work on this technique [287], which is depicted here in Fig. 3.2.

The use of the photopolymer based hologram removes several issues encountered when using an SLM directly. When using an SLM, light is not only diffracted by the computer generated pattern, but

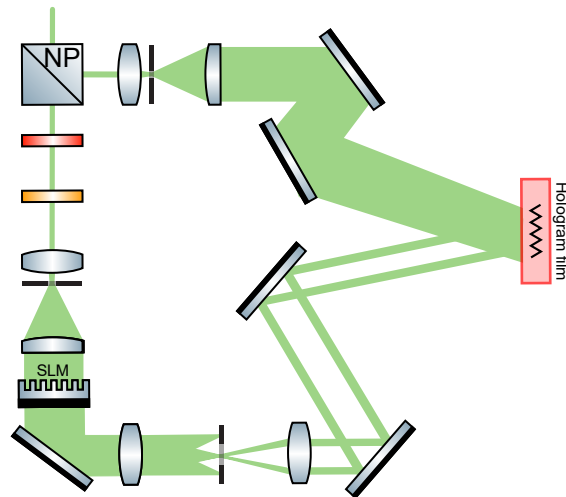


FIGURE 3.2: RECORDING TRANSMISSION HOLOGRAMS.

The laser beam is split in two on a non-polarising beam splitter, forming the object and reference beams. A polariser and $\lambda/2$ waveplate are used to control the polarisation and intensity of the beam passing through the SLM. Both beams pass through spatial filters formed by a pair of lenses and a pinhole. These are configured as telescopes to magnify the beams. The reference beam is chosen to match the size of the beam used to play back the hologram, while the object beam is expanded to overfill the SLM, producing almost uniform illumination across the device. A computer generated hologram is displayed on the SLM, and the first diffracted order is selected by a 1:1 spatial filter. The resulting object and reference beams are then combined onto the photopolymer film (mounted on a thin glass substrate) at an angle of 49° . The holograms are typically exposed with 10 mW of light at 532 nm for 0.2 s. Figure adapted from Tempone-Wiltshire et al. [287].

also by the grid structure of the pixels themselves. This generally results in a loss of around 50% of the optical power. The overall efficiency of diffraction into the desired mode is further reduced by the 2D nature of the device, resulting in multiple diffraction orders. Furthermore, the optical power diffracted by most SLMs exhibit fast intensity fluctuations due to phase flicker in the SLM pixels. This occurs in most consumer-grade devices due to pulse-width modulation used to adjust the value of each pixel [317, 318].

By selecting a single diffraction order of a desired pattern from an SLM, and recording it to a static hologram, we spatially filter out information about the SLM pixel structure. Recording this beam on a photopolymer with finite thickness forms a *volume* hologram, which can theoretically achieve unity playback efficiency into a single diffraction order. The BAYFOL HX photopolymer used here has been shown to achieve efficiencies up to 98% [319]. However, this assumes perfect spatial overlap between the input and output modes of a holographic grating. In our case, a $HG_{0,1}$ mode has around 50% overlap with a Gaussian mode of the same dimensions. Indeed, we see almost 50% diffraction efficiency when using the collimated output from an

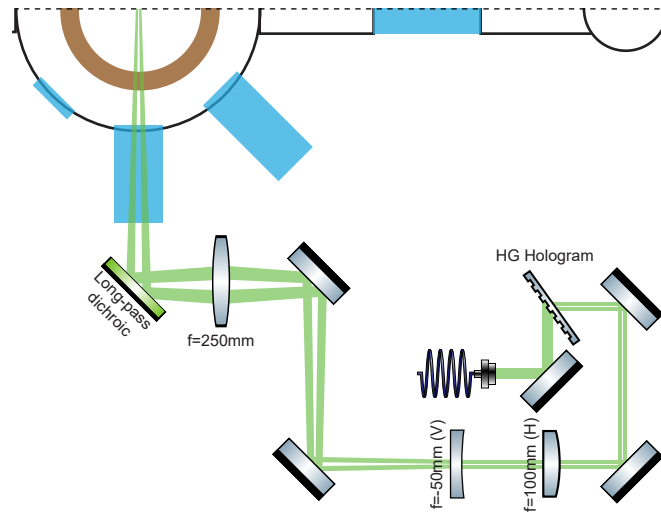


FIGURE 3.3: HERMITE-GAUSSIAN MODE HOLOGRAM OPTICS.

The HG mode is generated by passing a 1 mm diameter collimated beam through the hologram. The vertical direction is focussed onto the atoms by first expanding it with an $f = -50$ mm cylindrical lens, with the virtual focus re-imaged by an $f = 250$ mm spherical lens in approximately $2f$ configuration (drawing is not to scale). The mode is resized in the horizontal direction by an $f = 100$ mm cylindrical lens, which, in combination with the relay lens, defocuses the mode in this direction, changing the spatial extent at the atoms. Note that the nodal line shown is for illustrative purposes only, it is actually in the horizontal direction.

optical fibre to ‘play back’ the hologram mode on the apparatus. We have been using the same hologram for our HG mode for over two years now with no noticeable degradation.

Once generated, the HG mode passes through a pair of crossed cylindrical lenses, as shown in Fig. 3.3. The lens in the horizontal direction is used to alter the collimation in this ‘long’ dimension, to adjust the effective beam width at the atoms. The vertical lens on the other hand focuses the mode tightly. This focus is relayed onto the atoms by a single spherical lens in $2f$ configuration.

To load atoms into the HG mode, we typically evaporate until just before a BEC forms in the crossed dipole trap described in §2.7.3.4. We then ramp the quadrupole field over 300 ms, back on to the point where it cancels the effect of gravity, since the HG mode alone cannot hold atoms against gravity. Once the levitation field is on, the HG mode is ramped on over 300 ms. The crossed dipole trap is smoothly extinguished during the first half of the HG mode ramp. The bias fields in the trap plane are carefully tuned to minimise the movement of the atoms from the original crossed dipole position. The resulting radial confinement due to the quadrupole field will be discussed in §3.2.1.

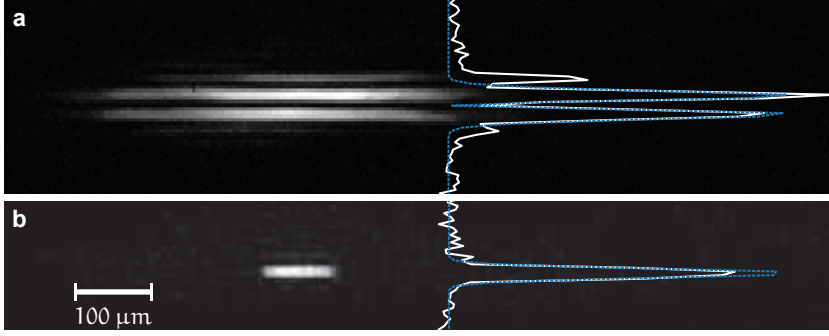


FIGURE 3.4: THE HERMITE–GAUSSIAN MODE TRAP.

(a) An image of the HG mode, taken on the side imaging camera. While a dichroic mirror blocks most of the trapping light from reaching the camera, there is enough leakage to take an image. The white line (right) shows the intensity profile along a line vertically through the centre of the mode, and the blue dotted line shows a fitted HG profile with $\sigma_z = 16 \mu\text{m}$. (b) An optical density image of a BEC taken after 1 ms time-of-flight after release from a trap formed by the HG mode and a $42 \mu\text{m}$ radius disc projected from the DMD (this will be discussed in §3.2.3). The white line (right) shows the OD along a vertical line through the centre of the cloud, and the blue dotted line shows a Gaussian fit with $\sigma_z = 5.7 \mu\text{m}$ (limited by the camera resolution).

The intensity profile of an ideal HG mode in the focal plane is given by

$$I(x, z) = \frac{8I_0 z^2}{\pi \sigma_z^2} e^{(-2z^2/\sigma_z^2)} e^{(-2x^2/\sigma_x^2)}, \quad (3.1)$$

where I_0 is the peak intensity of a Gaussian beam of size, σ_x, σ_z are the horizontal and vertical beam waists respectively. The peak intensity of the two lobes are positioned at $\pm\sigma_z$ from the nodal line through the centre of the mode. We typically operate with around 100 mW of light in the HG mode, focussed with $\sigma_z = 16 \mu\text{m}$ and $\sigma_x = 250 \mu\text{m}$, shown in Fig. 3.4. This provides an axial trap frequency of $\omega_z \approx 2\pi \times 100 \text{ Hz}$.

3.1.3 Tilting 2D traps

As mentioned in §1.2.7.3, our Monash BEC theory group proposed a method of vortex sign detection based on observing the gyroscopic motion of vortices after a flat BEC has been tilted. We attempted to implement this method in the lab by physically rotating the cylindrical focussing lens forming either the red- or blue-detuned trap. In the case of a red-detuned trap, it is obvious that rotating the cylindrical element about a round beam will cause the focal line to rotate. For the HG mode, the phase singularity associated with the nodal line should be rotated. As it would be difficult to rotate the hologram itself, we instead investigated the effect of simply rotating the cylindrical lens. For small angles, the two lobes of the HG mode appear to skew, with one shifting to the left slightly, while the other shifts to the right, with

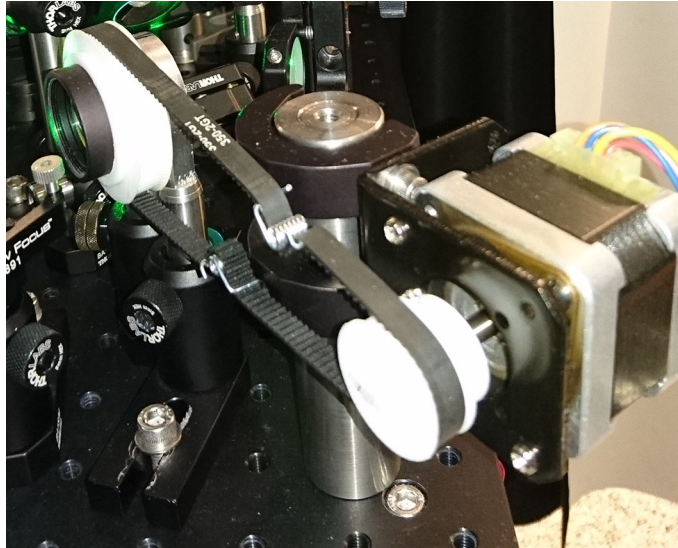


FIGURE 3.5: PHOTOGRAPH OF THE ROTATING LENS.

The lens (left) is held in a piece of lens tube, glued to a commercial rotational bearing. A 3D printed sleeve in the shape of a 72 tooth timing belt pulley surrounds the lens tube. A rubber GT2 timing belt connects the lens mount to a 36 tooth pulley on the shaft of the stepper motor. Tensioning clips are used to remove slack from the belt.

the pair of lines rotating with the lens. Within the range of angles required, the nodal line tilts, though the intensity either side of it does vary slightly.

We attempted to implement this by building a custom rotation mount for the cylindrical lens. This consisted of a piece of lens tube attached to a rotational bearing, with a large 3D printed pulley around it. A stepper motor (SANYO DENKI 103H5205-5240) was then used with a smaller pulley attached, with a ‘timing belt’ style band connecting the two (the pulleys had notches appropriate for the belt’s teeth), shown in Fig. 3.5. The ratio of teeth on the pulleys was 72:36, and the stepper motor has 200 steps per revolution, which can be ‘microstepped’ in 1/16 increments using the BIGEASYDRIVER control board by Brian Schmalz. This results in a theoretical resolution of 0.05625° of lens rotation per microstep. As the vortex gyroscope imaging technique requires around 20° ($\pi/9$) of trap tilt, this gave us 355 discrete steps during the rotation.

Control of the lens was then achieved by pre-generating the relative timing of pulses required to ramp the rotation with the form $\theta(t) = \theta_0 \left(1 - \frac{t}{T} + \frac{\sin(2\pi t/T)}{2\pi} \right)$ numerically, using the PYTHON code in Listing 3.1. The timings for movement pulses generated here was saved (due to the slow method for producing the sequence) to be loaded during the compilation of each experiment. These generated times are in the range $t \in (0, 1]$, allowing the ramp duration to be set

LISTING 3.1: PYTHON code used to calculate the times at which pulses should be sent to the stepper motor controller to achieve the desired smooth rotation.

```

1 from pylab import *
2 pulses_per_rev = 200*16*2 # 200 steps per revolution, 16
  microsteps, gear ratio 2.
3 d_theta = 2*pi/pulses_per_rev # rotation angle in radians, per
  microstep.
4 theta_0 = round((pi/9)/d_theta)*d_theta # desired rotation angle,
  rounded to the nearest microstep resolution.
5 T = 1 # Set time constant to unity, will rescale by multiplying
  time sequence later.
6 step_fn = lambda t: theta_0 * (1-t/T + sin(2*pi*t/T)/(2*pi))
7 ts = [] # A list to keep step times in.
8 dt = 1.64e-4 # Minimum time between steps.
9 thetas = linspace(theta_0,0,1+theta_0/d_theta)
10 for step in thetas:
11     i = 0
12     while step_fn(i*dt) > step:
13         i+=1
14     ts.append(i*dt)
15 ts = ts[1:] # We don't need to pulse to get to zero angle.

```

by multiplying the sequence by the desired duration. Ramp times as short as 20 ms could be achieved, limited by the motor.

While we managed to load atoms into the rotatable trap, and saw them follow the trap angle, we had difficulty tilting the atoms quickly enough to induce gyroscopic motion of vortices. Instead, the atoms tended to slip out of the trap for the fastest rotation times. It is likely that the potential was not deep enough to prevent the atoms from going through it as it pushed them. There was also significant heating of the atoms, indicating that the ramp may not have been smooth enough.

A video of the motion of the trap could be taken by taking a sequence of images at subsequently later times of repeated rotations. At the end of the motion, the trap appeared to ‘bounce’ slightly, with small oscillations in the angle. This was most likely due to the rubber drive belt stretching. As the gyroscope experiment would require releasing the atoms from the trap at the end of the ramp (or even part way through it) this was not seen as a significant issue.

These issues may have been overcome by using a different gearing on the motor to improve the step resolution during the rotation, and using more power in the HG mode. Ultimately, we did not spend a significant amount of time investigating solutions to the rotation issues, as an early version of the work by Seo et al. [21] appeared on the ARXIV preprint server. We decided that this Bragg method would be

faster to implement, and that we should focus on looking for vortex clustering in uniform potentials with this, rather than pursuing the gyroscope technique.

3.2 RADIAL CONFINEMENT

The axial confinement methods do not significantly effect the motion of atoms in the plane of the trap, though the red-detuned light sheet will add some slight harmonic component, and the blue-detuned mode tends to slightly repel atoms from the centre. The majority of the trapping in this plane is instead provided by a second trapping component.

3.2.1 *Harmonic confinement*

The simplest radial confinement to implement is provided by the quadrupole magnetic field gradient. When the vertical component of the quadrupole field is tuned to cancel gravity, the radial component will provide trapping. The strength of this trap depends on how close the magnetic field zero is to the atoms. The further away the zero, the smaller the radial component is, and the weaker the radial confinement (in fact, once the field produced by the bias coil which is opposing the nearest quadrupole coil is stronger than that quadrupole coil's field, the radial field profile should become anti-trapping). With the field zero centred around 1 mm above the atoms, the radial trap frequency is around $\omega_{\perp} \approx 2\pi \times 8$ Hz. The radial confinement becomes too low to measure once the bias field is approximately 30 G, corresponding to a shift of around 2 cm (assuming that the vertical component is linear in this range).

We have fine control over this parameter by tuning a bias field in the vertical direction. Due to stray magnetic fields, and imperfections in the coils, the in-plane bias fields also need tuning to keep the trap centred in the desired position (and stop the atoms from sloshing due to movements). We have also added a single coil of 20 turns around the flange of the square science cell, as this seems to be the main axis along which the trap moves. This coil is used to cancel the majority of the motion, limiting the currents needed on the ribbon cable bias coils.

3.2.2 *Holographic blue-detuned potentials*

As discussed in §1.3.2.3, it is easiest to observe signs of vortex clustering in a flat-bottomed potential. This requires an optical potential, rather than the magnetic trap. Such a potential was first demonstrated in 3D by Gaunt et al. [320], where atoms were trapped in the dark region of a hollow laser mode, capped with light sheets. A similar

arrangement was used by Chomaz et al. [321] to produce a quasi-2D BEC, with atoms trapped radially in a disk shape formed by the shadow of a mask, and axially between the lobes of a HG mode. Subsequently Ville et al. [322] used a DMD to provide an adjustable mask for uniform radial confinement, and a tunable optical lattice for axial confinement, to allow the loading of a truly 2D Bose gas.

Our first approach was to generate holograms of high order Laguerre-Gaussian (LG) modes, such as those we had tested in Tempone-Wiltshire et al. [287]. LG modes contain an optical vortex at their centre due to the phase winding of their profile. Unfortunately, we ran into issues generating an appropriately sized LG mode to trap atoms with.

We desired a mode on the order of 50 μm to 100 μm diameter, with a diameter-to-wall thickness ratio of at least 10. To obtain such narrow walls, we needed to focus the mode with a high resolution lens, meaning that the mode had to be focussed by the central chamber top imaging objective (§2.8.4). High order LG modes become significantly wider than their Gaussian counterparts, to the extent that we were limited to orders with winding numbers of around 5 or 6 due to the aperture size of the objective lens. Additionally, we found that any aberrations or other imperfections in the lens system tended to result in the mode breaking down into a set of discrete optical vortices, ruining the clean, flat central region desired for a trap.

Having read similar complaints in the thesis of Alex Gaunt [323], we instead tried generating an axicon-like hologram. Through its focus, the axicon mode goes from a broad walled ring shaped beam, to a sharp, narrow ring, then to a smaller diameter broad wall shape, until focussing to a point, shown in Fig. 3.6. This was tuned to provide the desired trap size, and inserted into the objective lens via a pair of relay lenses and a dichroic mirror. By adjusting the relay lenses, and the output collimation of the optical fibre supplying light to the hologram, we were able to both focus the mode, and make small adjustments to its overall size. The focussing and adjustment was achieved by moving the objective lens so that it focussed on the reflection of the mode in the top vacuum window, such that the small leakage through the dichroic mirror could be seen on the camera.

To load the atoms into this trap, we first load into the combined magnetic and HG mode trap. The radial hologram mode is turned on, then the quadrupole field zero is moved with a 700 ms ramp of the bias field, to the point where the radial component is negligible. As the radial component of the magnetic trap is lowered, the atoms expand until they hit the optical barrier. Depending on the size of the mode and the rate of the expansion, we find that vortices can be spontaneously generated, presumably due to sound waves forming as the condensate bounces off the hard barrier back into itself. This appears to be minimised by reducing the diameter of the optical mode.

We also found that this conical shaped beam, combined with gravity, could actually confine atoms in 3D, with only a few milliwatts of power.

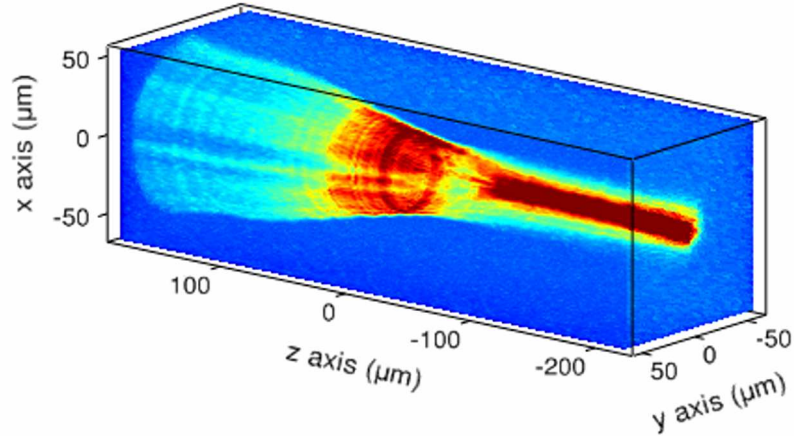


FIGURE 3.6: AXICON MODE PROFILE.

The beam profile of the axicon mode, taken by imaging the reflection of the mode off the top window of the vacuum chamber at varying objective lens positions. The beam propagates from positive to negative z (positive z is up on the apparatus), with the ideal focus at $z = 0$. At the focal plane the mode forms a sharp ring. The conical shape of the mode also makes it possible to confine atoms in three dimensions.

3.2.3 Digital micromirror device potentials

To provide more flexibility (particularly in terms of vortex creation, which will be discussed next), we switched from the axicon trap to one produced by a DMD [322, 324]. We based this trap on that of Gauthier et al. [324], projecting an image of the DMD chip onto the atoms. Our DMD is a TEXAS INSTRUMENTS DLP LIGHTCRAFTER evaluation module, with a 0.3 WVGA chipset. We again use the imaging objective to project the potential onto the atoms, rather than using a separate lens. The relay lenses previously used for the axicon mode were replaced to instead form a pair of magnifying telescopes, the final lens of which is the objective lens. Shown in Fig. 3.7, this provides an overall magnification of $0.1\times$. Each projected DMD pixel is approximately $0.6\mu\text{m}$ in the plane of the atoms, below the resolution of the objective.

We illuminate the DMD with around 150 mW of light, of which only ≈ 30 mW is reflected. Due to the pixel layout of our device, one direction is twice as wide as the other. To produce a round trap, we must generate an image of a circle, and stretch it by a factor of 2, using the code in Listing 3.2 The collimation of the light hitting the DMD was adjusted such that when an $80\mu\text{m}$ diameter disk is displayed, the intensity around the edges of it appears the brightest. The traps formed by the DMD are loaded in the same way as the axicon mode.

While the images displayed on the DMD naturally have hard edges, with each pixel being on or off, the image of these in the trapping plane will not be perfect due to the finite resolution of the lenses

LISTING 3.2: PYTHON code used to generate a circular mask on the DMD.

```

1 import StringIO
2 from PIL import Image, ImageDraw
3
4 # set up the DMD image. Start with a one-bit white canvas half
5   the size of the DMD frame:
6 img = Image.new('1', (608,342), 'white')
7
8 # now create a drawing object on it
9 draw = ImageDraw.Draw(img)
10
11 # Draw the ellipse which forms the disc, centred at the known
12   location of the crossed dipole trap
13 ring_centre = (320,200)
14 draw.ellipse([ring_centre[0]-disc_radius, ring_centre[1]-
15   disc_radius*ellipse_aspect_ratio, ring_centre[0]+disc_radius,
16   ring_centre[1]+disc_radius*ellipse_aspect_ratio], 'black')
17
18 # The image has been drawn on. Delete the drawing object
19 del draw
20
21 # Stretch to the full DMD frame size
22 img_final = img.resize((608,684))
23
24 # Save the image as a BMP in a memory buffer
25 img_out = StringIO.StringIO()
26 img_final.save(img_out, 'BMP')
27
28 # Set the DMD to use this image at time t in labscrip:
29 imaging_dmd.set_image(t, raw = img_out.getvalue())

```

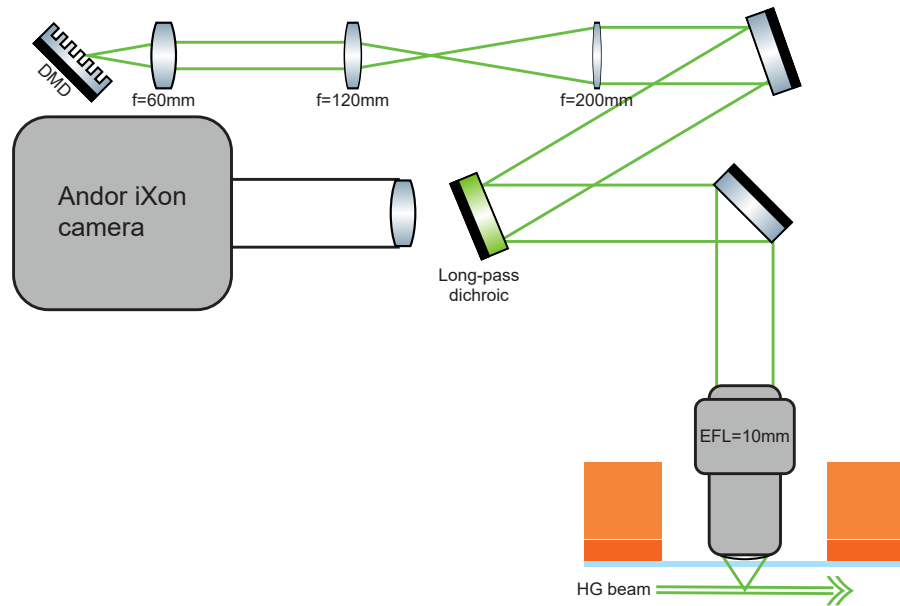


FIGURE 3.7: DIGITAL MICROMIRROR DEVICE POTENTIALS.

The **DMD** chip is imaged onto the plane of the **BEC** confined within the **HG** mode trap. A dichroic mirror allows the green light to be overlapped with the imaging system (c.f. Fig. 2.18). The series of relay lenses has an overall magnification of approximately $0.1\times$. The green rays show the imaging of a pixel from the **DMD** onto the atoms.

used. Imperfections in the alignment and focus will further distort the image, and any stray light could add to the overall potential seen by the atoms. In addition, there are magnetic field gradients present, due to the quadrupole coils, the bias coils (which are far from perfect Helmholtz coils) and stray fields (e.g., from the magnets in the ion pumps).

The most direct way to determine the overall shape of a trapping potential is to look at the *in situ* distribution of atoms within it. In evaluating the uniformity of the potentials, we are limited by the quality of the images we are able to take of the **BEC**—the noise in the images appears to be greater than any atomic density fluctuations. Looking at images after a very short time-of-flight shows a hard edge on the trap, which appears to be consistent with the blurring expected by both the projection of the potential, and the imaging of the atoms, given the $\approx 2\ \mu\text{m}$ resolution of the objective used for both.

3.3 GENERATING VORTICES

Once we had the atoms in a **2D** geometry, we began investigating methods for generating vortices on demand. We used slightly different techniques to generate vortices for each of the previously mentioned radial trapping configurations, though they all featured a re-

pulsive (532 nm) laser passing through the condensate, as discussed in §1.2.7.1.

3.3.1 *Moving the BEC through an obstacle*

In the harmonic trap, we made use of the ability to fine-tune the in-plane trap position using bias fields. Rather than moving a beam through the BEC, we moved the BEC through a beam, as was done by Neely et al. [157]. A laser was focussed onto the atoms using a single lens, relaying the image of the tip of an optical fibre. This was achieved using a 2" diameter, $f = 150$ mm spherical lens in roughly $2f$ configuration. A 50/50 non-polarising beam splitter was used to combine this beam on top of the central chamber top imaging beam, which enters the vacuum chamber from the bottom window via a flipper mirror inserted above the final MOT mirror. The size of this beam was limited to about $10\ \mu\text{m}$ by the numerical aperture available off the flipper mirror.

We were able to generate vortices by ramping this beam up to ≈ 1 mW and then off again, while displacing the trap, such that the beam was swept through the atoms. Despite fine control over the motion of the atoms, we were unable to systematically produce vortex dipole pairs. We suspect that this could be due to the lower atom number in our experiment leading to a lowered speed of sound, making it easier to stochastically excite vortices, compared with the parameters of Neely et al. [157]. The stirring beam size was also large relative to the trap size.

We also produced small vortex lattices by moving the trap on a circular path around the laser beam, shown in Fig. 3.8. Here we were able to control the average number of vortices injected by varying the rotation timing. We also found that the BEC and vortex lifetimes were extended in these cases, with small lattices observed beyond 30 s hold times. We attributed this to the thermal cloud being pushed away from the BEC due to the spinning motion.

3.3.2 *Moving an obstacle through the BEC*

When we swapped to the optical radial potential, we no longer had the ability to move the trap through the laser beam. Instead, we inserted a THORLABS GVS002 dual-axis galvanometer unit in the vortex beam path, along with an additional relay lens. With this, we were able to sweep the position of the beam across or around the trap. We found that in this case, we were unable to form vortex lattices, presumably since the single beam stirring around the edge of the trap was unable to transfer significant angular momentum to the atoms, compared with moving the atoms themselves.

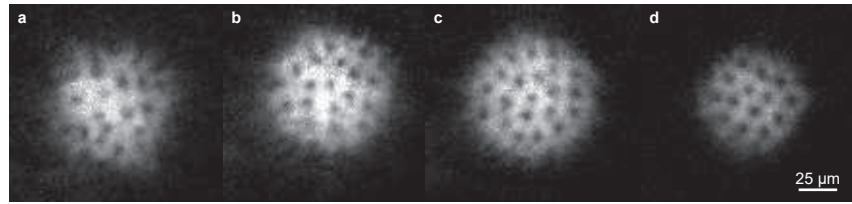


FIGURE 3.8: A VORTEX LATTICE IN THE HARMONIC 2D TRAP.

The BEC was moved on a circular path around the stirring beam by tuning bias fields to move the quadrupole field zero. The atoms orbited the beam 3 times in 1 s, during which time vortices were created. The BEC was left stationary for (a) 1 s, (b) 3 s, (c) 7 s and (d) 20 s. During the hold time, the vortices arrange themselves to be more ordered in the lattice pattern. The BEC is initially distorted due to the rotation, but regains a round shape over time, while decaying in size.

3.3.2.1 Multiple obstacles using the DMD

While the scan unit was sufficient for generating vortices, we were limited by the relatively large beam size. We wanted to be able to generate as many vortices as possible, in both random and clustered configurations, and with as little sound as possible. To achieve this, we instead switched to using a DMD to generate our vortex beam potentials.

As discussed in §3.2.3, we swapped to using the DMD for both the trapping and the vortex beam potentials. This was mostly to avoid having to combine the DMD image with the axicon mode before passing them through the objective—there was no real need to have separate sources for trapping and vortex creation (though perhaps having separate amplitude control could be beneficial). With the DMD, we are able to project arbitrary (up to the resolution limitations) shaped binary patterns (each pixel is either on or off) on top of the round trap. These can be played at rates up to 4000 frames per second, with up to 96 frames in total.

We typically use traps with a 124 pixel diameter, and allocate 89 frames to motion (we need a couple of spare frames at the start and end when the trap is static, and the DMD only has certain total frame counts allowed), which corresponds to 1.4 pixels of motion per frame for a sweep from one side to the other. A limitation of this method is that due to the pixellation and limited frame count, slow moving potentials will have jerky motion. For a typical 0.5 s sweep, the barrier jumps forward once every 5.6 ms. We used several different patterns to generate vortices, such as single round or elliptical obstacles, grids of elliptical obstacles (shown in Fig. 3.9), and pairs of paddles. Listing 3.3 gives an example of the generation of a single elliptical obstacle passing across the trap (following on from the code in Listing 3.2).

We attempted to generate large clusters of vortices using a paddle configuration, such as those observed by Gauthier et al. [259], how-

LISTING 3.3: PYTHON code used to move a single elliptical obstacle across the DMD. This code follows that in Listing 3.2.

```

1  ## Note, the object "img" already exists here, as the half-DMD
   sized drawing of a circle, generated above ##
2
3  dp = (disc_radius * 2 * ellipse_aspect_ratio + vortex_beam_depth
   )/ 89
4  dt = vortex_spoon_ramp_period/89
5
6  # loop over steps in the sweep of the obstacle:
7  for i in range(89):
8      # Make a copy of the image containing only the radial trap
9      img_cpy = img.copy()
10
11     # Add a new drawing to the image:
12     draw = ImageDraw.Draw(img_cpy)
13
14     # Calculate the vertical position of the object in this frame
15     pos = (ring_centre[0],ring_centre[1] + 44*dp - i * dp)
16
17     # Draw an ellipse on the frame, then clean up the drawing
   object
18     draw.ellipse([pos[0]-vortex_beam_radius,pos[1]-
   vortex_beam_depth,pos[0]+vortex_beam_radius,pos[1]+
   vortex_beam_depth], 'white')
19     del draw
20
21     # Resize, then clean up the temporary image
22     img_final = img_cpy.resize((608,684))
23     del img_cpy
24
25     # Save to buffer then set DMD output
26     img_out = StringIO.StringIO()
27     img_final.save(img_out, 'BMP')
28     imaging_dmd.set_image(t,raw = img_out.getvalue())
29
30     # Clean up objects ready for next iteration of the loop
31     del img_out
32     del img_final
33
34     # Add to time count and move on to the next frame
35     t += dt

```

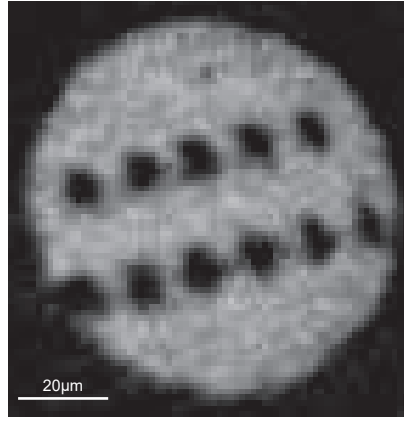


FIGURE 3.9: GRID OBSTACLES PASSING THROUGH A BEC.

A pair of interleaved grid obstacles were generated on the *DMD*, and swept approximately one third of the way through the *BEC* from opposite sides. The trap was extinguished and an absorption image was taken $100\ \mu\text{s}$ later, effectively imaging the *in situ* atomic distribution. In this case, the obstacles had a semi-major axis length of 5 *DMD* pixels in the direction of motion, and semi-minor length of 4 pixels in the transverse direction, corresponding to approximately $3\ \mu\text{m}$ by $2.4\ \mu\text{m}$ at the atoms.

ever could not find a configuration that worked well. This may have again been due to a lower atom number in our experiment, lowering the speed of sound, making it easier to generate vortices of both sign off imperfections in the obstacle. The experiments performed with the grids of obstacles will be discussed in detail in the following Chapter.

This Chapter describes a series of experiments performed in the [DMD](#)-based trap (depicted here in [Fig. 4.1B](#)), with vortices injected into the condensate by sweeping grids of obstacles through the trap. The subsequent evolution of the vortices was observed, and the statistical properties of the vortex distributions were compared for different obstacle grid sizes. The results presented in this Chapter are the basis of a manuscript [[325](#)] which is currently in peer review.

The analysis of these experiments was supported by a collaboration with Dr. Andrew Groszek, who recently completed his thesis on numerical studies of [2DQT](#) [[250](#)], and our supervisor, Dr. Tapio Simula. Andrew's main contribution to the work in this Chapter was to generate thermometry curves suited to the vortex numbers measured. Andrew also helped to develop the code used to generate energy spectra.

The experiment data and analysis code used to produce the results presented in this Chapter are available online [[326](#)].

4.1 GENERATING GRID TURBULENCE

To study the statistical properties of vortices in quantum turbulence, we wish to generate initial conditions with large numbers of vortices, and minimal sound waves, such that the superfluid flow is well approximated as incompressible. Control of the initial distribution of vortices is also desirable, as it allows the turbulent dynamics to be started in a dipole pair dominated, vortex cluster dominated or random state. A large number of vortices can be injected by sweeping an array of elliptical obstacles through a [BEC](#). The mechanism is the same as that for a single obstacle, discussed in [§1.2.7.1](#), repeated at multiple locations across the cloud. By changing the dimensions of the grids used, we can effectively alter the initial spatial distribution of vortices and antivortices. Wider grids generate a more clustered initial condition, as regions where vortices and antivortices are shed are well separated. Conversely, for finer scale grids, vortices and antivortices are generated close to each other, producing distributions that tend to consist of dipole pairs. In the intermediate regime, the vortex distributions are more disordered, as small clusters are generated, which interact with others to form dipole pairs.

In terms of Onsager's 'vortex temperature' description of point vortices ([§1.1.2.2](#)), a fine grid should produce a 'vortex gas' with a positive temperature, and a wide grid should produce a 'vortex gas' with a [NAT](#). For the experiments, we chose to use two counter-propagating grids of obstacles for two reasons: firstly, this increases the total num-

ber of obstacles passing through the BEC at once, increasing the number of vortex nucleation points; secondly, we effectively ‘push’ the BEC in both directions, minimising any residual centre-of-mass motion that may be induced during the sweep.

We generate the pair of grids using the code in Listing 4.1, which is an extended version of Listing 3.3. Note that one grid will have an odd number of points, centred on the trap, while the opposing grid has an even number of points, straddling the first. An example of the motion of the grids is shown in Fig. 4.1A. The grids are arranged such that all ellipses have the same dimensions, and spaced by three semi-major axis lengths of the ellipses. This ensures that there is always space between the grids as they pass (though for very fine grids this may not be true due to the finite resolution of the objective lens). We vary the size of the obstacles, using semi-major axis lengths of 7, 10, 13, 16 and 19 DMD pixels, corresponding to approximately $4.2\ \mu\text{m}$, $6.0\ \mu\text{m}$, $7.9\ \mu\text{m}$, $9.7\ \mu\text{m}$ and $11.5\ \mu\text{m}$ respectively. The obstacle size in the direction of motion is the same for each case, with a semi-minor axis length of 5 pixels ($\approx 3\ \mu\text{m}$). For each grid size, we ran experiments for evolution times of 0.5 s to 5.0 s (in 0.5 s increments) after the completion of the 0.5 s grid sweep. Each point in this parameter space was repeated 25 times to build up statistics for each data point, with a total of 250 runs of the experiment for each grid.

4.2 IMAGING THE VORTEX DISTRIBUTION

We measure the distribution of vortices using the Bragg spectroscopy technique of Seo et al. [21], which was discussed in §1.2.7.3. For our Bragg beams, we use light from the ^{87}Rb repump laser, and double-pass it through a 110 MHz AOM (see Figs. 2.4 and 2.6). We drive the AOM with two frequencies, by feeding two DDS outputs of a PULSE-BLASTER device into ports 1 and 2 of a MINICIRCUITS ZFSC-2-4-S+rf splitter/combiner. Both frequencies are then output from port S, which is fed into an rf amplifier, which drives the AOM. The two rf frequencies are driven with a difference δ_{rf} , which, after the double-pass, shifts light by frequencies $2f_0$, $2f_0 + 2\delta_{\text{rf}}$ and $2f_0 + \delta_{\text{rf}}$, where $f_0 = 100\ \text{MHz}$ is the rf base frequency. Overall this corresponds to light approximately 6.6 GHz blue detuned from resonance for the atoms. We tune the frequencies such that $\delta_{\text{rf}} \approx \delta_0/2$, where δ_0 corresponds to the Bragg resonance condition.

The beam is passed through the central vacuum chamber by overlapping it with a MOT beam using a polarising beam splitter before the MOT beam’s expansion telescope. The beam travels perpendicular to the square cell axis of the vacuum chamber, and is retro-reflected by the same mirror as the MOT beam (shown in Fig. 4.1B, note that the Bragg beam is along the MOT beam entering the chamber from the bottom-left of Fig. 2.15). Naturally, this beam has circular polarisation

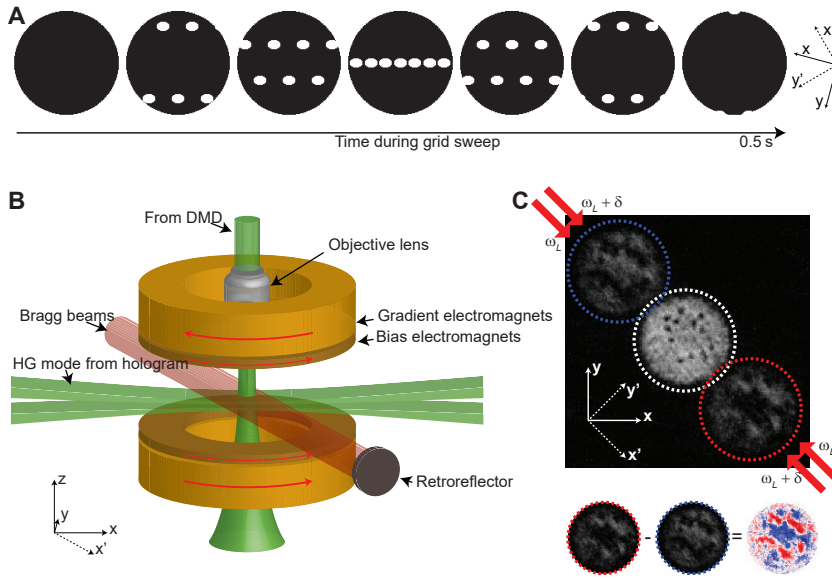


FIGURE 4.1: DMD TRAP LAYOUT.

(A) Example frames, as displayed on the DMD, for the $4.2\ \mu\text{m}$ grid. Here every 15th frame is shown from the 0.5 s sweep of the grid. The axes to the right show the orientation of the grid relative to the axes of images (x, y) and the Bragg beam (x', y'). (B) Schematic of the trapping geometry. The image of the DMD is projected onto the atoms via an objective lens in the bore of the top set of electromagnets, and the HG beam propagates along the x -axis. A magnetic field gradient is produced by a pair of coils in an approximately anti-Helmholtz configuration (light brown) combined with a linear bias field produced by a pair of coils in an approximately Helmholtz configuration (brown) which pushes the magnetic field zero above the atoms. The direction of current in each coil is indicated by red arrows. The Bragg beams propagate along the x' axis, at 45° to the imaging axes (determined by the orientation of the EMCCD camera sensor). The Bragg beams are retro-reflected and contain two frequencies, ω_L and $\omega_L + \delta$, where ω_L is the base frequency (approximately 6.6 GHz blue detuned from resonance frequency), and $\delta = \delta_0 + \delta_d$ is the sum of δ_0 , the detuning required for resonant Bragg scattering of atoms at rest, and δ_d , the Doppler detuning. (C) An example optical density image, from the data presented in the top row of Fig. 4.3, showing all three components after Bragg scattering. Atoms with a velocity component along the $\pm x'$ axis close to the detuned Bragg condition will be given a momentum kick in the direction of $\pm x'$. After 6 ms time-of-flight, the scattered components (circled in blue [$-x'$] and red [$+x'$]) fully separate from the unscattered component (circled in white, see also Fig. 4.3A). The region of the image containing the $-x'$ component is coloured blue and subtracted from the region containing the $+x'$ component, which is coloured red, to create a differential signal (bottom of panel C, see also Fig. 4.3D).

LISTING 4.1: PYTHON code used to produce a pair of grids on the DMD. This code replaces lines 14 to 18 within the for loop of Listing 3.3

```

1  # Calculate how many points to use in each grid
2  radial_odd_dots = int(floor((disc_radius - vortex_beam_radius)
3    / (5.0 * vortex_beam_radius)))
4
5  radial_even_dots = int(floor((disc_radius - (3.5 *
6    vortex_beam_radius)) / (5.0 * vortex_beam_radius))) + 1
7
8  # Calculate the vertical position of each grid in this frame
9  # odd dots at y = pos, even at y = pos2
10
11 pos = (ring_centre[0], ring_centre[1] + 44 * dp - i * dp)
12 pos2 = (ring_centre[0], ring_centre[1] - 44 * dp + i * dp)
13
14 # First, draw the centre dot on the 'odd' row:
15 draw.ellipse([pos[0] - vortex_beam_radius, pos[1] - vortex_beam_depth,
16   pos[0] + vortex_beam_radius, pos[1] + vortex_beam_depth], 'white')
17
18 # Now the rest of the 'odd' dots:
19 for dot in range(radial_odd_dots):
20     # draw the +x side
21     draw.ellipse([pos[0] + 4 * vortex_beam_radius + dot * 5 *
22       vortex_beam_radius, pos[1] - vortex_beam_depth, pos[0] + 6 *
23       vortex_beam_radius + dot * 5 * vortex_beam_radius, pos
24       [1] + vortex_beam_depth], 'white')
25     # and the -x side
26     draw.ellipse([pos[0] - 6 * vortex_beam_radius - dot * 5 *
27       vortex_beam_radius, pos[1] - vortex_beam_depth, pos[0] - 4 *
28       vortex_beam_radius - dot * 5 * vortex_beam_radius, pos
29       [1] + vortex_beam_depth], 'white')
30
31 # And now the even dots:
32 for dot in range(radial_even_dots):
33     # draw the +x side
34     draw.ellipse([pos2[0] + 1.5 * vortex_beam_radius + dot * 5 *
35       vortex_beam_radius, pos2[1] - vortex_beam_depth, pos2[0] +
36       3.5 * vortex_beam_radius + dot * 5 * vortex_beam_radius,
37       pos2[1] + vortex_beam_depth], 'white')
38     # and the -x side
39     draw.ellipse([pos2[0] - 3.5 * vortex_beam_radius - dot * 5 *
40       vortex_beam_radius, pos2[1] - vortex_beam_depth, pos2[0] -
41       1.5 * vortex_beam_radius - dot * 5 * vortex_beam_radius,
42       pos2[1] + vortex_beam_depth], 'white')

```

of the opposite handedness to the MOT beam, as it passes through the same $\lambda/4$ waveplates with the opposite initial linear polarisation. By adjusting the detuning, we find the Bragg frequency is centred at $\delta_0 = 2\pi \times 15.3$ kHz, with a width of $2\pi \times 1.8$ kHz. This frequency differs slightly from the expected value of $2\pi \times 15.084$ kHz, which we attribute to mean field effects [175].

We find that the shape of the Bragg-scattered components can be affected by the density of the BEC. For traps with a smaller radius, there is an increased s-wave scattering ‘halo’ of atoms due to collisions between the scattered component and the atoms still at rest. This is suppressed by allowing the cloud to expand for a short time before applying a Bragg pulse, and by choice of the trap size to reduce the atomic density. We allow the cloud to expand for $300 \mu\text{s}$ before applying the Bragg pulse for $600 \mu\text{s}$. We find that a detuning of $\delta = \delta_0 + \delta_d$ produces a good signal in the vicinity of each vortex for a Doppler detuning $\delta_d = 2\pi \times 900$ Hz. During the expansion and Bragg separation process we maintain the magnetic field gradient to levitate the atoms against gravity, preventing them from falling out of the imaging plane.

The speed at which the Bragg-scattered components separate must also be considered when choosing a trap size. The three components need to be spatially separated by the time the image is taken, while at the same time, the vortex cores in the expanding unscattered component will expand. We found that for our trap radius of $\approx 39 \mu\text{m}$ (62 pixels), the components separate in 6 ms, shown in Fig. 4.1C. During this time, the vortex cores grow to around $2 \mu\text{m}$, such that they are resolvable, but not so large that they begin to overlap significantly.

4.2.1 Processing the Bragg images

To obtain the position and sign of each vortex in a run of the experiment, we use the same differential signal as Seo et al. [21], but compute the best matching combination of vortex signs using the point vortex model, rather than manual inspection. To generate the differential signal, we begin by selecting three regions of interest (ROIs) of equal dimensions, centred on the scattered and unscattered components of the BEC. To select these we typically run several shots without generating vortices, with the Bragg beams tuned near resonance, and fit to the centre of each component. We then generate the differential signal by subtracting the optical density of one scattered ROI from the other. We fine-tune the position of the ROIs by again using near-resonant Bragg pulses, looking at condensates containing a few vortices. In this case, the position of the vortices should be visible in all three components, and the regions are adjusted to ensure that the relative coordinates in all three ROIs coincide. These regions are then used to process the images for each experiment, generating the differ-

ential signal by subtracting one scattered component from the other (Fig. 4.1C).

4.2.1.1 Vortex location detection

To obtain the position of each vortex, we have implemented a *blob detection* algorithm, as used by Rakonjac et al. [327]. The algorithm consists of a Gaussian blur on the order of the vortex core size, to smooth out smaller fluctuations in the image, followed by a Laplacian to produce positive features at each vortex core location. An amplitude threshold can then be used to form a binary image highlighting the vortex locations. All groups of pixels above a size threshold are assigned as vortices, with the location given by the centre of mass of the group.

Due to the large number of essentially randomly distributed vortices, and presence of sound waves and other image noise in our experiments, particularly at short hold times, we manually inspect the results of the vortex detection algorithm, and adjust if required. It was particularly hard to tune the algorithm to detect pairs of vortices that are close enough together to appear as a single feature in the image. This was incorporated into the algorithm by measuring the ellipticity of each detected feature. Any features with ellipticity above a threshold would be treated as a pair of vortices, spaced equally along the major axis of the feature. The threshold for this was highly sensitive, and depends on the size of the vortices after expansion.

The algorithm was implemented using functions of the `OPENCV` (`cv2`) package for `PYTHON`. Once a binary image has been generated following the Laplacian, we manually set the region outside the condensate to zero to suppress any background noise that may lead to spurious vortices being identified outside the BEC. A contour finding algorithm is then used, and the moments [328] are calculated for each resulting feature to determine its location, as well as detect pairs of vortices.

The moments, M_{ij} of an image, $I(x, y)$, are defined as

$$M_{ij} = \sum_x \sum_y x^i y^j I(x, y). \quad (4.1)$$

The centroid of an image can be calculated as $\bar{x} = \frac{M_{10}}{M_{00}}$ and $\bar{y} = \frac{M_{01}}{M_{00}}$, which, in general, gives us the location of each vortex. To check the ellipticity of each feature, we calculate a covariance matrix,

$$\text{cov} = \begin{bmatrix} \mu'_{20} & \mu'_{11} \\ \mu'_{11} & \mu'_{02} \end{bmatrix}, \quad (4.2)$$

where $\mu'_{ij} = \mu_{ij}/\mu_{00}$ are second order central moments, with first order central moments given by

$$\mu_{ij} = \sum_x \sum_y (x - \bar{x})^i (y - \bar{y})^j I(x, y). \quad (4.3)$$

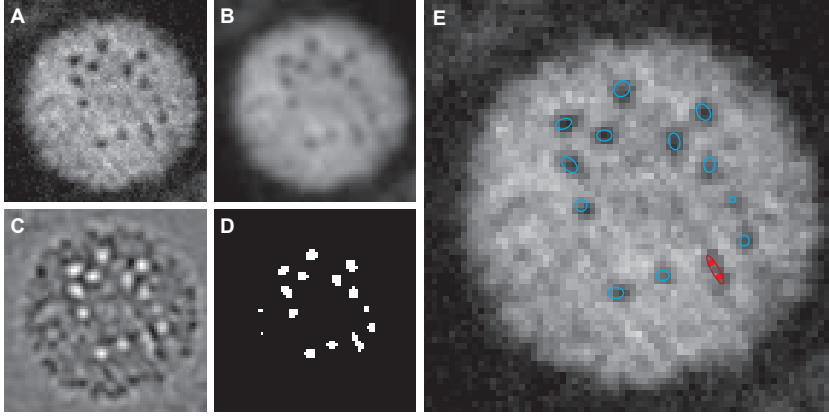


FIGURE 4.2: DETECTION OF VORTEX LOCATIONS.

To detect the position of vortices, first the OD image (A) is blurred (B) to reduce noise below the vortex core scale. (C) The Laplacian is taken to highlight the holes in the image corresponding to vortex cores, and (D) a binary threshold is performed. (E) A covariance matrix is calculated for each resulting group of white pixels containing more than 2 pixels, with the centre-of-mass determining the location of vortices (centre of blue circles). For features with high ellipticity (red), pairs of vortices are assigned (red dots).

The eigenvalues of this covariance matrix are

$$\lambda_i = \frac{1}{2} \left(\mu'_{20} + \mu'_{02} \pm \sqrt{4\mu'^2_{11} + (\mu'_{20} - \mu'_{02})^2} \right), \quad (4.4)$$

and can be used to obtain the semi-major and semi-minor axis lengths of the region, which are given by $l_i = 2\sqrt{\lambda_i}$ [328]. In our implementation, a slightly modified version of this expression was used, with the semi-major axis length given by [329]

$$l_{\text{semi-maj}} = \frac{1}{2} \sqrt{6 \left(\mu'_{20} + \mu'_{02} + \sqrt{4\mu'^2_{11} + (\mu'_{20} - \mu'_{02})^2} \right)}. \quad (4.5)$$

If the semi-major axis is larger than 1.5 times the width of a typical vortex, the feature is treated as containing two vortices. The angle of the ellipse can be calculated by

$$\theta = \arctan \left(\frac{2\mu'_{11}}{\mu'_{20} - \mu'_{02}} \right), \quad (4.6)$$

and the vortex locations are set symmetrically on this axis, separated by the semi-major axis. An example of this vortex detection is shown in Fig. 4.2.

This pair detection is not particularly robust, as it is highly sensitive to the size of the vortices, and presence of noise. Typically false negatives occur when a vortex has a slightly lower contrast in the image (and so the number of pixels in the Laplacian image above the binary threshold is low) or when a vortex–antivortex pair forms a crescent shape, which appears as a round blob. False positives arise when

The expression (4.5) was used in the code as it was the version I came across at the time. I'm unsure how it was derived, but it differs from the value derived in Ref. [328] by a factor of $\frac{2}{3}\sqrt{3}$, underestimating the ellipse dimension by around 15%. Overall this does not significantly impact the code, as the placement of the pair of vortices on the ellipse was only a rough approximation.

the noise in an image happens to highlight consecutive pixels, where there is no obvious characteristic vortex hole in the image. The choice of threshold for detecting a pair was chosen by trial and error to minimise the number of false positive and false negative detections when compared with manual inspection of the image. Even with these best parameters, each image was inspected and adjusted where obvious errors had occurred.

Of the 1250 runs of the experiment (25 repeats of 10 hold times after 5 different grids), 5% had vortex locations manually added but none removed (an average of 1.3 vortices were added to each of these shots), 19% had automatically detected vortex locations removed but none added (an average of 1.3 vortices were removed from each of these shots), 2% required minor adjustments to be made to vortex positions (vortices moved less than a vortex diameter, usually correcting a vortex dipole pair detection), while 5% required vortices to be both added and removed. A further 30% of shots were rejected entirely, in cases where the vortices were too hard to distinguish (this can occur, for example, if the fringes in the imaging probe are particularly strong, or if atoms become trapped outside the main nodal line of the HG mode, obscuring the BEC), or the atom number was significantly less than the average. After these rejections, the number of shots retained for each grid sweep and hold time varied between a minimum of 10 and a maximum of 25.

The placement of the pair of vortices within the ellipse is not necessarily the ideal location, but was chosen as the results appeared sensible by eye. The double vortex features are not always elliptical either, with dipole pairs forming a characteristic ‘crescent’ shape. The ellipse fitted to these crescents generally places the vortices in sensible (by eye) positions, however more advanced image recognition could be developed building on this work to better detect these shapes, and distinguish larger numbers of nearby vortices. This could be implemented by decomposing each detected region into constituent ellipses [329] and by tuning the algorithm with numerical data where the positions of the phase windings can be determined for comparison.

4.2.1.2 Vortex sign detection

Knowing the location of each vortex, and the direction of flow along the Bragg axis (from the differential signal), we determine the sign of each vortex by finding the combination in a point vortex model that best matches the Bragg signal. For every possible combination of vortex signs (for N_v vortices there will be 2^{N_v} combinations), we compute a the ideal flow field that would be produced by point vortices by (1.32), including the appropriate image vortices. We then project this velocity field onto the axis of the Bragg beams, and compare the sign of the field with the sign of the differential Bragg signal. We

make this comparison only within 4 pixels ($5\ \mu\text{m}$) of each vortex, to prevent noise in the far-field signal from dominating over the vortex signals. The configuration with the highest number of matching pixels is chosen as the matching vortex configuration.

This technique could be further refined by utilizing amplitude (as well as direction) information, for example by first selecting out only the velocity components that would be resonant for Bragg scattering, and then comparing the amplitudes of the constructed and experimental signals. However, we find that direction information is sufficient to obtain a unique solution, and hence more sophisticated analysis is unnecessary. In fact, as the most ambiguous cases are typically ones where a tightly bound dipole pair results in almost no Bragg signal, using the amplitude of the signal would further reduce the weighting in these cases, leading to smaller differences between the two possible orientations.

Figure 4.3 shows examples of the computed velocity fields, compared with the corresponding Bragg signals. We believe that the solution to the algorithm is generally unique, with one combination of signs matching significantly better than any other. As an example, Fig. 4.4 shows the number of matching pixels for each possible vortex configuration for the same data shown in Fig. 4.2 and the first row of Fig. 4.3, sorted from worst to best match. The distribution is anti-symmetric, due to the symmetry of the space of possible vortex signs—the worst match will have the opposite sign for every vortex compared with the best match. Typically the best match appears to stand out from other possible configurations, as changing the sign of any one vortex will change the match by approximately the same amount—for low vortex numbers distinct steps of N_v configurations often appear.

Our algorithm was optimised by recognising that the parameter space is symmetric: for every configuration of vortex signs, there is a configuration of signs where every sign is flipped, which will have a flow field in the opposite direction everywhere. We also split the parameter space across multiple cores of a computer to compute the merit functions in parallel. Even so, the algorithm is not viable for vortex numbers much higher than 20, which take several hours to compute, with the time doubling for each extra vortex added. We chose to try every combination of vortices, despite being computationally expensive, as an algorithm that flipped individual vortices to optimise the error signal was found to fail, as dipole pairs needed to be flipped together to find the true global maximum. A more sophisticated (perhaps genetic) algorithm may be able to find the global maximum more efficiently for large vortex numbers.

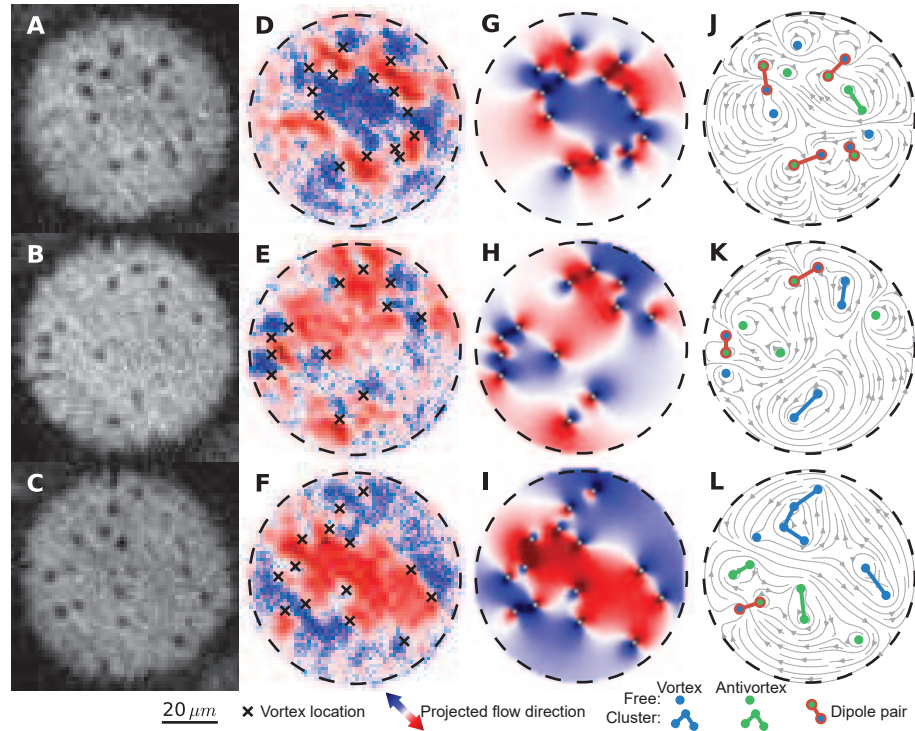


FIGURE 4.3: EXAMPLE VORTEX CONFIGURATIONS.

(A–C) The locations of vortices are visible as dark spots in the optical density images of the BEC. Here we show example distributions which are dipole dominated, random and cluster dominated, respectively. (D–F) The corresponding Bragg spectroscopy signals. (G–I) The computed velocity field projected onto the line defined by the directions of the Bragg spectroscopy laser beams. Colours in (D–I) indicate projections of the superfluid flow in the direction indicated by the arrow. (J–L) The classification of the vortices based on their signs and positions: vortices (antivortices) are indicated by blue (green) points; clusters by lines of the same colour; dipoles are linked by red lines. Streamlines of the computed flow are shown in grey.

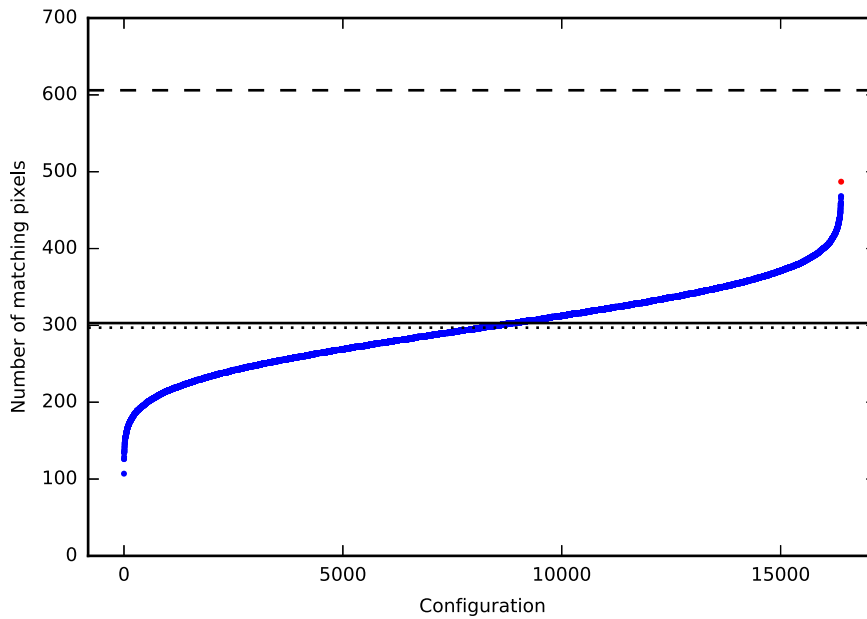


FIGURE 4.4: DETERMINING THE VORTEX SIGN CONFIGURATION.

The vortex sign configuration is determined by maximising the number of pixels (within a 4 pixel radius of a vortex) where the sign of the Bragg signal matches the sign of the flow calculated by a point vortex model. In this case (the same shot used in Figs. 4.2 and 4.3A), there are 14 vortices, with 2^{14} possible sign configurations, and the signal has been compared on 606 pixels (dashed line). The number of matching pixels are shown here, sorted from worst to best match, resulting in a symmetric signal due to the symmetry of configurations. The average number of matching pixels across all possible configurations is 297 (dotted line), just below half of all pixels (solid line), and the best match (red) was 487, corresponding to the configuration shown in Fig. 4.3].

4.3 ANALYSING THE VORTEX DISTRIBUTION

With the knowledge of the location and sign of each vortex in an experiment, we wish to measure several observables, and investigate the statistics of these over the repeated measurements of each combination of grid size and hold time. For each measurement, we take the mean value over the repeated measurements, with an uncertainty given by the standard error of the mean (s.e.m.). The ‘early time’ values of the key observables are compared for each grid size in Fig. 4.5, which give insight into the distributions produced by each grid. These early time values are taken by averaging the results from the three shortest hold times, 0.5 s, 1.0 s and 1.5 s. Similarly, ‘late time’ averages over 4.0 s, 4.5 s and 5.0 s hold times are shown for the measurements, to highlight their evolution. The dynamics of these observables will be shown later for each grid in Figs. 4.10, 4.11, 4.12, 4.13 and 4.14.

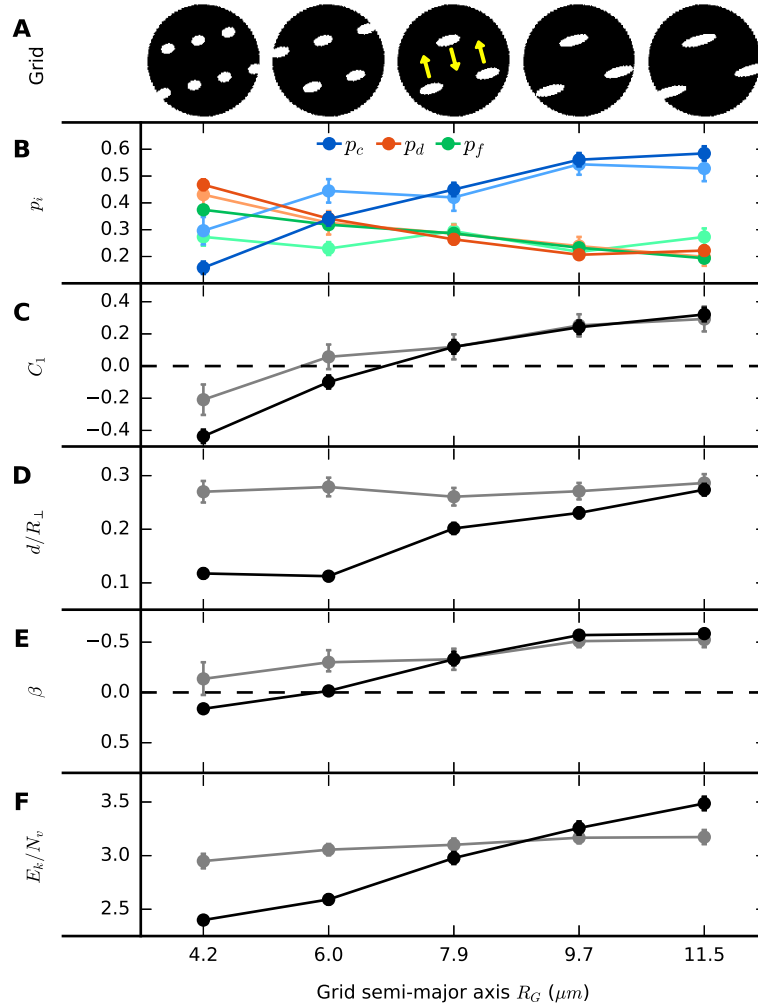


FIGURE 4.5: VORTICES AT POSITIVE AND NEGATIVE TEMPERATURES.

Vortex configuration data, time-averaged across early ($t \leq 1.5$ s, dark points) and late ($t \geq 4$ s, light points) hold times after the grids have passed through the BEC, for each grid used. (A) The grid configurations used are shown one third of the way through the 0.5 s sweep. White areas have high laser intensity, repelling the atoms and move through the BEC in the directions indicated by yellow arrows on the 7.9 μm grid (see also Fig. 4.1A). (B) Classified vortex populations of clustered (blue), dipole (red) and free (green) vortices. (C) Correlation function C_1 . (D) Dipole moment, scaled by the trap radius R_\perp . (E) Inverse temperature of the vortices, β . Positive (negative) values are scaled by the critical temperature $|\beta_{\text{BKT}}|$ ($|\beta_{\text{EBC}}|$). (F) Incompressible kinetic energy (in units of $\rho\kappa^2/4\pi$, where ρ is the superfluid density and $\kappa = h/m$ is the unit of circulation). Data in (B), (C), (D) and (F) are the mean \pm s.e.m. calculated from 10 to 25 measurements at each hold time, though most error bars fall within the points plotted.

4.3.1 Incompressible kinetic energy

Given that we have computed a reconstruction of the full velocity field, it is straightforward to calculate the incompressible part of the kinetic energy, and a spectrum of the incompressible kinetic energy density (see §1.2.6, [107]). We generate an ideal density profile of the condensate by estimating it as a uniform disc with a $2\ \mu\text{m}$ Gaussian blur. We imprint vortices using the vortex core ansatz (1.30), with a healing length $\xi = 0.8\ \mu\text{m}$. This is computed on a grid of 2048×2048 pixels, corresponding to a spatial domain of $800\ \mu\text{m} \times 800\ \mu\text{m}$, ensuring that we capture wavenumbers $k = 2\pi/r$ ranging from beyond the trap scale to below the healing length. The one-dimensional spectral density is then given by the radially averaging the Fourier transform of the density-weighted velocity field [107] into 1024 k bins and dividing by the number of vortices. We calculate the energies in units of $E_0 = \rho\kappa^2/4\pi$.

To generate spectra of the ensemble average over repeated experiments for each grid, we average the energy per vortex spectra for each hold time, which are shown for each grid in panel E of Figs. 4.10–4.14. The averaged spectra typically show a k^{-3} scaling for wavenumbers $k > 1/\xi$, which corresponds to the shape of the vortex core [107], and so is not necessarily indicative of an enstrophy cascade. At lower wavenumbers, down to the system size, the spectra appear to scale as k^{-1} , which is associated with the far-field flow of a vortex. In the intermediate regime, the spectra curve to join the two power-law-like regions. If an energy cascade is present, it would be expected to present itself as $k^{-5/3}$ scaling in this intermediate region. While some of our spectra appear to briefly follow this power-law, the region does not typically span a large range of length scales, and is hard to distinguish from a smooth curve between the high- and low-wavenumber regions. As discussed in §1.3.2.1, it is hard to make any interpretations of cascade processes from these spectra.

In some cases, we also see an increase in energy on the scale of the trap size. For finer grids, this appears to grow dynamically, while it is present from early hold times for coarser grids. A comparison of the early-time spectra is shown in Fig. 4.6, where measurements from the first three hold times (0.5 s, 1.0 s and 1.5 s) have been averaged for each grid. The presence of this ‘hump’ is indicative of the presence of large-scale flows, as produced by clusters of like-signed vortices [115].

To the low-wavenumber side of this energy maxima, the spectrum is predicted to scale as k in a random configuration, but as k^3 for a clustered configuration due to the ‘hump’ [243]. While we see this low- k scaling get steeper, from an approximate k scaling in the initial conditions of the finest grids, it does not appear to exceed k^2 . This less extreme scaling is possibly due to the low vortex numbers in

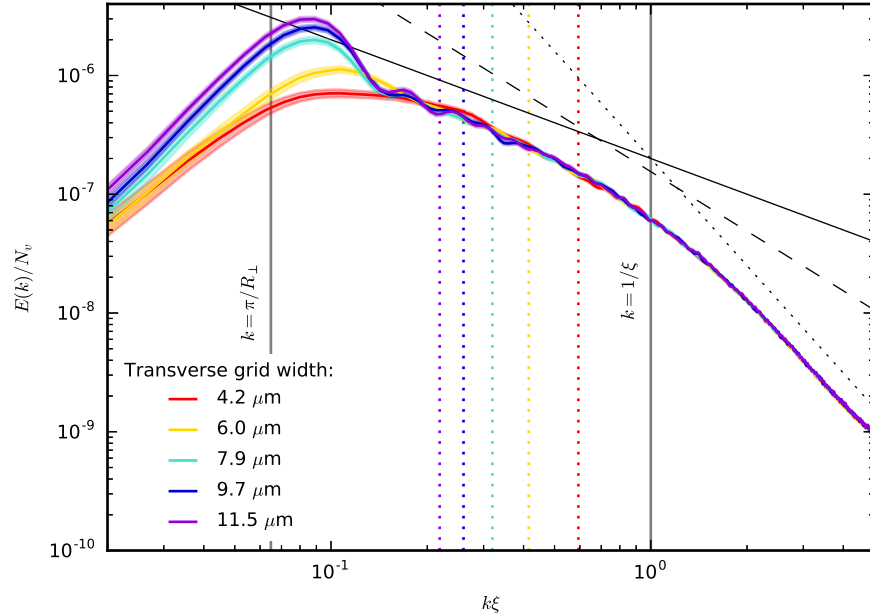


FIGURE 4.6: ENERGY SPECTRA FOR VARYING GRID SPACINGS.

Energy spectra (in units of $\rho\kappa^2/4\pi$) are averaged over early times for each grid size. As the grid becomes larger, an increase in energy is observed on scales on the order of the system size ($2R_\perp$). This is consistent with the observations of Fig. 4.5, indicating the clustering of same-sign vortices. Dotted vertical lines show $k = \pi/R_G$ for each grid used. Power-law scaling proportional to k^{-1} (solid line), $k^{-5/3}$ (dashed line) and k^{-3} (dotted line) are shown as guides to the eye. These are associated with the far field of an isolated vortex, the inertial range scaling expected in the presence of an energy cascade, and the shape of the imprinted vortex cores, respectively.

the experiment in comparison to the numerical simulations, and the small scale of the clusters formed.

The total incompressible kinetic energy can be calculated by integrating the spectrum over k , or, alternatively, integrating the square of the density-weighted velocity field (both were confirmed to give the same result). We have also independently computed the incompressible kinetic energy using the point vortex Hamiltonian (1.33). In this case, a trap-dependent energy shift, $\nu(N_v)$, needs to be applied to obtain the total energy [115]. Simulations performed by Andrew showed that this offset should be between 2 to 4 times $\rho\kappa^2/4\pi N_v$ for our system. When comparing to the numerically calculated energies, we find that a value of $\nu \approx 3.3 \rho\kappa^2/4\pi N_v$ produces consistent values.

4.3.2 Vortex cluster detection

As it is difficult to interpret energy spectra in $\mathcal{2DQT}$, we also looked at the statistical properties of the distribution of vortex signs, to make

measures of the degree of clustering. We utilise the vortex classification algorithm in the form described by Valani et al. [56], outlined in §1.3.2.2, to uniquely assign each vortex as belonging to a cluster, a dipole pair, or as a free vortex. Using these classifications, we find that as anticipated in §4.1, vortices generated by a fine grid are predominantly in dipole pairs, whereas vortices generated by a coarse grid are predominantly clustered. Figure 4.5 shows that the relative populations of dipole pairs decreases as the grid size increases, while the proportion of clustered vortices increases. We also see a slight increase in the clustered fraction over time for 6.0 μm grid (Fig. 4.11), which corresponds to the development of long-wavelength energy seen in the spectra.

As a secondary measure of clustering, we calculate the nearest-neighbour vortex correlation function C_1 , using Eq. (1.40). As discussed in §1.3.2.2, C_1 gives positive values for configurations dominated by clusters, and negative values for configurations dominated by dipoles. Note that the point at which C_1 crosses zero does not quite coincide with infinite temperature for small vortex numbers, instead crossing at slightly negative temperatures [234]. As seen in Figs. 4.5, 4.10–4.14, C_1 follows a similar trend to the classified vortex cluster fraction.

We also calculated the dipole moment (1.41) for each run of the experiment. This was seen to follow a similar trend to the cluster fraction and correlation function, with the notable exception that it remains high when these other measures appear to break down at the longest hold times for the finer grids. The dipole moment appears to evolve toward a common value for all grids. It is likely that this is due to the small final vortex numbers, where the large intervortex spacings dominate this measurement.

4.3.3 Thermometry

To analyse the observed vortex distributions in terms of Onsager’s thermodynamic framework, we first assign to them a vortex temperature. Since the turbulent BEC is in a highly non-equilibrium state, the vortex sub-system itself must be well isolated from the embedding fluid (e. g., the phonon bath), and also be in a state of quasiequilibrium, for the temperature to be a valid observable. It is reasonable to assume that this is the case here, since the timescale on which vortices move (and redistribute themselves) is much shorter than the timescales on which vortex–sound interactions become important.

In Ref. [242], vortices were assumed to be in a state of quasiequilibrium when the classified vortex populations (in particular the number of clustered vortices, N_c) began following a power-law as a function of the total number of vortices, i. e., $N_c \propto N_v^\alpha$. In our data, such power-law fits are less robust due to the comparably small range of vortex

numbers. Instead, we have used a criterion based on comparing the average distance moved by a vortex between each annihilation event. The time taken for a vortex to move by the mean inter-vortex spacing, $\langle l \rangle = R_{\perp} / \sqrt{N_v}$, traveling at an average speed of $v_{\text{avg}} = \hbar / (m \langle l \rangle)$ [248] is given by $t_{\langle l \rangle} = \langle l \rangle / v_{\text{avg}}$. When re-analyzing the data from Ref. [242], the point at which the mean time between vortex–antivortex annihilations, $t_{\text{ann}} = 2 / \partial_t N_v$, becomes longer than $t_{\langle l \rangle}$ always occurs shortly after the onset of the power-law scaling. We calculate t_{ann} for our data by taking the derivative of a cubic spline fit to the average $N_v(t)$ data for each grid. We find that $t_{\langle l \rangle} < t_{\text{ann}}$ for all grids and hold times, and therefore conclude that the vortices are in a quasiequilibrium for all data taken. As such, the vortices should always have a well-defined temperature in our experimental configurations.

Given the quasiequilibrium condition is met, and we have assigned vortex classifications, we can now calculate a vortex temperature [242]. Vortex thermometry curves $p_c^{\text{MC}}(\beta)$, $p_d^{\text{MC}}(\beta)$ and $p_f^{\text{MC}}(\beta)$ for the fractional populations of vortices that are in clusters, in dipole pairs and free, respectively, were generated by Andrew, using the same techniques as in Ref. [242], but for systems with lower vortex numbers, $N_v^{\text{MC}} = \{4, 6, 8, 10, 14, 20\}$, shown in Fig. 4.7. We fit to the set of Monte Carlo (MC) curves with N_v^{MC} closest to the ensemble average N_v for the experimental data. It should also be noted that the thermometry curves are generated assuming no net polarisation. In any given shot, we have polarisations of up to ± 6 , though the net polarisation averaged across repeated experiments approaches zero.

To assign a temperature, we first smooth the temperature curves using a Savitzky–Golay filter. We then take the root mean square difference,

$$R_{c,d}(\beta) = \sqrt{\Delta_c(\beta)^2 + \Delta_d(\beta)^2} \quad (4.7)$$

between the thermometry curves and the ensemble average measurement of the cluster fraction, $\Delta_c(\beta) = p_c^{\text{MC}}(\beta) - p_c$, and dipole fraction, $\Delta_d(\beta) = p_d^{\text{MC}}(\beta) - p_d$. The global minimum of (4.7) is taken to correspond to the measured β for each configuration. Since $p_c^{\text{MC}}(\beta)$ [$p_d^{\text{MC}}(\beta)$] monotonically decreases [increases] with increasing β (i.e. as β becomes more positive—note the inverted scale in our figures, consistent with Ramsey’s convention [265]), we estimate the uncertainty in the measurement of β by recalculating it with the extremes of the uncertainties in p_c and p_d , calculating β^{\pm} with p_c^{\mp} and p_d^{\pm} , where superscripts represent the upper (+) and lower (−) bounds of uncertainty (given by the s.e.m. for p_c and p_d). This uncertainty estimate is shown graphically in Fig. 4.8. Fits to the thermometry curves for each hold time after each grid are shown in Fig. 4.9. While we fit to only the dipole and cluster fractions, the fraction of free vortices generally lies close to the theoretical curve too. Note that we have scaled all positive inverse temperatures by the critical temperature

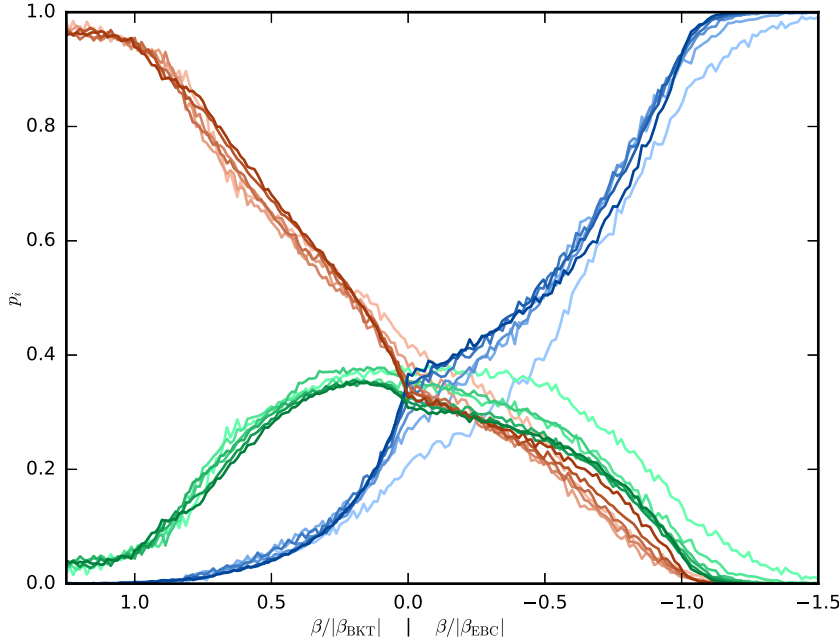


FIGURE 4.7: THERMOMETRY CURVES. Vortex thermometry curves $p_c(\beta)$ (blue), $p_d(\beta)$ (red) and $p_f(\beta)$ (green) are shown for $N_v^{MC} = \{4, 6, 8, 10, 14, 20\}$ (lightest to darkest, corresponding to Fig. 4.9). The positive (negative) temperature axis is scaled by the critical temperature $|\beta_{BKT}|$ ($|\beta_{EBC}|$). The curves are qualitatively similar, though the crossing of the populations is seen to shift slightly to more negative temperatures for lower vortex number.

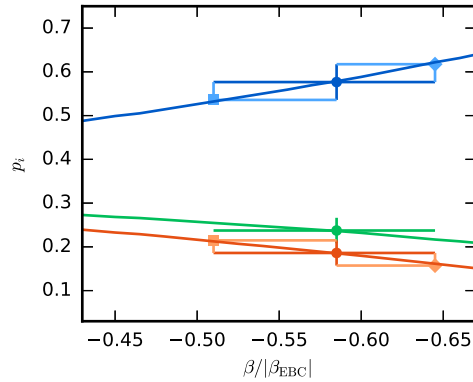


FIGURE 4.8: UNCERTAINTY IN TEMPERATURE MEASUREMENTS. An example temperature fit, including uncertainty estimate, for the ensemble averaged data for the $9.7 \mu\text{m}$ grid at 1.5 s hold time. The mean cluster and dipole fractions (blue and red dots respectively) are used to place the data on the temperature axis by finding the best fit to the corresponding thermometry curves. The uncertainty is then taken based on the *s.e.m.* of the cluster and dipole populations (vertical error bars). The upper bound of β is taken using the lower bound of the cluster fraction (light blue square) and the upper bound of the dipole fraction (light red square), while the opposite extremes are used to find the lower bound of β (light coloured diamonds). While the free vortex fraction (green dot) is not used in fitting, the data typically agrees well with the theoretical curve.

$|\beta_{\text{BKT}}|$ (1.12) corresponding to the BKT transition, and negative temperatures by $|\beta_{\text{EBC}}|$ (1.13) corresponding to the EBC (supercondensation) transition (see §1.1.2.4).

4.3.4 Vortex decay process

To investigate the vortex decay process, it would be ideal to fit the decay ansatz (1.42), with the optional addition of the extra factor of $N^{1/2}$ due to a background velocity correction (as discussed in §1.3.2.4), to the experimental data. Unfortunately there are no analytic solutions to (1.42) when all one- to four-body terms are included, and the low vortex numbers and temporal resolution of the data make it essentially meaningless to take a numerical derivative of the decay curves. However, generally one term in (1.42) will dominate at a given point in time, and when plotted on log-log axes in Fig. 4.15 (also shown in panel G of Figs. 4.10–4.14), the vortex decay curves do appear to follow linear segments.

Lines in Fig. 4.15 show guides to the eye at the power-laws expected for two- to four-body loss processes (black), as well as the corresponding adjusted laws taking into account the background velocity field of the vortices (grey). The initial decay rates appear to be consistent with a three-body loss process for all but the coarsest grid, which appears to involve a four-body process. With the limited data it is hard to determine if the velocity correction is required, though the $9.7\ \mu\text{m}$ grid appears to be closer to this curve (if not four-body for $t < 1\ \text{s}$). The $4.2\ \mu\text{m}$ and $6.0\ \mu\text{m}$ grids transition to a slope consistent with a two-body process with the velocity correction within the first second (in fact, the earlier three-body rate is not particularly convincing, as it only holds for 2 and 3 data points respectively), while the coarser grids transition to this rate after around 2 s (though they could be transitioning to a three-body curve without the velocity correction).

In the picture of NTFPs, the decay data are suggestive of an initial condition that has critically slowed dynamics, close to a NTFP, followed by a shift to faster evolution, possibly toward thermal equilibrium. To further investigate this, we inspected the dynamics of the mean nearest-neighbour inter-vortex spacing, shown in panel H of Figs. 4.10–4.14. The data for all grids appear to begin with a $t^{1/5}$ scaling, which matches the anomalous fixed point found by Karl and Gasenzer [248]. The vortices produced by finer grids transition to a $t^{1/2}$ scaling, associated with a Gaussian fixed point, while the vortices produced by the coarse grid remain close to the anomalous fixed point throughout the 5 s evolution.

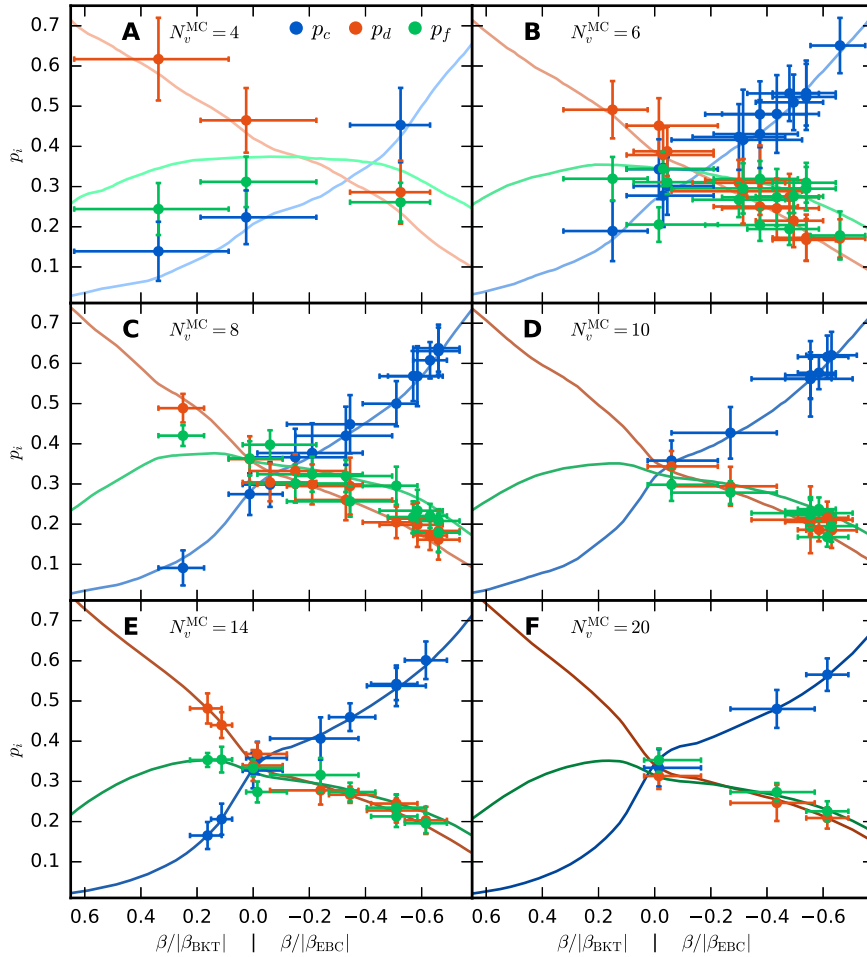


FIGURE 4.9: TEMPERATURE ASSIGNMENT.

Thermometry curves generated by MC simulations (solid lines) for $N_v^{\text{MC}} =$ (A) 4, (B) 6, (C) 8, (D) 10, (E) 14 and (F) 20 vortices. The curves are used to assign a temperature to the ensemble averaged vortex configuration at each hold time after the sweep of each obstacle grid, by a least squares fit of the mean fractional populations of clustered (blue) and dipole (red) vortices to the corresponding thermometry curves with N_v^{MC} closest to N_v . Free vortices (green) are not used in the fit, but typically fall close to the MC curve.

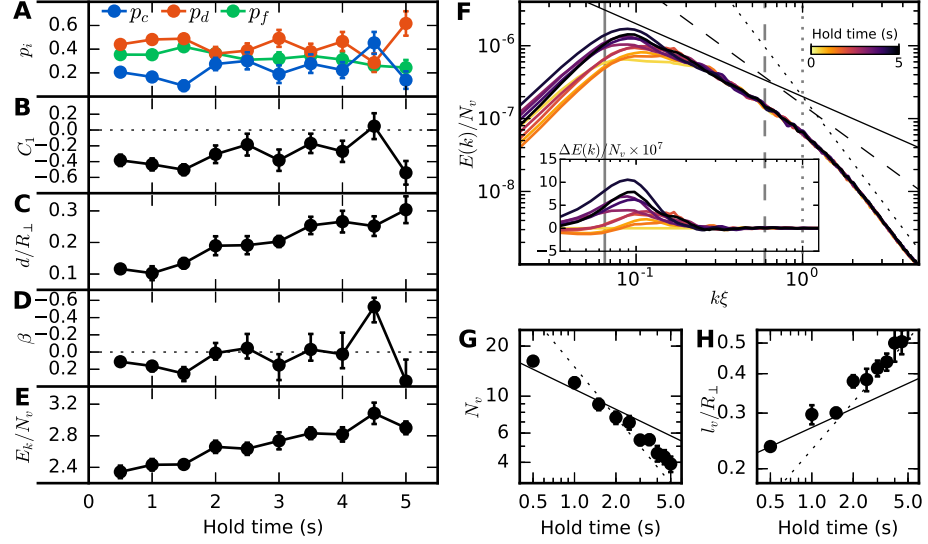


FIGURE 4.10: 4.2 μm GRID DYNAMICAL EVOLUTION.

(A) Evolution of the classified vortex populations of clustered (blue), dipole (red) and free (green) vortices over 5 s. (B) Nearest neighbour correlation function. (C) Dipole moment, scaled by R_\perp . (D) Inverse temperature of the vortices, β . Note that the lower error bar on the $t = 5$ s data point extends to $\beta = 0.6$. (E) Total incompressible kinetic energy per vortex (in units of $\rho\kappa^2/4\pi$). (F) Incompressible kinetic energy spectrum (in units of $\rho\kappa^2/4\pi$). For wavenumbers $k\xi > 1$ (dotted grey vertical line) the spectrum appears to scale as k^{-3} (dotted black line) corresponding to the shape of a vortex core, while k^{-1} (solid black line) corresponds to the far field of an isolated vortex [107]. A $k^{-5/3}$ scaling (dashed black line), shown for comparison, would be expected for an energy cascade in a driven classical system [34, 47]. Note that the power-laws are shown as a guide to the eye. The grid scale $k = \pi/R_G$ is indicated by the dashed grey vertical line, where $R_G = 4.2 \mu\text{m}$ is the semi-major axis of the grid. The system size $k = \pi/R_\perp$ is indicated by the solid grey vertical line. The inset shows the difference $\Delta E(k)/N_v$ from the 0.5 s hold time spectrum. (G) Vortex number decay. Lines show $t^{-2/5}$ (solid) and t^{-1} (dotted) power-laws for reference. (H) Mean inter-vortex separation. Lines show $t^{1/5}$ (solid) and $t^{1/2}$ (dotted) power-laws for reference. Points in (A–C), (E), (G) and (H) are the mean \pm s.e.m. Lines in (F) join the mean k -binned values. The s.e.m. is on the order of the separation between lines.

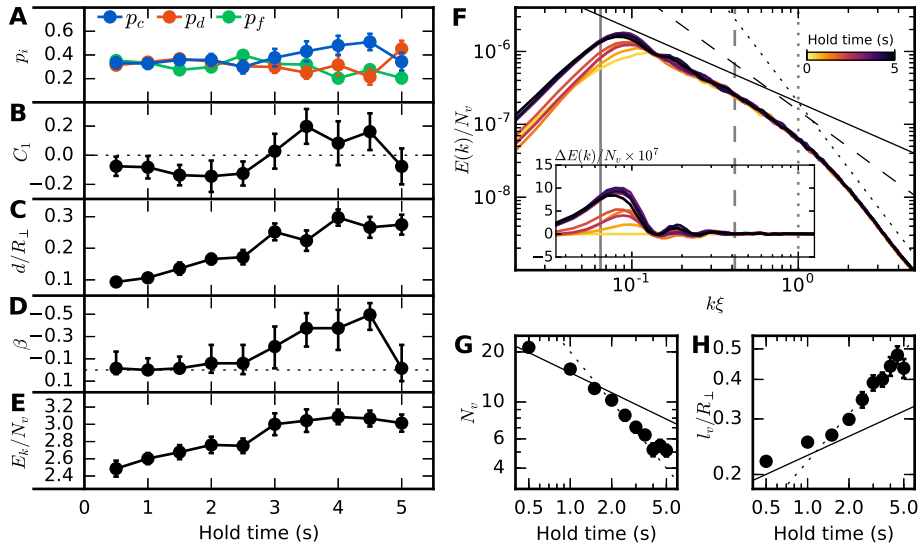


FIGURE 4.11: $6.0 \mu\text{m}$ GRID DYNAMICAL EVOLUTION. The same measurements as Fig. 4.10, taken for $R_G = 6.0 \mu\text{m}$. Here the configuration is seen to begin with an equal weighting of dipoles and clusters, and evolves to a more clustered configuration.

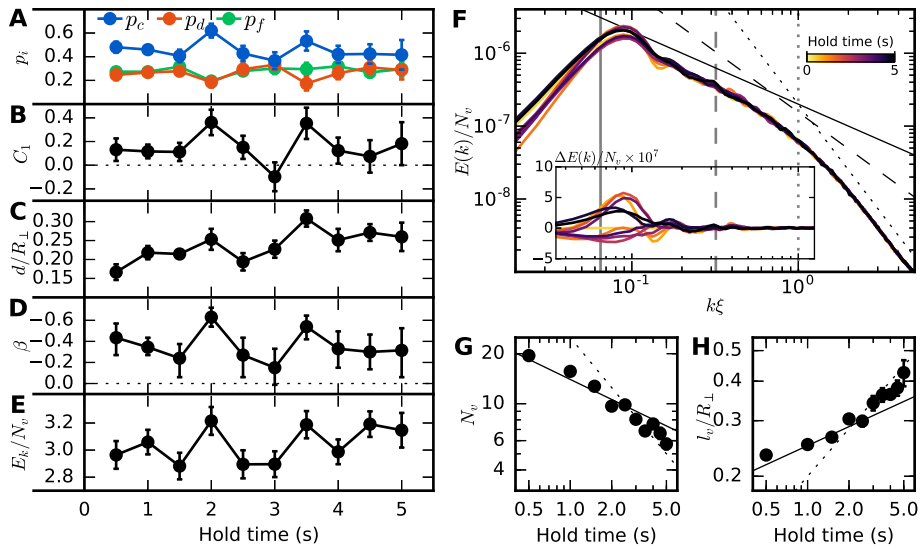
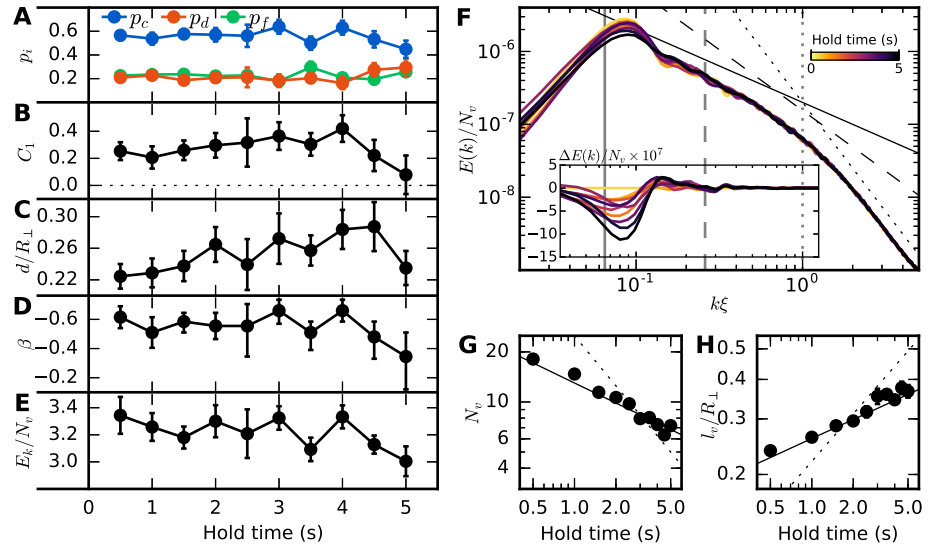
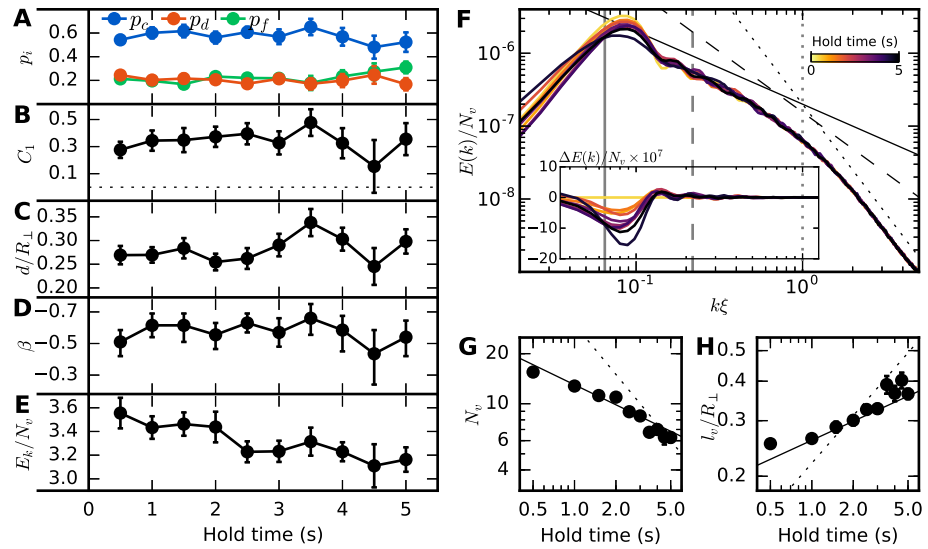


FIGURE 4.12: $7.9 \mu\text{m}$ GRID DYNAMICAL EVOLUTION. The same measurements as Fig. 4.10, taken for $R_G = 7.9 \mu\text{m}$. In this case, very little overall evolution occurs across the measurements, though the energy per vortex does increase slightly at low wavenumbers.


 FIGURE 4.13: $9.7 \mu\text{m}$ GRID DYNAMICAL EVOLUTION.

The same measurements as Fig. 4.10, taken for $R_G = 9.7 \mu\text{m}$. Here all measurements show a slight decrease over time, indicating that damping effects play a significant role.


 FIGURE 4.14: $11.5 \mu\text{m}$ GRID DYNAMICAL EVOLUTION.

The same measurements as Fig. 4.10, taken for $R_G = 11.5 \mu\text{m}$. This configuration shows a decrease in energy per vortex and correlation function, though the cluster fraction does not reduce significantly.

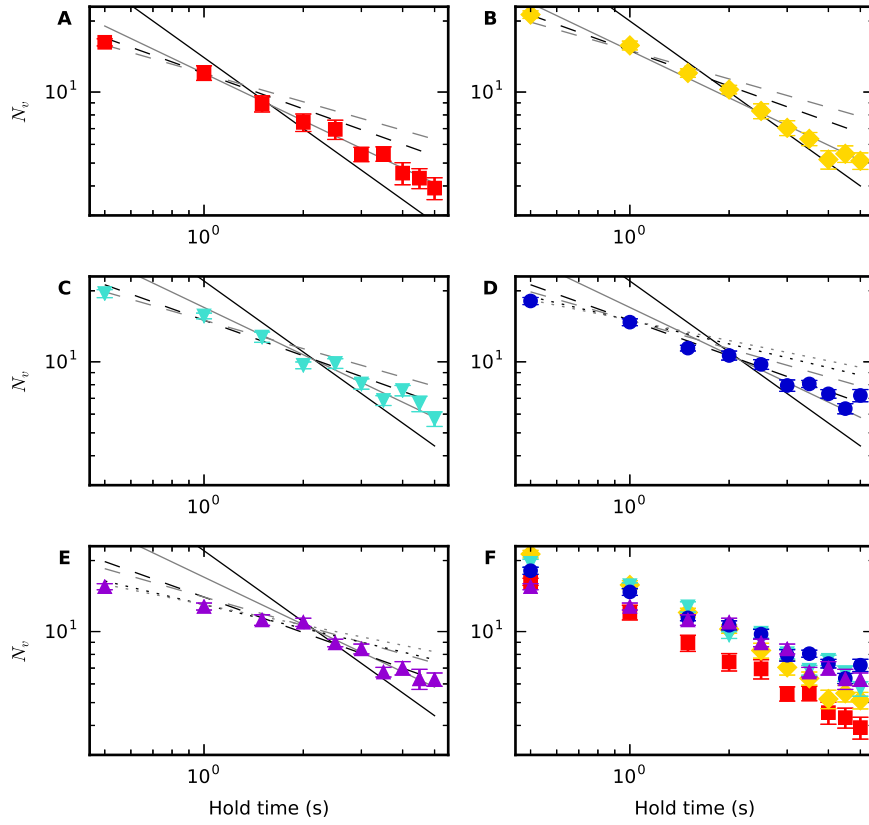


FIGURE 4.15: VORTEX NUMBER DECAY.

The mean vortex number plotted as a function of hold time for each grid size. Panels (A–E) show the data from grids with semi-major axis lengths $4.2\ \mu\text{m}$, $6.0\ \mu\text{m}$, $7.9\ \mu\text{m}$, $9.7\ \mu\text{m}$ and $11.5\ \mu\text{m}$ respectively, with all grids shown in (F) for comparison. The data show locally linear regions on the log-log scale, indicative of power-law scaling. Lines in black show the expected scaling of decay processes that are dominated by four-body losses [$\propto t^{-1/3}$, dotted line, not shown in (A–C)], three-body losses ($\propto t^{-1/2}$, dashed line) and two-body losses ($\propto t^{-1}$, solid line). Lines in grey show these loss processes when the background velocity field due to the vortices is taken into consideration (four-body $\propto t^{-2/7}$ [dotted], three-body $\propto t^{-2/5}$ [dashed] and two-body $\propto t^{-2/3}$ [solid]).

4.4 DISCUSSION

Figure 4.5 shows that as the grid size is increased, the vortex distribution swaps from being dominated by dipole pairs to clusters of same-sign vortices. This increase in cluster fraction produces a corresponding increase in the correlation function, temperature and energy per vortex. The increase in energy is seen in Fig. 4.6 to correspond to an increase in long-range (low k) energy.

The dynamics generally depend on the initial condition. For the $6.0\ \mu\text{m}$ grid (Fig. 4.11), the distribution begins with approximately equal weightings of clusters, dipoles and free vortices, corresponding to an inverse temperature close to zero [242]. During the hold time after the grid sweep, the vortex distribution evolves to a state with a higher clustered fraction (Fig. 4.11A), and to a negative temperature (Fig. 4.11D). The correlation function evolves from negative to positive values (Fig. 4.11B), and the dipole moment grows (Fig. 4.11C). The incompressible kinetic energy spectrum shows a buildup of energy at scales on the order of the system size (Fig. 4.11F), leading to an increase in the mean energy per vortex over time (Fig. 4.11E). These observations point towards the existence of an inverse energy cascade in decaying turbulence, driving the system toward ordered Onsager vortex states. Similar behaviour is observed for the finest grid ($4.2\ \mu\text{m}$, Fig. 4.10), though the consistently lower vortex number leads to higher fluctuations in the classified populations and hence vortex temperature.

For both of these fine grids, at the latest hold times the cluster fraction and correlation fraction both drop. We associate this with the breakdown of evaporative heating, as the total number of dipoles remaining becomes too low. In the $6\ \mu\text{m}$ case, the vortex number does not appear to change for the last three hold times, and so it is likely that as these small remaining clusters lose energy to phonons and thermal friction their configuration becomes slightly more dipole-like than cluster-like (consider a configuration of two vortices and two antivortices spread evenly across a BEC in two clusters—it would not take a significant change in positions for the classification to swap from a pair of clusters to a pair of dipoles). The observation that the dipole moment and energy per vortex (including the height of the low-wavenumber bump) do not change significantly in these cases adds weight to this argument, as the large-scale structure of the flow will not be impacted by these small vortex position changes whereas the correlation function and classification algorithm will be. This process is consistent with the system evolution being slowed as it approaches a NTFP, before rapidly moving to thermal equilibrium as the remaining vortices in the system decay (see, e. g., Fig. 1 in Ref. [241]).

For the $7.9\ \mu\text{m}$ grid, very little dynamic evolution is observed. In this case, around half the vortices are clustered. There is still a slight

increase in energy per vortex and dipole moment over time, however this is not significant, compared with the finer grids. The $9.7\ \mu\text{m}$ and $11.5\ \mu\text{m}$ grids show similar evolution to the $7.9\ \mu\text{m}$, however in these cases there is a *decrease* in energy per vortex. We believe that evaporative heating is suppressed in such configurations due to the small number of dipole pairs and free vortices available to annihilate. As there is no significant evaporative heating in this regime, the cooling effects of phonons and the thermal background dominate the vortex thermodynamics. We expect that for higher vortex numbers, with a similar cluster fraction, evaporative heating would in fact play a significant role, as the correspondingly higher number of vortices remaining in dipole pairs would allow for annihilations, as seen in numerical studies [115, 129].

The vortex decay rates seen in Fig. 4.15 are somewhat surprising. Numerical results with finite temperature considerations tend to show decay dominated by two-body losses [129, 246], though Baggaley and Barenghi [249] saw three-body loss at early times with dissipation. It is worth noting, however, that the numerical results that found only two-body loss rates were performed in a harmonic trap, whereas the results that showed three-body loss were performed in periodic boundary conditions, neither of which match the bounded uniform trap used here. These numerical results were also performed with a random initial condition. As it is likely that the vortex decay process is determined by the vortex configuration, it is not appropriate to compare these with the coarser grid data, which has a large cluster fraction.

The vortex decay data could be interpreted as follows: For configurations with many dipole pairs, at finite (BEC) temperatures, the decay is predominantly due to two-body losses, with the background velocity field of the system's vortices affecting the process. For configurations with higher cluster fractions, the decay is slowed due to the spatial separation of vortices and antivortices. The three-body rate seen in this case may be, as suggested by Karl and Gasenzer [248], due to the small number of dipole pairs in the system interacting with other vortices as they travel around the clusters. For even higher cluster fractions, the vortices and antivortices are further separated, and so the decay is even slower. The apparent loss rate may actually be due to this separation rather than a true four-body process. To highlight this, in the highly clustered state formed by Gauthier et al. [259], in which every vortex is a member of one of two giant clusters, there was almost no vortex loss at all over 10 s. The speed-up of the loss in our clustered data at later times may be due to the decay of the BEC, increasing the level of damping in the system over time.

In summary, we have generated two-dimensional grid turbulence using a range of grid barriers of different dimensions. The absolute temperature of the resulting vortex distributions was measured to

range from positive through to negative values, with evidence of evaporative heating in their time evolution. Along with simultaneous observations by Gauthier et al. [259], this is the first experimental observation of NATs in the context of Onsager's statistical description of two-dimensional turbulence.

CONCLUSIONS

5.1 SUMMARY

In this thesis, I have presented a brief introduction to the field of quantum turbulence (QT), a description of an apparatus for performing 2DQT experiments, and the results of one such set of experiments. Direct predictions of QT dynamics, as with the classical case, are hampered by the non-linear nature of the fluid motion. A statistical approach can be taken, however analysis of the kinetic energy spectrum, which has proved extremely powerful in classical systems, can be difficult in the quantum case. In 2DQT, due to the quantised nature of vortices, statistics of their configuration, such as the degree of clustering of same-sign vortices, or the decay rate of the total vortex number, provide alternative measures of the dynamical processes.

Bose–Einstein condensates (BECs) are well suited to studying 2DQT, as their confinement can readily be tuned such that vortex motion in one dimension is effectively frozen out. In Chapter 2 I introduced the Monash University ‘KRb’ BEC apparatus, which was constructed during my candidature. This apparatus involves a vacuum chamber, to isolate the BEC from room temperature atoms, and lasers and magnetic fields to cool, trap, manipulate and probe the atoms. We can trap and cool both ^{87}Rb and ^{41}K , though the experiments presented in this thesis used only ^{87}Rb . Chapter 3 discussed the ways in which we can provide the 2D confinement, and generate vortices in the resulting planar BECs. Ultimately, we used a holographically generated Hermite–Gaussian (HG) mode to provide the tight confinement, and a digital micromirror device (DMD) to provide a hard-walled radial trap. This DMD was also used to project moving obstacles onto the trap to generate vortices.

In Chapter 4 I presented the results of experiments probing the degree of vortex clustering as the geometry of the stirring obstacles was changed. To allow the clustering to be probed, a recently developed vortex sign detection technique was implemented. A ‘vortex temperature’ was assigned to the resulting configurations, revealing dynamical heating of the vortices, and configurations with negative absolute temperatures (NATs). These results confirmed Onsager’s description of vortex clustering, and the presence of NAT states in a confined 2D vortex system.

5.2 OUTLOOK

The experimental investigation of 2DQT is still in its infancy. Vortex generation, manipulation, imaging and sign detection techniques are constantly improving, enabling more complex and detailed experiments. Here I will discuss ways in which I believe future experiments could build on the work of this thesis.

Repeating the experiments of [Chapter 4](#) with larger numbers of vortices may enhance the effect of the evaporative heating mechanism, providing further evidence for the role it plays in the turbulent dynamics. To achieve this, higher density BECs may be required, to reduce the vortex core size, and larger trapping areas, to allow a higher total vortex number. This in turn presents new challenges, balancing imaging resolution with a wide field of view, to allow the vortex cores to be imaged across the whole trap, as well as the Bragg-scattered components for sign detection. As the trap size is increased, the time taken for the scattered components to separate will also increase, and may result in vortex cores expanding and overlapping, reducing the ability to identify them. Higher densities also tend to result in collisions between the scattered and unscattered components, distorting both distributions. Perhaps with a careful choice of time-of-flight expansion, and higher order Bragg scattering, these could be overcome, allowing the technique to be used in larger, denser traps. Transferring the scattered atoms to a different internal state via a Raman transfer could also allow their imaging without requiring spatial separation of the components. Alternatively, the vortex gyroscope imaging technique may prove to be a more appropriate approach to vortex sign detection in such conditions, or the development of high frame-rate non-destructive imaging may allow vortex signs to be determined by tracking their trajectories.

The use of a [DMD](#) to provide both a uniform radial potential, and the generation of dynamic obstacles for vortex generation, coupled with vortex sign detection techniques, opens the way for the investigation of new trapping geometries and vortex generation and manipulation techniques. Novel stirring and pinning potentials could be generated, allowing ‘designer’ vortex configurations. This may allow highly repeatable initial vortex configurations to be generated on demand. This will enable more detailed probing of vortex interactions, and the generation of turbulent states with initial conditions that can be matched in simulations.

One such possibility could be the study of the thermalisation process of vortex temperatures. In a sufficiently large trap, it is conceivable that a differential temperature could be generated, by preferentially generating vortex dipole pairs in one region, and clusters in another. Defining a ‘local’ temperature, based on the vortex configuration within a finite range, could help to answer questions such

as *what happens when negative temperature vortices interact with positive temperature vortices?* Of course the expectation would be that the resulting thermal state will have a temperature somewhere between the two initial states, however, could the infinite temperatures separating the two impact the result? Evaporative heating in the dipole-dominated side would also complicate the process, leading to a hotter equilibrium temperature (it may not be clear when the system has finished mixing between the hot and cold sides, as it would continue to evolve, though there may be characteristic timescales that can be observed to identify the two processes). This would serve as an interesting system to study heat conduction and particle transport (of the vortices). Other interesting configurations to study could be other ordered states beside dipole pairs and giant clusters—arrays of clusters (or similarly, dipoles of multiquantum vortices) have been a popular initial condition for numerical studies.

While it seems clear that uniform traps support vortex clustering, and harmonic potentials inhibit it, there is a need for further experimental probing of the transition between these two cases. Furthermore, the role of the boundary conditions could be investigated by generating potentials with uniform interiors, surrounded by walls of varying steepness and profile. The nature of vortex loss mechanisms is an open question, and likely depends on both the geometry and the degree of clustering or pairing of the vortices. With DMD-generated potentials, both of these degrees of freedom could be systematically varied to observe the resulting vortex number decay rates.

Another 2D vortex phenomena that is yet to be experimentally realised is the EBC transition. While it is unlikely that the evaporative heating of vortices will lead to the crossing of this transition from a turbulent system, it should be possible to observe the crossing from the cooling of a condensed initial condition. This could be achieved by observing the intervortex spacing during the breakdown of a large multiquantum vortex.

Beyond 2D, the world of 3DQT awaits. While liquid helium features a more favourable range of length scales than atomic BECs, it is interesting to probe the universality of turbulence by looking at different types of systems. The tunability of BECs also allows more flexibility than helium, and could, for example, allow an investigation of the role of the vortex core size. In 3D, the detection of tangled vortex cores will be the biggest challenge. Tomographic imaging of basic vortex configurations has been demonstrated, using thin sheets of repump light to allow imaging of particular planes of a BEC [168]. While only relatively coarse slices have been used to date, these could be narrowed, allowing greater resolution in this third dimension. This could possibly be achieved beyond the scale of a focussed light sheet (which would become limited by the Rayleigh range), e. g., by using a two-photon process to pump atoms into the imaging state, with a

pair of partially overlapped, appropriately shaped beams, or other methods that are highly sensitive to a laser intensity (perhaps recent work on super-resolved imaging of optical lattices [330, 331] could be adapted to this geometry).

It may also be possible to extend this technique to resolve the in-plane superfluid flow by implementing velocity-selective Bragg spectroscopy of the whole cloud, before rapidly imaging slices. Correlating this one dimensional flow direction with vortex core locations may be enough to uniquely determine the circulation of each vortex, allowing full vortex circulation tomography. A second pair of Bragg beams, in the imaging plane, orthogonal to the first, may help this identification process by providing 2D flow direction information.

BECs also offer the ability to smoothly cross from 2D to 3D. This raises the interesting question of when does the cascade process change direction? The intermediate ‘thick’ 2D regime may have similarities to atmospheric dynamics, where both forward and inverse cascades can be seen depending on what length scale is being integrated over.

While the scalar condensates considered in this thesis have vortices with quantised flow, the additional degrees of freedom of spinor BECs facilitate more exotic features. Spin quantum turbulence has been studied theoretically in spin-1 systems [182], and the first experiments have recently been performed [332, 333]. For spin-2 systems, non-Abelian vortices have been predicted, which could lead to non-Abelian quantum turbulence [334, 335]. Experiments in these systems would presumably be complex, requiring both state- and velocity-selective imaging, preferably simultaneously, however with the continual improvements to imaging techniques this may be within the realm of possibility.

Ultimately, the work in this thesis is a stepping stone toward these more detailed experiments, which may lead to refinements of numerical and analytic descriptions of QT. It is hoped that this may in turn guide the description of the dynamical processes involved in classical fluids, leading to a better understanding of one of the greatest unsolved problems in classical physics, and the world around us.

BIBLIOGRAPHY

- [1] F. Dalfovo, S. Giorgini, L. P. Pitaevskii *et al.*, ‘Theory of Bose–Einstein condensation in trapped gases’, *Reviews of Modern Physics*, vol. 71, no. 3, pp. 463–512, 1999. DOI: [10.1103/RevModPhys.71.463](https://doi.org/10.1103/RevModPhys.71.463) (cit. on pp. 1, 15).
- [2] C. J. Pethick and H. Smith, *Bose–Einstein Condensation in Dilute Gases*. Cambridge University Press, 2002 (cit. on pp. 1, 15).
- [3] L. P. Pitaevskii and S. Stringari, *Bose–Einstein Condensation*. Oxford: Clarendon Press, 2003 (cit. on pp. 1, 15).
- [4] O. Reynolds, ‘XXIX. An experimental investigation of the circumstances which determine whether the motion of water shall be direct or sinuous, and of the law of resistance in parallel channels’, *Philosophical Transactions of the Royal Society of London*, vol. 174, pp. 935–982, 1883. DOI: [10.1098/rstl.1883.0029](https://doi.org/10.1098/rstl.1883.0029) (cit. on p. 1).
- [5] W. H. Bell, ‘The influence of turbulence on drag’, *Ocean Engineering*, vol. 6, no. 3, pp. 329–340, 1979. DOI: [10.1016/0029-8018\(79\)90021-0](https://doi.org/10.1016/0029-8018(79)90021-0) (cit. on p. 1).
- [6] H. E. A. Van den Akker, ‘The details of turbulent mixing process and their simulation’, in *Advances in Chemical Engineering*, ser. Computational Fluid Dynamics, G. B. Marin, Ed., vol. 31, Academic Press, 2006, pp. 151–229. DOI: [10.1016/S0065-2377\(06\)31003-4](https://doi.org/10.1016/S0065-2377(06)31003-4) (cit. on p. 1).
- [7] Z. Han and R. D. Reitz, ‘Turbulence modeling of internal combustion engines using RNG κ - ϵ models’, *Combustion Science and Technology*, vol. 106, no. 4-6, pp. 267–295, 1995. DOI: [10.1080/00102209508907782](https://doi.org/10.1080/00102209508907782) (cit. on p. 1).
- [8] T. Gasenzer, B. Nowak and D. Sexty, ‘Charge separation in reheating after cosmological inflation’, *Physics Letters B*, vol. 710, no. 4, pp. 500–503, 2012. DOI: [10.1016/j.physletb.2012.03.031](https://doi.org/10.1016/j.physletb.2012.03.031) (cit. on pp. 1, 42).
- [9] P. Arnold and G. D. Moore, ‘QCD plasma instabilities: The non-Abelian cascade’, *Physical Review D*, vol. 73, no. 2, p. 025006, 2006. DOI: [10.1103/PhysRevD.73.025006](https://doi.org/10.1103/PhysRevD.73.025006) (cit. on pp. 1, 42).
- [10] S. Ghashghaie, W. Breymann, J. Peinke *et al.*, ‘Turbulent cascades in foreign exchange markets’, *Nature*, vol. 381, no. 6585, pp. 767–770, 1996. DOI: [10.1038/381767a0](https://doi.org/10.1038/381767a0) (cit. on p. 1).

- [11] R. B. Scott and F. Wang, 'Direct evidence of an oceanic inverse kinetic energy cascade from satellite altimetry', *Journal of Physical Oceanography*, vol. 35, no. 9, pp. 1650–1666, 2005. DOI: [10.1175/JPO2771.1](https://doi.org/10.1175/JPO2771.1) (cit. on pp. 1, 12).
- [12] R. Tulloch, J. Marshall, C. Hill *et al.*, 'Scales, growth rates, and spectral fluxes of baroclinic instability in the ocean', *Journal of Physical Oceanography*, vol. 41, no. 6, pp. 1057–1076, 2011. DOI: [10.1175/2011JPO4404.1](https://doi.org/10.1175/2011JPO4404.1) (cit. on pp. 1, 12).
- [13] G. D. Nastrom, K. S. Gage and W. H. Jasperson, 'Kinetic energy spectrum of large- and mesoscale atmospheric processes', *Nature*, vol. 310, no. 5972, pp. 36–38, 1984. DOI: [10.1038/310036a0](https://doi.org/10.1038/310036a0) (cit. on pp. 1, 12).
- [14] A. R. Vasavada and A. P. Showman, 'Jovian atmospheric dynamics: An update after Galileo and Cassini', *Reports on Progress in Physics*, vol. 68, no. 8, p. 1935, 2005. DOI: [10.1088/0034-4885/68/8/R06](https://doi.org/10.1088/0034-4885/68/8/R06) (cit. on pp. 1, 12).
- [15] R. M. B. Young and P. L. Read, 'Forward and inverse kinetic energy cascades in Jupiter's turbulent weather layer', *Nature Physics*, vol. 13, no. 11, pp. 1135–1140, 2017. DOI: [10.1038/nphys4227](https://doi.org/10.1038/nphys4227) (cit. on pp. 1, 12).
- [16] A. Adriani, A. Mura, G. Orton *et al.*, 'Clusters of cyclones encircling Jupiter's poles', *Nature*, vol. 555, no. 7695, pp. 216–219, 2018. DOI: [10.1038/nature25491](https://doi.org/10.1038/nature25491) (cit. on pp. 1, 12).
- [17] J. Westerweel, G. E. Elsinga and R. J. Adrian, 'Particle image velocimetry for complex and turbulent flows', *Annual Review of Fluid Mechanics*, vol. 45, no. 1, pp. 409–436, 2013. DOI: [10.1146/annurev-fluid-120710-101204](https://doi.org/10.1146/annurev-fluid-120710-101204) (cit. on p. 2).
- [18] M. Raffel, C. E. Willert, F. Scarano *et al.*, *Particle Image Velocimetry: A Practical Guide*. Springer, 2018 (cit. on p. 2).
- [19] G. P. Bewley, M. S. Paoletti, K. R. Sreenivasan *et al.*, 'Characterization of reconnecting vortices in superfluid helium', *Proceedings of the National Academy of Sciences*, vol. 105, no. 37, pp. 13 707–13 710, 2008. DOI: [10.1073/pnas.0806002105](https://doi.org/10.1073/pnas.0806002105) (cit. on pp. 2, 28).
- [20] D. Celik and S. W. Van Sciver, 'Tracer particle generation in superfluid helium through cryogenic liquid injection for particle image velocimetry (PIV) applications', *Experimental Thermal and Fluid Science*, vol. 26, no. 8, pp. 971–975, 2002. DOI: [10.1016/S0894-1777\(02\)00204-2](https://doi.org/10.1016/S0894-1777(02)00204-2) (cit. on p. 2).
- [21] S. W. Seo, B. Ko, J. H. Kim *et al.*, 'Observation of vortex-antivortex pairing in decaying 2D turbulence of a superfluid gas', *Scientific Reports*, vol. 7, no. 1, p. 4587, 2017. DOI: [10.1038/s41598-017-04122-9](https://doi.org/10.1038/s41598-017-04122-9) (cit. on pp. 2, 29, 30, 45, 46, 99, 110, 113).
- [22] M. Gad-el Hak, *Flow Control: Passive, Active, and Reactive Flow Management*. Cambridge University Press, 2007 (cit. on p. 3).

- [23] L. da Vinci, 'Studies of flowing water, with notes', in *Royal Collection Trust*, <https://www.royalcollection.org.uk>, circa 1510, RCIN 912660 (cit. on p. 3).
- [24] P. A. Davidson, *Turbulence: An Introduction for Scientists and Engineers*. Oxford: Oxford University Press, 2004 (cit. on pp. 3, 6).
- [25] U. Frisch, *Turbulence: The Legacy of A. N. Kolmogorov*. Cambridge: Cambridge University Press, 1995 (cit. on pp. 3, 6).
- [26] O. Reynolds, 'III. An experimental investigation of the circumstances which determine whether the motion of water shall be direct or sinuous, and of the law of resistance in parallel channels', *Proceedings of the Royal Society of London*, vol. 35, no. 224-226, pp. 84-99, 1883. DOI: [10.1098/rspl.1883.0018](https://doi.org/10.1098/rspl.1883.0018) (cit. on p. 4).
- [27] O. Reynolds, 'IV. On the dynamical theory of incompressible viscous fluids and the determination of the criterion', *Philosophical Transactions of the Royal Society of London A*, vol. 186, pp. 123-164, 1895. DOI: [10.1098/rsta.1895.0004](https://doi.org/10.1098/rsta.1895.0004) (cit. on p. 4).
- [28] L. F. Richardson, *Weather prediction by numerical process*. Cambridge: Cambridge University Press, 1922 (cit. on p. 5).
- [29] A. M. Obukhov, 'On the distribution of energy in the spectrum of turbulent flow', *Doklady Akademii Nauk SSSR*, vol. 32, pp. 22-24, 1941 (cit. on p. 5).
- [30] L. Onsager, 'The distribution of energy in turbulence', in *Physical Review*, vol. 68, Columbia University, New York, 1945, p. 286. DOI: [10.1103/PhysRev.68.281](https://doi.org/10.1103/PhysRev.68.281) (cit. on p. 5).
- [31] C. F. v Weizsäcker, 'Das spektrum der turbulenz bei großen Reynoldsschen zahlen', *Zeitschrift für Physik*, vol. 124, no. 7-12, pp. 614-627, 1948. DOI: [10.1007/BF01668898](https://doi.org/10.1007/BF01668898) (cit. on p. 5).
- [32] W. Heisenberg, 'Zur statistischen theorie der turbulenz', *Zeitschrift für Physik*, vol. 124, no. 7-12, pp. 628-657, 1948. DOI: [10.1007/BF01668899](https://doi.org/10.1007/BF01668899) (cit. on p. 5).
- [33] W. Heisenberg, 'On the theory of statistical and isotropic turbulence', *Proceedings of the Royal Society A*, vol. 195, no. 1042, pp. 402-406, 1948. DOI: [10.1098/rspa.1948.0127](https://doi.org/10.1098/rspa.1948.0127) (cit. on p. 5).
- [34] A. N. Kolmogorov, 'The local structure of turbulence in incompressible viscous fluid for very large Reynolds numbers', *Doklady Akademii Nauk SSSR*, vol. 30, no. 4, pp. 301-305, 1941 (cit. on pp. 5, 128).
- [35] H. von Helmholtz, 'On integrals of the hydrodynamic equations that correspond to vortex motions', *Journal für die reine und angewandte Mathematik*, vol. 55, pp. 25-55, 1858 (cit. on p. 7).

- [36] G. R. Kirchhoff, *Vorlesungen über mathematische Physik*. Leipzig: Teubner, 1876, vol. 1: Mechanik (cit. on p. 7).
- [37] C. C. Lin, 'On the motion of vortices in two dimensions—I. Existence of the Kirchhoff–Routh function', *Proceedings of the National Academy of Sciences*, vol. 27, no. 12, pp. 570–575, 1941. DOI: [10.1073/pnas.27.12.570](https://doi.org/10.1073/pnas.27.12.570) (cit. on p. 7).
- [38] C. C. Lin, *On the Motion of Vortices in Two Dimensions*. University of Toronto Press, 1943 (cit. on p. 7).
- [39] L. Onsager, 'Statistical hydrodynamics', *Il Nuovo Cimento*, vol. 6, no. 2, pp. 279–287, 1949. DOI: [10.1007/BF02780991](https://doi.org/10.1007/BF02780991) (cit. on pp. 7, 8, 19, 31).
- [40] R. A. Smith and T. M. O'Neil, 'Nonaxisymmetric thermal equilibria of a cylindrically bounded guiding-center plasma or discrete vortex system', *Physics of Fluids B: Plasma Physics*, vol. 2, no. 12, pp. 2961–2975, 1990. DOI: [10.1063/1.859362](https://doi.org/10.1063/1.859362) (cit. on p. 7).
- [41] J. Binney and S. Tremaine, *Galactic Dynamics: Second Edition*. Princeton University Press, 2011 (cit. on p. 7).
- [42] G. L. Eyink and K. R. Sreenivasan, 'Onsager and the theory of hydrodynamic turbulence', *Reviews of Modern Physics*, vol. 78, no. 1, pp. 87–135, 2006. DOI: [10.1103/RevModPhys.78.87](https://doi.org/10.1103/RevModPhys.78.87) (cit. on p. 8).
- [43] S. F. Edwards and J. B. Taylor, 'Negative temperature states of two-dimensional plasmas and vortex fluids', *Proceedings of the Royal Society A*, vol. 336, no. 1606, pp. 257–271, 1974. DOI: [10.1098/rspa.1974.0018](https://doi.org/10.1098/rspa.1974.0018) (cit. on p. 9).
- [44] J. Fröhlich and D. Ruelle, 'Statistical mechanics of vortices in an inviscid two-dimensional fluid', *Communications in Mathematical Physics*, vol. 87, no. 1, pp. 1–36, 1982. DOI: [10.1007/BF01211054](https://doi.org/10.1007/BF01211054) (cit. on p. 9).
- [45] T. D. Lee, 'Difference between turbulence in a two-dimensional fluid and in a three-dimensional fluid', *Journal of Applied Physics*, vol. 22, no. 4, pp. 524–524, 1951. DOI: [10.1063/1.1699997](https://doi.org/10.1063/1.1699997) (cit. on p. 9).
- [46] R. Fjørtoft, 'On the changes in the spectral distribution of kinetic energy for twodimensional, nondivergent flow', *Tellus*, vol. 5, no. 3, pp. 225–230, 1953. DOI: [10.3402/tellusa.v5i3.8647](https://doi.org/10.3402/tellusa.v5i3.8647) (cit. on p. 9).
- [47] R. H. Kraichnan, 'Inertial ranges in two-dimensional turbulence', *The Physics of Fluids*, vol. 10, no. 7, pp. 1417–1423, 1967. DOI: [10.1063/1.1762301](https://doi.org/10.1063/1.1762301) (cit. on pp. 10, 128).

- [48] G. K. Batchelor, 'Computation of the energy spectrum in homogeneous two-dimensional turbulence', *The Physics of Fluids*, vol. 12, no. 12, pp. II-233, 1969. DOI: [10.1063/1.1692443](https://doi.org/10.1063/1.1692443) (cit. on p. 10).
- [49] R. H. Kraichnan and D. Montgomery, 'Two-dimensional turbulence', *Reports on Progress in Physics*, vol. 43, no. 5, p. 547, 1980. DOI: [10.1088/0034-4885/43/5/001](https://doi.org/10.1088/0034-4885/43/5/001) (cit. on p. 11).
- [50] V. L. Berezinskii, 'Destruction of long-range order in one-dimensional and two-dimensional systems having a continuous symmetry group I. Classical systems', *Soviet Journal of Experimental and Theoretical Physics*, vol. 32, p. 493, 1971 (cit. on p. 11).
- [51] V. L. Berezinskii, 'Destruction of long-range order in one-dimensional and two-dimensional systems possessing a continuous symmetry group. II. Quantum systems', *Soviet Journal of Experimental and Theoretical Physics*, vol. 34, p. 610, 1972 (cit. on p. 11).
- [52] J. M. Kosterlitz and D. J. Thouless, 'Ordering, metastability and phase transitions in two-dimensional systems', *Journal of Physics C: Solid State Physics*, vol. 6, no. 7, p. 1181, 1973. DOI: [10.1088/0022-3719/6/7/010](https://doi.org/10.1088/0022-3719/6/7/010) (cit. on p. 11).
- [53] D. R. Nelson and J. M. Kosterlitz, 'Universal jump in the superfluid density of two-dimensional superfluids', *Physical Review Letters*, vol. 39, no. 19, pp. 1201-1205, 1977. DOI: [10.1103/PhysRevLett.39.1201](https://doi.org/10.1103/PhysRevLett.39.1201) (cit. on p. 11).
- [54] J. A. Viccelli, 'Equilibrium properties of the condensed states of a turbulent two-dimensional neutral vortex system', *Physics of Fluids*, vol. 7, no. 6, pp. 1402-1417, 1995. DOI: [10.1063/1.868528](https://doi.org/10.1063/1.868528) (cit. on pp. 11, 22).
- [55] X. Yu, T. P. Billam, J. Nian *et al.*, 'Theory of the vortex-clustering transition in a confined two-dimensional quantum fluid', *Physical Review A*, vol. 94, no. 2, p. 023602, 2016. DOI: [10.1103/PhysRevA.94.023602](https://doi.org/10.1103/PhysRevA.94.023602) (cit. on pp. 11, 39).
- [56] R. N. Valani, A. J. Groszek and T. P. Simula, 'Einstein-Bose condensation of Onsager vortices', *New Journal of Physics*, vol. 20, no. 5, p. 053038, 2018. DOI: [10.1088/1367-2630/aac0bb](https://doi.org/10.1088/1367-2630/aac0bb) (cit. on pp. 11, 36, 37, 39, 123).
- [57] K. S. Fine, A. C. Cass, W. G. Flynn *et al.*, 'Relaxation of 2D turbulence to vortex crystals', *Physical Review Letters*, vol. 75, no. 18, pp. 3277-3280, 1995. DOI: [10.1103/PhysRevLett.75.3277](https://doi.org/10.1103/PhysRevLett.75.3277) (cit. on p. 12).

- [58] D. Z. Jin and D. H. E. Dubin, 'Regional maximum entropy theory of vortex crystal formation', *Physical Review Letters*, vol. 80, no. 20, pp. 4434–4437, 1998. DOI: [10.1103/PhysRevLett.80.4434](https://doi.org/10.1103/PhysRevLett.80.4434) (cit. on p. 12).
- [59] D. A. Schecter, D. H. E. Dubin, K. S. Fine *et al.*, 'Vortex crystals from 2D Euler flow: Experiment and simulation', *Physics of Fluids*, vol. 11, no. 4, pp. 905–914, 1999. DOI: [10.1063/1.869961](https://doi.org/10.1063/1.869961) (cit. on p. 12).
- [60] Y. Kaspi, E. Galanti, W. B. Hubbard *et al.*, 'Jupiter's atmospheric jet streams extend thousands of kilometres deep', *Nature*, vol. 555, no. 7695, pp. 223–226, 2018. DOI: [10.1038/nature25793](https://doi.org/10.1038/nature25793) (cit. on p. 12).
- [61] T. Guillot, Y. Miguel, B. Militzer *et al.*, 'A suppression of differential rotation in Jupiter's deep interior', *Nature*, vol. 555, no. 7695, pp. 227–230, 2018. DOI: [10.1038/nature25775](https://doi.org/10.1038/nature25775) (cit. on p. 12).
- [62] <http://photojournal.jpl.nasa.gov> (cit. on p. 13).
- [63] H. Kellay and W. I. Goldburg, 'Two-dimensional turbulence: A review of some recent experiments', *Reports on Progress in Physics*, vol. 65, no. 5, p. 845, 2002. DOI: [10.1088/0034-4885/65/5/204](https://doi.org/10.1088/0034-4885/65/5/204) (cit. on pp. 12, 13).
- [64] H. J. H. Clercx and G. J. F. van Heijst, 'Two-dimensional Navier–Stokes turbulence in bounded domains', *Applied Mechanics Reviews*, vol. 62, no. 2, pp. 020802–020802–25, 2009. DOI: [10.1115/1.3077489](https://doi.org/10.1115/1.3077489) (cit. on p. 12).
- [65] H. Kellay, 'Hydrodynamics experiments with soap films and soap bubbles: A short review of recent experiments', *Physics of Fluids*, vol. 29, no. 11, p. 111113, 2017. DOI: [10.1063/1.4986003](https://doi.org/10.1063/1.4986003) (cit. on p. 12).
- [66] D. H. Kelley and N. T. Ouellette, 'Onset of three-dimensionality in electromagnetically driven thin-layer flows', *Physics of Fluids*, vol. 23, no. 4, p. 045103, 2011. DOI: [10.1063/1.3570685](https://doi.org/10.1063/1.3570685) (cit. on p. 12).
- [67] G. J.F. v. Heijst, 'Shallow flows: 2D or not 2D?', *Environmental Fluid Mechanics*, vol. 14, no. 5, pp. 945–956, 2014. DOI: [10.1007/s10652-013-9305-4](https://doi.org/10.1007/s10652-013-9305-4) (cit. on p. 12).
- [68] H. Xia and N. Francois, 'Two-dimensional turbulence in three-dimensional flows', *Physics of Fluids*, vol. 29, no. 11, p. 111107, 2017. DOI: [10.1063/1.5000863](https://doi.org/10.1063/1.5000863) (cit. on p. 12).
- [69] J. Sommeria, 'Experimental study of the two-dimensional inverse energy cascade in a square box', *Journal of Fluid Mechanics*, vol. 170, pp. 139–168, 1986. DOI: [10.1017/S0022112086000836](https://doi.org/10.1017/S0022112086000836) (cit. on pp. 12, 15).

- [70] J. Paret, D. Marteau, O. Paireau *et al.*, 'Are flows electromagnetically forced in thin stratified layers two dimensional?', *Physics of Fluids*, vol. 9, no. 10, pp. 3102–3104, 1997. DOI: [10.1063/1.869419](https://doi.org/10.1063/1.869419) (cit. on p. 12).
- [71] Y. Couder, 'Two-dimensional grid turbulence in a thin liquid film', *Journal de Physique Lettres*, vol. 45, no. 8, pp. 353–360, 1984. DOI: [10.1051/jphyslet:01984004508035300](https://doi.org/10.1051/jphyslet:01984004508035300) (cit. on p. 13).
- [72] M. Gharib and P. Derango, 'A liquid film (soap film) tunnel to study two-dimensional laminar and turbulent shear flows', *Physica D: Nonlinear Phenomena*, vol. 37, no. 1, pp. 406–416, 1989. DOI: [10.1016/0167-2789\(89\)90145-0](https://doi.org/10.1016/0167-2789(89)90145-0) (cit. on p. 13).
- [73] H. Kellay, X.-l. Wu and W. I. Goldburg, 'Experiments with turbulent soap films', *Physical Review Letters*, vol. 74, no. 20, pp. 3975–3978, 1995. DOI: [10.1103/PhysRevLett.74.3975](https://doi.org/10.1103/PhysRevLett.74.3975) (cit. on p. 13).
- [74] Y. Couder, J. M. Chomaz and M. Rabaud, 'On the hydrodynamics of soap films', *Physica D: Nonlinear Phenomena*, vol. 37, no. 1, pp. 384–405, 1989. DOI: [10.1016/0167-2789\(89\)90144-9](https://doi.org/10.1016/0167-2789(89)90144-9) (cit. on p. 13).
- [75] J. M. Chomaz and B. Cathalau, 'Soap films as two-dimensional classical fluids', *Physical Review A*, vol. 41, no. 4, pp. 2243–2245, 1990. DOI: [10.1103/PhysRevA.41.2243](https://doi.org/10.1103/PhysRevA.41.2243) (cit. on p. 13).
- [76] M. Rivera, P. Vorobieff and R. E. Ecke, 'Turbulence in flowing soap films: Velocity, vorticity, and thickness fields', *Physical Review Letters*, vol. 81, no. 7, pp. 1417–1420, 1998. DOI: [10.1103/PhysRevLett.81.1417](https://doi.org/10.1103/PhysRevLett.81.1417) (cit. on p. 13).
- [77] P. Vorobieff, M. Rivera and R. E. Ecke, 'Soap film flows: Statistics of two-dimensional turbulence', *Physics of Fluids*, vol. 11, no. 8, pp. 2167–2177, 1999. DOI: [10.1063/1.870078](https://doi.org/10.1063/1.870078) (cit. on p. 13).
- [78] M. A. Rutgers, X.-l. Wu, R. Bhagavatula *et al.*, 'Two-dimensional velocity profiles and laminar boundary layers in flowing soap films', *Physics of Fluids*, vol. 8, no. 11, pp. 2847–2854, 1996. DOI: [10.1063/1.869105](https://doi.org/10.1063/1.869105) (cit. on p. 13).
- [79] B. K. Martin, X. L. Wu, W. I. Goldburg *et al.*, 'Spectra of decaying turbulence in a soap film', *Physical Review Letters*, vol. 80, no. 18, pp. 3964–3967, 1998. DOI: [10.1103/PhysRevLett.80.3964](https://doi.org/10.1103/PhysRevLett.80.3964) (cit. on p. 13).
- [80] J. Paret and P. Tabeling, 'Experimental observation of the two-dimensional inverse energy cascade', *Physical Review Letters*, vol. 79, no. 21, pp. 4162–4165, 1997. DOI: [10.1103/PhysRevLett.79.4162](https://doi.org/10.1103/PhysRevLett.79.4162) (cit. on pp. 14, 15).

- [81] J. Paret, M.-C. Jullien and P. Tabeling, 'Vorticity statistics in the two-dimensional enstrophy cascade', *Physical Review Letters*, vol. 83, no. 17, pp. 3418–3421, 1999. DOI: [10.1103/PhysRevLett.83.3418](https://doi.org/10.1103/PhysRevLett.83.3418) (cit. on pp. 14, 15).
- [82] M. A. Rutgers, 'Forced 2D turbulence: Experimental evidence of simultaneous inverse energy and forward enstrophy cascades', *Physical Review Letters*, vol. 81, no. 11, pp. 2244–2247, 1998. DOI: [10.1103/PhysRevLett.81.2244](https://doi.org/10.1103/PhysRevLett.81.2244) (cit. on pp. 14, 15).
- [83] J. Paret and P. Tabeling, 'Intermittency in the two-dimensional inverse cascade of energy: Experimental observations', *Physics of Fluids*, vol. 10, no. 12, pp. 3126–3136, 1998. DOI: [10.1063/1.869840](https://doi.org/10.1063/1.869840) (cit. on p. 15).
- [84] A. Einstein, 'Quantentheorie des einatomigen idealen gases, zweite abhandlung', *Verlag der Königlich-Preussischen Akademie der Wissenschaften*, vol. 1, p. 3, 1925 (cit. on p. 15).
- [85] S. N. Bose, 'Plancks gesetz und lichtquantenhypothese', *Zeitschrift für Physik*, vol. 26, no. 1, pp. 178–181, 1924. DOI: [10.1007/BF01327326](https://doi.org/10.1007/BF01327326) (cit. on p. 15).
- [86] P. Kapitza, 'Viscosity of liquid helium below the λ -point', *Nature*, vol. 141, p. 74, 1938. DOI: [10.1038/141074a0](https://doi.org/10.1038/141074a0) (cit. on p. 15).
- [87] J. F. Allen and A. D. Misener, 'Flow of liquid helium II', *Nature*, vol. 141, p. 75, 1938. DOI: [10.1038/141075a0](https://doi.org/10.1038/141075a0) (cit. on p. 15).
- [88] F. London, 'The λ -phenomenon of liquid helium and the Bose–Einstein degeneracy', *Nature*, vol. 141, p. 643, 1938. DOI: [10.1038/141643a0](https://doi.org/10.1038/141643a0) (cit. on p. 15).
- [89] L. Tisza, 'Transport phenomena in helium II', *Nature*, vol. 141, no. 3577, p. 913, 1938. DOI: [10.1038/141913a0](https://doi.org/10.1038/141913a0) (cit. on p. 15).
- [90] L. Landau, 'Theory of the superfluidity of helium II', *Physical Review*, vol. 60, no. 4, p. 356, 1941. DOI: [10.1103/PhysRev.60.356](https://doi.org/10.1103/PhysRev.60.356) (cit. on pp. 15, 19).
- [91] N. Bogoliubov, 'On the theory of superfluidity', *Journal of Physics*, vol. 11, no. 1, p. 23, 1947 (cit. on pp. 15, 18).
- [92] O. Penrose, 'CXXXVI. On the quantum mechanics of helium II', *The London, Edinburgh, and Dublin Philosophical Magazine and Journal of Science*, vol. 42, p. 1373, 1951. DOI: [10.1080/14786445108560954](https://doi.org/10.1080/14786445108560954) (cit. on p. 15).
- [93] O. Penrose and L. Onsager, 'Bose–Einstein condensation and liquid helium', *Physical Review*, vol. 104, no. 3, pp. 576–584, 1956. DOI: [10.1103/PhysRev.104.576](https://doi.org/10.1103/PhysRev.104.576) (cit. on p. 15).

- [94] M. H. Anderson, J. R. Ensher, M. R. Matthews *et al.*, ‘Observation of Bose–Einstein condensation in a dilute atomic vapor’, *Science*, vol. 269, no. 5221, pp. 198–201, 1995. DOI: [10.1126/science.269.5221.198](https://doi.org/10.1126/science.269.5221.198) (cit. on p. 15).
- [95] K. B. Davis, M. O. Mewes, M. R. Andrews *et al.*, ‘Bose–Einstein condensation in a gas of sodium atoms’, *Physical Review Letters*, vol. 75, no. 22, pp. 3969–3973, 1995. DOI: [10.1103/PhysRevLett.75.3969](https://doi.org/10.1103/PhysRevLett.75.3969) (cit. on p. 15).
- [96] C. C. Bradley, C. A. Sackett, J. J. Tollett *et al.*, ‘Evidence of Bose–Einstein condensation in an atomic gas with attractive interactions’, *Physical Review Letters*, vol. 75, no. 9, pp. 1687–1690, 1995. DOI: [10.1103/PhysRevLett.75.1687](https://doi.org/10.1103/PhysRevLett.75.1687) (cit. on p. 15).
- [97] E. P. Gross, ‘Structure of a quantized vortex in boson systems’, *Il Nuovo Cimento*, vol. 20, no. 3, pp. 454–477, 1961. DOI: [10.1007/BF02731494](https://doi.org/10.1007/BF02731494) (cit. on p. 15).
- [98] L. P. Pitaevskii, ‘Vortex lines in an imperfect Bose gas’, *Soviet Journal of Experimental and Theoretical Physics*, vol. 13, no. 2, p. 646, 1961 (cit. on p. 15).
- [99] <http://jilawww.colorado.edu/bec/CornellGroup> (cit. on p. 17).
- [100] P. A. M. Dirac, ‘Quantised singularities in the electromagnetic field’, *Proceedings of the Royal Society A*, vol. 133, no. 821, pp. 60–72, 1931. DOI: [10.1098/rspa.1931.0130](https://doi.org/10.1098/rspa.1931.0130) (cit. on p. 19).
- [101] R. P. Feynman, ‘Application of quantum mechanics to liquid helium’, in *Progress in Low Temperature Physics*, C. J. Gorter, Ed., vol. 1, Elsevier, 1955, pp. 17–53. DOI: [10.1016/S0079-6417\(08\)60077-3](https://doi.org/10.1016/S0079-6417(08)60077-3) (cit. on pp. 19, 31).
- [102] F. London, ‘On the problem of the molecular theory of superconductivity’, *Physical Review*, vol. 74, no. 5, pp. 562–573, 1948. DOI: [10.1103/PhysRev.74.562](https://doi.org/10.1103/PhysRev.74.562) (cit. on p. 19).
- [103] F. London, *Superfluids*. New York: John Wiley & Sons, 1950, vol. 1 (cit. on p. 19).
- [104] A. Abrikosov, ‘On the magnetic properties of superconductors of the second group’, *Journal of Experimental and Theoretical Physics*, vol. 5, no. 6, p. 1174, 1957 (cit. on p. 19).
- [105] J. F. Nye and M. V. Berry, ‘Dislocations in wave trains’, *Proceedings of the Royal Society A*, vol. 336, no. 1605, pp. 165–190, 1974. DOI: [10.1098/rspa.1974.0012](https://doi.org/10.1098/rspa.1974.0012) (cit. on p. 19).
- [106] M. F. Andersen, C. Ryu, P. Cladé *et al.*, ‘Quantized rotation of atoms from photons with orbital angular momentum’, *Physical Review Letters*, vol. 97, no. 17, p. 170406, 2006. DOI: [10.1103/PhysRevLett.97.170406](https://doi.org/10.1103/PhysRevLett.97.170406) (cit. on p. 19).

- [107] A. S. Bradley and B. P. Anderson, 'Energy spectra of vortex distributions in two-dimensional quantum turbulence', *Physical Review X*, vol. 2, no. 4, p. 041 001, 2012. DOI: [10.1103/PhysRevX.2.041001](https://doi.org/10.1103/PhysRevX.2.041001) (cit. on pp. 20, 24, 35, 37, 121, 128).
- [108] H. Pu, C. K. Law, J. H. Eberly *et al.*, 'Coherent disintegration and stability of vortices in trapped Bose condensates', *Physical Review A*, vol. 59, no. 2, pp. 1533–1537, 1999. DOI: [10.1103/PhysRevA.59.1533](https://doi.org/10.1103/PhysRevA.59.1533) (cit. on p. 20).
- [109] J. A. M. Huhtamäki, M. Möttönen, T. Isoshima *et al.*, 'Splitting times of doubly quantized vortices in dilute Bose–Einstein condensates', *Physical Review Letters*, vol. 97, no. 11, p. 110 406, 2006. DOI: [10.1103/PhysRevLett.97.110406](https://doi.org/10.1103/PhysRevLett.97.110406) (cit. on p. 20).
- [110] Y. Shin, M. Saba, M. Vengalattore *et al.*, 'Dynamical instability of a doubly quantized vortex in a Bose–Einstein condensate', *Physical Review Letters*, vol. 93, no. 16, p. 160 406, 2004. DOI: [10.1103/PhysRevLett.93.160406](https://doi.org/10.1103/PhysRevLett.93.160406) (cit. on p. 20).
- [111] J. R. Abo-Shaeer, C. Raman, J. M. Vogels *et al.*, 'Observation of vortex lattices in Bose–Einstein condensates', *Science*, vol. 292, no. 5516, pp. 476–479, 2001. DOI: [10.1126/science.1060182](https://doi.org/10.1126/science.1060182) (cit. on pp. 20, 21).
- [112] T. P. Simula, S. M. M. Virtanen and M. M. Salomaa, 'Stability of multiquantum vortices in dilute Bose–Einstein condensates', *Physical Review A*, vol. 65, no. 3, p. 033 614, 2002. DOI: [10.1103/PhysRevA.65.033614](https://doi.org/10.1103/PhysRevA.65.033614) (cit. on p. 20).
- [113] J. A. M. Huhtamäki, M. Möttönen and S. M. M. Virtanen, 'Dynamically stable multiply quantized vortices in dilute Bose–Einstein condensates', *Physical Review A*, vol. 74, no. 6, p. 063 619, 2006. DOI: [10.1103/PhysRevA.74.063619](https://doi.org/10.1103/PhysRevA.74.063619) (cit. on p. 20).
- [114] S. J. Rooney, P. B. Blakie, B. P. Anderson *et al.*, 'Suppression of kelvon-induced decay of quantized vortices in oblate Bose–Einstein condensates', *Physical Review A*, vol. 84, no. 2, p. 023 637, 2011. DOI: [10.1103/PhysRevA.84.023637](https://doi.org/10.1103/PhysRevA.84.023637) (cit. on p. 21).
- [115] T. Simula, M. J. Davis and K. Helmerson, 'Emergence of order from turbulence in an isolated planar superfluid', *Physical Review Letters*, vol. 113, no. 16, p. 165 302, 2014. DOI: [10.1103/PhysRevLett.113.165302](https://doi.org/10.1103/PhysRevLett.113.165302) (cit. on pp. 21, 22, 24, 34, 35, 37, 38, 121, 122, 133).
- [116] A. L. Fetter, 'Vortices in an imperfect Bose gas. IV. Translational velocity', *Physical Review*, vol. 151, no. 1, pp. 100–104, 1966. DOI: [10.1103/PhysRev.151.100](https://doi.org/10.1103/PhysRev.151.100) (cit. on p. 21).

- [117] A. J. Groszek, D. M. Paganin, K. Helmerson *et al.*, ‘Motion of vortices in inhomogeneous Bose–Einstein condensates’, *Physical Review A*, vol. 97, no. 2, p. 023 617, 2018. DOI: [10.1103/PhysRevA.97.023617](https://doi.org/10.1103/PhysRevA.97.023617) (cit. on p. 21).
- [118] Y. B. Pointin and T. S. Lundgren, ‘Statistical mechanics of two-dimensional vortices in a bounded container’, *The Physics of Fluids*, vol. 19, no. 10, pp. 1459–1470, 1976. DOI: [10.1063/1.861347](https://doi.org/10.1063/1.861347) (cit. on p. 22).
- [119] O. Bühler, ‘Statistical mechanics of strong and weak point vortices in a cylinder’, *Physics of Fluids*, vol. 14, no. 7, pp. 2139–2149, 2002. DOI: [10.1063/1.1483305](https://doi.org/10.1063/1.1483305) (cit. on p. 22).
- [120] Y. Yatsuyanagi, Y. Kiwamoto, H. Tomita *et al.*, ‘Dynamics of two-sign point vortices in positive and negative temperature states’, *Physical Review Letters*, vol. 94, no. 5, p. 054 502, 2005. DOI: [10.1103/PhysRevLett.94.054502](https://doi.org/10.1103/PhysRevLett.94.054502) (cit. on p. 22).
- [121] L. M. Pismen, *Vortices in Nonlinear Fields: From Liquid Crystals to Superfluids, from Non-equilibrium Patterns to Cosmic Strings*. Clarendon Press, 1999 (cit. on pp. 22, 23).
- [122] S. V. Nazarenko, ‘Absorption of sound by vortex filaments’, *Physical Review Letters*, vol. 73, no. 13, pp. 1793–1796, 1994. DOI: [10.1103/PhysRevLett.73.1793](https://doi.org/10.1103/PhysRevLett.73.1793) (cit. on p. 23).
- [123] N. G. Parker, A. J. Allen, C. F. Barenghi *et al.*, ‘Coherent cross talk and parametric driving of matter-wave vortices’, *Physical Review A*, vol. 86, no. 1, p. 013 631, 2012. DOI: [10.1103/PhysRevA.86.013631](https://doi.org/10.1103/PhysRevA.86.013631) (cit. on p. 23).
- [124] M. Leadbeater, T. Winiecki, D. C. Samuels *et al.*, ‘Sound emission due to superfluid vortex reconnections’, *Physical Review Letters*, vol. 86, no. 8, pp. 1410–1413, 2001. DOI: [10.1103/PhysRevLett.86.1410](https://doi.org/10.1103/PhysRevLett.86.1410) (cit. on p. 23).
- [125] S. Zuccher, M. Caliari, A. W. Baggaley *et al.*, ‘Quantum vortex reconnections’, *Physics of Fluids*, vol. 24, no. 12, p. 125 108, 2012. DOI: [10.1063/1.4772198](https://doi.org/10.1063/1.4772198) (cit. on p. 23).
- [126] C. A. Jones and P. H. Roberts, ‘Motions in a Bose condensate. IV. Axisymmetric solitary waves’, *Journal of Physics A: Mathematical and General*, vol. 15, no. 8, p. 2599, 1982. DOI: [10.1088/0305-4470/15/8/036](https://doi.org/10.1088/0305-4470/15/8/036) (cit. on p. 23).
- [127] C. A. Jones, S. J. Putterman and P. H. Roberts, ‘Motions in a Bose condensate. V. Stability of solitary wave solutions of non-linear Schrödinger equations in two and three dimensions’, *Journal of Physics A: Mathematical and General*, vol. 19, no. 15, p. 2991, 1986. DOI: [10.1088/0305-4470/19/15/023](https://doi.org/10.1088/0305-4470/19/15/023) (cit. on p. 23).

- [128] N. G. Berloff and C. F. Barenghi, 'Vortex nucleation by collapsing bubbles in Bose–Einstein condensates', *Physical Review Letters*, vol. 93, no. 9, p. 090401, 2004. DOI: [10.1103/PhysRevLett.93.090401](https://doi.org/10.1103/PhysRevLett.93.090401) (cit. on p. 23).
- [129] A. J. Groszek, T. P. Simula, D. M. Paganin *et al.*, 'Onsager vortex formation in Bose–Einstein condensates in two-dimensional power-law traps', *Physical Review A*, vol. 93, no. 4, p. 043614, 2016. DOI: [10.1103/PhysRevA.93.043614](https://doi.org/10.1103/PhysRevA.93.043614) (cit. on pp. 23, 37–40, 42, 133).
- [130] G. Moon, W. J. Kwon, H. Lee *et al.*, 'Thermal friction on quantum vortices in a Bose–Einstein condensate', *Physical Review A*, vol. 92, no. 5, p. 051601, 2015. DOI: [10.1103/PhysRevA.92.051601](https://doi.org/10.1103/PhysRevA.92.051601) (cit. on pp. 23, 24).
- [131] S. Middelkamp, P. J. Torres, P. G. Kevrekidis *et al.*, 'Guiding-center dynamics of vortex dipoles in Bose–Einstein condensates', *Physical Review A*, vol. 84, no. 1, p. 011605, 2011. DOI: [10.1103/PhysRevA.84.011605](https://doi.org/10.1103/PhysRevA.84.011605) (cit. on p. 24).
- [132] R. Navarro, R. Carretero-González, P. J. Torres *et al.*, 'Dynamics of a few corotating vortices in Bose–Einstein condensates', *Physical Review Letters*, vol. 110, no. 22, p. 225301, 2013. DOI: [10.1103/PhysRevLett.110.225301](https://doi.org/10.1103/PhysRevLett.110.225301) (cit. on p. 24).
- [133] A. V. Murray, A. J. Groszek, P. Kuopanportti *et al.*, 'Hamiltonian dynamics of two same-sign point vortices', *Physical Review A*, vol. 93, no. 3, p. 033649, 2016. DOI: [10.1103/PhysRevA.93.033649](https://doi.org/10.1103/PhysRevA.93.033649) (cit. on p. 24).
- [134] J. M. Vaughan and D. V. Willetts, 'Interference properties of a light beam having a helical wave surface', *Optics Communications*, vol. 30, no. 3, pp. 263–267, 1979. DOI: [10.1016/0030-4018\(79\)90350-X](https://doi.org/10.1016/0030-4018(79)90350-X) (cit. on p. 25).
- [135] C. Tamm, 'Frequency locking of two transverse optical modes of a laser', *Physical Review A*, vol. 38, no. 11, pp. 5960–5963, 1988. DOI: [10.1103/PhysRevA.38.5960](https://doi.org/10.1103/PhysRevA.38.5960) (cit. on p. 25).
- [136] J. Leach, M. J. Padgett, S. M. Barnett *et al.*, 'Measuring the orbital angular momentum of a single photon', *Physical Review Letters*, vol. 88, no. 25, p. 257901, 2002. DOI: [10.1103/PhysRevLett.88.257901](https://doi.org/10.1103/PhysRevLett.88.257901) (cit. on p. 25).
- [137] M. Uchida and A. Tonomura, 'Generation of electron beams carrying orbital angular momentum', *Nature*, vol. 464, no. 7289, p. 737, 2010. DOI: [10.1038/nature08904](https://doi.org/10.1038/nature08904) (cit. on p. 25).
- [138] J. Verbeeck, H. Tian and P. Schattschneider, 'Production and application of electron vortex beams', *Nature*, vol. 467, no. 7313, p. 301, 2010. DOI: [10.1038/nature09366](https://doi.org/10.1038/nature09366) (cit. on p. 25).

- [139] B. J. McMorran, A. Agrawal, I. M. Anderson *et al.*, ‘Electron vortex beams with high quanta of orbital angular momentum’, *Science*, vol. 331, no. 6014, pp. 192–195, 2011. DOI: [10.1126/science.1198804](https://doi.org/10.1126/science.1198804) (cit. on p. 25).
- [140] C. W. Clark, R. Barankov, M. G. Huber *et al.*, ‘Controlling neutron orbital angular momentum’, *Nature*, vol. 525, no. 7570, p. 504, 2015. DOI: [10.1038/nature15265](https://doi.org/10.1038/nature15265) (cit. on p. 25).
- [141] K. G. Lagoudakis, M. Wouters, M. Richard *et al.*, ‘Quantized vortices in an exciton–polariton condensate’, *Nature Physics*, vol. 4, no. 9, p. 706, 2008. DOI: [10.1038/nphys1051](https://doi.org/10.1038/nphys1051) (cit. on p. 25).
- [142] W. F. Vinen, ‘The detection of single quanta of circulation in liquid helium II’, *Proceedings of the Royal Society A*, vol. 260, no. 1301, pp. 218–236, 1961. DOI: [10.1098/rspa.1961.0029](https://doi.org/10.1098/rspa.1961.0029) (cit. on p. 25).
- [143] U. Essmann and H. Träuble, ‘The direct observation of individual flux lines in type II superconductors’, *Physics Letters A*, vol. 24, no. 10, pp. 526–527, 1967. DOI: [10.1016/0375-9601\(67\)90819-5](https://doi.org/10.1016/0375-9601(67)90819-5) (cit. on p. 25).
- [144] M. R. Matthews, B. P. Anderson, P. C. Haljan *et al.*, ‘Vortices in a Bose–Einstein condensate’, *Physical Review Letters*, vol. 83, no. 13, pp. 2498–2501, 1999. DOI: [10.1103/PhysRevLett.83.2498](https://doi.org/10.1103/PhysRevLett.83.2498) (cit. on pp. 25, 27).
- [145] B. P. Anderson, ‘Resource article: Experiments with vortices in superfluid atomic gases’, *Journal of Low Temperature Physics*, vol. 161, no. 5-6, pp. 574–602, 2010. DOI: [10.1007/s10909-010-0224-1](https://doi.org/10.1007/s10909-010-0224-1) (cit. on p. 25).
- [146] B. P. Anderson, *BEC vortex project*, <http://becvortex.com> (cit. on p. 25).
- [147] L. D. Landau and E. M. Lifshitz, *Fluid Mechanics*. Oxford: Pergamon, 1987 (cit. on p. 26).
- [148] C. Huepe and M.-E. Brachet, ‘Scaling laws for vortical nucleation solutions in a model of superflow’, *Physica D: Nonlinear Phenomena*, vol. 140, no. 1, pp. 126–140, 2000. DOI: [10.1016/S0167-2789\(99\)00229-8](https://doi.org/10.1016/S0167-2789(99)00229-8) (cit. on p. 26).
- [149] N. G. Berloff and P. H. Roberts, ‘Motions in a Bose condensate: VII. Boundary-layer separation’, *Journal of Physics A: Mathematical and General*, vol. 33, no. 22, p. 4025, 2000. DOI: [10.1088/0305-4470/33/22/307](https://doi.org/10.1088/0305-4470/33/22/307) (cit. on p. 26).
- [150] S. Rica, ‘A remark on the critical speed for vortex nucleation in the nonlinear Schrödinger equation’, *Physica D: Nonlinear Phenomena*, vol. 148, no. 3, pp. 221–226, 2001. DOI: [10.1016/S0167-2789\(00\)00168-8](https://doi.org/10.1016/S0167-2789(00)00168-8) (cit. on p. 26).

- [151] C.-T. Pham, C. Nore and M.-É. Brachet, 'Boundary layers and emitted excitations in nonlinear Schrödinger superflow past a disk', *Physica D: Nonlinear Phenomena*, vol. 210, no. 3, pp. 203–226, 2005. DOI: [10.1016/j.physd.2005.07.013](https://doi.org/10.1016/j.physd.2005.07.013) (cit. on p. 26).
- [152] F. Pinsker and N. G. Berloff, 'Transitions and excitations in a superfluid stream passing small impurities', *Physical Review A*, vol. 89, no. 5, p. 053605, 2014. DOI: [10.1103/PhysRevA.89.053605](https://doi.org/10.1103/PhysRevA.89.053605) (cit. on p. 26).
- [153] G. W. Stagg, N. G. Parker and C. F. Barenghi, 'Quantum analogues of classical wakes in Bose–Einstein condensates', *Journal of Physics B: Atomic, Molecular and Optical Physics*, vol. 47, no. 9, p. 095304, 2014. DOI: [10.1088/0953-4075/47/9/095304](https://doi.org/10.1088/0953-4075/47/9/095304) (cit. on pp. 26, 32).
- [154] C. Raman, M. Köhl, R. Onofrio *et al.*, 'Evidence for a critical velocity in a Bose–Einstein condensed gas', *Physical Review Letters*, vol. 83, no. 13, pp. 2502–2505, 1999. DOI: [10.1103/PhysRevLett.83.2502](https://doi.org/10.1103/PhysRevLett.83.2502) (cit. on p. 26).
- [155] R. Onofrio, C. Raman, J. M. Vogels *et al.*, 'Observation of superfluid flow in a Bose–Einstein condensed gas', *Physical Review Letters*, vol. 85, no. 11, pp. 2228–2231, 2000. DOI: [10.1103/PhysRevLett.85.2228](https://doi.org/10.1103/PhysRevLett.85.2228) (cit. on p. 26).
- [156] S. Inouye, S. Gupta, T. Rosenband *et al.*, 'Observation of vortex phase singularities in Bose–Einstein condensates', *Physical Review Letters*, vol. 87, no. 8, p. 080402, 2001. DOI: [10.1103/PhysRevLett.87.080402](https://doi.org/10.1103/PhysRevLett.87.080402) (cit. on pp. 26, 28).
- [157] T. W. Neely, E. C. Samson, A. S. Bradley *et al.*, 'Observation of vortex dipoles in an oblate Bose–Einstein condensate', *Physical Review Letters*, vol. 104, no. 16, p. 160401, 2010. DOI: [10.1103/PhysRevLett.104.160401](https://doi.org/10.1103/PhysRevLett.104.160401) (cit. on pp. 26, 27, 105).
- [158] W. J. Kwon, G. Moon, S. W. Seo *et al.*, 'Critical velocity for vortex shedding in a Bose–Einstein condensate', *Physical Review A*, vol. 91, no. 5, p. 053615, 2015. DOI: [10.1103/PhysRevA.91.053615](https://doi.org/10.1103/PhysRevA.91.053615) (cit. on p. 26).
- [159] S. Tung, V. Schweikhard and E. A. Cornell, 'Observation of vortex pinning in Bose–Einstein condensates', *Physical Review Letters*, vol. 97, no. 24, p. 240402, 2006. DOI: [10.1103/PhysRevLett.97.240402](https://doi.org/10.1103/PhysRevLett.97.240402) (cit. on p. 26).
- [160] C. Ryu, M. F. Andersen, P. Cladé *et al.*, 'Observation of persistent flow of a Bose–Einstein condensate in a toroidal trap', *Physical Review Letters*, vol. 99, no. 26, p. 260401, 2007. DOI: [10.1103/PhysRevLett.99.260401](https://doi.org/10.1103/PhysRevLett.99.260401) (cit. on p. 26).

- [161] E. C. Samson, K. E. Wilson, Z. L. Newman *et al.*, ‘Deterministic creation, pinning, and manipulation of quantized vortices in a Bose–Einstein condensate’, *Physical Review A*, vol. 93, no. 2, p. 023 603, 2016. DOI: [10.1103/PhysRevA.93.023603](https://doi.org/10.1103/PhysRevA.93.023603) (cit. on p. 26).
- [162] B. Gertjerenken, P. G. Kevrekidis, R. Carretero-González *et al.*, ‘Generating and manipulating quantized vortices on-demand in a Bose–Einstein condensate: A numerical study’, *Physical Review A*, vol. 93, no. 2, p. 023 604, 2016. DOI: [10.1103/PhysRevA.93.023604](https://doi.org/10.1103/PhysRevA.93.023604) (cit. on p. 26).
- [163] K. W. Madison, F. Chevy, W. Wohlleben *et al.*, ‘Vortex formation in a stirred Bose–Einstein condensate’, *Physical Review Letters*, vol. 84, no. 5, pp. 806–809, 2000. DOI: [10.1103/PhysRevLett.84.806](https://doi.org/10.1103/PhysRevLett.84.806) (cit. on p. 27).
- [164] B. P. Anderson, P. C. Haljan, C. E. Wieman *et al.*, ‘Vortex precession in Bose–Einstein condensates: Observations with filled and empty cores’, *Physical Review Letters*, vol. 85, no. 14, pp. 2857–2860, 2000. DOI: [10.1103/PhysRevLett.85.2857](https://doi.org/10.1103/PhysRevLett.85.2857) (cit. on p. 27).
- [165] D. V. Freilich, D. M. Bianchi, A. M. Kaufman *et al.*, ‘Real-time dynamics of single vortex lines and vortex dipoles in a Bose–Einstein condensate’, *Science*, vol. 329, no. 5996, pp. 1182–1185, 2010. DOI: [10.1126/science.1191224](https://doi.org/10.1126/science.1191224) (cit. on p. 27).
- [166] C. J. Billington, ‘State-dependent forces in cold quantum gases’, PhD Thesis, Monash University, 2018. DOI: [10.26180/5bd68acaf0696](https://doi.org/10.26180/5bd68acaf0696) (cit. on pp. 28, 52).
- [167] K. E. Wilson, Z. L. Newman, J. D. Lowney *et al.*, ‘In situ imaging of vortices in Bose–Einstein condensates’, *Physical Review A*, vol. 91, no. 2, p. 023 621, 2015. DOI: [10.1103/PhysRevA.91.023621](https://doi.org/10.1103/PhysRevA.91.023621) (cit. on p. 28).
- [168] K. E. Wilson, ‘Developing a toolkit for experimental studies of two-dimensional quantum turbulence in Bose–Einstein condensates’, PhD thesis, The University of Arizona, 2015. DOI: [10.1501/577309](https://doi.org/10.1501/577309) (cit. on pp. 28, 137).
- [169] F. Chevy, K. W. Madison, V. Bretin *et al.*, ‘Interferometric detection of a single vortex in a dilute Bose–Einstein condensate’, *Physical Review A*, vol. 64, no. 3, p. 031 601, 2001. DOI: [10.1103/PhysRevA.64.031601](https://doi.org/10.1103/PhysRevA.64.031601) (cit. on p. 28).
- [170] A. White, C. Smith, N. Heckenberg *et al.*, ‘Interferometric measurements of phase singularities in the output of a visible laser’, *Journal of Modern Optics*, vol. 38, no. 12, pp. 2531–2541, 1991. DOI: [10.1080/09500349114552651](https://doi.org/10.1080/09500349114552651) (cit. on p. 28).

- [171] A. T. Powis, S. J. Sammut and T. P. Simula, 'Vortex gyroscope imaging of planar superfluids', *Physical Review Letters*, vol. 113, no. 16, p. 165303, 2014. DOI: [10.1103/PhysRevLett.113.165303](https://doi.org/10.1103/PhysRevLett.113.165303) (cit. on p. 29).
- [172] E. Hodby, S. A. Hopkins, G. Hechenblaikner *et al.*, 'Experimental observation of a superfluid gyroscope in a dilute Bose–Einstein condensate', *Physical Review Letters*, vol. 91, no. 9, p. 090403, 2003. DOI: [10.1103/PhysRevLett.91.090403](https://doi.org/10.1103/PhysRevLett.91.090403) (cit. on p. 29).
- [173] N. L. Smith, W. H. Heathcote, J. M. Krueger *et al.*, 'Experimental observation of the tilting mode of an array of vortices in a dilute Bose–Einstein condensate', *Physical Review Letters*, vol. 93, no. 8, p. 080406, 2004. DOI: [10.1103/PhysRevLett.93.080406](https://doi.org/10.1103/PhysRevLett.93.080406) (cit. on p. 29).
- [174] M. Kozuma, L. Deng, E. W. Hagley *et al.*, 'Coherent splitting of Bose–Einstein condensed atoms with optically induced Bragg diffraction', *Physical Review Letters*, vol. 82, no. 5, pp. 871–875, 1999. DOI: [10.1103/PhysRevLett.82.871](https://doi.org/10.1103/PhysRevLett.82.871) (cit. on p. 29).
- [175] J. Stenger, S. Inouye, A. P. Chikkatur *et al.*, 'Bragg spectroscopy of a Bose–Einstein condensate', *Physical Review Letters*, vol. 82, no. 23, pp. 4569–4573, 1999. DOI: [10.1103/PhysRevLett.82.4569](https://doi.org/10.1103/PhysRevLett.82.4569) (cit. on pp. 29, 113).
- [176] P. B. Blakie and R. J. Ballagh, 'Spatially selective Bragg scattering: A signature for vortices in Bose–Einstein condensates', *Physical Review Letters*, vol. 86, no. 18, pp. 3930–3933, 2001. DOI: [10.1103/PhysRevLett.86.3930](https://doi.org/10.1103/PhysRevLett.86.3930) (cit. on p. 29).
- [177] S. R. Muniz, D. S. Naik and C. Raman, 'Bragg spectroscopy of vortex lattices in Bose–Einstein condensates', *Physical Review A*, vol. 73, no. 4, p. 041605, 2006. DOI: [10.1103/PhysRevA.73.041605](https://doi.org/10.1103/PhysRevA.73.041605) (cit. on p. 29).
- [178] S. R. Muniz, D. S. Naik, M. Bhattacharya *et al.*, 'Dynamics of rotating Bose–Einstein condensates probed by Bragg scattering', *Mathematics and Computers in Simulation, Nonlinear Waves: Computation and Theory VI*, vol. 74, no. 4, pp. 397–404, 2007. DOI: [10.1016/j.matcom.2006.10.029](https://doi.org/10.1016/j.matcom.2006.10.029) (cit. on p. 29).
- [179] <http://creativecommons.org/licenses/by/4.0/> (cit. on p. 30).
- [180] M. Tsubota, 'Quantum turbulence', *Journal of the Physical Society of Japan*, vol. 77, no. 11, p. 111006, 2008. DOI: [10.1143/JPSJ.77.111006](https://doi.org/10.1143/JPSJ.77.111006) (cit. on p. 31).
- [181] M. Tsubota, 'Turbulence in quantum fluids', *Journal of Statistical Mechanics: Theory and Experiment*, vol. 2014, no. 2, P02013, 2014. DOI: [10.1088/1742-5468/2014/02/P02013](https://doi.org/10.1088/1742-5468/2014/02/P02013) (cit. on pp. 31, 33).

- [182] M. Tsubota, K. Fujimoto and S. Yui, 'Numerical studies of quantum turbulence', *Journal of Low Temperature Physics*, vol. 188, no. 5-6, pp. 119–189, 2017. DOI: [10.1007/s10909-017-1789-8](https://doi.org/10.1007/s10909-017-1789-8) (cit. on pp. 31, 138).
- [183] M. Tsubota and W. Halperin, Eds., *Quantum Turbulence*, ser. Progress in Low Temperature Physics. Elsevier, 2009, vol. 16 (cit. on p. 31).
- [184] C. F. Barenghi, L. Skrbek and K. R. Sreenivasan, 'Introduction to quantum turbulence', *Proceedings of the National Academy of Sciences*, vol. 111, no. Supplement 1, pp. 4647–4652, 2014. DOI: [10.1073/pnas.1400033111](https://doi.org/10.1073/pnas.1400033111) (cit. on p. 31).
- [185] W. F. Vinen and L. Skrbek, 'Quantum turbulence generated by oscillating structures', *Proceedings of the National Academy of Sciences*, vol. 111, no. Supplement 1, pp. 4699–4706, 2014. DOI: [10.1073/pnas.1312551111](https://doi.org/10.1073/pnas.1312551111) (cit. on p. 31).
- [186] A. C. White, B. P. Anderson and V. S. Bagnato, 'Vortices and turbulence in trapped atomic condensates', *Proceedings of the National Academy of Sciences*, vol. 111, no. Supplement 1, pp. 4719–4726, 2014. DOI: [10.1073/pnas.1312737110](https://doi.org/10.1073/pnas.1312737110) (cit. on p. 31).
- [187] C. F. Barenghi, V. S. L'vov and P.-E. Roche, 'Experimental, numerical, and analytical velocity spectra in turbulent quantum fluid', *Proceedings of the National Academy of Sciences*, vol. 111, no. Supplement 1, pp. 4683–4690, 2014. DOI: [10.1073/pnas.1312548111](https://doi.org/10.1073/pnas.1312548111) (cit. on p. 31).
- [188] P. Walmsley, D. Zmeev, F. Pakpour *et al.*, 'Dynamics of quantum turbulence of different spectra', *Proceedings of the National Academy of Sciences*, vol. 111, no. Supplement 1, pp. 4691–4698, 2014. DOI: [10.1073/pnas.1312544110](https://doi.org/10.1073/pnas.1312544110) (cit. on pp. 31, 33).
- [189] W. F. Vinen, 'Mutual friction in a heat current in liquid helium II I. Experiments on steady heat currents', *Proceedings of the Royal Society A*, vol. 240, no. 1220, pp. 114–127, 1957. DOI: [10.1098/rspa.1957.0071](https://doi.org/10.1098/rspa.1957.0071) (cit. on p. 31).
- [190] W. F. Vinen, 'Mutual friction in a heat current in liquid helium II. II. Experiments on transient effects', *Proceedings of the Royal Society A*, vol. 240, no. 1220, pp. 128–143, 1957. DOI: [10.1098/rspa.1957.0072](https://doi.org/10.1098/rspa.1957.0072) (cit. on p. 31).
- [191] W. F. Vinen, 'Mutual friction in a heat current in liquid helium II III. Theory of the mutual friction', *Proceedings of the Royal Society A*, vol. 242, no. 1231, pp. 493–515, 1957. DOI: [10.1098/rspa.1957.0191](https://doi.org/10.1098/rspa.1957.0191) (cit. on p. 31).
- [192] A. P. Finne, T. Araki, R. Blaauwgeers *et al.*, 'An intrinsic velocity-independent criterion for superfluid turbulence', *Nature*, vol. 424, no. 6952, pp. 1022–1025, 2003. DOI: [10.1038/nature01880](https://doi.org/10.1038/nature01880) (cit. on p. 32).

- [193] G. E. Volovik, 'Classical and quantum regimes of superfluid turbulence', *Journal of Experimental and Theoretical Physics Letters*, vol. 78, no. 9, pp. 533–537, 2003. DOI: [10.1134/1.1641478](https://doi.org/10.1134/1.1641478) (cit. on p. 32).
- [194] L. Onsager, 'Introductory talk [on liquid helium]', in *Proceedings of International Conference in Theoretical Physics*, Tokyo: Science Council of Japan, 1953, pp. 877–880 (cit. on p. 32).
- [195] V. S. L'vov, L. Skrbek and K. R. Sreenivasan, 'Viscosity of liquid ^4He and quantum of circulation: Are they related?', *Physics of Fluids*, vol. 26, no. 4, p. 041703, 2014. DOI: [10.1063/1.4871291](https://doi.org/10.1063/1.4871291) (cit. on p. 32).
- [196] C. Nore, M. Abid and M. E. Brachet, 'Kolmogorov turbulence in low-temperature superflows', *Physical Review Letters*, vol. 78, no. 20, pp. 3896–3899, 1997. DOI: [10.1103/PhysRevLett.78.3896](https://doi.org/10.1103/PhysRevLett.78.3896) (cit. on p. 32).
- [197] M. Abid, M. E. Brachet, J. Maurer *et al.*, 'Experimental and numerical investigations of low-temperature superfluid turbulence', *European Journal of Mechanics - B/Fluids*, Special Issue Dynamics and Statistics of Concentrated Vortices in Turbulent Flow (Euromech Colloquium 364), vol. 17, no. 4, pp. 665–675, 1998. DOI: [10.1016/S0997-7546\(98\)80019-8](https://doi.org/10.1016/S0997-7546(98)80019-8) (cit. on p. 32).
- [198] C. Nore, C. Huepe and M. E. Brachet, 'Subcritical dissipation in three-dimensional superflows', *Physical Review Letters*, vol. 84, no. 10, pp. 2191–2194, 2000. DOI: [10.1103/PhysRevLett.84.2191](https://doi.org/10.1103/PhysRevLett.84.2191) (cit. on p. 32).
- [199] R. Hänninen, M. Tsubota and W. F. Vinen, 'Generation of turbulence by oscillating structures in superfluid helium at very low temperatures', *Physical Review B*, vol. 75, no. 6, p. 064502, 2007. DOI: [10.1103/PhysRevB.75.064502](https://doi.org/10.1103/PhysRevB.75.064502) (cit. on p. 32).
- [200] K. Sasaki, N. Suzuki and H. Saito, 'Bénard–von Kármán vortex street in a Bose–Einstein condensate', *Physical Review Letters*, vol. 104, no. 15, p. 150404, 2010. DOI: [10.1103/PhysRevLett.104.150404](https://doi.org/10.1103/PhysRevLett.104.150404) (cit. on p. 32).
- [201] W. J. Kwon, J. H. Kim, S. W. Seo *et al.*, 'Observation of von Kármán vortex street in an atomic superfluid gas', *Physical Review Letters*, vol. 117, no. 24, p. 245301, 2016. DOI: [10.1103/PhysRevLett.117.245301](https://doi.org/10.1103/PhysRevLett.117.245301) (cit. on pp. 32, 45).
- [202] <http://creativecommons.org/licenses/by/3.0/> (cit. on p. 32).
- [203] M. T. Reeves, T. P. Billam, B. P. Anderson *et al.*, 'Identifying a superfluid Reynolds number via dynamical similarity', *Physical Review Letters*, vol. 114, no. 15, p. 155302, 2015. DOI: [10.1103/PhysRevLett.114.155302](https://doi.org/10.1103/PhysRevLett.114.155302) (cit. on p. 32).

- [204] D. Kivotides, J. C. Vassilicos, D. C. Samuels *et al.*, ‘Kelvin waves cascade in superfluid turbulence’, *Physical Review Letters*, vol. 86, no. 14, pp. 3080–3083, 2001. DOI: [10.1103/PhysRevLett.86.3080](https://doi.org/10.1103/PhysRevLett.86.3080) (cit. on p. 33).
- [205] W. F. Vinen, M. Tsubota and A. Mitani, ‘Kelvin-wave cascade on a vortex in superfluid ^4He at a very low temperature’, *Physical Review Letters*, vol. 91, no. 13, p. 135301, 2003. DOI: [10.1103/PhysRevLett.91.135301](https://doi.org/10.1103/PhysRevLett.91.135301) (cit. on p. 33).
- [206] J. Maurer and P. Tabeling, ‘Local investigation of superfluid turbulence’, *Europhysics Letters*, vol. 43, no. 1, p. 29, 1998. DOI: [10.1209/epl/i1998-00314-9](https://doi.org/10.1209/epl/i1998-00314-9) (cit. on p. 33).
- [207] S. R. Stalp, L. Skrbek and R. J. Donnelly, ‘Decay of grid turbulence in a finite channel’, *Physical Review Letters*, vol. 82, no. 24, pp. 4831–4834, 1999. DOI: [10.1103/PhysRevLett.82.4831](https://doi.org/10.1103/PhysRevLett.82.4831) (cit. on p. 33).
- [208] J. Salort, C. Baudet, B. Castaing *et al.*, ‘Turbulent velocity spectra in superfluid flows’, *Physics of Fluids*, vol. 22, no. 12, p. 125102, 2010. DOI: [10.1063/1.3504375](https://doi.org/10.1063/1.3504375) (cit. on p. 33).
- [209] J. Salort, B. Chabaud, E. Lévêque *et al.*, ‘Energy cascade and the four-fifths law in superfluid turbulence’, *Europhysics Letters*, vol. 97, no. 3, p. 34006, 2012. DOI: [10.1209/0295-5075/97/34006](https://doi.org/10.1209/0295-5075/97/34006) (cit. on p. 33).
- [210] E. Kozik and B. Svistunov, ‘Kelvin-wave cascade and decay of superfluid turbulence’, *Physical Review Letters*, vol. 92, no. 3, p. 035301, 2004. DOI: [10.1103/PhysRevLett.92.035301](https://doi.org/10.1103/PhysRevLett.92.035301) (cit. on p. 33).
- [211] V. S. L’vov and S. Nazarenko, ‘Spectrum of Kelvin-wave turbulence in superfluids’, *Journal of Experimental and Theoretical Physics Letters*, vol. 91, no. 8, pp. 428–434, 2010. DOI: [10.1134/S002136401008014X](https://doi.org/10.1134/S002136401008014X) (cit. on p. 33).
- [212] A. W. Baggaley, C. F. Barenghi and Y. A. Sergeev, ‘Quasiclassical and ultraquantum decay of superfluid turbulence’, *Physical Review B*, vol. 85, no. 6, p. 060501, 2012. DOI: [10.1103/PhysRevB.85.060501](https://doi.org/10.1103/PhysRevB.85.060501) (cit. on p. 33).
- [213] U. Fano, ‘Sullo spettro di assorbimento dei gas nobili presso il limite dello spettro d’arco’, *Il Nuovo Cimento*, vol. 12, no. 3, pp. 154–161, 1935. DOI: [10.1007/BF02958288](https://doi.org/10.1007/BF02958288) (cit. on p. 34).
- [214] H. Feshbach, ‘Unified theory of nuclear reactions’, *Annals of Physics*, vol. 5, no. 4, pp. 357–390, 1958. DOI: [10.1016/0003-4916\(58\)90007-1](https://doi.org/10.1016/0003-4916(58)90007-1) (cit. on p. 34).
- [215] H. Feshbach, ‘A unified theory of nuclear reactions. II’, *Annals of Physics*, vol. 19, no. 2, pp. 287–313, 1962. DOI: [10.1016/0003-4916\(62\)90221-X](https://doi.org/10.1016/0003-4916(62)90221-X) (cit. on p. 34).

- [216] S. Inouye, M. R. Andrews, J. Stenger *et al.*, ‘Observation of Feshbach resonances in a Bose–Einstein condensate’, *Nature*, vol. 392, no. 6672, pp. 151–154, 1998. DOI: [10.1038/32354](https://doi.org/10.1038/32354) (cit. on p. 34).
- [217] U. Fano, G. Pupillo, A. Zannoni *et al.*, ‘On the absorption spectrum of noble gases at the arc spectrum limit’, *Journal of Research of the National Institute of Standards and Technology*, vol. 110, no. 6, pp. 583–587, 2005. DOI: [10.6028/jres.110.083](https://doi.org/10.6028/jres.110.083) (cit. on p. 34).
- [218] C. Chin, R. Grimm, P. Julienne *et al.*, ‘Feshbach resonances in ultracold gases’, *Reviews of Modern Physics*, vol. 82, no. 2, pp. 1225–1286, 2010. DOI: [10.1103/RevModPhys.82.1225](https://doi.org/10.1103/RevModPhys.82.1225) (cit. on p. 34).
- [219] M. Kobayashi and M. Tsubota, ‘Kolmogorov spectrum of superfluid turbulence: Numerical analysis of the Gross–Pitaevskii equation with a small-scale dissipation’, *Physical Review Letters*, vol. 94, no. 6, p. 065 302, 2005. DOI: [10.1103/PhysRevLett.94.065302](https://doi.org/10.1103/PhysRevLett.94.065302) (cit. on p. 34).
- [220] M. Kobayashi and M. Tsubota, ‘Quantum turbulence in a trapped Bose–Einstein condensate’, *Physical Review A*, vol. 76, no. 4, p. 045 603, 2007. DOI: [10.1103/PhysRevA.76.045603](https://doi.org/10.1103/PhysRevA.76.045603) (cit. on p. 34).
- [221] M. Kobayashi and M. Tsubota, ‘Quantum turbulence in a trapped Bose–Einstein condensate under combined rotations around three axes’, *Journal of Low Temperature Physics*, vol. 150, no. 3-4, pp. 587–592, 2008. DOI: [10.1007/s10909-007-9594-4](https://doi.org/10.1007/s10909-007-9594-4) (cit. on p. 34).
- [222] N. Sasa, T. Kano, M. Machida *et al.*, ‘Energy spectra of quantum turbulence: Large-scale simulation and modeling’, *Physical Review B*, vol. 84, no. 5, p. 054 525, 2011. DOI: [10.1103/PhysRevB.84.054525](https://doi.org/10.1103/PhysRevB.84.054525) (cit. on p. 34).
- [223] E. A. L. Henn, J. A. Seman, G. Roati *et al.*, ‘Emergence of turbulence in an oscillating Bose–Einstein condensate’, *Physical Review Letters*, vol. 103, no. 4, p. 045 301, 2009. DOI: [10.1103/PhysRevLett.103.045301](https://doi.org/10.1103/PhysRevLett.103.045301) (cit. on p. 34).
- [224] N. Navon, A. L. Gaunt, R. P. Smith *et al.*, ‘Emergence of a turbulent cascade in a quantum gas’, *Nature*, vol. 539, no. 7627, pp. 72–75, 2016. DOI: [10.1038/nature20114](https://doi.org/10.1038/nature20114) (cit. on p. 34).
- [225] N. Navon, C. Eigen, J. Zhang *et al.*, ‘Synthetic dissipation and cascade fluxes in a turbulent quantum gas’, 2018. arXiv: [1807.07564](https://arxiv.org/abs/1807.07564) [cond-mat.quant-gas] (cit. on p. 34).

- [226] R. Numasato and M. Tsubota, ‘Possibility of inverse energy cascade in two-dimensional quantum turbulence’, *Journal of Low Temperature Physics*, vol. 158, no. 3-4, p. 415, 2010. DOI: [10.1007/s10909-009-9965-0](https://doi.org/10.1007/s10909-009-9965-0) (cit. on pp. 34, 38).
- [227] R. Numasato, M. Tsubota and V. S. L’vov, ‘Direct energy cascade in two-dimensional compressible quantum turbulence’, *Physical Review A*, vol. 81, no. 6, p. 063 630, 2010. DOI: [10.1103/PhysRevA.81.063630](https://doi.org/10.1103/PhysRevA.81.063630) (cit. on pp. 34, 38).
- [228] M. T. Reeves, B. P. Anderson and A. S. Bradley, ‘Classical and quantum regimes of two-dimensional turbulence in trapped Bose–Einstein condensates’, *Physical Review A*, vol. 86, no. 5, p. 053 621, 2012. DOI: [10.1103/PhysRevA.86.053621](https://doi.org/10.1103/PhysRevA.86.053621) (cit. on p. 34).
- [229] N. G. Parker and C. S. Adams, ‘Emergence and decay of turbulence in stirred atomic Bose–Einstein condensates’, *Physical Review Letters*, vol. 95, no. 14, p. 145 301, 2005. DOI: [10.1103/PhysRevLett.95.145301](https://doi.org/10.1103/PhysRevLett.95.145301) (cit. on p. 34).
- [230] T.-L. Horng, C.-H. Hsueh, S.-W. Su *et al.*, ‘Two-dimensional quantum turbulence in a nonuniform Bose–Einstein condensate’, *Physical Review A*, vol. 80, no. 2, p. 023 618, 2009. DOI: [10.1103/PhysRevA.80.023618](https://doi.org/10.1103/PhysRevA.80.023618) (cit. on p. 34).
- [231] M. T. Reeves, T. P. Billam, B. P. Anderson *et al.*, ‘Inverse energy cascade in forced two-dimensional quantum turbulence’, *Physical Review Letters*, vol. 110, no. 10, p. 104 501, 2013. DOI: [10.1103/PhysRevLett.110.104501](https://doi.org/10.1103/PhysRevLett.110.104501) (cit. on pp. 34–37).
- [232] T. Kusumura, H. Takeuchi and M. Tsubota, ‘Energy spectrum of the superfluid velocity made by quantized vortices in two-dimensional quantum turbulence’, *Journal of Low Temperature Physics*, vol. 171, no. 5-6, pp. 563–570, 2013. DOI: [10.1007/s10909-012-0827-9](https://doi.org/10.1007/s10909-012-0827-9) (cit. on p. 34).
- [233] D. Kobayakov, A. Bezett, E. Lundh *et al.*, ‘Turbulence in binary Bose–Einstein condensates generated by highly nonlinear Rayleigh–Taylor and Kelvin–Helmholtz instabilities’, *Physical Review A*, vol. 89, no. 1, p. 013 631, 2014. DOI: [10.1103/PhysRevA.89.013631](https://doi.org/10.1103/PhysRevA.89.013631) (cit. on pp. 34, 35).
- [234] T. P. Billam, M. T. Reeves, B. P. Anderson *et al.*, ‘Onsager–Kraichnan condensation in decaying two-dimensional quantum turbulence’, *Physical Review Letters*, vol. 112, no. 14, p. 145 301, 2014. DOI: [10.1103/PhysRevLett.112.145301](https://doi.org/10.1103/PhysRevLett.112.145301) (cit. on pp. 34, 35, 37, 123).
- [235] T. P. Billam, M. T. Reeves and A. S. Bradley, ‘Spectral energy transport in two-dimensional quantum vortex dynamics’, *Physical Review A*, vol. 91, no. 2, p. 023 615, 2015. DOI: [10.1103/PhysRevA.91.023615](https://doi.org/10.1103/PhysRevA.91.023615) (cit. on pp. 34, 35).

- [236] A. Skaugen and L. Angheluta, 'Vortex clustering and universal scaling laws in two-dimensional quantum turbulence', *Physical Review E*, vol. 93, no. 3, p. 032 106, 2016. DOI: [10.1103/PhysRevE.93.032106](https://doi.org/10.1103/PhysRevE.93.032106) (cit. on pp. 34, 37).
- [237] A. Skaugen and L. Angheluta, 'Origin of the inverse energy cascade in two-dimensional quantum turbulence', *Physical Review E*, vol. 95, no. 5, p. 052 144, 2017. DOI: [10.1103/PhysRevE.95.052144](https://doi.org/10.1103/PhysRevE.95.052144) (cit. on p. 34).
- [238] M. T. Reeves, T. P. Billam, X. Yu *et al.*, 'Enstrophy cascade in decaying two-dimensional quantum turbulence', *Physical Review Letters*, vol. 119, no. 18, p. 184 502, 2017. DOI: [10.1103/PhysRevLett.119.184502](https://doi.org/10.1103/PhysRevLett.119.184502) (cit. on pp. 34, 35).
- [239] R. Zamora-Zamora, O. Adame-Arana and V. Romero-Rochin, 'Macroscopic excitations in confined Bose–Einstein condensates, searching for quantum turbulence', *Journal of Low Temperature Physics*, vol. 180, no. 1-2, pp. 109–125, 2015. DOI: [10.1007/s10909-015-1300-3](https://doi.org/10.1007/s10909-015-1300-3) (cit. on p. 35).
- [240] A. C. White, C. F. Barenghi and N. P. Proukakis, 'Creation and characterization of vortex clusters in atomic Bose–Einstein condensates', *Physical Review A*, vol. 86, no. 1, p. 013 635, 2012. DOI: [10.1103/PhysRevA.86.013635](https://doi.org/10.1103/PhysRevA.86.013635) (cit. on p. 35).
- [241] J. Schole, B. Nowak and T. Gasenzer, 'Critical dynamics of a two-dimensional superfluid near a nonthermal fixed point', *Physical Review A*, vol. 86, no. 1, p. 013 624, 2012. DOI: [10.1103/PhysRevA.86.013624](https://doi.org/10.1103/PhysRevA.86.013624) (cit. on pp. 35, 40, 42, 132).
- [242] A. J. Groszek, M. J. Davis, D. M. Paganin *et al.*, 'Vortex thermometry for turbulent two-dimensional fluids', *Physical Review Letters*, vol. 120, no. 3, p. 034 504, 2018. DOI: [10.1103/PhysRevLett.120.034504](https://doi.org/10.1103/PhysRevLett.120.034504) (cit. on pp. 37, 42, 123, 124, 132).
- [243] M. T. Reeves, T. P. Billam, B. P. Anderson *et al.*, 'Signatures of coherent vortex structures in a disordered two-dimensional quantum fluid', *Physical Review A*, vol. 89, no. 5, p. 053 631, 2014. DOI: [10.1103/PhysRevA.89.053631](https://doi.org/10.1103/PhysRevA.89.053631) (cit. on pp. 37, 121).
- [244] H. Salman and D. Maestrini, 'Long-range ordering of topological excitations in a two-dimensional superfluid far from equilibrium', *Physical Review A*, vol. 94, no. 4, p. 043 642, 2016. DOI: [10.1103/PhysRevA.94.043642](https://doi.org/10.1103/PhysRevA.94.043642) (cit. on p. 37).
- [245] W. J. Kwon, G. Moon, J.-y. Choi *et al.*, 'Relaxation of superfluid turbulence in highly oblate Bose–Einstein condensates', *Physical Review A*, vol. 90, no. 6, p. 063 627, 2014. DOI: [10.1103/PhysRevA.90.063627](https://doi.org/10.1103/PhysRevA.90.063627) (cit. on pp. 40, 45).

- [246] G. W. Stagg, A. J. Allen, N. G. Parker *et al.*, ‘Generation and decay of two-dimensional quantum turbulence in a trapped Bose–Einstein condensate’, *Physical Review A*, vol. 91, no. 1, p. 013 612, 2015. DOI: [10.1103/PhysRevA.91.013612](https://doi.org/10.1103/PhysRevA.91.013612) (cit. on pp. 40, 133).
- [247] A. Cidrim, F. E. A. dos Santos, L. Galantucci *et al.*, ‘Controlled polarization of two-dimensional quantum turbulence in atomic Bose–Einstein condensates’, *Physical Review A*, vol. 93, no. 3, p. 033 651, 2016. DOI: [10.1103/PhysRevA.93.033651](https://doi.org/10.1103/PhysRevA.93.033651) (cit. on p. 40).
- [248] M. Karl and T. Gasenzer, ‘Strongly anomalous non-thermal fixed point in a quenched two-dimensional Bose gas’, *New Journal of Physics*, vol. 19, no. 9, p. 093 014, 2017. DOI: [10.1088/1367-2630/aa7eeb](https://doi.org/10.1088/1367-2630/aa7eeb) (cit. on pp. 41–43, 124, 126, 133).
- [249] A. W. Baggaley and C. F. Barenghi, ‘Decay of homogeneous two-dimensional quantum turbulence’, *Physical Review A*, vol. 97, no. 3, p. 033 601, 2018. DOI: [10.1103/PhysRevA.97.033601](https://doi.org/10.1103/PhysRevA.97.033601) (cit. on pp. 41, 133).
- [250] A. J. Groszek, ‘Vortex dynamics in two-dimensional Bose–Einstein condensates’, PhD Thesis, Monash University, 2018. DOI: [10.4225/03/5aaef47cb1eeb](https://doi.org/10.4225/03/5aaef47cb1eeb) (cit. on pp. 42, 109).
- [251] B. Nowak, D. Sexty and T. Gasenzer, ‘Superfluid turbulence: Nonthermal fixed point in an ultracold Bose gas’, *Physical Review B*, vol. 84, no. 2, p. 020 506, 2011. DOI: [10.1103/PhysRevB.84.020506](https://doi.org/10.1103/PhysRevB.84.020506) (cit. on p. 42).
- [252] B. Nowak, J. Schole, D. Sexty *et al.*, ‘Nonthermal fixed points, vortex statistics, and superfluid turbulence in an ultracold Bose gas’, *Physical Review A*, vol. 85, no. 4, p. 043 627, 2012. DOI: [10.1103/PhysRevA.85.043627](https://doi.org/10.1103/PhysRevA.85.043627) (cit. on p. 42).
- [253] H. Reinhardt, F. Böhm, B. Drossel *et al.*, ‘Nonequilibrium critical behavior of a species coexistence model’, *The European Physical Journal B - Condensed Matter and Complex Systems*, vol. 51, no. 2, pp. 245–255, 2006. DOI: [10.1140/epjb/e2006-00217-7](https://doi.org/10.1140/epjb/e2006-00217-7) (cit. on p. 42).
- [254] S. L. Veatch, O. Soubias, S. L. Keller *et al.*, ‘Critical fluctuations in domain-forming lipid mixtures’, *Proceedings of the National Academy of Sciences*, vol. 104, no. 45, pp. 17 650–17 655, 2007. DOI: [10.1073/pnas.0703513104](https://doi.org/10.1073/pnas.0703513104) (cit. on p. 42).
- [255] D. J. Bishop and J. D. Reppy, ‘Study of the superfluid transition in two-dimensional ^4He films’, *Physical Review Letters*, vol. 40, no. 26, pp. 1727–1730, 1978. DOI: [10.1103/PhysRevLett.40.1727](https://doi.org/10.1103/PhysRevLett.40.1727) (cit. on p. 43).

- [256] Z. Hadzibabic, P. Krüger, M. Cheneau *et al.*, ‘Berezinskii–Kosterlitz–Thouless crossover in a trapped atomic gas’, *Nature*, vol. 441, no. 7097, pp. 1118–1121, 2006. DOI: [10.1038/nature04851](https://doi.org/10.1038/nature04851) (cit. on p. 43).
- [257] K. E. Wilson, E. C. Samson, Z. L. Newman *et al.*, ‘Experimental methods for generating two-dimensional quantum turbulence in Bose–Einstein condensates’, in *Annual Review of Cold Atoms and Molecules*, vol. 1, World Scientific, 2013, pp. 261–298. DOI: [10.1142/9789814440400_0007](https://doi.org/10.1142/9789814440400_0007) (cit. on p. 43).
- [258] T. W. Neely, A. S. Bradley, E. C. Samson *et al.*, ‘Characteristics of two-dimensional quantum turbulence in a compressible superfluid’, *Physical Review Letters*, vol. 111, no. 23, p. 235 301, 2013. DOI: [10.1103/PhysRevLett.111.235301](https://doi.org/10.1103/PhysRevLett.111.235301) (cit. on p. 44).
- [259] G. Gauthier, M. T. Reeves, X. Yu *et al.*, ‘Giant vortex clusters in a two-dimensional quantum fluid’, 2018. arXiv: [1801.06951](https://arxiv.org/abs/1801.06951) [cond-mat.quant-gas] (cit. on pp. 46, 106, 133, 134).
- [260] E. M. Purcell and R. V. Pound, ‘A nuclear spin system at negative temperature’, *Physical Review*, vol. 81, no. 2, pp. 279–280, 1951. DOI: [10.1103/PhysRev.81.279](https://doi.org/10.1103/PhysRev.81.279) (cit. on p. 47).
- [261] S. Braun, J. P. Ronzheimer, M. Schreiber *et al.*, ‘Negative absolute temperature for motional degrees of freedom’, *Science*, vol. 339, no. 6115, pp. 52–55, 2013. DOI: [10.1126/science.1227831](https://doi.org/10.1126/science.1227831) (cit. on p. 47).
- [262] J. C. Gartside, D. M. Arroo, D. M. Burn *et al.*, ‘Realization of ground state in artificial kagome spin ice via topological defect-driven magnetic writing’, *Nature Nanotechnology*, vol. 13, no. 1, pp. 53–58, 2018. DOI: [10.1038/s41565-017-0002-1](https://doi.org/10.1038/s41565-017-0002-1) (cit. on p. 47).
- [263] J. P. P. Vieira, C. T. Byrnes and A. Lewis, ‘Cosmology with negative absolute temperatures’, *Journal of Cosmology and Astroparticle Physics*, vol. 2016, no. 08, p. 060, 2016. DOI: [10.1088/1475-7516/2016/08/060](https://doi.org/10.1088/1475-7516/2016/08/060) (cit. on p. 47).
- [264] S. Saha, A. Mondal and C. Corda, ‘Ideal gas with a varying (negative absolute) temperature: An alternative to dark energy?’, *International Journal of Theoretical Physics*, vol. 57, no. 5, pp. 1417–1424, 2018. DOI: [10.1007/s10773-018-3670-1](https://doi.org/10.1007/s10773-018-3670-1) (cit. on p. 47).
- [265] N. F. Ramsey, ‘Thermodynamics and statistical mechanics at negative absolute temperatures’, *Physical Review*, vol. 103, no. 1, pp. 20–28, 1956. DOI: [10.1103/PhysRev.103.20](https://doi.org/10.1103/PhysRev.103.20) (cit. on pp. 47, 49, 124).
- [266] V. Berdichevsky, I. Kunin and F. Hussain, ‘Negative temperature of vortex motion’, *Physical Review A*, vol. 43, no. 4, pp. 2050–2051, 1991. DOI: [10.1103/PhysRevA.43.2050](https://doi.org/10.1103/PhysRevA.43.2050) (cit. on p. 48).

- [267] D. Montgomery, ‘Comment on “negative temperature of vortex motion”’, *Physical Review A*, vol. 44, no. 12, pp. 8437–8438, 1991. DOI: [10.1103/PhysRevA.44.8437](https://doi.org/10.1103/PhysRevA.44.8437) (cit. on p. 48).
- [268] V. Berdichevsky, I. Kunin and F. Hussain, ‘Reply to “comment on ‘negative temperature of vortex motion’ ”’, *Physical Review A*, vol. 44, no. 12, pp. 8439–8440, 1991. DOI: [10.1103/PhysRevA.44.8439](https://doi.org/10.1103/PhysRevA.44.8439) (cit. on p. 48).
- [269] K. O’Neil and L. J. Campbell, ‘Comment on “negative temperature of vortex motion”’, *Physical Review E*, vol. 47, no. 4, pp. 2966–2967, 1993. DOI: [10.1103/PhysRevE.47.2966](https://doi.org/10.1103/PhysRevE.47.2966) (cit. on p. 48).
- [270] V. Berdichevsky, I. Kunin and F. Hussain, ‘Reply to “comment on ‘negative temperature of vortex motion’ ”’, *Physical Review E*, vol. 47, no. 4, pp. 2968–2969, 1993. DOI: [10.1103/PhysRevE.47.2968](https://doi.org/10.1103/PhysRevE.47.2968) (cit. on p. 49).
- [271] V. Romero-Rochín, ‘Nonexistence of equilibrium states at absolute negative temperatures’, *Physical Review E*, vol. 88, no. 2, p. 022 144, 2013. DOI: [10.1103/PhysRevE.88.022144](https://doi.org/10.1103/PhysRevE.88.022144) (cit. on p. 49).
- [272] J. Dunkel and S. Hilbert, ‘Consistent thermostatics forbids negative absolute temperatures’, *Nature Physics*, vol. 10, no. 1, p. 67, 2014. DOI: [10.1038/nphys2815](https://doi.org/10.1038/nphys2815) (cit. on p. 49).
- [273] J. Poulter, ‘In defense of negative temperature’, *Physical Review E*, vol. 93, no. 3, p. 032 149, 2016. DOI: [10.1103/PhysRevE.93.032149](https://doi.org/10.1103/PhysRevE.93.032149) (cit. on p. 49).
- [274] J. M. G. Vilar and J. M. Rubi, ‘Communication: System-size scaling of Boltzmann and alternate Gibbs entropies’, *The Journal of Chemical Physics*, vol. 140, no. 20, p. 201 101, 2014. DOI: [10.1063/1.4879553](https://doi.org/10.1063/1.4879553) (cit. on p. 49).
- [275] D. Frenkel and P. B. Warren, ‘Gibbs, Boltzmann, and negative temperatures’, *American Journal of Physics*, vol. 83, no. 2, pp. 163–170, 2015. DOI: [10.1119/1.4895828](https://doi.org/10.1119/1.4895828) (cit. on p. 49).
- [276] S. Hilbert, P. Hänggi and J. Dunkel, ‘Thermodynamic laws in isolated systems’, *Physical Review E*, vol. 90, no. 6, p. 062 116, 2014. DOI: [10.1103/PhysRevE.90.062116](https://doi.org/10.1103/PhysRevE.90.062116) (cit. on p. 49).
- [277] M. Campisi, ‘Construction of microcanonical entropy on thermodynamic pillars’, *Physical Review E*, vol. 91, no. 5, p. 052 147, 2015. DOI: [10.1103/PhysRevE.91.052147](https://doi.org/10.1103/PhysRevE.91.052147) (cit. on p. 49).
- [278] L. Cerino, A. Puglisi and A. Vulpiani, ‘A consistent description of fluctuations requires negative temperatures’, *Journal of Statistical Mechanics: Theory and Experiment*, vol. 2015, no. 12, P12002, 2015. DOI: [10.1088/1742-5468/2015/12/P12002](https://doi.org/10.1088/1742-5468/2015/12/P12002) (cit. on p. 50).

- [279] R. H. Swendsen and J.-S. Wang, ‘Gibbs volume entropy is incorrect’, *Physical Review E*, vol. 92, no. 2, p. 020 103, 2015. DOI: [10.1103/PhysRevE.92.020103](https://doi.org/10.1103/PhysRevE.92.020103) (cit. on p. 50).
- [280] D.-V. Anghel, ‘The stumbling block of the Gibbs entropy: The reality of the negative absolute temperatures’, in *EPJ Web of Conferences*, vol. 108, Mathematical Modeling and Computational Physics (MMCP 2015), Stará Lesná, Slovakia: EDP Sciences, 2016, p. 02 007. DOI: [10.1051/epjconf/201610802007](https://doi.org/10.1051/epjconf/201610802007) (cit. on p. 50).
- [281] P. Buonsante, R. Franzosi and A. Smerzi, ‘On the dispute between Boltzmann and Gibbs entropy’, *Annals of Physics*, vol. 375, pp. 414–434, 2016. DOI: [10.1016/j.aop.2016.10.017](https://doi.org/10.1016/j.aop.2016.10.017) (cit. on p. 50).
- [282] P. Buonsante, R. Franzosi and A. Smerzi, ‘Phase transitions at high energy vindicate negative microcanonical temperature’, *Physical Review E*, vol. 95, no. 5, p. 052 135, 2017. DOI: [10.1103/PhysRevE.95.052135](https://doi.org/10.1103/PhysRevE.95.052135) (cit. on p. 50).
- [283] R. H. Swendsen, ‘Thermodynamics, statistical mechanics and entropy’, *Entropy*, vol. 19, no. 11, p. 603, 2017. DOI: [10.3390/e19110603](https://doi.org/10.3390/e19110603) (cit. on p. 50).
- [284] E. Abraham and O. Penrose, ‘Physics of negative absolute temperatures’, *Physical Review E*, vol. 95, no. 1, p. 012 125, 2017. DOI: [10.1103/PhysRevE.95.012125](https://doi.org/10.1103/PhysRevE.95.012125) (cit. on p. 50).
- [285] P. T. Starkey, ‘A software framework for control and automation of precisely timed experiments’, PhD thesis, Monash University, to be submitted 2019 (cit. on pp. 51, 60).
- [286] P. T. Starkey, C. J. Billington, S. P. Johnstone *et al.*, ‘A scripted control system for autonomous hardware-timed experiments’, *Review of Scientific Instruments*, vol. 84, no. 8, p. 085 111, 2013. DOI: [10.1063/1.4817213](https://doi.org/10.1063/1.4817213) (cit. on pp. 52, 64, 66).
- [287] S. Tempone-Wiltshire, S. Johnstone and K. Helmerson, ‘High efficiency, low cost holographic optical elements for ultracold atom trapping’, *Optics Express*, vol. 25, no. 1, pp. 296–304, 2017. DOI: [10.1364/OE.25.000296](https://doi.org/10.1364/OE.25.000296) (cit. on pp. 52, 94, 95, 101).
- [288] S. J. Tempone-Wiltshire, S. P. Johnstone and K. Helmerson, ‘Optical vortex knots – one photon at a time’, *Scientific Reports*, vol. 6, p. 24 463, 2016. DOI: [10.1038/srep24463](https://doi.org/10.1038/srep24463) (cit. on p. 53).
- [289] M. Jasperse, ‘Faraday magnetic resonance imaging of Bose–Einstein condensates’, PhD thesis, Monash University, 2015. DOI: [1959.1/1231988](https://doi.org/10.1959.1/1231988) (cit. on pp. 53, 61).
- [290] A. Wood, ‘Spinor Bose–Einstein condensates in magnetic field gradients’, PhD thesis, Monash University, 2015. DOI: [1959.1/1228163](https://doi.org/10.1959.1/1228163) (cit. on pp. 53, 74).

- [291] <http://labscriptsuite.org> (cit. on p. 64).
- [292] https://bitbucket.org/labscript_suite (cit. on p. 64).
- [293] H. J. Metcalf and P. van der Straten, *Laser Cooling and Trapping*. New York: Springer-Verlag, 1999 (cit. on p. 68).
- [294] C. J. Foot, *Atomic physics*. New York: Oxford University Press, 2005 (cit. on p. 68).
- [295] J. Schoser, A. Batär, R. Löw *et al.*, ‘Intense source of cold Rb atoms from a pure two-dimensional magneto-optical trap’, *Physical Review A*, vol. 66, no. 2, p. 023 410, 2002. DOI: [10.1103/PhysRevA.66.023410](https://doi.org/10.1103/PhysRevA.66.023410) (cit. on p. 69).
- [296] G. Roati, ‘Quantum degenerate potassium-rubidium mixtures’, PhD thesis, University of Trento, 2003 (cit. on p. 71).
- [297] C.-H. Wu, ‘Strongly interacting quantum mixtures of ultracold atoms’, PhD thesis, Massachusetts Institute of Technology, 2013. DOI: [1721.1/83817](https://doi.org/10.1721.1/83817) (cit. on p. 73).
- [298] M. Landini, S. Roy, L. Carcagnì *et al.*, ‘Sub-Doppler laser cooling of potassium atoms’, *Physical Review A*, vol. 84, no. 4, p. 043 432, 2011. DOI: [10.1103/PhysRevA.84.043432](https://doi.org/10.1103/PhysRevA.84.043432) (cit. on p. 73).
- [299] G. Modugno, G. Ferrari, G. Roati *et al.*, ‘Bose–Einstein condensation of potassium atoms by sympathetic cooling’, *Science*, vol. 294, no. 5545, pp. 1320–1322, 2001. DOI: [10.1126/science.1066687](https://doi.org/10.1126/science.1066687) (cit. on p. 74).
- [300] T. Kishimoto, J. Kobayashi, K. Noda *et al.*, ‘Direct evaporative cooling of ^{41}K into a Bose–Einstein condensate’, *Physical Review A*, vol. 79, no. 3, p. 031 602, 2009. DOI: [10.1103/PhysRevA.79.031602](https://doi.org/10.1103/PhysRevA.79.031602) (cit. on p. 74).
- [301] E. Majorana, ‘Atomi orientati in campo magnetico variabile’, *Il Nuovo Cimento*, vol. 9, no. 2, pp. 43–50, 1932. DOI: [10.1007/BF02960953](https://doi.org/10.1007/BF02960953) (cit. on pp. 75, 81).
- [302] C. V. Sukumar and D. M. Brink, ‘Spin-flip transitions in a magnetic trap’, *Physical Review A*, vol. 56, no. 3, pp. 2451–2454, 1997. DOI: [10.1103/PhysRevA.56.2451](https://doi.org/10.1103/PhysRevA.56.2451) (cit. on p. 75).
- [303] D. M. Brink and C. V. Sukumar, ‘Majorana spin-flip transitions in a magnetic trap’, *Physical Review A*, vol. 74, no. 3, p. 035 401, 2006. DOI: [10.1103/PhysRevA.74.035401](https://doi.org/10.1103/PhysRevA.74.035401) (cit. on p. 75).
- [304] R. Grimm, M. Weidemüller and Y. B. Ovchinnikov, ‘Optical dipole traps for neutral atoms’, in *Advances In Atomic, Molecular, and Optical Physics*, B. Bederson and H. Walther, Eds., vol. 42, Academic Press, 2000, pp. 95–170. DOI: [10.1016/S1049-250X\(08\)60186-X](https://doi.org/10.1016/S1049-250X(08)60186-X) (cit. on p. 75).

- [305] Y.-J. Lin, A. R. Perry, R. L. Compton *et al.*, ‘Rapid production of ^{87}Rb Bose–Einstein condensates in a combined magnetic and optical potential’, *Physical Review A*, vol. 79, no. 6, p. 063 631, 2009. DOI: [10.1103/PhysRevA.79.063631](https://doi.org/10.1103/PhysRevA.79.063631) (cit. on p. 75).
- [306] E. W. Hagley, J. E. Simsarian, J. Wen *et al.*, ‘Four-wave mixing with matter waves’, *Nature*, vol. 398, no. 6724, p. 218, 1999. DOI: [10.1038/18395](https://doi.org/10.1038/18395) (cit. on p. 78).
- [307] S. Schmid, G. Thalhammer, K. Winkler *et al.*, ‘Long distance transport of ultracold atoms using a 1D optical lattice’, *New Journal of Physics*, vol. 8, no. 8, p. 159, 2006. DOI: [10.1088/1367-2630/8/8/159](https://doi.org/10.1088/1367-2630/8/8/159) (cit. on p. 78).
- [308] J. Léonard, M. Lee, A. Morales *et al.*, ‘Optical transport and manipulation of an ultracold atomic cloud using focus-tunable lenses’, *New Journal of Physics*, vol. 16, no. 9, p. 093 028, 2014. DOI: [10.1088/1367-2630/16/9/093028](https://doi.org/10.1088/1367-2630/16/9/093028) (cit. on p. 79).
- [309] L. D. Landau, ‘Zur theorie der energieübertragung II’, *Physikalische Zeitschrift der Sowjetunion*, vol. 2, pp. 46–51, 1932 (cit. on p. 81).
- [310] C. Zener, ‘Non-adiabatic crossing of energy levels’, *Proceedings of the Royal Society A*, vol. 137, no. 833, pp. 696–702, 1932. DOI: [10.1098/rspa.1932.0165](https://doi.org/10.1098/rspa.1932.0165) (cit. on p. 81).
- [311] E. Stueckelberg, ‘Theorie der unelastischen Stöße zwischen atomen’, *Helvetica Physica Acta*, vol. 5, pp. 369–422, 1932 (cit. on p. 81).
- [312] N. V. Vitanov, T. Halfmann, B. W. Shore *et al.*, ‘Laser-induced population transfer by adiabatic passage techniques’, *Annual Review of Physical Chemistry*, vol. 52, no. 1, pp. 763–809, 2001. DOI: [10.1146/annurev.physchem.52.1.763](https://doi.org/10.1146/annurev.physchem.52.1.763) (cit. on p. 81).
- [313] X. Li, M. Ke, B. Yan *et al.*, ‘Reduction of interference fringes in absorption imaging of cold atom cloud using eigenface method’, *Chinese Optics Letters*, vol. 5, no. 3, pp. 128–130, 2007 (cit. on p. 90).
- [314] C. F. Ockeloen, A. F. Tauschinsky, R. J. C. Spreeuw *et al.*, ‘Detection of small atom numbers through image processing’, *Physical Review A*, vol. 82, no. 6, p. 061 606, 2010. DOI: [10.1103/PhysRevA.82.061606](https://doi.org/10.1103/PhysRevA.82.061606) (cit. on p. 90).
- [315] A. Görlitz, J. M. Vogels, A. E. Leanhardt *et al.*, ‘Realization of Bose–Einstein condensates in lower dimensions’, *Physical Review Letters*, vol. 87, no. 13, p. 130 402, 2001. DOI: [10.1103/PhysRevLett.87.130402](https://doi.org/10.1103/PhysRevLett.87.130402) (cit. on p. 93).

- [316] N. L. Smith, W. H. Heathcote, G. Hechenblaikner *et al.*, ‘Quasi-2D confinement of a BEC in a combined optical and magnetic potential’, *Journal of Physics B: Atomic, Molecular and Optical Physics*, vol. 38, no. 3, p. 223, 2005. DOI: [10.1088/0953-4075/38/3/007](https://doi.org/10.1088/0953-4075/38/3/007) (cit. on p. 94).
- [317] J. García-Márquez, V. López, A. González-Vega *et al.*, ‘Flicker minimization in an LCoS spatial light modulator’, *Optics Express*, vol. 20, no. 8, pp. 8431–8441, 2012. DOI: [10.1364/OE.20.008431](https://doi.org/10.1364/OE.20.008431) (cit. on p. 95).
- [318] Y. Calderón-Hermosillo, J. García-Márquez, R. Espinosa-Luna *et al.*, ‘Flicker in a twisted nematic spatial light modulator’, *Optics and Lasers in Engineering*, vol. 51, no. 6, pp. 741–748, 2013. DOI: [10.1016/j.optlaseng.2013.01.013](https://doi.org/10.1016/j.optlaseng.2013.01.013) (cit. on p. 95).
- [319] H. Berneth, F. K. Bruder, T. Fäcke *et al.*, ‘Holographic recording aspects of high-resolution bayfol HX photopolymer’, in *Proceedings of SPIE*, vol. 7957, Practical Holography XXV: Materials and Applications, San Francisco, USA: International Society for Optics and Photonics, 2011, 79570H. DOI: [10.1117/12.876202](https://doi.org/10.1117/12.876202) (cit. on p. 95).
- [320] A. L. Gaunt, T. F. Schmidutz, I. Gotlibovych *et al.*, ‘Bose–Einstein condensation of atoms in a uniform potential’, *Physical Review Letters*, vol. 110, no. 20, p. 200406, 2013. DOI: [10.1103/PhysRevLett.110.200406](https://doi.org/10.1103/PhysRevLett.110.200406) (cit. on p. 100).
- [321] L. Chomaz, L. Corman, T. Bienaimé *et al.*, ‘Emergence of coherence via transverse condensation in a uniform quasi-two-dimensional Bose gas’, *Nature Communications*, vol. 6, p. 6162, 2015. DOI: [10.1038/ncomms7162](https://doi.org/10.1038/ncomms7162) (cit. on p. 101).
- [322] J. L. Ville, T. Bienaimé, R. Saint-Jalm *et al.*, ‘Loading and compression of a single two-dimensional Bose gas in an optical accordion’, *Physical Review A*, vol. 95, no. 1, p. 013632, 2017. DOI: [10.1103/PhysRevA.95.013632](https://doi.org/10.1103/PhysRevA.95.013632) (cit. on pp. 101, 102).
- [323] A. L. Gaunt, ‘Degenerate Bose gases: Tuning interactions & geometry’, PhD Thesis, University of Cambridge, 2014 (cit. on p. 101).
- [324] G. Gauthier, I. Lenton, N. M. Parry *et al.*, ‘Direct imaging of a digital-micromirror device for configurable microscopic optical potentials’, *Optica*, vol. 3, no. 10, pp. 1136–1143, 2016. DOI: [10.1364/OPTICA.3.001136](https://doi.org/10.1364/OPTICA.3.001136) (cit. on p. 102).
- [325] S. P. Johnstone, A. J. Groszek, P. T. Starkey *et al.*, ‘Evolution of large-scale flow from turbulence in a two-dimensional superfluid’, 2018. arXiv: [1801.06952](https://arxiv.org/abs/1801.06952) [cond-mat.quant-gas] (cit. on p. 109).

- [326] *Data and analysis code for "Evolution of large-scale flow from turbulence in a two-dimensional superfluid"*, Figshare. DOI: [10.26180/5bdf9e6d58d59](https://doi.org/10.26180/5bdf9e6d58d59) (cit. on p. 109).
- [327] A. Rakonjac, A. L. Marchant, T. P. Billam *et al.*, 'Measuring the disorder of vortex lattices in a Bose–Einstein condensate', *Physical Review A*, vol. 93, no. 1, p. 013 607, 2016. DOI: [10.1103/PhysRevA.93.013607](https://doi.org/10.1103/PhysRevA.93.013607) (cit. on p. 114).
- [328] S. Birchfield, *Image Processing and Analysis*. Cengage Learning, 2016 (cit. on pp. 114, 115).
- [329] L. Rocha, L. Velho and P. C. P. Carvalho, 'Image moments-based structuring and tracking of objects', in *Proceedings of the XV Brazilian Symposium on Computer Graphics and Image Processing*, Fortaleza-CE, Brazil: IEEE, 2002, pp. 99–105. DOI: [10.1109/SIBGRA.2002.1167130](https://doi.org/10.1109/SIBGRA.2002.1167130) (cit. on pp. 115, 116).
- [330] S. Subhankar, Y. Wang, T.-C. Tsui *et al.*, 'A wavefunction microscope for ultracold atoms', 2018. arXiv: [1807.02871](https://arxiv.org/abs/1807.02871) [[cond-mat.quant-gas](#)] (cit. on p. 138).
- [331] M. McDonald, J. Trisnadi, K.-X. Yao *et al.*, 'Super-resolution microscopy of cold atoms in an optical lattice', 2018. arXiv: [1807.02906](https://arxiv.org/abs/1807.02906) [[cond-mat.quant-gas](#)] (cit. on p. 138).
- [332] S. W. Seo, W. J. Kwon, S. Kang *et al.*, 'Collisional dynamics of half-quantum vortices in a spinor Bose–Einstein condensate', *Physical Review Letters*, vol. 116, no. 18, p. 185 301, 2016. DOI: [10.1103/PhysRevLett.116.185301](https://doi.org/10.1103/PhysRevLett.116.185301) (cit. on p. 138).
- [333] S. Kang, S. W. Seo, J. H. Kim *et al.*, 'Emergence and scaling of spin turbulence in quenched antiferromagnetic spinor Bose–Einstein condensates', *Physical Review A*, vol. 95, no. 5, p. 053 638, 2017. DOI: [10.1103/PhysRevA.95.053638](https://doi.org/10.1103/PhysRevA.95.053638) (cit. on p. 138).
- [334] M. Kobayashi, Y. Kawaguchi, M. Nitta *et al.*, 'Collision dynamics and rung formation of non-Abelian vortices', *Physical Review Letters*, vol. 103, no. 11, p. 115 301, 2009. DOI: [10.1103/PhysRevLett.103.115301](https://doi.org/10.1103/PhysRevLett.103.115301) (cit. on p. 138).
- [335] T. Mawson, G. Ruben and T. Simula, 'Route to non-Abelian quantum turbulence in spinor Bose–Einstein condensates', *Physical Review A*, vol. 91, no. 6, p. 063 630, 2015. DOI: [10.1103/PhysRevA.91.063630](https://doi.org/10.1103/PhysRevA.91.063630) (cit. on p. 138).

COLOPHON

This document was typeset using the typographical look-and-feel `classicthesis` developed by André Miede and Ivo Pletikosić. The style was inspired by Robert Bringhurst’s seminal book on typography “*The Elements of Typographic Style*”. `classicthesis` is available for both \LaTeX and $\text{L}\text{\AA}\text{X}$:

<https://bitbucket.org/amiede/classicthesis/>

Hermann Zapf’s *Palatino* and *Euler* type faces were used. The “typewriter” text is typeset in *Bera Mono*, originally developed by Bitstream, Inc. as “Bitstream Vera”.

Graphs were generated using `PYTHON 2.7` with `matplotlib`. Most figures were drawn in Adobe Illustrator CC—the drawing of the vacuum system was generated in SolidWorks and the axicon mode was visualised using `visvis` in `PYTHON`. Diagrams of optical layouts included in this thesis made use of `ComponentLibrary`, a free, open collection of images for drawing diagrams related to laser optics. `ComponentLibrary` was created by Alexander Franzen and is licensed under a Creative Commons Attribution-NonCommercial 3.0 Unported License, available at:

<https://creativecommons.org/licenses/by-nc/3.0/>

`ComponentLibrary` is available for free download at:

<http://www.gwoptics.org/ComponentLibrary/>